COMMUNICATIONS

COMMUNICATIONS

Dear reader,

It is my pleasure to introduce you this special issue of COMMUNICATIONS – Scientific Letters of the University of Zilina, which is a post-conference issue of the ELEKTRO 2010 Conference.

The ELEKTRO 2010 Conference, organized by the Faculty of Electrical Engineering, was the eighth of the international series of conferences which began in 1995 initially as a national conference with international participation. The purpose of this Conference is to provide an international forum for researches, professionals and educationists interested in electrical and electronic engineering as well as boundary areas with the main attention to the following topics: Information and Communication Technologies and Services, Mechatronics and Electronics, Control and Information Systems in Transport and Industry, Trends in Theoretical and Applied Electrical Engineering, Materials and Technologies for Electrical Engineering.

The best papers of the Conference, selected by reviewers, have been extended, reviewed and published in this special issue. Let me express thanks to all authors, colleagues, reviewers, technical support of the Czechoslovakia section of IEEE, Industrial Application Society (IAS), Industrial Electronics Society (IES) and conference team who contributed and prepared this special post-conference issue of Communications - Scientific Letters of the University of Zilina.

Pavol Rafajdus

Felix A. Himmelstoss – Helmut L. Votzi *

COMBINED FORWARD-FLYBACK-CONVERTER WITH ONLY TWO DIODES – FUNCTION AND MODELLING

A combined forward and flyback converter with a simple two windings transformer, an inductor, an active switch, two diodes and a buffer capacitor is explained. The voltage transfer ratio and the demagnetizing condition are derived. The voltage transfer ratio of the new converter is significantly higher compared to the forward and the flyback converters. The converter is useful for applications where a flyback converter is too small and a forward converter with its complicate transformer is too expensive. By shunting the two diodes by a third one the efficiency can be increased and due to the reduced losses the cooling is easier. The state space equations of the different states of the converter are derived.

1. Introduction

The well-known classical forward converter [1, 2, 3, 4, 5] needs three windings. Two are used to transform the energy and the third one is necessary to demagnetize the core. The new combined forward-flyback converter (Fig. 1) needs only two windings [6]. The transformer is therefore easier to manufacture, is smaller, has lower weight and is therefore cheaper. No additional component compared to the classical forward converter is necessary. Some other concepts for forward converters are published [7, 8, 9, 10, 11, 12 and 13].

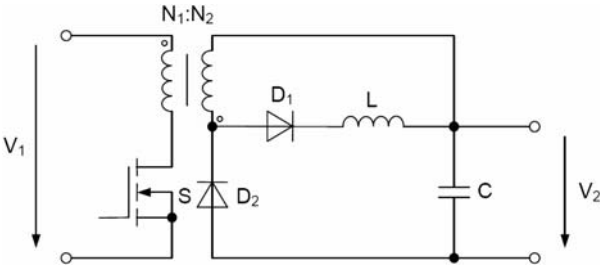

Fig. 1 Circuit of the combined forward-flyback converter

2. Function

To explain the principal function, the following assumptions are made: ideal devices, discontinuous inductor current mode (DICM), the circuit is in steady state condition, the output capacitor is so large that the output voltage is constant, and the input of the circuit is fed by a constant voltage source. The switching period can be divided into three states (Fig. 2).

A. State 1

The circuit diagram of state 1 is shown in Fig 2a. The active switch S is closed. The input voltage is applied to the primary winding N_1 and the input current rises linearly (dot and dash line). The voltage $(N_2/N_1)V_1$ is now across the secondary winding N_2. The secondary current now closes over the diode D_1, the output inductor L, and the secondary winding N_2 (dotted line). The current rises linearly according to

$$\frac{di_{N2}}{dt} = \frac{N_2}{N_1} \cdot \frac{V_1}{L}. \tag{1}$$

The load is supplied by the capacitor C (long dashed line). The input current consists of two components: the transformed secondary current and the current to magnetize the transformer (primary inductancewhich has N1 turns)

$$i_{N1} = \left[\left(\frac{N_2}{N_1}\right)^2 \cdot \frac{V_1}{L} + \frac{V_1}{L_1}\right] \cdot t \tag{2}$$

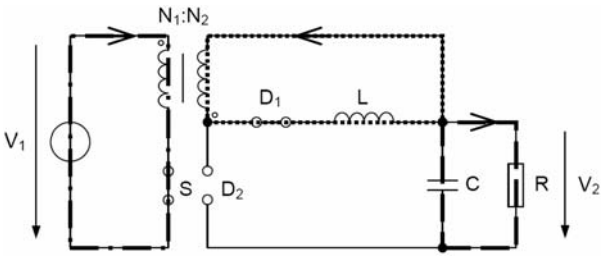

Fig. 2a State 1 of the combined forward-flyback converter

* **Felix A. Himmelstoss[1], Helmut L. Votzi[2]**
[1] University of Applied Science Technikum, Wien, Austria, E-mail: felix.himmelstoss@technikum-wien.at
[2] University of Technology Vienna, Institute of Electrical Drives and Machines, Wien, Austria

B. State 2

The circuit diagram of state 2 is shown in Fig 2b. The active switch S is turned off. As the magnetic fluxes have to be steady, two new current loops start to function. The current through the storage inductor L closes via capacitor C and the diodes D_1 and D_2 (short dash line). The magnetizing current commutates from winding N_1 into winding N_2 and closes via capacitor C and the diode D_2 (dotted line). The value of the magnetizing current in N_2 jumps at this moment to

$$i_{N2} = \frac{N_1}{N_2}\frac{V_1}{L_1}t_1 \tag{3}$$

and increases according

$$\frac{di_{N2}}{dt} = -\frac{V_2}{L_1}\cdot\left(\frac{N_1}{N_2}\right)^2 \tag{4}$$

until the current reaches zero and the transformer is demagnetized (cf. Fig. 3b). As in state 1 the load is parallel to the capacitor C (long dashed line). To avoid the loss caused by the series connection of the two diodes, a third diode in forward direction between the anode of the second diode D_2 and the cathode of the first diode D_1 has to be connected.

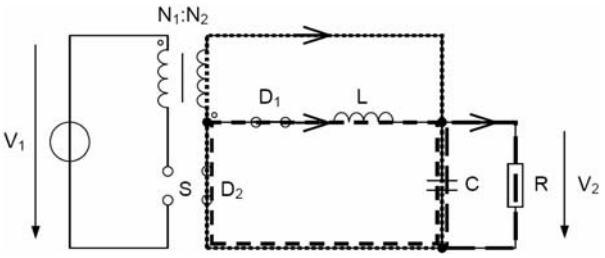

Fig. 2b State 2 of the combined forward-flyback converter

C. State 3

The circuit diagram of state 3 is shown in Fig. 2c. Both the transformer and the storage inductor are demagnetized. The load is supplied by capacitor C (long dashed line). Stage three ends when S is turned on again. The circuit is now in state1 again.

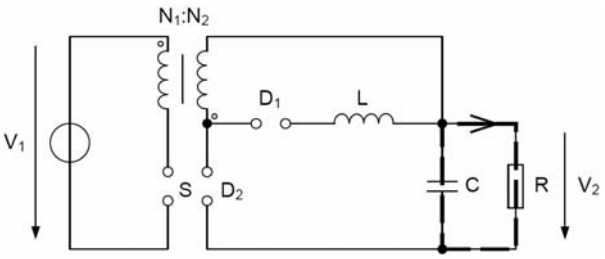

Fig. 2c State 3 of the combined forward-flyback converter

3. Voltage Transfer Rate

A. Combined forward-flyback converter

To calculate the voltage transfer rate of the combined forward-flyback converter, the assumption is used that the output power must be the same as the input power when ideal components are used

$$P_{out} = \frac{V_2^2}{R} = P_m\,. \tag{5}$$

The current in the inductor L (Fig. 3.a) rises during the on-time of the switch S according to

$$\Delta I_L = \frac{V_1}{L}\cdot\frac{N_2}{N_1}\cdot d\cdot T \tag{6}$$

and leads to a stored energy at the end of the on-time of the active switch of

$$W_L = \frac{\Delta I_L^2}{2}\cdot L\,. \tag{7}$$

The magnetizing energy of the transformer increases with the magnetizing current, which reaches

$$\Delta I_m = \frac{V_1}{L_1}\cdot d\cdot T \tag{8}$$

at the end of the turn-on time of the active switch leading to

$$W_m = \frac{\Delta I_m^2}{2}\cdot L_1\,. \tag{9}$$

During the off-time of the active switch this energy has to be decreased to zero, so that both inductive components are demagnetized again. Within one second the absorbed power of the converter is

$$\frac{V_2^2}{R} = f\cdot\left(W_L + W_m\right). \tag{10}$$

The output voltage can now be calculated according to

$$V_2 = \sqrt{R}\cdot\frac{V_1\cdot d}{\sqrt{2\cdot f}}\cdot\sqrt{\left(\frac{N_2}{N_1}\right)^2\cdot\frac{1}{L}+\frac{1}{L_1}} = K_C\cdot\sqrt{R}\cdot V_1\cdot d \tag{11}$$

with K_C as a constant consisting of the converter parameters inductor L, magnetizing (primary) inductance L_1, winding ratio N_2/N_1, and switching frequency f.

To compare the combined converter with the conventional forward and the conventional flyback converter, we have to calculate the output voltage in the discontinuous mode. The discontinues mode is necessary to demagnetize the inductive devices completely.

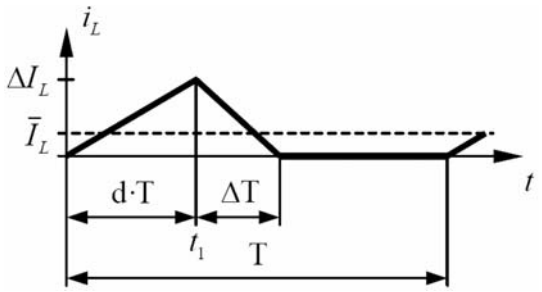

Fig. 3a Current through the inductor L

The transformer has to be demagnetized before the active switch is turned on again.

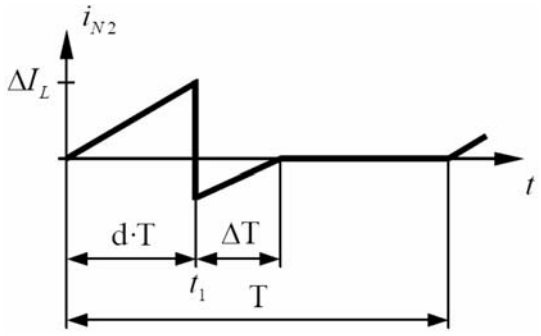

Fig. 3b Current through the secondary winding N_2

Duty cycle requirement

The converter has to be operated in the discontinuous mode. The maximum current through the inductor is

$$\Delta I_L = V_1 \cdot \frac{N_2}{N_1} \cdot \frac{d \cdot T}{L} \tag{12}$$

and the time that is needed for demagnetizing this coil is

$$T_{DL} = \frac{L \cdot \Delta I_L}{V_2} = d \cdot T \cdot \frac{V_1}{V_2} \cdot \frac{N_2}{N_1}. \tag{13}$$

It must be valid

$$d \cdot T + T_{DL} < T \tag{14}$$

and therefore we get the constraint

$$d \cdot \left(1 + \frac{V_1}{V_2}\frac{N_2}{N_1}\right) < 1\,. \tag{15}$$

The transformer has to be demagnetized completely. The maximum magnetizing current (8) on the primary side has to be converted by the winding ratio to the secondary side. The necessary demagnetization time of the converter is now

$$T_{DT} = \frac{V_1}{V_2} \cdot d \cdot T \cdot \frac{N_2}{N_1}. \tag{16}$$

It must be valid

$$d \cdot T + T_{DT} < T \tag{17}$$

and therefore we get again the constraint

$$d \cdot \left(1 + \frac{V_1}{V_2}\frac{N_2}{N_1}\right) < 1\,. \tag{18}$$

The demagnetizing time is the same for the inductor and the transformer.

With (11) and (18) we can write

$$d < 1 - \frac{N_2}{N_1} \cdot \frac{1}{K_C \cdot \sqrt{R}} \tag{19}$$

with converter coefficient

$$K_C = \sqrt{\left[\left(\frac{N_2}{N_1}\right)^2 \cdot \frac{1}{L} + \frac{1}{L_1}\right] \cdot \frac{1}{2 \cdot f}}\,. \tag{20}$$

B. Forward converter

To calculate the output voltage of the forward converter (Fig. 4), only the energy in the inductor has to be taken into consideration, the magnetizing energy of the transformer is fed-back to the input voltage source via the additional winding N_3. The maximum stored energy depends on the maximum inductor current which is reached at the end of the on-interval of the active switch

$$\Delta I_L = \left(\frac{N_2}{N_1} \cdot V_1 - V_2\right) \cdot \frac{1}{L} \cdot d \cdot T\,. \tag{21}$$

Within the time

$$\Delta T = L \cdot \Delta I_L \cdot \frac{1}{V_2} = \left(\frac{N_2}{N_1} \cdot V_1 - V_2\right) \cdot \frac{d \cdot T}{V_2} \tag{22}$$

the inductor is discharged. The mean value of the inductor current must be the same as the load current.

The input power of the converter is the input voltage multiplied by the mean value of the input current. The input current is triangular in shape. The input power is therefore

$$P_{in} = V_1 \cdot \frac{1}{T} \cdot \frac{1}{2} \cdot \frac{N_2}{N_1} \cdot \left(\frac{N_2}{N_1} \cdot V_1 - V_2\right) \cdot \frac{1}{L} \cdot d^2 \cdot T^2 \tag{23}$$

and this must be equal to the output power

$$P_{out} = \frac{V_2^2}{R} = V_1 \cdot \bar{I}_1 = P_{in}\,. \tag{24}$$

The output voltage of the forward converter in discontinuous mode can now be evaluated according to

$$V_2 = \frac{N_2}{N_1} \cdot \frac{R \cdot V_1 \cdot d^2}{4 \cdot L \cdot f} \cdot \left(-1 + \sqrt{1 + \frac{8 \cdot L \cdot f}{R \cdot d^2}}\right). \tag{25}$$

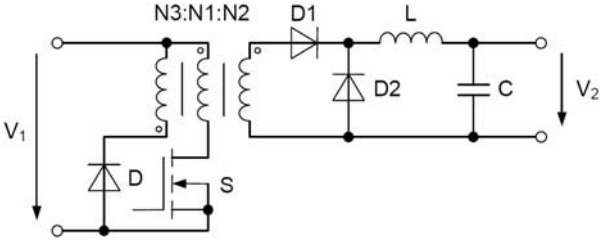

Fig. 4 Circuit of the classical forward converter

C. Flyback converter

The circuit diagram of the flyback converter is shown in Fig 5. Under the assumption of ideal components the output power must be the same as the input power

$$P_{out} = \frac{V_2^2}{R} = P_{in} . \tag{26}$$

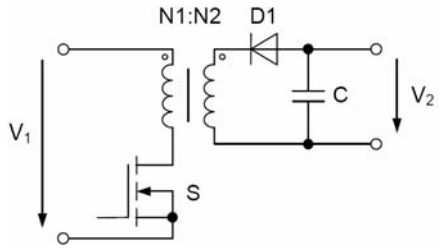

Fig. 5 Circuit of the classical flyback converter

The magnetizing energy of the transformer increases with the magnetizing current, which reaches

$$\Delta I_m = \frac{V_1}{L} \cdot d \cdot T \tag{27}$$

at the end of the turn-on time of the active switch leading to.

$$W_m = \frac{\Delta I_m^2}{2} \cdot L_1 \tag{28}$$

$$\frac{V_2^2}{R} = f \cdot W_m . \tag{29}$$

The output voltage can now be calculated according to

$$V_2 = \sqrt{\frac{1}{2 \cdot f \cdot L_1}} \cdot \sqrt{R} \cdot V_1 \cdot d = K_F \cdot \sqrt{R} \cdot V_1 \cdot d , \tag{30}$$

with K_F as a constant consisting of the magnetizing inductance L_1, and the switching frequency f.

4. Theoretical Results

The voltage transfer ratio of the three converters is compared for the same different load resistances, constant input voltage, and the same component values for all three topologies $L_1 = L_3 = = 300$ µH, $L_2 = 75$ µH, $L = 50$ µH.

The scales are the same for all diagrams. Fig. 6a shows the voltage transfer ratio of the combined forward-flyback converter and Figs. 6b and 6c show the voltage transfer rate for the forward and the flyback converter, respectively. The voltage transfer ratio of the new converter is significantly higher compared to the forward and the flyback converters.

5. Statespace Description of the Combined Converter

The state variables are the flux ϕ of the transformer, the inductor current i_L, and the capacitor voltage u_C. The input variable is the input voltage u_1. The fixed forward voltage of the diodes (the diodes are modeled as fixed forward voltages V_{D1}, V_{D2} and additional voltage drops depending on the differential resistors of the diodes R_{D1}, R_{D2}) are included as additional vectors. The parasitic

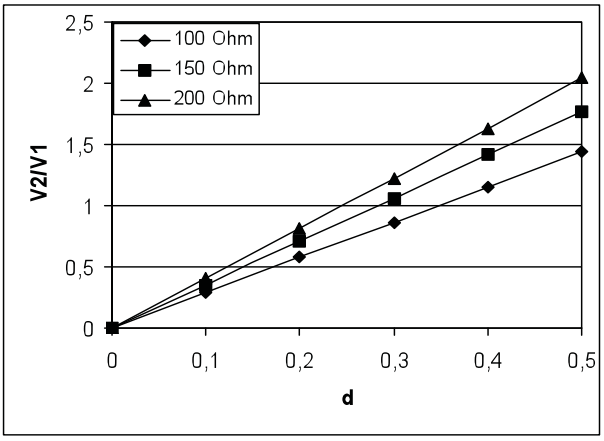

Fig. 6a Voltage transfer ratio of the combined forward-flyback converter

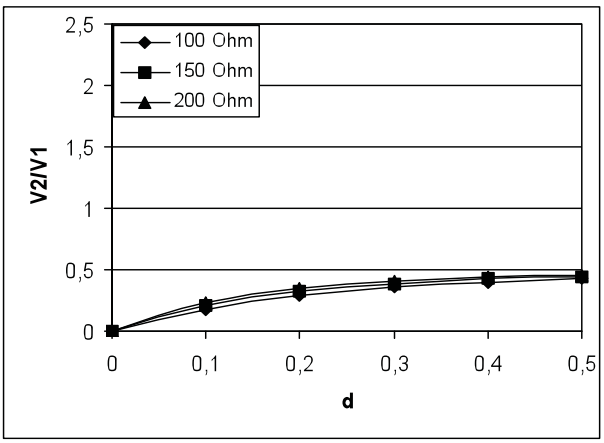

Fig. 6b Voltage transfer ratio of the classical forward converter

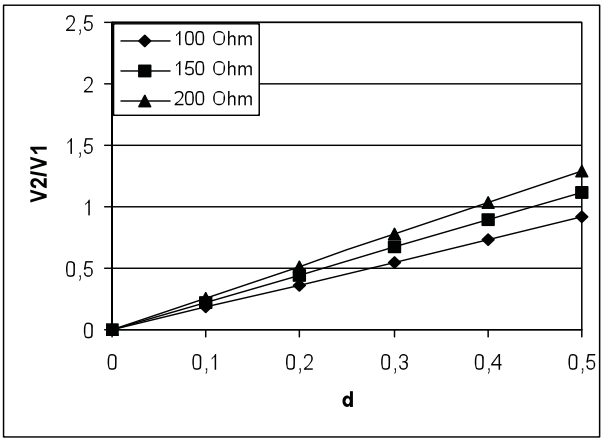

Fig. 6c Voltage transfer ratio of the classical flyback converter

resistances are the on-resistance of the active switch R_S, the series resistance of the coil R_L, the series resistor of the capacitor R_C, and the differential resistors of the diodes R_{D1}, R_{D2}. With the A_L value of the transformer material the primary inductor is $L_1 = = A_L \cdot N_1^2$ and the secondary inductor is $L_2 = A_L \cdot N_2^2$. The abbreviation $R_C//R$ describes the parallel connection of the serial resistor of the output capacitor and the load resistor.

In discontinuous inductor current mode there are three states. In state one the active switch is turned on and also the passive switch D_1 turns on. Fig. 7a shows this switching state one. There are other possibilities to analyze circuits with different methods like shown e.g. in [14]. This would be especially useful for calculating the spectrum for EMC analyses. The leakage inductor is not included. (The leakage inductor is small because of the bifilar winding and leads in practice to small reduction of the input voltage. The energy which is stored must be transformed into heat by a snubber circuit when the overvoltage across the active switch is too high.) The complete flux which is connected with the winding is $\psi = N \cdot \phi$.

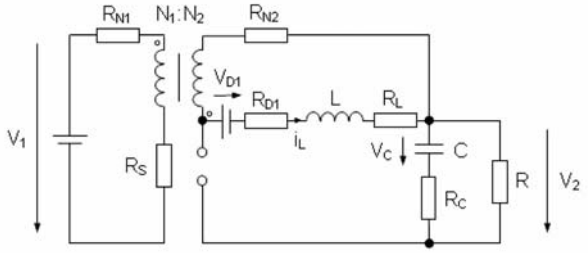

Fig. 7a Equivalent circuit for stage one

The state space description is

$$\frac{d}{dt}\begin{pmatrix}\phi\\ i_L\\ v_C\end{pmatrix} = \begin{bmatrix} -\dfrac{R_{N1}+R_S}{L_1} & 0 & 0 \\ -\dfrac{N_2}{L}\left(\dfrac{R_{N1}+R_S}{L_1}+\dfrac{R_{N2}}{L_2}\right) & -\dfrac{R_{D1}+R_L}{L} & 0 \\ 0 & 0 & -\dfrac{1}{C(R+R_C)} \end{bmatrix} \cdot \begin{pmatrix}\phi\\ i_L\\ v_C\end{pmatrix} + \begin{bmatrix}\dfrac{1}{N_1}\\ \dfrac{1}{L}\\ 0\end{bmatrix} \cdot v_1 \begin{pmatrix}0\\ -\dfrac{1}{L}\\ 0\end{pmatrix} \cdot V_{D1} \tag{31}$$

In state two the active switch S is turned off, the passive switch D_1 is still conducting, and the second passive switch D_2 turns on. Fig. 7b shows this switching state two. The state space description is

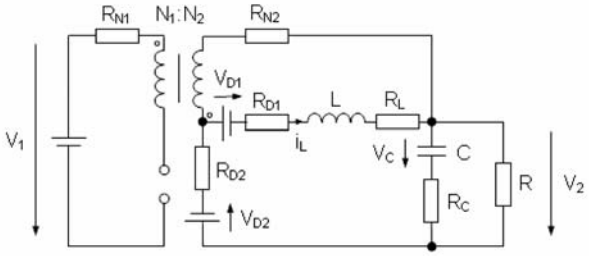

Fig. 7b Equivalent circuit for stage two

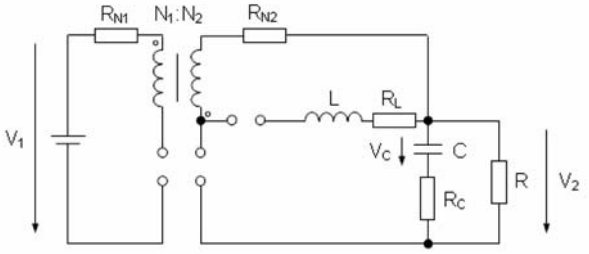

Fig. 7c Equivalent circuit for stage three

When the transformer and the coil are demagnetized the load current discharges the capacitor. Fig. 7c shows this switching state three. The change of the capacitor voltage is now

$$\frac{d}{dt}v_C = -\frac{v_C}{C(R+R_C)}. \tag{33}$$

$$\frac{d}{dt}\begin{pmatrix}\phi\\ i_L\\ v_C\end{pmatrix} = \begin{bmatrix} -\dfrac{R_C//R+R_{D2}+R_{N2}}{L_2} & -\dfrac{R_C//R+R_{D2}}{N_2} & -\dfrac{R}{N_2(R+R_C)} \\ -\dfrac{R_C//R+R_{D2}}{L\cdot L_2} & -\dfrac{R_C//R+R_{D1}+R_{D2}+R_L}{L} & -\dfrac{R}{L(R+R_C)} \\ \dfrac{R}{C(R+R_C)} & \dfrac{N_2R}{CL_2(R+R_C)} & -\dfrac{1}{C(R+R_C)} \end{bmatrix} \cdot \begin{pmatrix}\phi\\ i_L\\ v_C\end{pmatrix} + \begin{bmatrix}0\\ 1\\ \dfrac{L}{0}\end{bmatrix} \cdot V_{D1} \begin{pmatrix}-\dfrac{1}{N_2}\\ 0\\ 0\end{pmatrix} \cdot V_{D2} \tag{32}$$

6. Measurement Results

Now some experimental results of the new converter topology will be shown. In Fig. 8 the voltage across the active switch (Ch2:

20 V/div) and the current through the inductor (Ch1: 2 A/Div) can be seen. The results follow as predicted.

For more convenient measuring, a two-diode-combined-forward-flyback converter with a tapped inductor (autotransformer) was built (Fig. 9). The winding ratio is one to one and the windings are bifilar. The inductor L was realized with an isolated stranded wire and with a gapped core. No snubber was necessary because of the low leakage inductance of the autotransformer. The converter was used with open loop control.

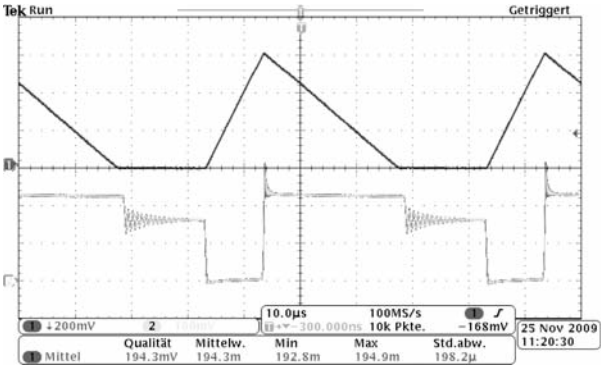

Fig. 8 Current through the inductor (Ch1: 2 A/Div) and voltage across the active switch (Ch2: 20 V/div)

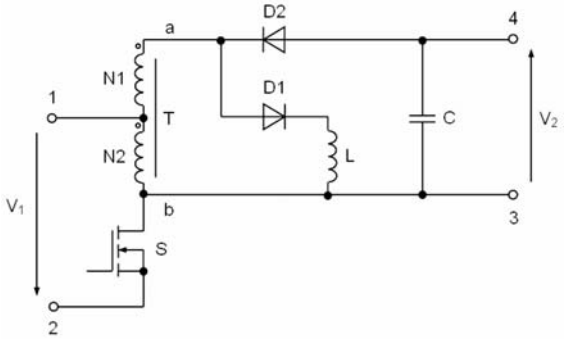

Fig. 9 Autotransformer two-diode-combined-forward-flyback converter

Figs. 10 and 11 show (up to down) the voltage across the active switch, the current through the inductor, and the current through the winding N_1; the input voltage is 24 V, the load is 11 Ohm and the duty cycle is 16% and 45% respectively. The output voltage is 14 V with the small duty cycle, and 38 V with the higher one.

The most interesting signal is the current through the autotransformer winding N_1. During the on-time of the active switch, the current is the same as the one in the filter inductor. When the transistor turns off, the current of the inductor is freewheeling, and through N_1 now flows the magnetizing current of the autotransformer.

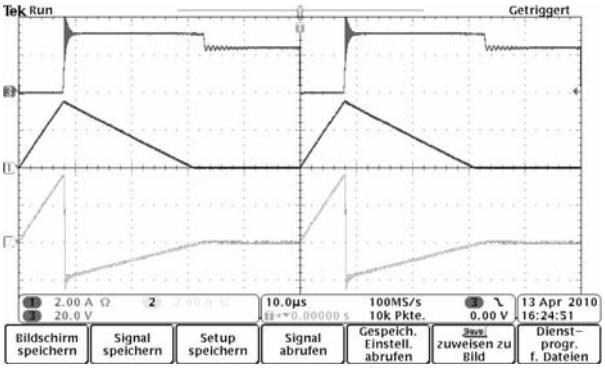

Fig. 10 Voltage across the active switch (Ch3: 20 V/div), current through the inductor (Ch1: 2 A/Div), and current through the winding N1 (Ch2: 2 A/Div); input voltage 24 V, duty cycle 16%, output voltage 14 V, load 11 Ohm.

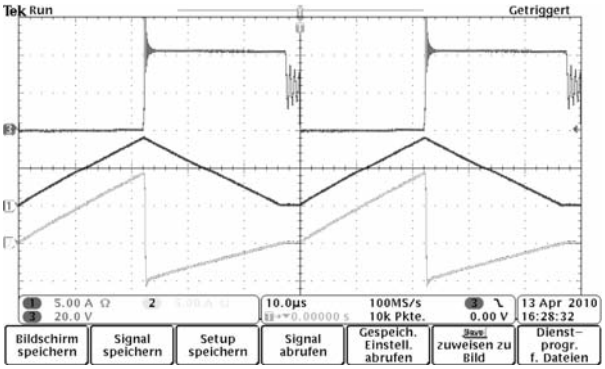

Fig. 11 Voltage across the active switch (Ch3: 20 V/div), current through the inductor (Ch1: 5 A/Div), and current through the winding N1 (Ch2: 5 A/Div); input voltage 24 V, duty cycle 45%, output voltage 38 V, load 11 Ohm.

7. Conclusion

The combined forward-flyback converter with two diodes has three interesting aspects. Due to the fact that the voltage across the secondary winding N_2 and across the inductor L is the same, the converter must be used in the discontinuous mode. The transformer has to be demagnetized before the active switch is turned on again. This has the advantage that from the control point of view the converter is only a first order system, as all magnetic elements have no energy at the beginning of all switching periods. All diodes turn off naturally, no forced commutation occurs and this leads to reduced switching losses and a better efficiency. For the same values of the components more power can be transformed compared to the forward and flyback converter. A higher output voltage can be achieved by the same duty ratio compared to the forward and flyback converter. The converter is useful for applications where a flyback converter is too small (flyback converters have the disadvantage that for higher power ranges a big trans-

former has to be used) and a forward converter with its complicated transformer is too expensive. By shunting the two diodes by a third one, the efficiency can be increased and due to the reduced losses the cooling is easier. The converter is especially useful for renewable energy applications and for compact systems.

Acknowledgment

The authors are very grateful to the city council of Vienna which supports the Technikum Wien with new measurement equipment by the project MA 27-Projekt 09-32.

References

[1] MOHAN, N., UNDELAND, T., ROBBINS, W. P.: Power Electronics. *John Wiley & Sons,* New York, 2003.
[2] ZACH, F.: Leistungselektronik. *Springer,* Wien, 2010.
[3] ERICKSON, R. W., MAKSIMOVIC, D.: Fundamentals of Power Electronics. *Springer Science+Business Media,* Inc., New York, 2001.
[4] BOSE, B.: *Power Electronics and Motor Drives.* Elsevier Academic Press, 2006.
[5] KAZMIERKOWSKI, M. P.: Control in Power Electronics. Selected Problems. *Academic Press Series in Engineering,* 2002.
[6] HIMMELSTOSS, F., HOFFELNER, A., VOTZI, H.: *Kombinierter Sperr-Durchflusswandler.* Austrian Patent AT 506327 B1, Aug. 2009.
[7] CHANGCHIEN, S.K., LIANG, T.J., TSENG, K.C., CHEN, J.F., LIN, R.L.: A Demagnetization Circuit for Single-ended Forward Converter. *IEEE IECON*. pp. 1390–1395, 2007.
[8] JIN, T., ZHANG, K., AZZOLINI, A., SMEDLEY, K.M.: A New Interleaved Forward Converter with Inherent Demagnetizing Feature. *IEEE IAS*. Vol. 1, pp.625–630, 2005.
[9] FARCAS, C., PETREUS, D., SIMION, E., PALAGHITA, N., JIHOS, Z.: A Novel Topology Based on Forward Converter with Passive Power Factor Correction. *ISSE*. pp. 268–272, Oct. 2006.
[10] GALLO, C.A.,TOFOLI, F.L.,SCARPA, V.V.R., DE FREITAS, E.A.A. , VIEIRA, J.B. Jr.: Proposal of a SMPS with AC Output Voltage Employing a Quadratic Boost Converter, a new Topology of Soft-switched Two-switch Forward Converter and a New Topology of PWM Three-level Half-bridge Inverter. *IEEE PESC*, Vol. 4, pp. 2604–2610, June, 2004.
[11] ZHANG, M.T., JOVANOVIC, M.M., LEE, F.C.: Analysis, Design, and Evaluation of Forward Converter with Distributed Magnetics-interleaving and Transformer Paralleling. *APEC*, Vol. 1, pp. 315–321, March, 1995.
[12] BRIDGE. C.D.: Clamp Voltage Analysis for RCD Forward Converters. *IEEE APEC*, Vol. 2, pp. 959–965, Feb. 2000.
[13] HIMMELSTOSS, F.A., VOTZI, H.L.: Comparison of a New Combined Four-diode Forward-flyback Converter with the Classical Forward Converter. *IEEE ISSCS*, pp. 493–496, July 2009.
[14] ZASKALICKA, M., ZASKALICKY, P., BENOVA, M., ABDALMULA, M.A.R., DOBRUCKY, B.:Analysis of Complex Time Functions of Converter Output Quantities Using Complex Fourier Transform/Series, *Communications - Scientific Letters of the University of Zilina,* No. 1, pp. 23–30, 2010.

Asimakis Lykourgiotis – Stavros Kotsopoulos *

PROTOCOLS PERFORMANCE IN NEXT GENERATION NETWORKS

Next Generation Network (NGN) is a packet-based network integrating legacy networks and providing "anywhere, anytime and on any device" ubiquitous services. One of the prerequisites of NGN is to support generalized mobility making Mobility Management (MM) a crucial factor towards a seamless provision of multimedia applications. A very promising scenario is the design and implementation of a UMTS / WLAN interworking architecture. In literature a variety of MM protocols operating from different layers of the protocol stack have been proposed. Nevertheless, the comparison of them has been less extensive mainly narrowed between extensions of the same protocol or different basic protocols. In this article a comprehensive comparison between the most efficient approaches of well-known mobility protocols in UMTS/WLAN networks is presented. It is worth noting that the comparison includes not only theoretical but also experimental handoff analysis using OPNET Modeler 15.0 and evaluating the protocols on both non real-time and real-time applications.

1. Introduction

A NGN is a packet-based network able to provide services including Telecommunication Services and able to make use of multiple broadband, QoS-enabled transport technologies in which service-related functions are independent from underlying transport-related technologies. It supports generalized mobility which will allow consistent and ubiquitous provision of services to users.

Evolution to NGN is a process in which parts of the existing networks are replaced or upgraded to the corresponding NGN components providing similar or better functionality, while maintaining the services provided by the original network. One of the most attractive ideas is the design and implementation of a UMTS/WLAN interworking architecture.

In telecommunications, Internet and Mobile Telecommunications services are deemed as the most important breakthroughs over the past decades. Through Third Generation (3G) systems Mobile Telecommunications gained access to the Internet. Universal Mobile Telecommunication System (UMTS) is the most widely deployed 3G network. UMTS provides high mobility and wide coverage area but lacks in means of data rate and cost. Conversely, Wireless Local Area Networks (WLAN) services are inexpensive and have a high bandwidth but cover small areas and allow limited mobility. These complementary characteristics of both wireless technologies in conjunction with their high penetration prompt the idea of interoperability.

This requires inter-technology MM, which can take place in several layers of communication. MM is divided into two tasks: Location Management and Handoff Management. The former enables the system to track the locations of Mobile Nodes (MNs) between consecutive communications. The latter is the process by which a MN keeps its connection active when it moves from one access point to another. The most important characteristic of the Handoff Management is the Handoff Delay, which is the time interval between last packet received before the link loss and the first packet received through the new link. In NGN there are two types of handoff: Horizontal and Vertical. A horizontal handoff is a handoff between two network access points (AP) that use the same network technology where as a Vertical handoff is a handoff between APs of different network technologies.

Several MM protocols have been proposed through the years implemented in different layers of protocol stack. The Mobile Internet Protocol (MIP) [1], [2] is the most well known Network-layer solution for MM. Despite the fact that is a mature protocol it has been slowly deployed in real networks as it suffers from high Handoff Delay due to Triangular Routing, high packet loss rate and conflicting security issues. On the other hand, mobile Stream Control Transmission Protocol (mSCTP) [3] is a Transport-layer efficient solution with main characteristic the multi-homing, which allows a MN to be reachable through different IP addresses. Finally, in the Application Layer, the Session Initiation Protocol (SIP) [4] has been proposed as a MM protocol.

The rest of the article is organized as follows. In Section 2 a brief description of the most important candidate protocols for MM is given. In Section 3 a theoretical analysis of Handoff Delay for the most efficient extensions of the basic protocols is presented. In Section 4, the results were obtained through simulation using

* **Asimakis Lykourgiotis, Stavros Kotsopoulos**
Wireless Telecommunications Laboratory, Department of Electrical and Computer Engineering, University of Patras, Greece,
E-mail: asly@ece.upatras.gr

OPNET Modeler 15.0 are discussed. In Section 5, we conclude the paper by summarizing our findings and suggesting potential future research efforts.

2. Basic Mobility Protocols

2.1 Mobile IP

The MIPv4[1] was introduced to allow the MN to gain access to the Internet by utilizing two IP Addresses, one for identification called Home Address (HoA), the other for routing called Care of Address (CoA). According to MIPv4, every domain must have a router called Home Agent (HA), so as to allow roaming of its users and a router called Foreign Agent (FA), so as to accept visitors. Every time a MN enters a Foreign Network, it registers with the FA and obtains a CoA. Then the FA informs the HA of the MN's current CoA. Every time a Correspondent Node (CN) establishes a connection with the MN, it sends packets to MN through the HA. This deficient way of communication is called Triangular Routing and is one of the main downsides of the protocol. Some other drawbacks of the protocol are the limited number of IP addresses and the vulnerability against malicious attacks. The Mobile IPv6 (MIPv6) [2] was introduced as a standard that surpasses the drawbacks of the previous version. A fundamental sub-protocol of Mobile IPv6 is the Return Routability Protocol (RRP). The RRP is a procedure by which a CN carries out a minimal verification that a MN owns an address (HoA) and is reachable at another (CoA). With the RRP the CN can be informed for the CoA and send packets directly to the MN, solving the problem of Triangular Routing. Moreover, MIPv6 also eliminates the use of FA as the MN is capable of performing its own mobility procedures, involves more sophisticated security procedures and provides a wider range of IP addresses.

2.2 Mobile SCTP

Stream Control Transmission Protocol (SCTP) is a Transport-layer protocol which was designed to face the drawbacks of TCP. A dominant characteristic of SCTP is multi-homing, making it a candidate protocol for Handoff Management in all-IP networks. To accomplish that, a new module was added called ADD-IP which leaded to the extension named mSCTP [3]. On the other hand, mSCTP does not support Location Management and must be used along with another mobility protocol such as MIP or SIP. A connection between two SCTP-endpoints is called an association. Multi-homing allows each point of the association to maintain more than one IP Address. Among that set of addresses one is used as Primary Address. The ADD-IP module allows the endpoints to add, delete or change the Primary IP address dynamically during the handoff procedure. As a result, a MN can prepare a new path before the breakdown of the active one and perform a soft handoff. mSCTP can be used to provide seamless handoff without requiring any additional mobility agents. So, the only requirement for providing the soft handoff is that both the MN and CN are equipped with the mSCTP implementations.

2.3 Session Initiation Protocol

SIP [4] is a signaling protocol which was initially used to handle multimedia sessions such as Voice over IP (VoIP). SIP was accepted as a 3GPP signaling protocol and permanent element of the IP Multimedia Subsystem (IMS) architecture for IP based streaming multimedia services [5]. Additionally, SIP resides at the Application Layer and can support MM. SIP introduces several new entities like User Agent (UA), proxy server and registrar. An UA is an interface agent responsible for initiating, exchanging messages and terminating a SIP session. A proxy server is an intermediate entity that receives a request and forwards it on behalf of the requestor. Proxy server uses location services to trace an UA and checks its ability to communicate. Finally, the registrar server enables clients to alter the address at which they can be contacted. The SIP user address is called Uniform Resource Identifier (URI) and has an email format (user@host). The SIP protocol supports two kinds of handoffs. The former is called Pre-Call as it determines that the MN enters a new foreign network before the initiation of a session. The latter is called Mid-Call because the MN enters a new foreign network while having an ongoing session. In this case the SIP re-INVITE method is used. One of the advantages of SIP is that it supports session mobility without any modifications of lower layer protocols. As for data delivery, with SIP data are exchanged directly between MN and CN without involving any tunneling.

3. Handoff Delay Analysis

Below, the Handoff Delay analysis of the four more efficient extensions, as indicated in publications, of the forementioned basic protocols is presented. As mentioned before, two types of handoff occur in an integrated UMTS / WLAN architecture: horizontal and vertical. The horizontal handoff procedure can be divided in four stages. Firstly, the MN detects it has moved to a different network (Move Detection – MD) and authenticates itself to an Authentication, Authorization, and Accounting (AAA) server so as to get access to the network. Afterwards, the MN obtains a new IP address (Address Configuration – AC). Finally, MN registers its new location and address (Registration-REG).

In the vertical handoff scheme, assuming that the MN can use the two different interfaces simultaneously, the MD and AC procedures are performed while the connection with the CN is continued. Thus, the vertical handoff delay is decreased to the AAA and REG delay. In further analysis, the delay of procedure X is denoted by T_X and the one-way transmission delay between node X and Y by T_{X-Y}.

3.1 Route Optimization in MIPv4

The most important extension of MPIv4 is the Route Optimization in MIPv4 (MIPv4-RO) [6], which solves the Triangular Routing problem. The handoff procedure comprises the following steps. Firstly, the MN moves into a new subnetwork and the MD

process is initiated. Then the MN performs the AAA process. The MD process is performed by receiving an Agent Advertisement (AA) message from the new Foreign Agent (FA), containing the network prefix. Then, the MN obtains a new Care-of-Address (CoA) from the FA or a DHCP server. In the end, the REG process takes place by sending a Registration Request (RR) to the FA. FA forwards a BU to the HA. The HA replies with a Binding Acknowledgement (BA) message. The FA notifies the MN of the successful registration with a Registration Reply (RRp) message. Direct communication between MN and CN is possible through Route Optimization. The MN can send a registration packet to the CN to inform it for its new CoA. The CN, then sends a BA to both MN and HA. For our analysis we assume that $T_{HA\text{-}CN} < T_{CN\text{-}MN}$, and so we use the latter. Therefore, the T_{REG} is:

$$T_{REG}^{MIPv4-RO} = T_{VHO} = T_{MN-HA} + T_{HA-CN} + T_{CN-MN}, \quad (3)$$

While, the horizontal handoff delay:

$$D_{HO}^{MIPv4-RO} = T_{MD} + T_{AAA} + T_{AC1} + T_{REG}^{MIPv4-RO}, \quad (4)$$

3.2 Proxy Mobile IPv6

PMIPv6 is a protocol implementing MM procedures in network part without involving the MN. For that purpose, two new functional entities are introduced in PMIPv6, the Local Mobility Anchor (LMA) and the Mobility Access Gateway (MAG).The LMA is the topological anchor point for the MN's home network prefix, receiving any packets that are sent to the MN by any node in or outside the PMIPv6 domain. The LMA is Home Agent with enhanced capabilities for supporting PMIPv6. The MAG is a new functional entity that emulates the MN's home link on the access link. To do so, the MAG sends Router Advertisement messages, containing the MN's home network prefix. Typically, it is a function runs on an Access Router (AR). PMIPv6 supports multihoming by allowing the MN to connect to a domain through multiple interfaces for simultaneous access. By this means, PMIPv6 does not require move detection and address configuration procedures to be performed during handoff reducing handoff delay and signaling. Additionally, network-based mobility management is compatible with current devices and reduces signaling exchange through the wireless link, so as to accomplish the initial goals.

In this analysis, we investigate only the handoffs occurred between PMIPv6 subnets. When a MN enters the serving area of a MAG performs the AAA. Then the MAG obtains the MN's profile and sends PBU to the LMA. Finally the LMA replies with a Proxy Binding Acknowledgement (PBA) and sets up a bidirectional tunnel with the MAG in order to use the MN's home network prefix over it.

So the registration delay, which is also the vertical handoff delay (VHO), is constrained to the messages exchange between MAG and LMA and the transmission of packets from the MAG to the MN:

$$T_{REG}^{PMIPv6} = T_{VHO} = 2 \times T_{MAG-LMA} + T_{MAG-MN}, \quad (1)$$

And the horizontal handoff delay:

$$D_{HO}^{PMIPv6} = T_{AAA} + T_{REG}^{PMIPv6}, \quad (2)$$

3.3 Cellular SCTP

The Cellular SCTP (cSCTP) [9] is an extension of mSCTP. In contrast with mSCTP, the cSCTP does not await the ADD-IP_set_primary chunk to be sent to the CN but sends duplicate packets through old and new path by the receiving of the ADD-IP ASCONF-ACK chunk. With this extension the registration delay is reduced and less packet retransmissions occur as the data are transferred via two different paths reducing the probability of MN's missing the packets. cSCTP is proposed to be used with SIP because, as mSCTP, doesn't support Location Management. Hence, the registration delay for the cSCTP is the time between sending an ASCONF_add_ip chunk and receiving an ASCONF-ACK_add_ip chunk:

$$T_{REG}^{cSCTP} = T_{VHO} = 2 \times T_{MN-CN}, \quad (5)$$

The horizontal handoff delay is:

$$D_{HO}^{cSCTP} = T_{MD} + T_{AAA} + T_{AC2} + T_{REG}^{cSCTP}, \quad (6)$$

3.4 Mobility Management Using SIP Extension

MMUSE [10] is an important extension of SIP as shown by the results. MMUSE introduces a new intermediate entity named Mobility Management Server (MMS) to be in charge of managing terminal mobility. The MMS can be considered as an extended Session Border Controller (SBC). A SBC is a router which is located at the border of the Home Network and acts as a SIP proxy for signaling. With the legacy SIP re-INVITE method signaling messages are exchanged between the MN and the CN, whereas with the MMUSE approach the exchange is between MN and MMS. By controlling the location of MMS, MMUSE decreases the handoff delay. Additionally, as the CN is not involved in the handoff procedure legacy devices can be used. In MMUSE, when the MN enters a new subnet, it obtains a new IP address through a DHCP server. Afterwards, the registration process is performed where the MN sends a SIP HO-Reg to the MMS, which responds with a 200 OK message. Then, the registration delay is:

$$T_{REG}^{MMUSE} = T_{VHO} = 2 \times T_{MN-MMS}, \quad (7)$$

And the horizontal handoff delay is:

$$D_{HO}^{MMUSE} = T_{MD} + T_{AAA} + T_{AC2} + T_{REG}^{MMUSE}, \quad (8)$$

For analytical purpose, we will take the following assumption:

1. Based on the protocol architectures the entities introduced from each protocol follow the mapping shown in Fig. 1. For example, the FA location of MIPv4 is the same as the MAG

of PMIPv6 because both reside in the AR of the Foreign Network.

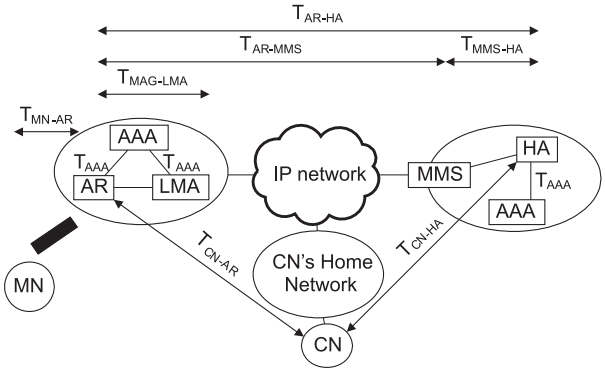

Fig. 1 Architectural Model

2. The delay of DAD procedure is extremely high and it is inefficient to use it. As our main goal is to examine the handoff signaling delay of the protocols we will not take in to account the DAD delay.
3. The AAA procedure (like DIAMETER) is the same for all evaluated protocols.

Moreover, we have made the following calculations:

1. The SIP and mSCTP protocols do not support any MD mechanism and thus they use the one implemented by the Network Layer called Router Discovery. In [2] it is specified that routers must send unsolicited RA in small intervals with MinRtrAdvIntrvl as smaller value and MaxRtrAdvIntrvl as maximum. So the MD mechanism is the same for all the protocols with a mean value of :

$$T_{MD} = \frac{MaxRirAdvIntrvl + MinRtrAdvIntrvl}{2}, \qquad (9)$$

2. For the current analysis, we will consider Stateful Address Configuration through a DHCP server. For MIP-based protocols, this is a one round-trip process, so:

$$T_{AC1} = 2 \times T_{MN-DHCP}, \qquad (10)$$

For SIP-based protocols, this is a two round-trip process, so:

$$T_{AC2} = 4 \times T_{MN-DHCP}, \qquad (11)$$

Fig. 2 summarizes the message flows of the forementioned protocols.

4. Experimental Handoff Analysis

The simulation results were obtained by OPNET Modeler 15.0. The main idea was to create a custom node model (named Mobility Node) which intervenes between the MN and CN and simulates the mobility's protocol behavior similar with [11]. In

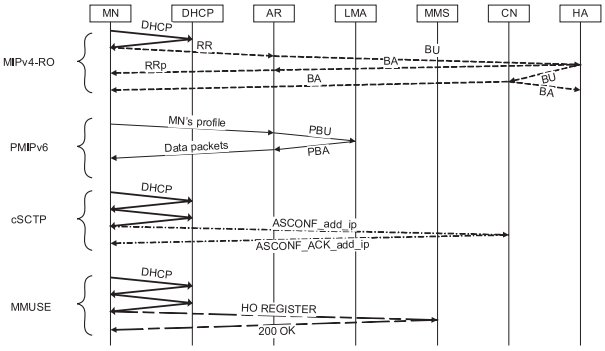

Fig. 2 Message Flow

[11] the assumption that T_{REG} and T_{MN-CN} are proportional is made. According to previous analysis T_{REG} is also affected by T_{MN-HA}. In our proposed model T_{REG} is calculated based on our analysis showing the influence of both factors.

In Fig. 3 the Logic Diagram of our proposed model is presented. Each time a new packet arrives to the Mobility Node, it is checked if the packet is a handoff initiation message. If so, the Mobility Node is set to handoff mode. Then, the handoff delay is calculated. The Mobility Node stays in handoff mode for a time interval equals to the handoff delay, dropping every packet that arrives during this interval. The Mobility Node returns to normal mode when the handoff delay time passes. If the arriving packet is a data packet, it is checked if the Mobility Node is in handoff mode. If so, the packet is dropped, if not it is forwarded, adding the related transmission delay. In our simulation, both IEEE 802.11g WLAN and UMTS operate at full mobility (80 km\hr). That results to a data rate of 384 Kbps for UMTS and 15 Mbps for WLAN. An extra delay is added or subtracted due to wireless link's data rate.

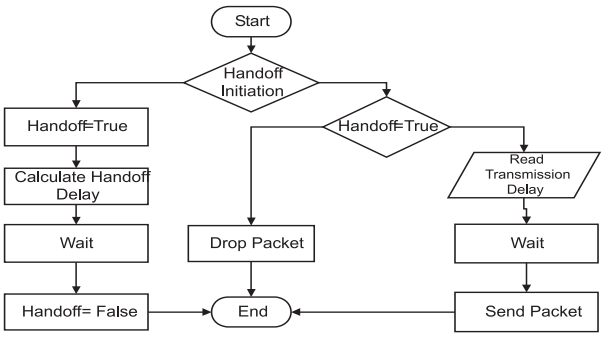

Fig. 3 Logic Diagram

For our analysis, we used the parameters that are outlined in Table 1. All these values are similar to those given in related work in [8], [12].

Firstly, in order to evaluate the four handoff mechanisms we plot the handoff delay as function of T_{MN-CN} (Fig. 4) and as function of T_{MN-HA} (Fig. 5).

Parameter setting values Table 1.

Parameter	Value	Parameter	Value
T_{AAA}	**12 ms**	$T_{HA–MN}$	**20 ms**
$T_{MN–CN}$	**20 ms**	$T_{MN–MMS}$	**10 ms**
$T_{MN–DHCP}$	**12 ms**	T_{MD}	**50 ms**
$T_{MAG–LMA}$	**10 ms**	$T_{HA–CN}$	**10 ms**

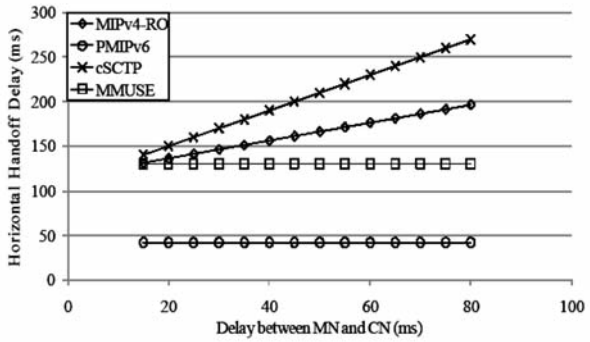

Fig. 4 Handoff Delay vs. delay between MN and CN

It can be observed that handoff delay of PMIPv6 is the smallest, because the MD and AC procedures are not required. Moreover, the protocol is not affected by the change of $T_{MN–CN}$ or $T_{MN–HA}$. On the other hand MIPv4-RO is affected by both factors. The MMUSE is only affected by $T_{MN–HA}$ whereas the cSCTP is only affected by $T_{MN–CN}$. Both protocols have a greater slope than MIPv4-RO.

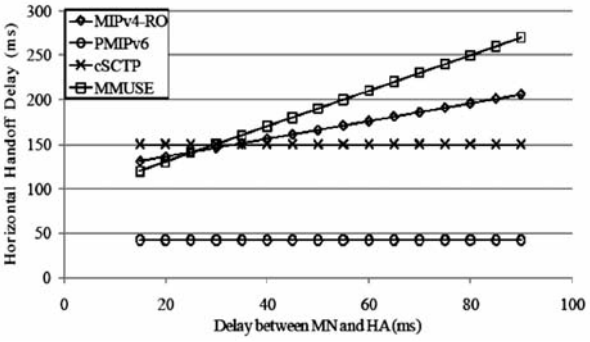

Fig. 5 Handoff Delay vs. delay between MN and HA

Consequently, we evaluated the protocols on both non real-time (FTP) and real-time (VoIP) applications. For FTP, the important metric is the throughput which is affected by the transmission delay. For MIPv4-RO, cSCTP and MMUSE the transmission delay is the same as these protocols enabled direct communication between MN and CN, resulting to same throughput. On the other hand, in PMIPv6 the traffic is sent through the tunnel between LMA and MAG, resulting to larger transmission delay. Fig. 7 shows the impact of all types of handoff that can occur in a UMTS / WLAN network on throughput. It is observed that PMIPv6 has smaller throughput than other protocols especially in WLAN where the wireless link delay is smaller.

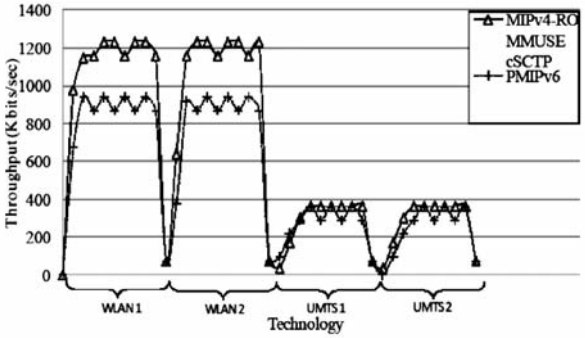

Fig. 7 Throughput vs. Technology

For VoIP we used the G.711 codec which provides a data rate equal to 100 packets/sec and we set $T_{MN–CN} = T_{MN–HA} = 30$ ms. The important metric in this simulation is the number of lost packets during handoff. As shown in Fig. 8 PMIPv6 achieves less packet loss for all types of handoff.

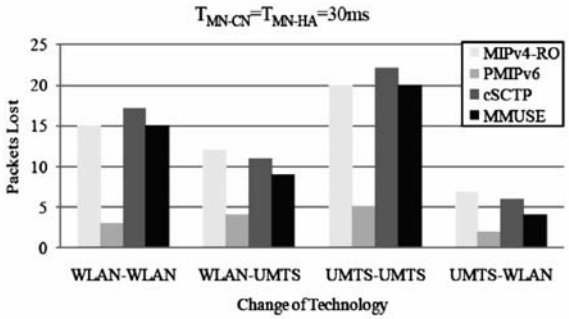

Fig. 8 Lost Packet vs. Type of Handoff
($T_{MN–CN} = T_{MN–HA} = 30$ ms.)

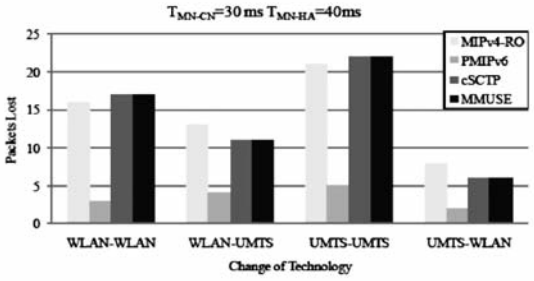

Fig. 9 Lost Packet vs. Type of Handoff
($T_{MN–CN} = 30$ ms, $T_{MN–HA} = 40$ ms.)

Furthermore, we repeated the simulation in order to observe the impact of $T_{MN–HA}$, by increasing its value to 40 ms. As shown in Fig. 9 PMIPv6 and cSCTP are not influenced as Handoff Delay is the same. On the contrary, in MIPv4–RO lost packets increased by one and in MMUSE by two.

Finally, we set $T_{MN–CN}$ to 40 ms. As shown in Fig. 10, in this case PMIPv6 and MMUSE are not influenced as Handoff Delay is the same. On the contrary, in MIPv4–RO lost packets increased by one and in cSCTP by two.

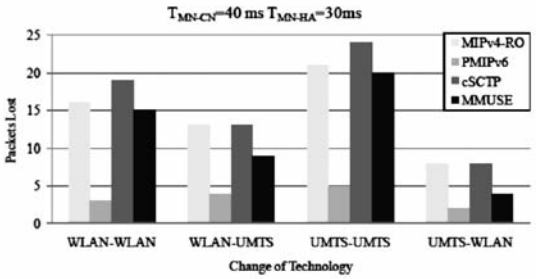

Fig. 10 Lost Packet vs. Type of Handoff ($T_{MN–CN}$ = 40 ms , $T_{MN–HA}$ = 30 ms.)

5. Conclusions

To the best of our knowledge, this is the first article that evaluates PMIPv6 against the most efficient protocols for mobility management in integrated UMTS/WLAN networks. In this article, we presented a PMIPv6 protocol overview. Firstly we obtained analytical results for performance evaluation of the candidate protocols and then proceeded to simulations for both real-time and non-real-time applications PMIPv6 is proven to be the best solution, in terms of handoff delay as it does not have any dependence on the distance between MN and both CN and HA because the MD and AC are not required. As a result the PMIPv6 is the protocol with the least packet loss during handoff. Simulation results showed that PMIPv6 is a feasible solution even for real time applications such as VoIP.

However, the deficiency of the protocol is the tunneling between LMA and MAG, adding delay to packet transmission. As a result PMIPv6 provides lower throughput than the other candidate protocols. Simulation results showed that this reduction is greater in WLAN as the wireless link delay is smaller. Moreover, PMIPv6 does not support global mobility and future research should focus on better protocol design to cope with these drawbacks.

References

[1] PERKINS, C.: *IP Mobility Support for IPv4.* IETF RFC 3444, 2002.
[2] JOHNSON, D., PERKINS, C., ARKKO, J.: *Mobility Support in IPv6,* IETF RFC 3775, 2004.
[3] RIEGEL, M., TUEXEN, M.: *Mobile SCTP.* draft-riegel-tuexen-mobile-sctp-09, 2007.
[4] HANDLEY, M., SCHULZRINNE, H., SCHOOLER, E., ROSENBERG, J. *SIP*: Session Initiation Protocol, IETF RFC, 2543. 1999.
[5] KOVACIKOVA, T., SEGEC, P., BRUNCKO, M.: Standardization Paths for NGN IMS-based architecture, *Communications - Scientific Letters of the University of Zilina,* No. 4, 2008.
[6] PERKINS, C., JOHNSON, D.: *Route Optimization in Mobile IP*, draft-ietf-mobileip-optim-11.txt, 2001.
[7] GUNDAVELLI, S., LEUNG, ED. K., DEVARAPALLI, V., CHOWDHURY, K., PATIL, B.: Proxy Mobile IPv6, *IETF RFC* 5213, 2008.
[8] KONG, K., LEE, W., HAN, Y., SHIN, M. (2008). Mobility Management for all-IP Mobile Networks: Mobile IPv6 vs. Proxy mobile IPv6, *IEEE Wireless Communications vol. 15,* pp. 36–45.
[9] AYDIN, I., SEOK, W., SHEN, C.-C.: *Cellular SCTP: A Transport-layer Approach to Internet Mobility*, IEEE Int'l Conference on Computer Communications and Networks, pp. 285–290, 2003.
[10] SALSANO, S., POLIDORO, A., MINGARDI, C., NICCOLINI, S., VELTRI, L.: SIP-based Mobility Management in Next Generation Networks, *IEEE Wireless Communications, Vol 15,* pp. 92–99, 2008.
[11] ABDEL-GHAFFAR, H.S. EBRAHIM, H.A.-A. KHALIFA, A.A.: Efficient Mobility Management Protocols for Integrated UMTS and Outdoor WLAN 802.11g, *Wireless Communications and Mobile Computing Conference,* pp. 552–558, 2008.
[12] POLIDORO, A., SALSANO, S., NICCOLINI. S.: Performance Evaluation of Vertical Handover Mechanisms in IP Networks, *IEEE Wireless Communications and Networking Conference,* pp. 2783–2788, 2008.

Ivo Dolezel – Bohus Ulrych *

INDUCTION HEATING OF VERY THIN METAL PLATES MODELLED BY ELECTRIC VECTOR POTENTIAL

A novel way of modelling of induction heating of very thin nonferromagnetic plates exposed by periodically varying magnetic flux is presented. The currents induced in the plate are described by means of the T-electric vector potential. The mathematical model is solved numerically, by a code developed and written by the authors. The methodology is illustrated with an example whose results are discussed.

1. Introduction

Induction heating is a process that nowadays belongs to widely spread and well elaborated technologies of heat treatment of metal bodies from both theoretical and practical viewpoints. The process is based on the induction of electric currents (and consequent production of heat) in the body, usually as a consequence of one of the two following mechanisms – exposition of the body by a time variable magnetic field (the most frequent case) or movement of the body in a static magnetic field.

The theory of induction heating is well known. The principal mathematical model of this process consists of two partial differential equations describing the distribution of magnetic and temperature fields in the system. Magnetic field is usually formulated in terms of magnetic vector potential $\boldsymbol{A}$ [1–3], while temperature field is described by the heat transfer equation [4, 5].

Nevertheless, from time to time we must face problems where this classical way of solution fails. Such problems are typically characterized by geometrical incommensurability. This means that one dimension of the investigated system is much smaller than the other dimensions, but it is also important and cannot be neglected. We can mention, for instance:

- nonferromagnetic plate **1** of very small thickness δ locally exposed by a time varying irrotational magnetic field $\boldsymbol{B}_{\mathrm{ext}}$ generated in magnetic circuit **2** by field coil **3** and concentrated by appropriate magnetic focusators **4.1** and **4.2**, see Fig. 1,
- electrically conductive band **1** of very small thickness δ moving at a velocity $\boldsymbol{w}$ between two systems of direct current-carrying field coils or appropriately oriented permanent magnets **2.1** and **2.2** (see Fig. 2).

Handling such a problem as a geometrically 3D task (dependent on quantities *x, y, z, t*), formulating it in the classical manner (in terms of magnetic vector potential $\boldsymbol{A}$) and solving it by the finite element method is often unreal. This is because the thickness δ of the plate (or band) is negligible with respect to its remaining dimensions, which represents the fundamental complication for building the finite-element mesh. Moreover, the definition area of the task is three-dimensional and often large, which leads to a long computation time.

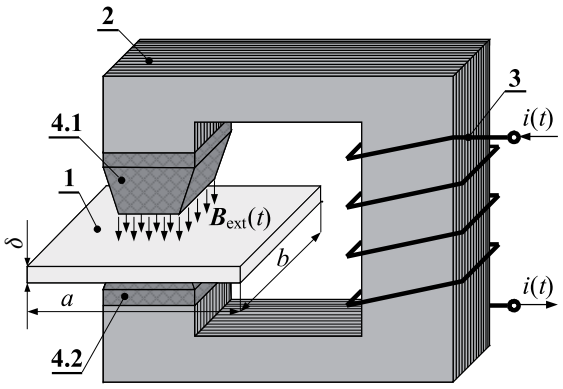

Fig. 1 Induction heating of a very thin plate ($\delta << a,b$):
1-*locally heated thin nonferromagnetic plate,*
2-*laminated magnetic circuit,* **3**-*field coil,*
4.1, **4.2**-*ferromagnetic focusators of magnetic field*

* **Ivo Dolezel[1], Bohus Ulrych[2]**
[1] Department of Electrical Power Engineering, Faculty of Electrical Engineering, Czech Technical University, Czech Republic,
E-mail: dolezel@fel.cvut.cz
[2] Department of Theory of Electrical Engineering, Faculty of Electrical Engineering, University of West Bohemia, Czech Republic

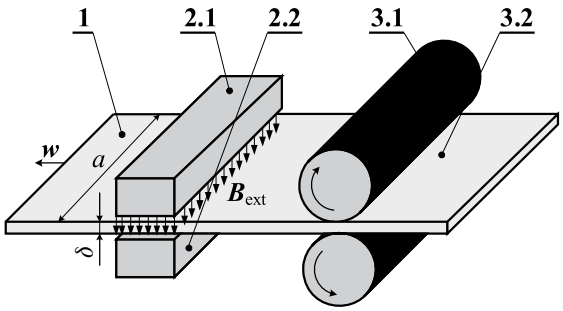

*Fig. 2 Induction heating of a very thin electrically conductive band $\delta << a$ moving at a velocity **w** in time invariable magnetic field generated by a system of permanent magnets:* **1***-moving band,* **2.1**, **2.2***-systems of permanent magnets,* **3.1**, **3.2***-front roll stand*

On the other hand, considering the problem as a 2D task described by the magnetic vector potential $\boldsymbol{A}$ (thickness δ being neglected) is also counterproductive because it is not possible to numerically approximate the boundary conditions for this quantity along the plate.

In similar cases it is often advantageous to use for modeling of the electromagnetic field the electric vector potential $\boldsymbol{T}$, as is shown in this paper.

2. Formulation of the Problem

Consider a very thin nonferromagnetic and electrically conductive circular plate of thickness $\delta \to 0$ and electrical conductivity γ_{el}, whose surface is denoted as Ω_1 and its boundary Γ (see Fig. 3). The plate is locally (in a subdomain $\Omega_2 \subset \Omega_1$) exposed by a time variable external irrotational magnetic field $\boldsymbol{B}_{ext}(t)$.

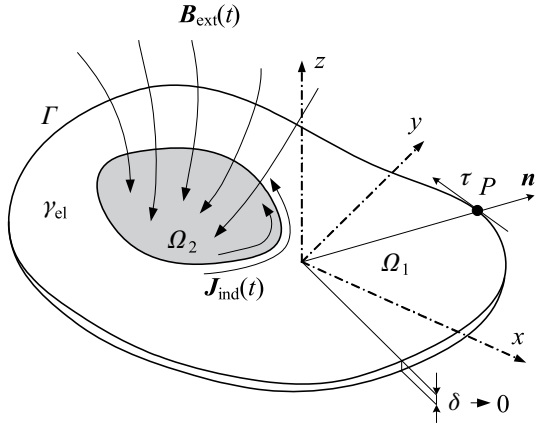

Fig. 3 General arrangement of a very thin ($\delta \to 0$) nonferromagnetic plate exposed by local time variable magnetic field

Denoting the electric field strength in the plate $\boldsymbol{E}$, the corresponding eddy current density induced in it is

$$J_{ind} = \gamma_{el} E \,, \tag{1}$$

and the corresponding volumetric Joule losses are

$$w_{J,ind} = \frac{1}{\gamma_{el}} \left| J_{ind} \right|^2 . \tag{2}$$

The aim of the paper is to determine the distribution of $\boldsymbol{J}_{ind}$ and $w_{J,ind}$ in the plate, whose knowledge is the crucial condition for finding the time evolution of its temperature.

If the problem were solved in the classical way using magnetic vector potential $\boldsymbol{A}$, the quantity $\boldsymbol{B}_{ext}(t)$ would be a boundary condition over the locally exposed surface Ω_2 of the heated plate. But in this case the plate would have to be considered 3D and when its thickness δ would be small, meshing of the plate could cause crucial difficulties.

The method described in the paper uses the electric vector potential $\boldsymbol{T}$. As we will see in the next section, this allows the external irrotational magnetic magnetic flux density $\boldsymbol{B}_{ext}(t)$ becoming the right-hand part of the partial differential equation describing the distribution of $\boldsymbol{T}$. The numerical discretization is now only carried out in the 2D area $\Omega_2(x,y)$, no matter how small is the thickness δ. The only disadvantage of this approach is that the density of eddy currents along the thickness of the plate is uniform. But with respect to very small value of δ this error plays no significant role.

3. Continuous Mathematical Model

Introduce the electric vector potential T by

$$E = -\operatorname{curl} T \,. \tag{3}$$

Now the second Maxwell equation describing the electric field in the plate reads

$$\operatorname{curl} E = -\operatorname{curl}(\operatorname{curl} T) = -\frac{\partial B}{\partial t} \,, \tag{4}$$

where B is the total flux density in the plate. This consists of two parts: the mentioned external magnetic flux density B_{ext} from the external source and magnetic flux density B_{ind} produced by the induced eddy currents J_{ind} (1). Now, we can transform (4) into the form

$$\operatorname{curl}(\operatorname{curl} T) = \frac{\partial B_{ext}}{\partial t} + \frac{\partial B_{ind}}{\partial t} \,. \tag{5}$$

Using the first Maxwell equation as the relation between J_{ind} and H_{ind} (the displacement currents being neglected)

$$J_{ind} = \operatorname{curl} H_{ind} \tag{6}$$

we can write

$$J_{ind} = \gamma_{el} E = -\gamma_{el} \operatorname{curl} T = \frac{1}{\mu_0} \operatorname{curl} B_{ind} \,, \tag{7}$$

and hence

$$T = -\frac{1}{\gamma_{el}\mu_0}B_{ind} - \mathrm{grad}\,\psi\,, \tag{8}$$

where ψ is an arbitrary scalar function. But in our case T represents the electric vector potential only produced by the induced magnetic flux density B_{ind}. That is why we can put $\psi = 0$ and

$$T = -\frac{B_{ind}}{\gamma_{el}\mu_0} \Rightarrow B_{ind} = -\gamma_{el}\mu_0 T\,. \tag{9}$$

After inserting (9) into (5) we obtain the fundamental equation for the electric vector potential in the form

$$\mathrm{curl}\big(\mathrm{curl}T\big) + \gamma_{el}\mu_0\frac{\partial T}{\partial t} = \frac{\partial B_{ext}}{\partial t}\,. \tag{10}$$

The initial and boundary conditions for potential T can be derived from the physical aspects of the problem.

The initial condition follows from the fact that before the plate is exposed by external magnetic field, $B_{ext}(\Omega_2, t = 0) = 0$, so that $E(\Omega_1, t = 0) = 0$, and, hence, curl$T = 0$. This results in $T =$ gradΦ, where Φ is any scalar function. Without any loss of generality we can put $\Phi = 0$, so that $T(\Omega_1, t = 0) = 0$.

The boundary condition follows from the fact that the currents induced in the plate in the direction of its any outward normal to the plate vanish ($J_{n,ind}(\Gamma, t) = 0$. This gives $-\gamma_{el} \cdot \partial T(\Gamma, t)/\partial\tau =$ $= 0 \Rightarrow T(\Gamma, t) = C$ (symbol τ denoting the tangent, see Fig. 3), where C is a constant vector. In order to preserve the consistency with the above initial condition $T(\Omega_1, t = 0) = 0$, we immediately obtain $C = 0$.

From the above formulas we can see two principal advantages of introducing the electric T potential for such kinds of problems:

- Potential T is only defined in the electrically conductive domain, in our case only in the plate. On the other hand, the magnetic vector potential A would have to be determined everywhere in the whole system (i.e., inductor, magnetic cores, flux concentrators, ambient air), which would require much larger 3D mesh. The transversal discretisation of the thin plate, moreover, could lead to complications.
- The boundary conditions for the electric vector potential T can be derived very easily. On the other hand, finding the value of the magnetic vector potential A along the boundary Γ is impossible and for solution we would have to introduce a sufficiently distant artificial Dirichlet boundary.
- The only drawback of the presented approach is that the currents induced in the disk have the same density along its thickness. But this is not very significant when thickness δ of the plate is substantially smaller than the depth of penetration.

Solution of (10) provides the distribution of the electric vector potential T and, consequently, distribution of all remaining electric and magnetic quantities in the plate. Distribution of current density in the plate is then given by formula

$$J_{ind} = \gamma E = -\gamma_{el}\mathrm{curl}T \tag{11}$$

and the corresponding volumetric Joule losses are

$$w_J = \gamma_{el}\left|\mathrm{curl}T\right|^2\,. \tag{12}$$

4. Analogy with Magnetic Vector Potential for Planar Plates

In this section we will show an important analogy of equation (10) with the equation for vector potential A in case that the plate under inspection is planar (it lies in the plane x,y in Cartesian coordinates) and vector B_{ext} is perpendicular to it (it is parallel with the z-axis.

For this specific case equation (10) can be written in the form

$$\frac{\partial^2 T_z}{\partial x^2} + \frac{\partial^2 T_z}{\partial y^2} - \gamma_{el}\mu_0\frac{\partial T_z}{\partial t} = -\frac{\partial B_{z,ext}}{\partial t}\,, \tag{13}$$

because now both vectors T and B_{ext} have only the -components T_z and $B_{z,ext}$.

Consider another situation. An infinitely long massive nonmagnetic cylindrical body V_1 (with the axis identical with axis z) of electric conductivity γ_{el} and cross section $\Omega_1(x,y)$ carries time-variable electric current $i(t)$ of density $\gamma_{z,ext}(x,y,t)$ that passes in the z-direction through body V_2 of cross section Ω_2 (see Fig. 3). The region Ω_2 is insulated from $\Omega_2 - \Omega_2$ by a perfect, infinitely thin insulating layer.

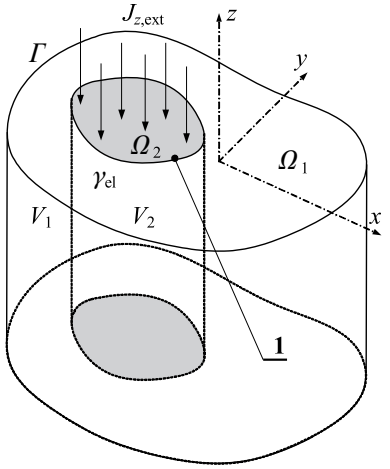

Fig. 4 Infinitely long nonmagnetic cylindrical body carrying time-varying current: **1***-infinitely thin perfectly insulating interface*

Now, the time variable magnetic field in the whole body produced by current $i(t)$ can be described by the well-known partial differential equation of parabolic type for magnetic vector potential A (that also exhibits only one nonzero component A_z in the z-direction) in the form

$$\frac{\partial^2 A_z}{\partial x^2} + \frac{\partial^2 A_z}{\partial y^2} - \gamma_{el}\mu_0\frac{\partial A_z}{\partial t} = -\mu_0 J_{z,ext}\,, \tag{14}$$

It is obvious that equations (13) and (14) are quite analogous. The same holds for the derived quantities: in case of the electric vector potential T we have

$$J_{x,\mathrm{ind}} = \gamma_{\mathrm{el}} \frac{\partial T_z}{\partial y}, \; J_{y,\mathrm{ind}} = -\gamma_{\mathrm{el}} \frac{\partial T_z}{\partial x} \tag{15}$$

while in case of the electric vector potential A we analogously obtain

$$B_x = \frac{\partial A_z}{\partial y}, \; B_y = \frac{\partial A_z}{\partial x}. \tag{16}$$

This analogy results in the fact that the indicated linear problem described in terms of the electric vector potential T_z can easily be solved by any software working with the magnetic vector potential A_z (while the codes working with the magnetic vector potential A abound, practically no professional code – except for user's programs – works with the electric vector potential T). We can proceed in the following way:

- First we model the arrangement in Fig. 4. Then we substitute for $J_{z,\mathrm{ext}}$ the value $\frac{1}{\mu_0}\frac{\partial B_{z,\mathrm{ext}}}{\partial t}$ and put $A_z(\Gamma_1, t) = 0$.
- After computing the distribution of $A_z \approx T_z$ using (14), we calculate the distribution of B_x, B_y (16) and multiplying them by γ_{el} we immediately obtain the corresponding distribution of $J_{x,\mathrm{ind}}$ and $J_{y,\mathrm{ind}}$.

5. Illustrative Example

Consider a thin circular aluminum plate (Fig. 5) of dimensions $\delta = 0.001$ m, $r_{\max} = 0.1$ m and electrical conductivity $\gamma_{\mathrm{el}} = 3.4 \times 10^7$ S/m. The plate is exposed by an external magnetic field $B_{z,\mathrm{ext}}(t)$ in a concentric circle of radius $r_{\min} = 0.02$ m.

The time evolution of magnetic flux density $B_{z,\mathrm{ext}}(t)$ is described by periodic saw-like oscillations whose parameters follow from Fig. 6.

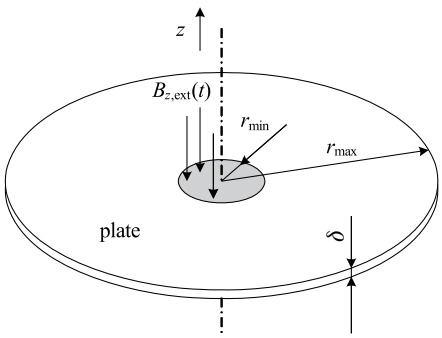

Fig. 5 Thin aluminum circular plate exposed by time-variable magnetic field

The aim of the solution is to determine the spatial and temporal distribution (module of the corresponding vector) of the induced current density $J_{\varphi,\mathrm{ind}}(r,t)$ (φ denoting the circumferential direction) and volumetric Joule losses $w_J(r,t)$.

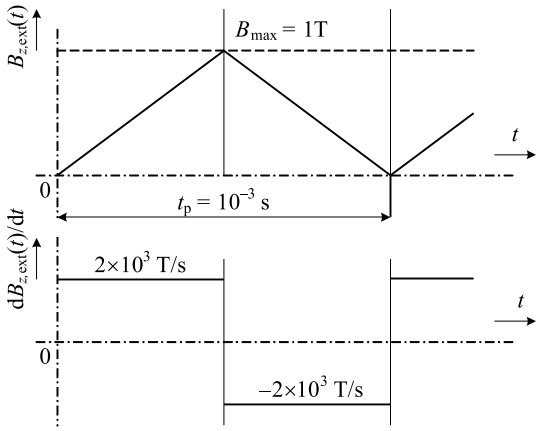

Fig. 6 Time evolution of magnetic flux density $B_{z,\mathrm{ext}}(t)$ and its time derivative (f = 1000 Hz, t_p = 0.001 s, $B_{\max}$ = 1 T)

All the results presented in the following figures correspond to the situation in the 10th period, which practically means the steady state (with one exception that will be discussed later).

The orientation of the induced current density $J_{\mathrm{ind}}(r,t) = \varphi_0 J_{\varphi,\mathrm{ind}}(r,t)$ in the period is obvious from Figs. 7a, 7b. It is connected with the change of sign of the time derivative $\mathrm{d}B_{z,\mathrm{ext}}(t)/\mathrm{d}t$, see Fig. 6.

The time evolution of module $J_{\varphi,\mathrm{ind}}(r,t)$ along different radii of the plate is depicted in Fig. 8. The highest values are on the circle of $r = r_{\min} = 0.02$ m, i.e., along the boundary of the domain exposed by the external magnetic field $B_{z,\mathrm{ext}}(t)$. But not too far from this boundary, for example along the radii $r = 0.015$ m or $r = 0.025$ m, its values are significantly lower.

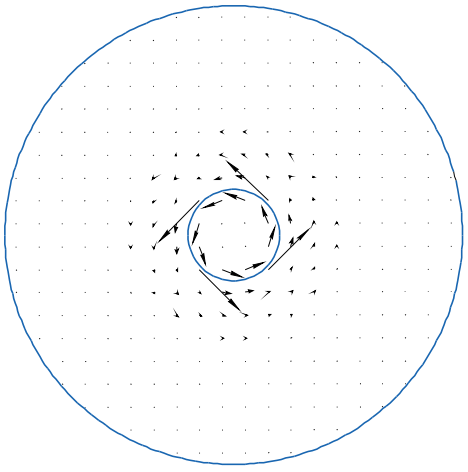

Fig. 7a Distribution of the induced current density $J_{\mathrm{ind}}(r,t)$ in the plate in the first half of the period

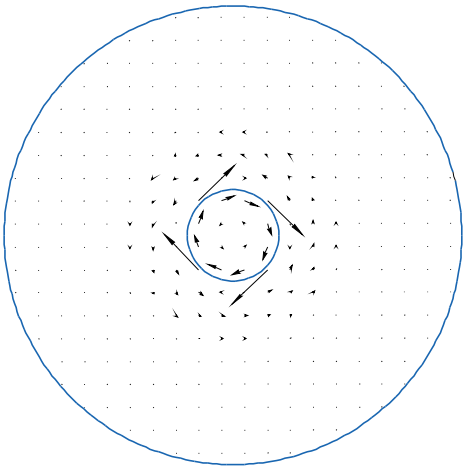

Fig. 7b Distribution of the induced current density $J_{ind}(r,t)$ in the plate in the second half of the period

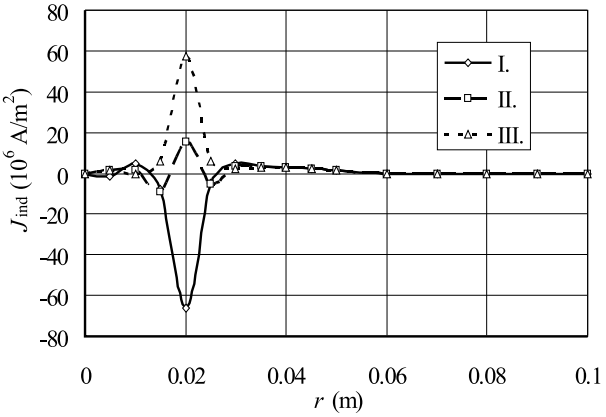

Fig. 9 Time evolution of $J_{\varphi,ind}(r,t)$ for three various radii of the plate within the 10th period
I. - $t/t_p = 0$, II. - $t/t_p = 0.2$, III. - $t/t_p = 0.4$

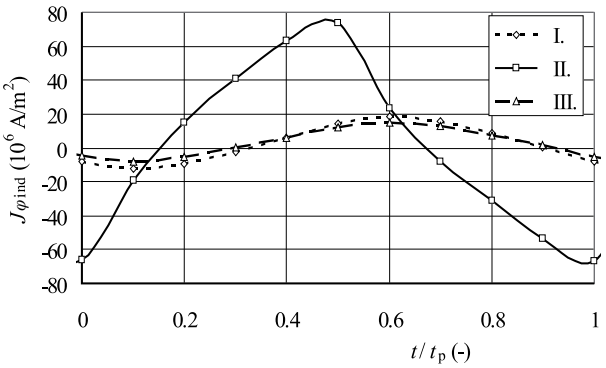

Fig. 8 Time evolution of $J_{\varphi,ind}(r,t)$ for three various radii of the plate within the 10th period (being the relative time in this period)
I. - $r = 0.015$ m, II. - $r = 0.02$ m, III. - $r = 0.025$ m

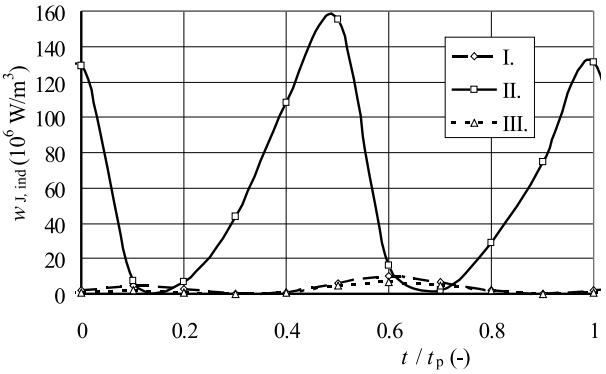

Fig. 10 Time evolution of volumetric Joule losses $w_{J,ind}(r,t)$ for three various radii of the plate within the 10th period (t/t_p being the relative time in this period)
I. - $r = 0.015$ m, II. - $r = 0.02$ m, III. - $r = 0.025$ m

The distribution of module $J_{\varphi,ind}(r,t)$ of vector J_{ind} along the radius r of the plate at different time levels of the 10th period, depicted in Fig. 9, also confirms the above conclusions. The figure shows that the highest values of the induced current density occur just on the radius $r = r_{min} = 0.02$ m, i.e., on the external boundary of the area exposed by the magnetic flux density $B_{z,ext}(t)$. These values vary with time, similarly as the mentioned magnetic flux density.

The distribution of the volumetric Joule losses $w_{J,ind}(r,t)$ along different radii of the plate within the 10th period (depicted in Fig. 10) also confirms the above statements. The highest losses are also produced on radius $r = r_{min} = 0.02$. On the other hand, observable is there certain disproportion between the value $w_{J,ind}(r = 0.02, t/t_p = 0.5)$ and other value $w_{J,ind}(r = 0.02, t/t_p = 1)$, where t/t_p is relative time in the period of length t_p. This is probably connected with the asymmetry of the distribution of $J_{\varphi,ind}(r,t)$ (see Fig. 8). It is obvious that the 10th period is not yet the ideal steady state.

6. Conclusion

Electric vector potential seems to be a powerful tool for modeling induction heating in linear systems characterized by geometrically incommensurable elements, because it allows handling specific 3D arrangements as 2D problems. Another advantage consists in the formal similarity of equations for the electric vector potential and magnetic vector potential, which makes possible to use classical FEM codes for numerical computation of such tasks.

Next work in the field will be aimed at the following problems:

- Application of the method in case that the external magnetic field is generally rotational.
- Model of heating taking into account the temperature variations of physical parameters of the system.
- Modeling of the whole problem in the hard-coupled formulation (heating of the plate affects its electrical conductivity) together

with the thermoelastic changes (leading to small variations of its dimensions) using our own library Hermes [6] with interface Agros based on a fully adaptive higher-order finite element method.

Acknowledgement

The financial support of the Grant Agency of the Czech Republic (project No. 102/09/1305) and Research Plan MSM 6840770017 is gratefully acknowledged.

References

[1] ZINN, S., SEMIATIN, S. L.: Elements of Induction Heating: Design, Control and Applications, *ASM International,* USA, 1988.
[2] RAPOPORT, E., PLESHIVTSEVA, Y.: Optimal Control of Induction Heating Processes. *CRC Press,* Boca Raton, FL, 2007.
[3] RUDNEV, V. I., LOVELESS, D., COOK, R., BLACK, M.: Handbook of Induction Heating, *Marcel Dekker,* New York, NY, 2003.
[4] HOLMAN, J. P.: *Heat Transfer,* McGrawHill, New York, NY. 2001.
[5] KOVACIK, O., ORSANSKY, P.: Partial Differential Equation for Heat Conduction and its Solvability, *Communicastions - Scientific Letters of the University of Zilina,* 2010, No. 1, pp. 20–22.
[6] hpfem.org.

Branislav Dobrucky – Mariana Benova – Michal Frivaldsky – Michal Prazenica *

CHOOSING MODULATION STRATEGIES FOR 2-STAGE COMBINE LLC- AND DIRECT CONVERTER–MODELLING, SIMULATION, APPLICATION

The paper deals with design of switching and control strategy of 2-stage combine LLC- and matrix converter, supplied from DC voltage source. It also deals with comparison of the four different switching control modes: phase-mode control, sinusoidal PWM mode control, pulse-depletion mode control and packet-mode control. Numerical harmonic analysis for total harmonic distortion is used. Simulation and preliminary results of experimental verification are given in the paper.

1. Introduction

It's known that direct converters can be operated from AC network (or generator) by voltage with relative low frequency of 50-, 60-, 100-, 400 Hz using triac- (or thyristor) switches with phase-control. On the other side, matrix converters with fast IGBT and MOSFET switching devices can operate with relatively high frequencies of tens- up hundreds kHz. The AC voltage source can be effectively created by LLC type resonant converter.

Overal connection of converter system

The block scheme of converter system is presented in Fig. 1, [1], [3].

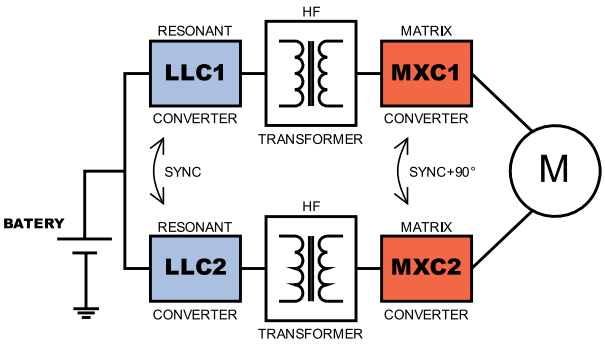

Fig. 1 Block scheme of converter system

Converter system consisting of two branches operates with two phase output voltage shifted by 90 degrees created by matrix converters MXC1 and MXC2. High frequency transformers provide galvanic insulation and increase battery voltage to the rate value for the motor. LLC resonant converters work at switching frequency of 10- up hundreds kHz and must be synchronized each to other.

2. Operation of One Single Branch

Power circuitry scheme of converters

The main power schemes are depicted in Fig. 2.

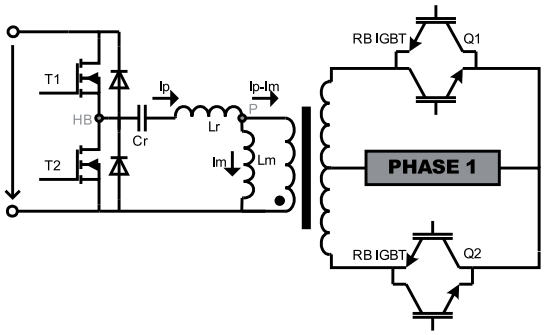

Fig. 2 Circuit diagram of single branch of the system

Operation of 1-stage LLC converter is illustrates in work [2]. Important is that converter operates at zero-voltage-switching (ZVS) mode with consequently minimal switching losses.

Design of LLC resonant converter is described in detail in [2] – [4]. Regarding to its simulated output quantities it is shown in Figs. 3 and 4 that current is well sinusoidal and the voltage can be

* **Branislav Dobrucky[1], Mariana Benova[2], Michal Frivaldsky[1], Michal Prazenica[1]**
[1] Dept. of Mechatronics and Electronics, Faculty of Electrical Engineering, University of Zilina, Slovakia, E-mail: branislav.dobrucky@fel.uniza.sk
[2] Dept. of Theoretical Electrotechnics and Biomedical Engineering, Faculty of Electrical Engineering, University of Zilina, Slovakia

sinusoidal or trapezoidal one depending on type of the load (linear or nonlinear rectifier load.

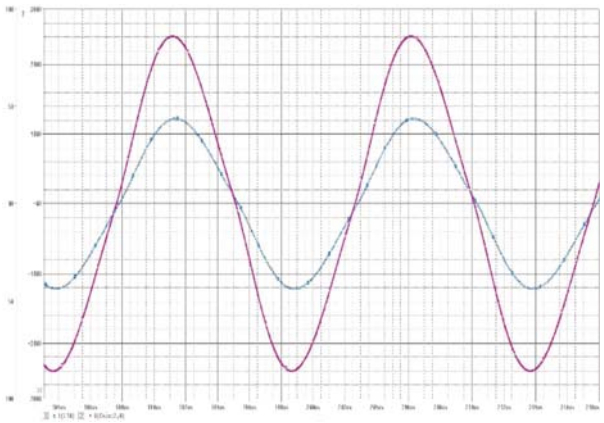

Fig. 3 Principle time waveforms of LLC converter

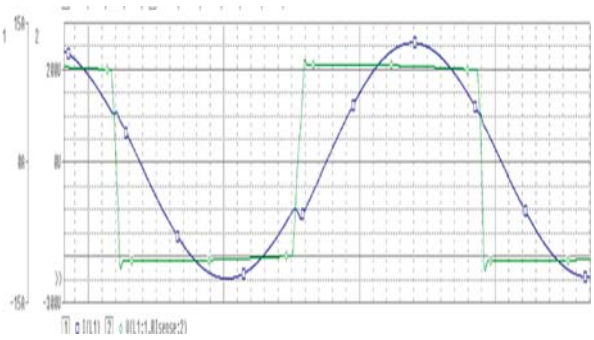

Fig. 4 Time waveforms of LLC converter at 20 kHz frequency

Output voltage is slightly decreasing during each half-period, and at higher switching frequencies it can be more trapezoidal and distorted one according to fixed dead-time of the converter switches (see experimental section).

The second stage matrix converter can be in half- or full bridge connection. It also operates at ZVS mode. Its output voltage can be controlled by different control modes with different achieved quality.

3. Modelling and Simulation of Half-Bridge Matrix Converter with RL Load at Different switching Strategies

Simulated time waveforms of the output voltage and current are shown in the next Figs. 5 – 8 using different switching modes.

3.1 Phase-mode control using low frequency triac-switches and sinusoidal input voltage [7]

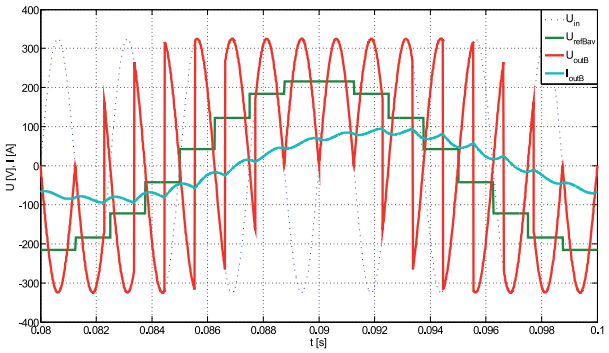

Fig. 5 Time waveforms of output voltage and current at 400 Hz input frequency using phase-mode control

3.2 Sinusoidal PWM mode control using fast IGBT switches and rectangular input voltage [10]

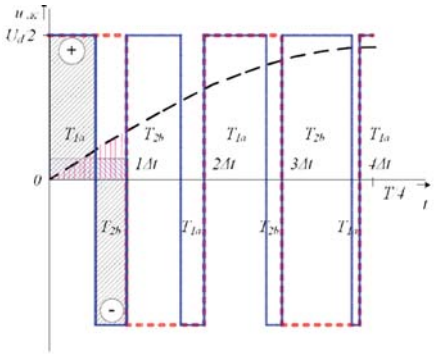

Fig. 6 Time waveforms of output voltage and current at 20 kHz input frequency using sinusoidal PWM control

3.3 Pulse-depletion-mode control using fast IGBT switches and sinusoidal or rectangular input voltage

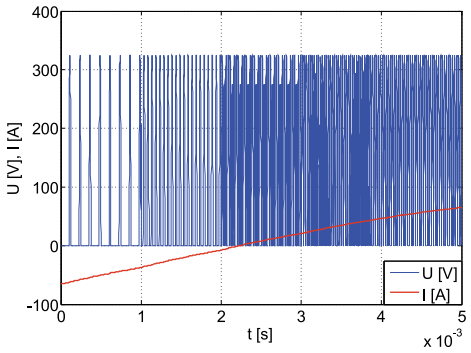

Fig. 7 Time waveforms of output voltage and current at 20 kHz input frequency using pulse-depletion mode control

3.4 Packed-mode control using fast triac or GTO switches and sinusoidal or rectangular input voltage

This type of control mode uses also unequal sample- and switching frequency. So, during sample interval the packet of pulses of input voltage is generated. Its average value could follow average value of reference voltage.

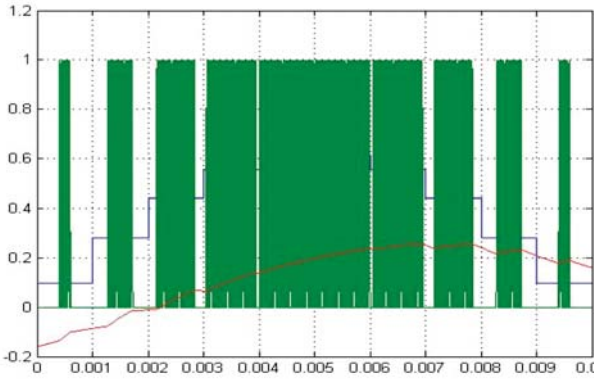

Fig. 8 Time waveforms of output voltage and current at 20 kHz input frequency using packed mode control

4. Qulaity of output Quantities of the Converter System Comparison Using Numerical Fourier Analysis and THD Calculation

4.1 Numerical analysis and THD calculation of output voltages

The numerical Fourier analysis was used for content of harmonics of investigated voltage waveforms (detailed in appendix).

- *Low frequency triac switches converter - phase control mode*
  Calculated value of THD referred to fundamental harmonic component:

$$THD_u = U_z/U_1 = 1.8237 \quad 182.366\ \%$$

Calculated value of THD referred to total rms value of voltage waveform:

$$THD_u = U_z/U = 0.8711 \quad 87.107\ \%$$

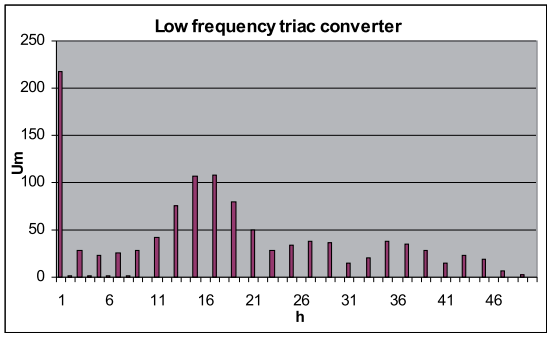

Fig. 9 Voltage amplitude spectrum of low frequency triac converter at 400 Hz

- *Fast triac/GTO switches converter - phase control*
  Calculated value of THD referred to fundamental harmonic component:

$$THD_u = U_z/U_1 = 0.8280 \quad 82.797\ \%$$

Calculated value of THD referred to total rms value of voltage waveform:

$$THD_u = U_z/U = 0.6374 \quad 63.737\ \%$$

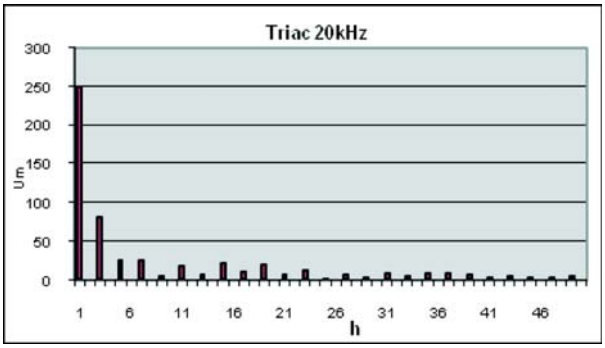

Fig. 10 Voltage amplitude spectrum of fast triac- or GTO converter at 20 kHz

- *Fast IGBT switches converter - S-PWM control*

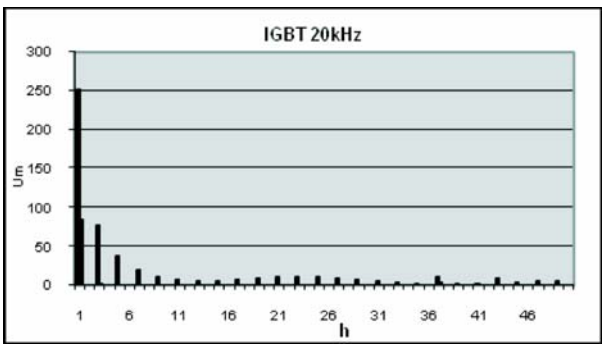

Fig. 11 Voltage amplitude spectrum of IGBT converter at 20 kHz

Calculated value of THD referred to fundamental harmonic component:

$$THD_u = U_z/U_1 = 0.82108 \quad 82.108\ \%$$

Calculated value of THD referred to total rms value of voltage waveform:

$$THD_u = U_z/U = 0.63423 \quad 63.423\ \%$$

- *Fast triac/GTO switches converter - depletion mode control*

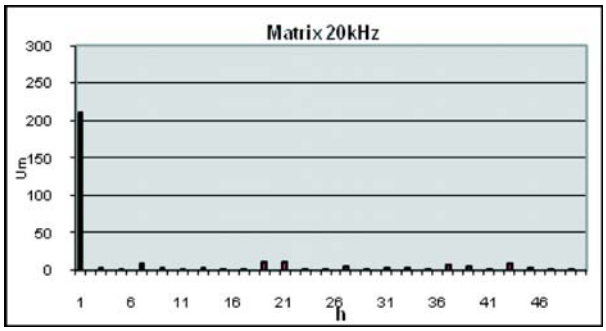

Fig. 12 Voltage amplitude spectrum of fast triac- or GTO converter at 20 kHz

Calculated value of THD referred to fundamental harmonic component:

$THD_u = U_z/U_1 = 0.75474 \quad 75.475\ \%$

Calculated value of THD referred to total rms value of voltage waveform:

$THD_u = U_z/U = 0.60203 \quad 60.204\ \%$

- *Fast triac/GTO switches converter - packed mode control*

Calculated value of THD referred to fundamental harmonic component:

$THD_u = U_z/U_1 = 0.7882 \quad 78.8185\ \%$

Calculated value of THD referred to total rms value of voltage waveform:

$THD_u = U_z/U = 0.6186 \quad 61.8647\ \%$

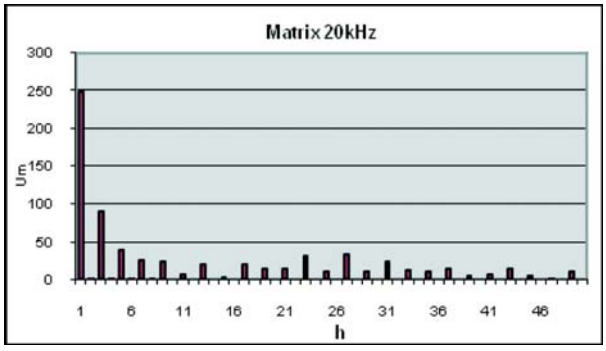

Fig. 13 Voltage amplitude spectrum of fast triac- or GTO converter at 20 kHz

4.2 Numerical analysis and THD calculation of output currents

The numerical Fourier analysis was also used for content of harmonics of investigated current waveforms (detailed in appendix).

Worst case calculation:

- *Fast triac/GTO switches converter - packed mode control*

Calculated value of THD referred to fundamental harmonic component:

$THD_I = I_z/I_1 = 0.0638 \quad 6.3766\ \%$

Calculated value of THD referred to total rms value of voltage waveform:

$THD_I = I_z/I = 0.0636 \quad 6.3575\ \%$

Regarding to rather high frequency and advanced mode control the current harmonic contents are very small ones, from:

$THD_I = I_z/I = 0.0072 \quad 0.7209\ \%$

up to

$THD_I = I_z/I = 0.0131 \quad 1.3192\ \%$

5. Experimentation with 2-Stage Converter System Under R-L Load

Experimental verification was done using a single-phase LLC inverter and single-phase bridge matrix converter for test rig system, Fig. 14 and 15, respectively.

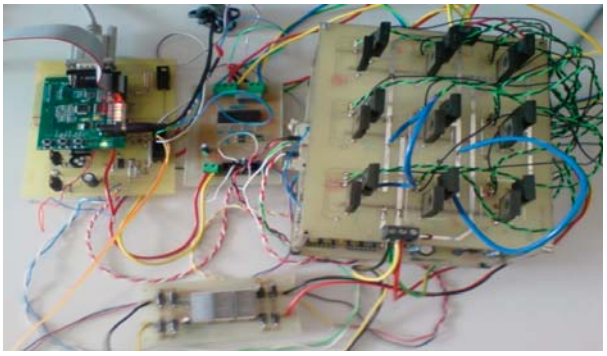

Fig. 14 Physical model of single-phase inverter and matrix converter based on [1]

Output voltage and current of first-stage LLC converter are depicted in Fig. 16a.

Output voltage and current of matrix converter stage are depicted in Fig. 16b.

The second stage was assembled with classical IGBT devices type of IRG4PH40KD, Fig. 14. It is also possible to use bidirectional types.

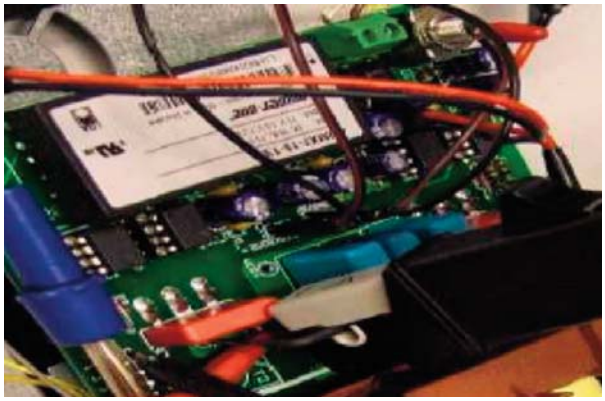

Fig. 15 Physical model of LLC - converter based on [2]

As application there are shown:

Power supply with sinusoidal output voltage in Figs. 17–18, and 2-phase electric drive with matrix converters and 2-phase induction motor in Figs. 19–20.

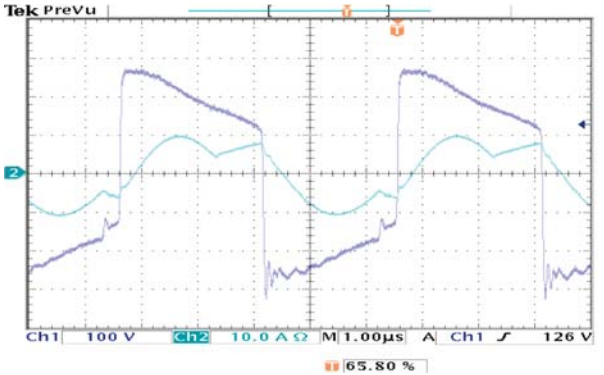

a)

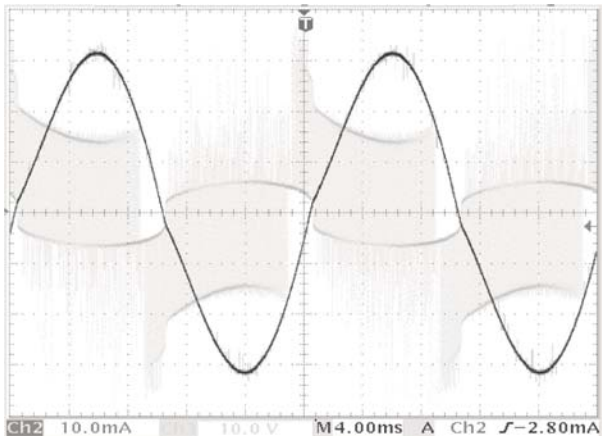

b)

Fig. 16 Output voltage and current of the physical model of LLC converter (a), output voltage and current of the physical model of single-phase inverter and matrix converter system (b)

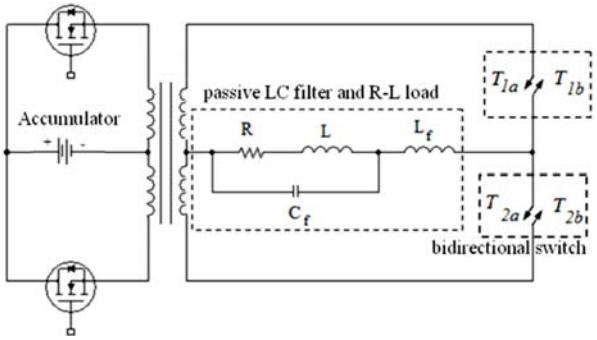

Fig. 17 Power supply with matrix converter and sinusoidal output voltage

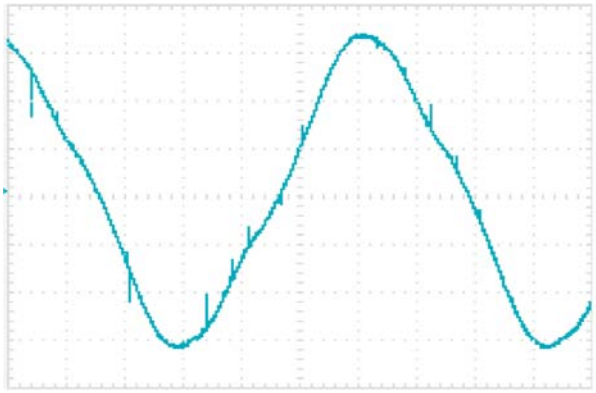

Fig. 18 Time-waveform of output voltage of the matrix converter with bipolar PWM modulation and passive LC filter

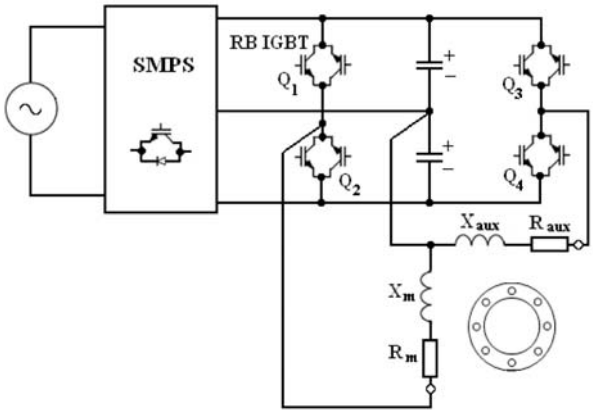

Fig. 19 Connection diagram of matrix converters and investigated 2-phase induction motor

6. Conclusions

The LLC-connection and the half-bridge connection of matrix converters with bipolar PWM modulation were chosen for the next

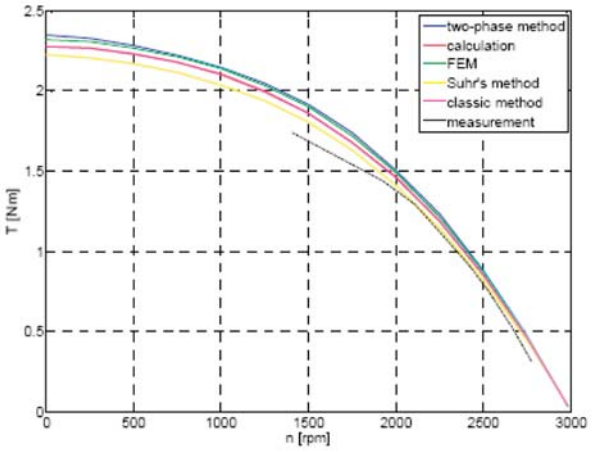

Fig. 20 Comparison between measured and simulated torque-speed characteristics of IM with two-phase supply

applications. Using of those the number of power switching elements of the two-stage converter can be reduced and smaller then those of classical three-phase voltage inverter.

Comparison of different switching mode showed that since the sinusoidal PWM mode is the best from point of view of total harmonic distortion of the output quantities, the pulse depletion mode is the most suitable from the point of view of switching losses of the converter in bridge connection. So, the trade-off between both strategies should be taken into account. Let's notice that LLC operates with soft commutation and switching-off process of matrix converters is provided by AC interlink. So, the switching-off losses of the converters are minimized, and the efficiency higher than classical connection.

Experimental verification shows very good agreement between experimental- and theoretical analysis results, so far for R-L load. Based on this it is possible to provide the design and power dimensioning of the converters.

(Fig. 14b). There are defined both amplitude- and frequency modulation ratios m_a and m_f as

$$m_n = \frac{U_{1m}}{U}; \quad m_f = \frac{f_s}{f_1}$$

where U_{1m} is reference amplitude of fundamental harmonic, U is magnitude of supply voltage, f_s is switching frequency, f_1 is fundamental frequency.

So, the peak amplitude of the fundamental harmonic component (equal to reference voltage) is m_a times U, and varies linearly with m_a (provided $m_a \leq 1$).

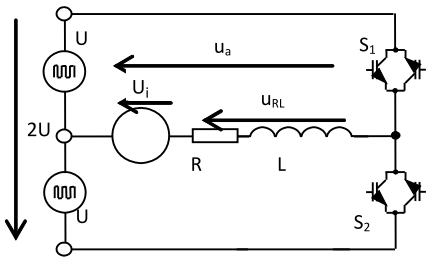

a)

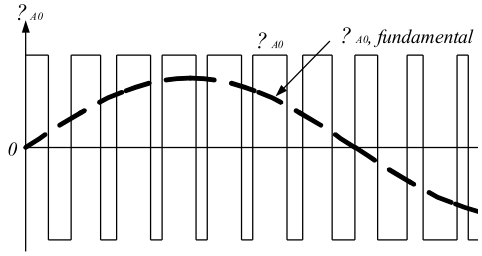

b)

Fig. 21 Single-phase half-bridge inverter (a) with PWM (b)

Then total voltage time waveform will be [8]:

$$u(t) = \sum_{v=1}^{\infty} \frac{4U_{DC}}{v\pi} \sum_{k=0}^{\frac{(m_f-2)}{4}-1} \left\{ \left[\cos\left(vk\frac{2\pi}{m_f}\right) - \cos\left(vk\frac{2\pi}{m_f} + v\omega t_s(k)\right) \right] - \left[\cos\left(v(k+1)\cdot\frac{2\pi}{m_f} - v\omega t_s(k)\right) - \cos\left(vk\frac{2\pi}{m_f}\right) \right] + \right.$$
$$\left. + \left[\cos\left(v\frac{2\pi}{m_f}\frac{m_f-2}{4}\right) - \cos\left(v\left(\frac{2\pi}{m_f}\frac{m_f-2}{4} + \frac{\pi}{m_f}\right)\right) \right] \right\} \cdot \sin(v\omega t)$$

APPENDIX – Voltage- and Current Analysis of AC/AC Half – Bridge Matrix Converter System

Equivalent circuit diagram of half-bridge single phase converter (one of two-phase orthogonal systems) is depicted in Fig. 21a, and bipolar pulse-width modulation in Fig. 21b.

Switching-pulse-width can be determined based on equivalence of average values of reference waveform and resulting average value of positive and negative switching pulses during switching period

where switching instant is equal to:

$$t_s(k) = \frac{1}{2U_{DC}} \cdot S_\Delta(k) + \frac{T_s}{2}$$

and

$$t_s\left(\frac{m_f-2}{4}\right) = \frac{T_s}{2}$$

and $S\Delta(k)$ is area under sinewave during k-switched interval:

$$S_{\Delta}(k) = U_m \frac{m_f}{2\pi}\left[\cos\left(\frac{2\pi}{m_f}k\right) - \cos\left(\frac{2\pi}{m_f}(k+1)\right)\right]$$

$$S_{\Delta}\left(\frac{m_f-2}{4}\right) = U_m \frac{m_f}{2\pi}\left[\cos\left(v\frac{2\pi}{m_f}\frac{m_f-2}{4}\right) - \cos\left(v\left(\frac{2\pi}{m_f}\frac{m_f-2}{4}+\frac{\pi}{m_f}\right)\right)\right]$$

The frequency modulation ratio mf should be an odd integer. Choosing *mf* as odd integer results in an odd symmetry [$f(-t) = -f(t)$] as well as half-wave symmetry [$f(-t) = -f(t + T_s/2)$] with the time origin shown in Fig. 17b. Therefore, only odd harmonics are present and the even harmonics disappear from the wave form of u_a. Moreover, only the coefficients if the sine series in Fourier analysis are finite; those for the cosine series are zero.

Acknowledgement

The authors wish to thank for the financial support to the Education operational program Centre of Systemization of advanced technology and knowledge transfer between industrials sphere and university environment No. ITMS 26110230004 funded by European regional development fund (ERDF), and VEGA project No. 1/0470/09.

References

[1] PRAZENICA, M., DOBRUCKY, B., BENOVA, M., KASSA, J.: Comparative Study of 2-phase Low Frequency Triac Converter- and High Frequency Two-stage Matrix Converter Systems, *Elektronika in Elektrotechnika* T 190, No. 4(100), 2010, ISSN 1392 – 1215, pp. 15–20.

[2] FRIVALDSKY, M., DRGONA, P., PRIKOPOVA, A.: *Design and Modeling of 200 kHz 1,5kW LLC Power Semiconductor Resonant Converter,* IEEE Int'l Conf. on Applied Electronics, PLZEN 2009, ISBN 9788070437810, pp. 111–114.

[3] SZYCHTA, E.: *Multi-resonant ZVS DC-DC Converters (in Polish).* Monograph, Publish Office of the University of Zielona Gora (PL), 2006, ISBN 83-7481-040-08.

[4] LUFT, M., SZYCHTA, E.: Commutation Processes in Multiresonant ZVS Bridge Converter, *AEEE - Advances in Electrical and Electronic Engineering,* University of Zilina (SK), No. 1-2, Vol. 7/2008, pp. 84-91, ISSN 1336-1736.

[5] DOBRUCKY, B., SPANIK, P., KABASTA, M.: Power Electronics Two-Phase Orthogonal System with HF Input and Variable Output, *Elektronika ir Elektrotechnika,* 2009, No. 1(89).

[6] DOBRUCKY, B., BENOVA, M., SPANIK, P.: Using Complex Conjugated Magnitudes – and Orthogonal Park/Clarke Transformation Methods of DC/AC Frequency Converter, *Electronics and Electrical Engineering,* Vol. 93 (2009), No. 5, Kaunas (LT), pp. 29–34 ISSN 1392 – 1215.

[7] JEEVANANTHAN, S., DANANJAYAN, P., MADHAVAN, R.: Novel Single-Phase To Single-Phase Cyclo-conversion Strategies: Mathematical and Simulations Studies, *Int'l J. of Power and Energy Systems,* Vol. 27(2004), No. 4, pp. 414–423 ISSN 1078-3466.

[8] ZASKALICKY, P., ZASKALICKA, M.: Behaviour of the Two-phase Permanent Magnet Synchronous Motor Supplied by Triacs from Single-Phase Voltage, *Acta Electrotechnica et Informatica*, TU Kosice (SK), Vol. 5 (2005), No. 3, pp. 1–5, ISSN 1335-8243.

[9] BLAABJERG, F. et al.: *Evaluation of Low-Cost Topologies for Two-Phase IM Drives in Industrial Application,* Record of 37th IEEE IAS Annual Meeting on Industry Application, Vol. 4, pp. 2358-2365, ISSN 0197-2618.

[10] BENOVA, M., DOBRUCKY, B., SZYCHTA, E., PRAZENICA, M.: Modelling and Simulation of HF Half-Bridge Matrix Converter System in Frequency Domain, *Logistyka*, 2009, No. 6, ISSN 1231-5478, pp.87.

[11] DOBRUCKY, B., BENOVA, M., MARCOKOVA, M., SUL, R.: *Analysis of Bipolar PWM Functions Using Discrete Complex Fourier Transform in MATLAB,* Proc. of Technical Computing Prague 2009, Praha (CZ), Nov. 2009, pp. 22, ISBN: 978-80-7080-733-0

[12] BALA, S., VENKATARAMANAN, G.: *Matrix Converter BLDC Drive using Reverse-Blocking IGBTs,* Proc. of IEEE APEC '06 Int'l Conf., Dallas, Texas (US), March 2006, pp. 660–666.

Peter Drgona – Anna Prikopova – Michal Frivaldsky – Martin Priecinsky *

SIMULATION BASED METHOD FOR DESIGN AND APPLICATION OF DIGITAL CONTROL SYSTEM

With increasing number of microprocessors and DSP use as a control system in power semiconductor converters, the new approaches for design of digital control system must be implemented. Designing a digital control system requires use of control to output transfer function. For new, frequency controlled resonant converters, like LLC converter, standard averaging methods cannot be applied for revealing the transfer function. Instead of that, new simulation based, numerical methods must be employed.

1. Introduction

In the field of DC/DC converters for switching power supplies, the main focus is on implementation of digital control, which means use of microcontrollers or DSP with implemented control algorithms and functions for communication with user as well. Analog control systems are well known and their design procedure is mastered, so it is easy to convert analog (continuous) controller into discrete and consequently implementing in microcontroller and DSP. But these methods ignore sample and hold effect of A/D converter and computing time of microprocessor. For proper discrete controller design, the method named direct digital design can be used. This method uses transfer function of converter in discrete form, including effect of sampling and computation delay [1].

For controller design purposes, transfer function of converter is necessary. This transfer function is based on model of power stage of controller. For PWM converters such as buck, boost, etc. the averaging method is widely used, but for new resonant topologies such as LLC converter, with this averaging method, the control to output transfer function cannot be used.

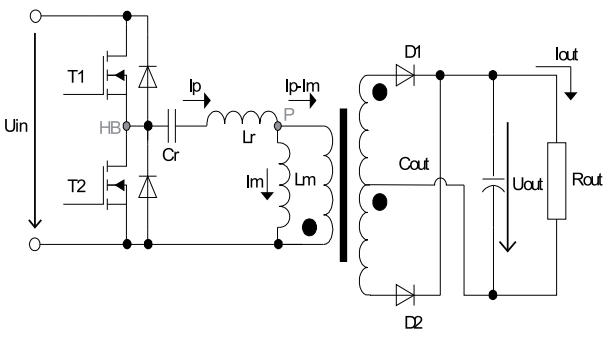

Fig. 1 Principal scheme of LLC converter

Resonant converters are well-known due to their high efficiency and low EMI (Electromagnetic Interference) noise. Despite of that, their utilization in most of industry and consumer applications is still limited due to their disadvantages [2, 3, 4, 5].

The perspective topology for such application is LLC resonant converter (Fig. 1), which exists for very long time but because of lack of understanding of characteristic of this converter, it was used as a series resonant converter with passive load. The benefit of frequency controlled LLC resonant converter is narrow switching frequency range, with light load and ZVS (Zero Voltage Switching) capability with even no load also with wide input voltage range [6, 7].

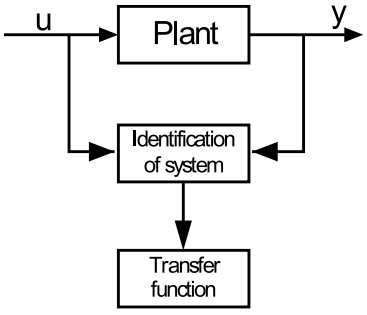

Fig. 2 Process of transfer function evaluation

In this paper, new simulation based method for obtaining the transfer function of converter is discussed. This method uses MATLAB and OrCad PSPICE environments for revealing the transfer

* **Peter Drgona, Anna Prikopova, Michal Frivaldsky, Martin Priecinsky**
Department of Mechatronics and Electronics, Faculty of Electrical Engineering, University of Zilina, Slovakia, E-mail: drgona@fel.uniza.sk

function. Advantage of this method is that it can be used for every type of power converter. Next in the paper, the direct digital design of controller based on transfer function is discussed. This method uses MATLAB environment for designing the discrete controller.

2. Transfer Function of Converter

Design of digital control system for power converter requires control-to-output transfer function. Based on this transfer function, digital controller can be obtained. For PWM converters, standard "averaged" methods can be used for revealing the transfer function of converter. One method with good results is "direct circuit averaging". This method defines "local average operator", which means average value of parameter during unit of time.

$$\bar{x}(t) = \frac{1}{T}\int_{t-T}^{t} x(t)dt \qquad (1)$$

The operator is defined at neglected ripple, which is caused by switching of semiconductor devices. After application of above mentioned operator, switching elements in power converter changes into blocks represented by functions of duty cycle and state variables. This method can be easily implemented for standard PWM converters such as boost, buck, flyback etc. Transfer function obtained with this method has a duty cycle as an input value and output voltage as an output value.

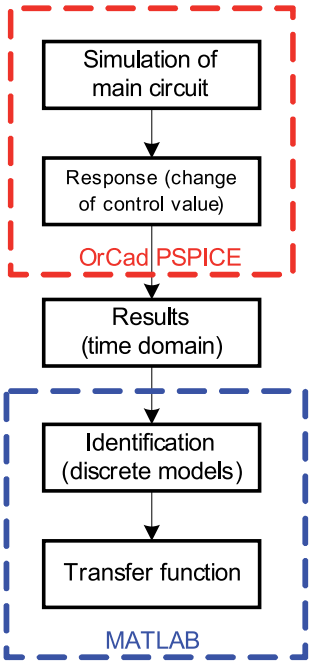

Fig. 3 Simulation based method for identification of transfer function

Unlike the PWM converters, the control transfer function of frequency controlled resonant converters cannot be obtained by the state space averaging method, due to different ways of energy processing. While the state space averaging methods eliminate the information about switching frequency, they cannot predict dynamic properties of resonant converters, so the proper control-to-output transfer function cannot be evaluated.

There are several methods for solving this problem, but some of them are too simplified and idealized, others are too complex and difficult to use [2, 3]. In this paper, a new simulation based method for revealing the control transfer function is proposed.

This method is based on PSPICE simulation and use of System Identification Toolbox in MATLAB environment. First, the simulation of main circuit in PSPICE must be created. The simulation in PSPICE must be exact with all parasitic components taken into account. Using of PSPICE simulation, the dependency of output (voltage, current) on input (switching frequency, duty cycle) can be simulated. Data acquired from simulation in PSPICE are used in MATLAB System Identification Toolbox. Whole process used in this method is shown in Fig. 3.

Using this toolbox offers several models for identification of the system. With use of different models from System Identification Toolbox (SIT), identification of all converters is possible.

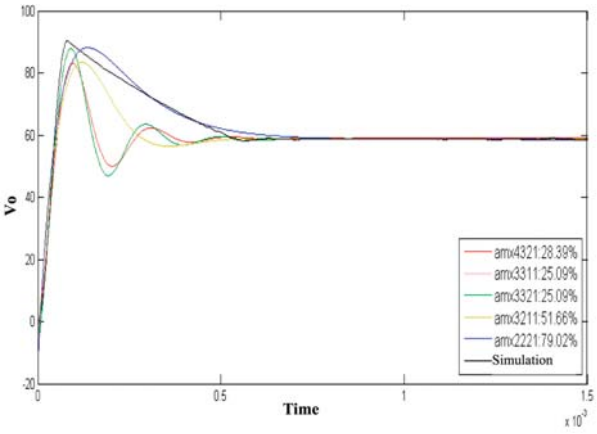

Fig. 4 Accuracy of ARMAX models with different degree (up to down 4, 3, 2)

System Identification Toolbox includes a number of models in continuous or discrete form, which can be used for identification of systems:

- ARX (Auto Regressive Exogenous Input Model)
- ARMAX (Auto Regressive Moving Average Exogenous Input Model)
- OE (Output Error Model)
- BJ (Box-Jenkins Model), SS (State-Space Model).

The simplest model is ARX, best accuracy offers models ARMAX, BJ and OE. Accuracy of the model depends also on degree of polynomials used in transfer function. Fig.4 shows accuracy of identified transfer function on its polynomial degree for ARMAX

model of LLC converter. In most types of converters degree from 2 to 4 is sufficient. All models are in discrete form (z-domain), so the exact specification of sampling interval is necessary [8]. Sampling interval used for models in SIT must be equivalent with integration step used for simulation in OrCad PSPICE. Requested discrete transfer function is in form:

$$G(z) = \frac{B(z)}{A(z)} = \frac{b_0 + b_1 z^{-1} + b_2 z^{-2} + \ldots + b_{nb} z^{-nb}}{a_0 + a_1 z^{-1} + a_2 z^{-2} + \ldots + a_{na} z^{-na}} \quad (2)$$

The coefficients of the transfer function were acquired from ARMAX model of 2nd degree. This model was chosen due to its best accuracy (79%). After acquiring the transfer function, the proper discrete controller can be designed.

3. Design of Discrete Controller

Due to implementation in microprocessor, the controller must be in discrete form. There are two ways to design a discrete controller - design by emulation and direct digital design [5].

In the design by emulation approach, also known as digital redesign method (see Fig. 5), first an analog controller is designed in the continuous domain, by ignoring the effects of sampling and hold of A/D converter and computing delay of microprocessor. In next step, the controller can be converted into discrete-time domain by one of discretization method.

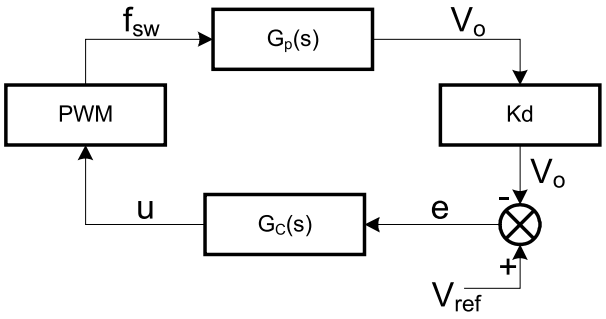

Fig. 5 Design of discrete controller by emulation

This approach is good for systems of lower degree, but in discrete systems of higher degree, the transient responses does not reflect the required values because of ignoring sample and hold and computation delay effects.

On the other hand, the direct digital design approach offers design of controller directly in z-domain, without conversion, including effects of A/D converter and microprocessor. Block diagram of this approach is in Fig. 6.

Sampling of measured value with A/D converter can be represented by ideal Zero-Order-Hold block with sample time T_s. Gain of A/D converter is represented by block K_{adc}. Computing delay of microprocessor, also with delay from PWM module are represented by block T_{comp}. A/D converter with PWM module together form a sampling-and-hold device. Sample and hold block brings additional time delay of $T_s/2$ and phase lag of $\omega T_s/2$, which means that reconstructed signal has time or phase lag [1, 9, 10, 11]. The s-domain transfer function of sample and hold device is:

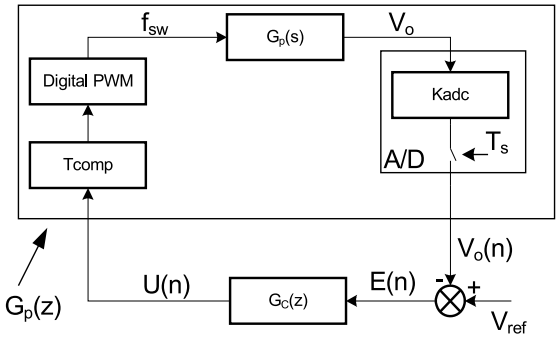

Fig. 6 Direct digital design control loop.

$$SH(s) = \frac{1 - e^{-sT_s}}{s} \quad (3)$$

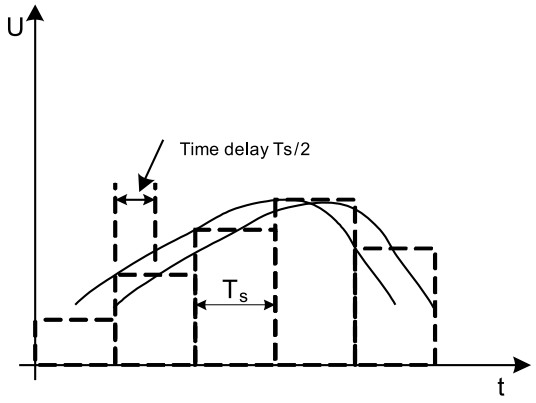

Fig. 7 Effect of "sample and hold" in discrete system

Block T_{comp} represents delay between conversion of A/D converter and PWM duty cycle or modulo update. Time between these two events is necessary for computing the values for PWM block. Transfer function of block Tcomp is:

$$H_C(s) = e^{-sT_d} \quad (4)$$

Discrete transfer function of the whole converter including Zero-Order block, Sample-and-Hold effect and gain of A/D converter is:

$$G(z) = Z\left\{\frac{1}{s}(1 - e^{sT_s}) \cdot H_C(s) \cdot G_P(s) \cdot K_d\right\} \quad (5)$$

Fig. 8 shows effect of sampling interval with computing delay on stability of closed control loop. Table 1 shows different transfer functions with different sampling intervals and different computational delays. Transfer functions without computing delay, are marked Gz1 and Gz2. In transfer functions marked Gdlyz1 to Gdlyz4, the effects of computing delays from 3 to 6 μs are implemented. Sampling times were used from A/D converter included in DSC 56F8013 also the computing times were used from same processor. Application was for digital control system for 200 kHz multiresonant converter. In this system discrete regulator of third order was used [4].

Sampling times and computational delays for transfer functions in Fig. 6 — Tab. 1

Sampling time T_s	Computing delay T_{comp}	Mark
5 μs	0	Gz1
10 μs	0	Gz2
5 μs	3 μs	Gdlyz1
10 μs	3 μs	Gdlyz2
5 μs	6 μs	Gdlyz3
10 μs	6 μs	Gdlyz4

From Fig. 8 is clear that computing delay has significant effect on stability of closed control loop. With rising computing and sampling time stability of control system drops.

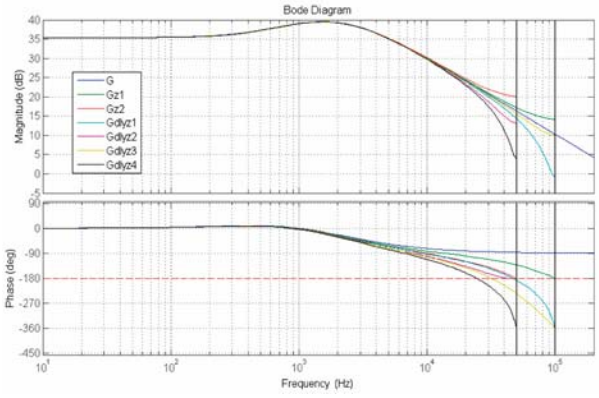

Fig. 8 Effect of sample and hold and computation delay on stability of control loop

For design of controller in z-domain, all above mentioned delays must be taken into account. With use of MATLAB Siso Design Tool, the proper discrete controller can be designed. This tool offers a wide palette of tools, including Graphic User Interface for direct controller design in discrete or continuous domain. Advantage of this tool is possibility of direct placing of zeroes and poles of controller on point diagram of closed or open loop. After placing the poles or zeros of controller, the different responses of closed control loop can be displayed for verification.

4. Implementation in DSC

Discrete controller proposed in previous chapter was implemented into 16b digital signal controller (DSC) Freescale 56F8013, which is primary designed for motor and converter control. Advantage of this microprocessor are high performance peripherals which can operate with 96Mhz clock frequency. On the other hand, disadvantage of this processor is low core frequency – 32MHz, and fixed point arithmetic. For better performance, fraction arithmetic with intrinsic functions were used in this DSC [12, 13].

Block scheme of digital control system with DSC 56F8013 on 200 kHz LLC converter is in Fig. 9. For better performance and lower amount of additional hardware, the concept with microprocessor on secondary side of converter was used. Also, new available fast digital isolators were used instead of standard optocouplers.

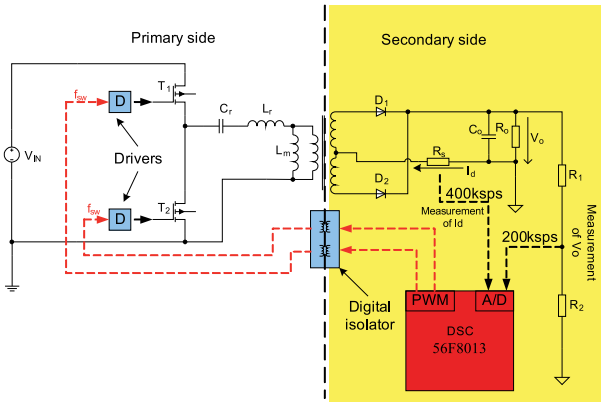

Fig. 9 Block scheme of full digital control system with DSC 56F8013

Another option for implementation is use of 32b microprocessor ColdFire V1 which offers better computing performance, but sampling time of A/D converter is twice as in DSC 56F8013. For measurement of output voltage, this time is sufficient, but for current sensing, the A/D converter on ColdFire is too slow. This problem was eliminated by use of special algorithm for computing of diode current from value of output voltage, value of load and ripple of output voltage. This algorithm is based on computing of output current from output voltage drop, during load connection. Detailed method is described in [3]. Times required for computing on both processors are in Table 2.

5. Verification ofProposed Full Digital System

Measurements of the full digital control system were realized on 60V/25A LLC converter with use of 16b 56F8013 DSC. The block scheme for measurement circuit is shown in Fig. 9. For correct

Sampling times and computational delays for two processors — Table 2

Processor	Bits	Core frequency	A/D sampling time	Computing of control loop	Computing of current value
56F8013	16b	32Mhz	1.126µs	2.98µs	3.01µs
ColdFireV1	32b	50.3Mhz	2.252µs	1.8µs	1.12µs

start of the converter, the soft-start algorithm, when switching frequency is twice as normal (400 kHz), was used. Fig. 10 shows point when soft-start ends and algorithm takes control.

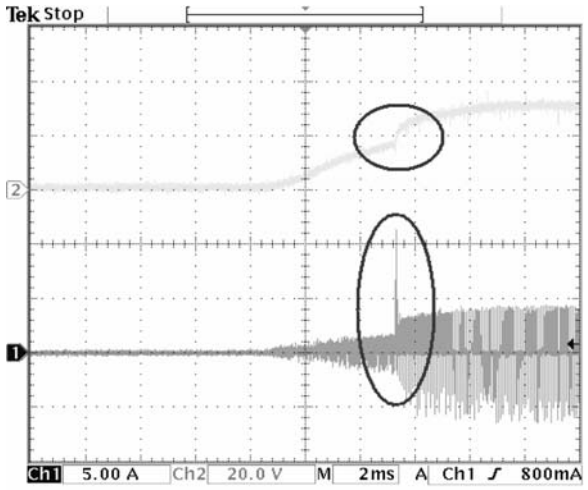

Fig. 10 Measured waveforms during soft start: (top to down): output voltage (2), load current(1)

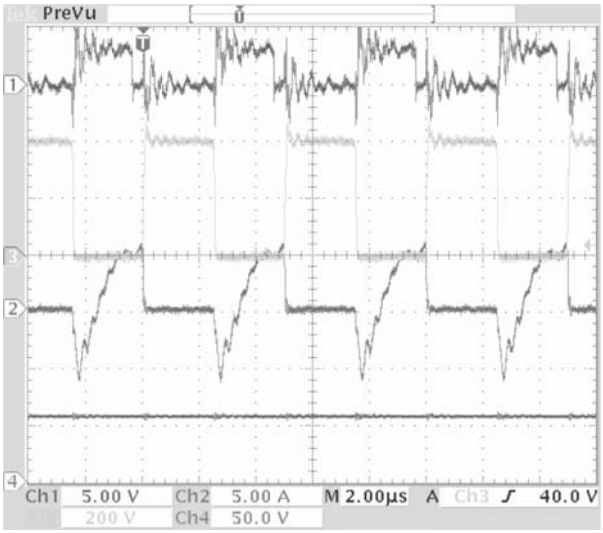

Fig. 11 Measured waveforms with digital control system - no load: (top to down): pwm pulses(1), transistor voltage(3), transistor current(2), output voltage(4)

Waveforms from digital control system at no load condition are shown in Fig. 11 – output voltage 58.8V at 201 kHz switching frequency.

For measurements of control systems at full load conditions, the requested output voltage was changed to 50V due to lower tolerance of used MOSFETs against current peaks. Input voltage was 325V due to verification of dynamic properties of controllers. Fig. 12 shows waveforms from digital control system with microprocessor. Output voltage was 48V at 160 kHz switching frequency.

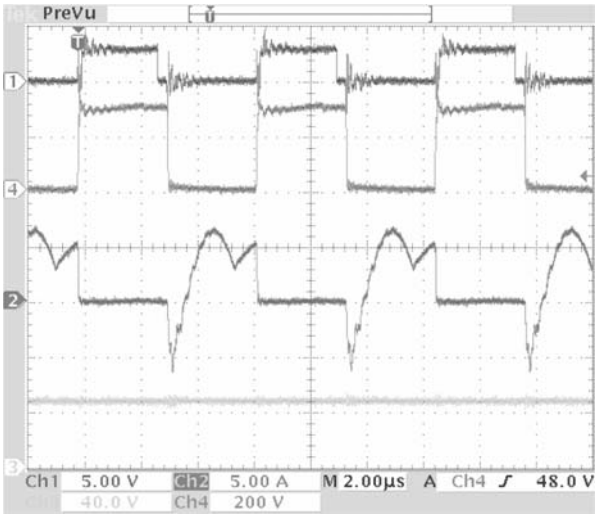

Fig. 12 Measured waveforms with digital control system - full load: (top to down): pwm pulses(1), transistor voltage(4), transistor current(2), output voltage(3)

6. Conclusion

In this paper the new approach for design of digital control system with discrete controller is described. Proposed method for revealing the control to output transfer function is based on numerical simulations from widely used OrCad PSPICE environment. Major advantage of this method is possibility of use for every power semiconductor converter, non-isolated, isolated, PWM, PSM or frequency controlled. Also, the exact analysis of operating intervals is not necessary, because this method requires only two values – control (input) and output.

Consequently, for discrete controller design, two methods were proposed. While both methods of digital controller design "design by emulation and direct digital design – have their benefits to the developer, the first method, namely design by emulation, allows the power supply designers to do the control design in the familiar s-domain and then convert it to a discrete/digital controller. Disadvantage of this method is inaccurate representation in digital control system.

The second approach known as direct digital design, allows digital controller design directly in z-domain and results in better

dynamic performance for the closed loop operation of the converter – especially with use in microcontroller or DSP. All of these MATLAB based designed controllers were finally validated by experimental results. Comparison of measured waveforms at full load shows good accuracy for digital control system. On the other hand, from measurements at no load condition results that digital control system has lower resistance against EMI [14, 15]. Also, the stability of digital control system was low, due to longer computing time compared to switching frequency of converter (200 k Hz). This problem can by solved by the use of faster microprocessor as described in the paper, or by eliminating of current control loop with special algorithm for computing of output current – this option is described in [4].

All experimental results are described more in detail in [2, 3, 4].

Acknowledgment

The authors wish to thank for the project VEGA "Research of Topology and Control of Power Electronic Supply System with Single-Phase HF Input and Two-Phase Orthogonal Output for Two-Phase SM/IM Electrical Motors". Next to grant agency APVV project No. 20-051705 and no. APVV-0535-07. Also we would like to thank for VMSP-P-0085-09 and LPP-0366-09

References

[1] CHOUDBURY, S.: *Designing a DSP-based Digitally Controlled DC-DC Switching Power Supply,* Texas Instruments, 2006
[2] YANG, B.: *Topology Investigation of Front end DC/DC Converter for Distributed Power System.* Dissertation Thesis, Virginia Tech, 2003
[3] FRIVALDSKY, M.: *Experimental Analysis of Commutation Modes of Various Power Transistor Structures and its Verification and Implementation in Selected Converter's Topology.* Dissertation Thesis, University of Zilina, 2009
[4] DRGONA, P.: *Optimisation of Control System of Power LLC Converter.* Dissertation Thesis, University of Zilina, 2009
[5] FAIRCHILD SEMICONDUCTOR: Half-bridge LLC Resonant Converter Design Using FSFR Series Fairchild Power Switch, *Application Note,* AN-4151, 2007
[6] HANGSEOK, CH.: *Analysis and Design of LLC Resonant Converter with Integrated Transformer,* 1-4244-0714-1/07, 2007 IEEE
[7] JEE-HOON, J., JOONG-GI, K.: *Theoretical Analysis and Optimal Design of LLC Resonant Converter,* SAMSUNG Electronics CO., Lts./Digital Printing Division
[8] MOUDGALYA, K.N.: *Digital Control,* John Wiley and Sons, p.157-237, 2007
[9] LIJUNG, H., ZHENGYU, L., ZHAOMING, O.: *Research of Digital Control Strategy for Multi-resonant LLC Converter,* 1-4244-0755-9/07, 2007 IEEE
[10] BALATE, J.: Automatic Control (in Czech), *BEN – technicka literatura,* Praha, 2004
[11] PEPA, E.: *Adaptive Control of a Step-Up Full-Bridge DC-DC Converter for Variable Low Input Voltage Applications,* Virginia Polytechnic Institute, 2004
[12] FILKA R., BALAZOVIC P., DOBRUCKY, B.: A Sensorless PM Synchronous Motor Drive for Electric Washers, *Communications – Scientific Letters of the University of Zilina,* 2007
[13] ASHRAFZADEH, A.: Power Management: Analog control vs. Digital, *EE Times Online,* Embedded.com, 2007
[14] HRIANKA, M., LAKATOS, J., HARGAS, L., KONIAR, D.: Modeling Simulation and Verification of Heat Transfer in Power Transistor Cooler, *Metalurgija (Metallurgy)*, Vol. 49, No. 2, 2010, ISSN 1334-2576
[15] DOBRUCKY, B., SPANIK, P., SUL, R.: Improvement of Power Electronic Structure Characteristics Using SiC Technology-overview, *Communications – Scientific Letters of the University of Zilina*, 2006.

Daniela Gombarska – Barbora Czippelova – Ivo Cap *

THE INVESTIGATION OF TERMINAL SEGMENT EFFECT ON BLOOD PRESSURE PROPAGATION PATTERNS IN CARDIOVASCULAR SYSTEM MODELS

The electro-mechanical analogy method is used for the simulation of blood flow in blood vessels. Particularly the subject of this paper is the investigation of the influence of terminal segment topology on the blood pressure propagation patterns. The cardiovascular system is widely branched and therefore very complex. Thus, it is impractical to create the simulation model consisting of all blood vessels and attention is focused to development of models for smaller parts of vascular system. The selection and adjustment of terminal segments for such simulation model is important on behalf of the model accuracy. Three different types of terminal segments were implemented in order to show their influence to the blood pressure and blood flow propagation patterns in two model complexities.

1. Introduction

The living organism in general, can be described as a complex system of many component systems. Cardiovascular system is highly complex structure able to regulate itself under physiological condition. Despite this fact some pathological conditions may develop and interfere with self-regulation mechanism (e.g., a fat deposit can reduce vessel section diameter – stenosis, an aneurysm may develop or the arterial wall may become more rigid due to aging). The consequences of these pathologies on the hemodynamical quantities as well as the possible outcome of a treatment may be studied by simulations. Such a model requires patient's data that can be acquired via standard angiologic diagnostic methods (e.g. CT, MRI, angiography, USG).

The principle of duality among hemodynamic characteristic variables and electric variables can be utilised in the process of model development. This approach makes possible to transform physical process from one environment to the other easier solvable one. Despite this, in relation to utilised model type the description of whole circulatory system can become far too complex and simulation model computationally expensive. For detailed description it is usually chosen only small area of interest, which can be exactly separated from the rest of system and its relationship to the other parts can be well defined and described. Comparison of boundary model elements influence to the simulation results for simplified and more complex model of human upper limb is the object of this paper.

2. Theory

The blood flow is formally analogical to propagation of electric current along electric lines. Differential equations of hydrodynamic processes in a tube are similar to those describing transmission of electric charge in an electric line.

The blood flow in physiological case is considered to be laminar. As the blood vessels forks, the sum of diameters of all branches can differ from the diameter of the original vessel. This sudden change of tube diameter usually followed with change of tube direction can cause reflections in propagating flow. Reflections or other hydrodynamic processes can occur also in pathologic case, when

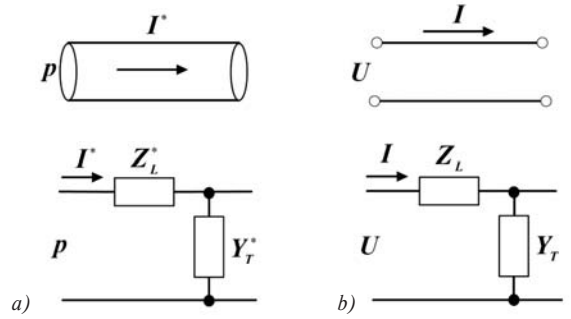

Fig. 1 Analogy of a tube with liquid and an electric line: a) Section of a homogeneous tube, b) Section of a homogeneous two-wire line.

* **Daniela Gombarska, Barbora Czippelova, Ivo Cap**
Faculty of Electrical Engineering of the University of Zilina, Slovakia, E-mail: gombarska@fel.uniza.sk, web: http://fel.uniza.sk/ktebi/

the sudden change in vessel diameter is caused by disease, for example stenosis in vessel wall. [1]

The analogy of hydrodynamic process in a tube and transmission of electric current can be demonstrated by schematic drawing in Fig. 1. Longitudinal impedances Z_L* and Z_L represent conservative and dissipative components, transversal admittances Y_T* and Y_T describe cross elasticity and inter-wire capacity and cross losses. The detailed depiction of equivalent circuit for one blood vessel segment is shown in Fig. 2 (a) and is in more detail described in [2]. Values of longitudinal impedance parameters depend on blood flow and blood pressure ratio. Formulas for estimation of elements in longitudinal and transversal part of equivalent circuit are based on work of Gaelings [3]. Elements of equivalent circuit of blood vessel can be derived by means of equations describing hemodynamics (Navier – Stokes equation, continuity equation) and by using electromechanical analogy.

$$R_n = \frac{8\eta}{\pi r_0^4} n, \qquad L_n = \frac{1}{2n-1}\frac{\rho}{\pi r_0^2}, \tag{1}$$

$$C_p = \frac{2\pi r_0}{\kappa E}, \qquad R_p = \frac{\kappa \eta_w}{2\pi r_0}, \; n = 1, 2, 3 \tag{2}$$

where r_0 is radius of the vessel wall, ρ is the blood density, η – dynamic viscosity, E is the volume stiffness of the tube wall and η_w – coefficient of internal friction (cause of deformation losses), κ – geometrical factor. All the longitudinal and transversal parameters of the equivalent circuit are per-unit values.

The cardiovascular system can be divided into cascade sequence of small segments. The model of cardiovascular system is then composed of equivalent circuits of these segments linked together [3, 4, 5]. Despite the electric circuit analogy computation efficiency, modelling of each individual vessel of blood circulatory system is impractical. Therefore, the detailed model is created only for the area of interest and all the contiguous and distal parts are lumped together and substituted by equivalent circuit, Fig. 2b, c and d.

For comparison of terminal segment influence on blood circulation simulation results three types of lumped equivalent circuits are utilised. The simplest model of terminal segment, named Case A, is two-element Windkessel model, shown in Fig. 2b. Parameters R_T, C_T of equivalent circuit represent peripheral resistance and compliance. One possible estimation method of these parameters is by impedance matching. In context of the electrical theory analogy these parameters are derived from characteristic impedance of vessel equivalent circuit. We assume the output impedance of vessel model to match the input impedance of terminal segment. The characteristic impedance of equivalent circuit is

$$\dot{Z}_0 = \sqrt{\frac{\dot{Z}_L}{\dot{Y}_T}}, \tag{3}$$

where $\dot{Z}_L$ is longitudinal impedance and $\dot{Y}_T$ is transversal admittance of vessel segment equivalent circuit. The terminal segment impedance is

$$\dot{Z}_T = \frac{R_T(-jX_{C_T})}{R_T - jX_{C_T}}, \tag{4}$$

The reflection in pulse and blood flow wave depends according to electric transmission line theory on the difference between the impedance of the line at the joint and impedance at the terminal segment.

$$\dot{r} = \frac{P^-}{P^+} = \frac{\dot{Z}_T - \dot{Z}_0}{\dot{Z}_T + \dot{Z}_0}, \tag{5}$$

Because in general within the periphery blood circulatory system is supposed to operate without reflections the reflection coefficient $\dot{r} = 0$ and $\dot{Z}_T = \dot{Z}_0$. Thus the R_T, C_T parameters of equivalent circuit are derived combining equations (3) and (4), from real and imaginary parts of $\dot{Z}_0$.

Second type of terminal segment topology, Case B in Fig. 2 (c), is three-element Windkessel model. Calculation of the parameters R_1, R_2 and C_2 is also derived from electric transmission lines theory – vessel segment characteristic impedance and terminal segment impedance [8].

$$\dot{Z}_T = R_1 + \frac{R_2(-jX_{C2})}{R_2 - jX_{C_2}}, \tag{6}$$

Total terminal resistance R_T is in this type of terminal segment equal to sum of R_1 and R_2. For derivation of R_1, R_2 and C_2 are applied the same assumptions as in two-element Windkessel model. However in this case the derivation leads to quadratic equation and only physically meaningful results should be taken into account.

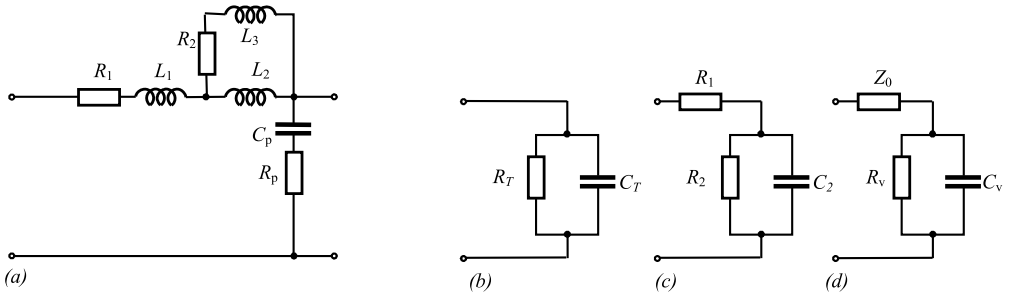

Fig. 2 a) Equivalent circuit of one segment of distributed parameters model, b) Case A, c) Case B and d) Case C are equivalent circuits of terminal segment

Case C in Fig. 2d is topologically similar to the Case B. However, for the parameter estimation the different approach is chosen. In previous two cases the transmission line is supposed to be lossy. Here we assume that the cut-off line is infinitely long and lossless [9]. Thus the characteristic impedance is frequency independent and depends only on the longitudinal inertia per segment length L and the compliance per segment length C

$$Z_0 = \sqrt{\frac{L}{C}}\,. \tag{7}$$

The characteristic impedance $\dot{Z}_0$ and resistance of distal segments R_v compose the total terminal resistance $R_T = Z_0 + R_v$. Compliance of the distal part behind the end segment C_v can be calculated with time constant τ

$$C_v = \frac{\tau}{R_v}\,. \tag{8}$$

According to [9] the typical value for τ is 1.5 s.

In all three terminal segment models is total terminal resistance expressed by means of mean pressure and mean flow with α the percentage of the cardiac output flowing through the vascular bed behind the end segment [9]

$$R_T = \frac{p}{\alpha q}\,. \tag{9}$$

3. Simulation and Results

For examination of terminal segment effect we chose human arm arteries, Fig. 3.

From the complexity point of view, two model structures are simulated. The first one, more complex model of human upper limb arterial tree consists of 24 segments of arteries (Brachialis, Radialis, Ulnaris and Arcus Palmaris) and 8 terminal segments for outgoing arteries (Profunda Brachii, Superior Ulnar Collateral, Inferior Ulnar Collateral, Interosseus, Policis and three Digitalis). The simplified version of the model consists of 19 segments of arteries (Brachialis, Radialis and Ulnaris) and 6 terminal segments for outgoing arteries (Profunda Brachii, Superior Ulnar Collateral, Inferior Ulnar Collateral, Interosseus, two parts of Arcus Palmaris).

Pressure waves are computed at two parts of model – at A. Radialis and A. Digitalis. The computation at A. Radialis is carried out at four points – on input of segments 16, 17, 18 and 19 for both the complex and simplified models. In more complex model the additional computation point is joined at A. Digitalis for comparison with sample of clinical measured data. The results of simulations are compared together to evaluate the influence of terminal segment type on pressure wave form.

Fig. 3c shows typical waveform and amplitude of pulse wave on A. Radialis. The results of simulation for both the model complexities and all three types of terminal segments are displayed in Fig. 5a, b and c.

The influence of terminal segment on the waveform match between the complex model and the simplified one is apparent from Fig. 5a, b and c. In accordance with transmission lines theory the blood pressure wave depends not only on time but also on the distance on the vessel, Figs. 6, 7 and 8. The amplitude of blood pressure increases with distance from the beginning of the vessel. This effect originates from circulatory system geometry, especially in branching parts. Similarly with the transmission line theory, there are segments there, terminated with impedance different from its characteristic impedance. Also the difference between pressure results for more complex and simplified model depends on the distance x on the vessel. The computed mean value of blood pressure difference $\Delta\varepsilon$ between complex and simplified model is shown

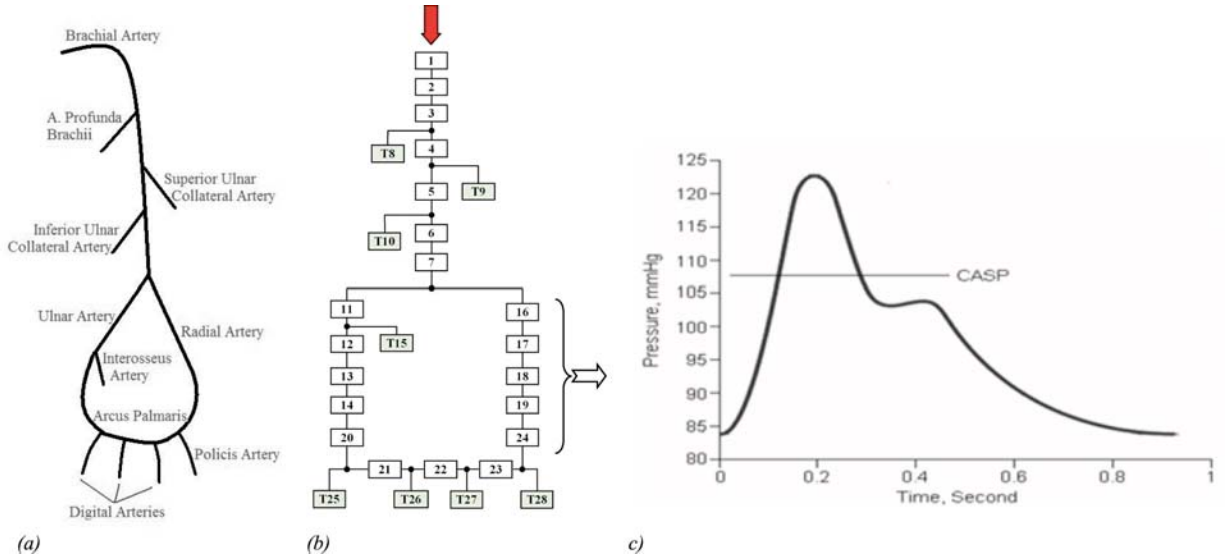

Fig. 3 a) scheme of arm arteries, b) model of arm composed of equivalent circuit segments, c) pressure waveform example in A. Radialis

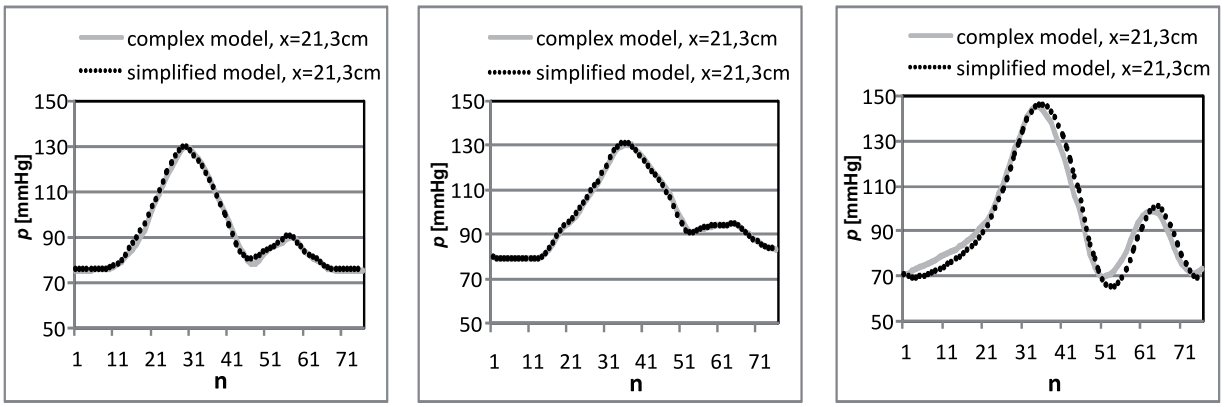

a) *b)* *c)*

Fig. 5 Pressure waveform in A. Radialis in x=21,3cm for: a) Case A terminal segment, b) Case B terminal segment and c) Case C terminal segment

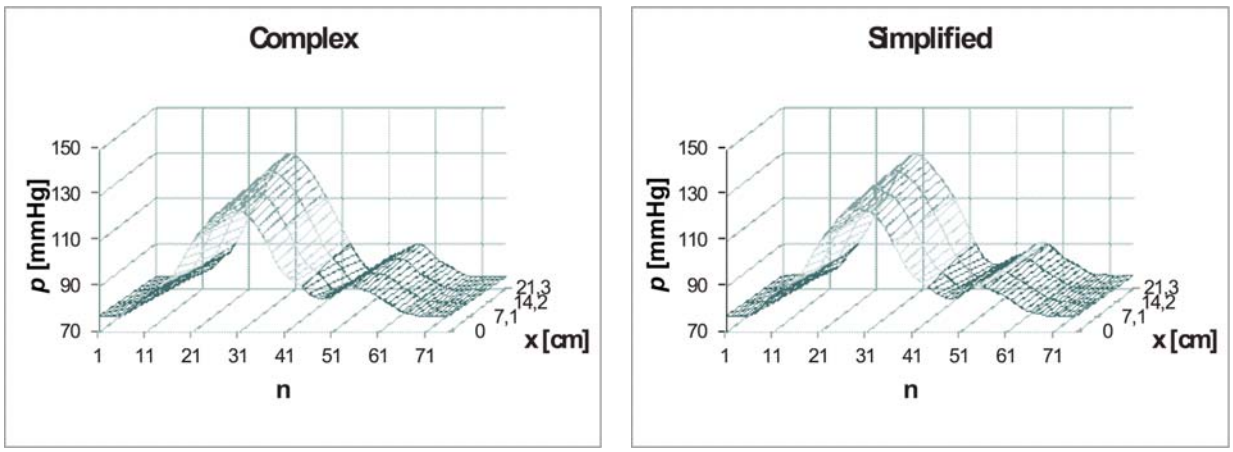

Fig. 6 Calculated pressure waveform vs. sample and distance x in A. Radialis for case A, complex and simplified model

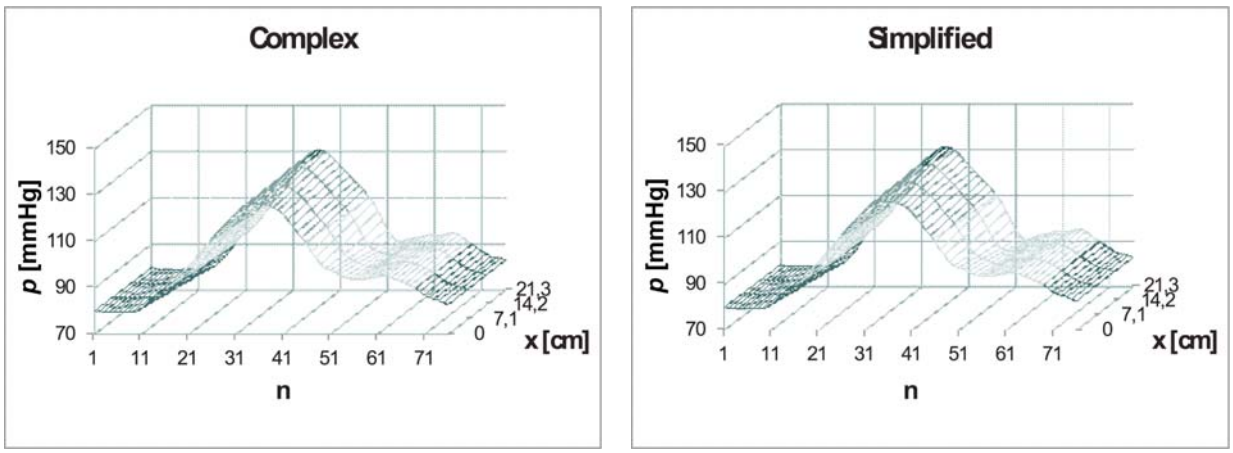

Fig. 7 Calculated pressure waveform vs. sample and distance x in A. Radialis for case B, complex and simplified model

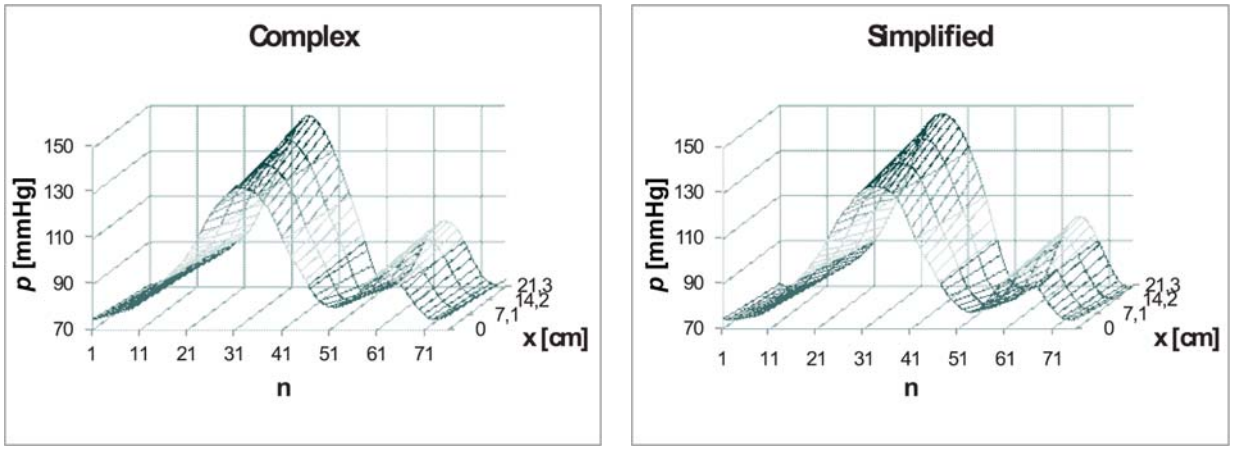

Fig. 8 Calculated pressure waveform vs. sample and distance x in A. Radialis for case C, complex and simplified model

in Fig. 9. The Case B terminal segment appears to have best match between simplified and complex model.

For illustration of the model nature the pressure in A. Digitalis for complex model is computed, Fig. 10a and the measured pressure wave example is shown in Fig. 10b. It is apparent that for the comparison with physiological values the model should be adjusted to the measured subject parameters. However, the pressure waveform of Case A and B show a good affinity to the measured one.

4. Conclusion

To show the difference between the three models of terminal segments Case A, Case B and Case C we used the two models of arm arterial tree. First one was the more complex one and the second was simplified by cutting the lower part of arteries off and substituting them by the same type of terminal segments as in a more complex model.

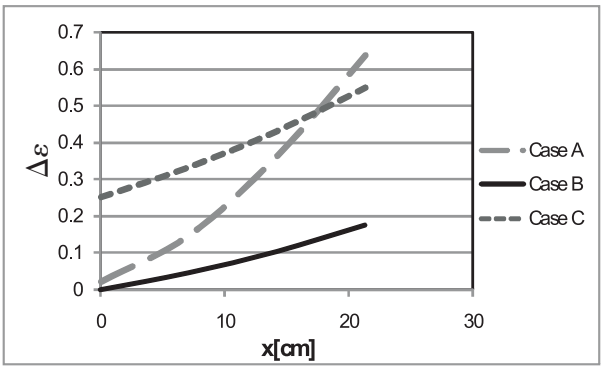

Fig. 9 Mean Δε vs. distance x

From all the simulated cases the best matching showed the Case B – three element Windkessel model. The Case A – two element Windkessel model had similar influence on the pressure wave on the beginning of the vessel, but the difference increases

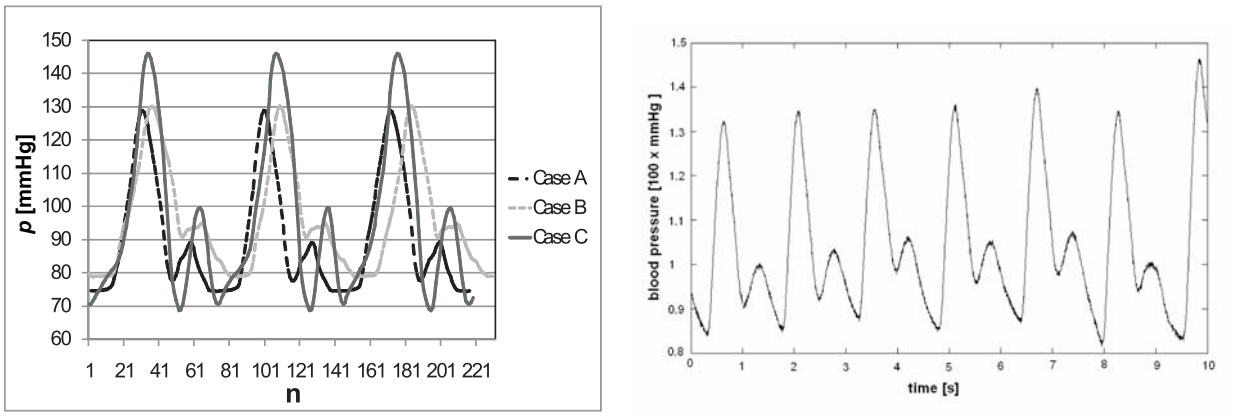

a) *b)*

Fig. 10 a) Calculated pressure waveforms in A. Digitalis; b) Measured pressure waveforms in A. Digitalis

with the distance. The third model of terminal segment Case C appears to be unsuitable for arterial circulatory system simulation purposes.

The human vascular system is highly complex structure with self-regulation ability. It should be emphasized that for the comparison with physiological values the model parameters should be adjusted for the measured subject. Also some regulatory mechanisms of the system should be considered in the model. All parameters for simulated arteries were obtained from the literature [11], [12]. Therefore the results of this study should be considered as strictly theoretical.

References

[1] CZIPPELOVA, B., GOMBARSKA, D.: *Investigation of Blood Pressure and Blood Flow Wave Propagation on Arterial Bifurcation*, In *IEEE* 2009 – Kraliky, Proc. of conference, Vysoke uceni technicke v Brne, Fakulta elektrotechniky a komunikacnich technologii, 2009. ISBN 978-80-214-3938-2, p. 44–47

[2] CAP, I., CZIPPELOVA, B.: Electromechanical Model of Blood Flow in Vessels, *Advances in Electrical and Electronic Engineering,* Vol. 7, 2008, pp. 338–341, ISSN 1336 – 1376

[3] GAELINGS, E. W.: *Numerische Simulation Haemodynamischer Processe in Vascularen Netzen,* Shaker Verlag Aachen, 1996, ISBN-3-8265-1509-9, Germany.

[4] WESTERHOF N., STERGIOPULOS N, NOBLE, M.I.M.: *Snapshots of Hemodynamics,* ISBN 0-387-23345-8

[5] WANG, J.J., PARKER, K.H.: Wave Propagation in a Model of the Arterial Circulation, *J. of Biomechanics*, Vol. 37, No. 4, 2004, pp. 457–470, ISSN 0021-9290

[6] CZIPPELOVA, B., CAP, I.: Pulse Wave Velocity Calculation by Means of Electromechanical Model of Blood Vessel, *Trends in Biomedical Engineering,* 2009, pp 149–153, ISBN 978-80-227-3105-8

[7] SACKL-PIETSCH, E.: *Continuous* Non-invasive *Arterial Pressure Shows High Accuracy in Comparison to Invasive Intra-arterial Blood Pressure Measurement,* online https://www.biopac.com/Manuals/nibp100d_white_paper.pdf [1.4.2010]

[8] WAITE, L, FINNE, J.: *Applied Biofluid Mechanics,* The McGraw.Hill companies, United States of America, 2007, ISBN-13: 978-0-07-147217-3; ISBN-13:0-07-147217-7

[9] EMMER, M., *Lumped Parameter and Experimental Model of Endoleakage After Endovascular Treatment of Abdominal Aortic Aneurysms,* Master thesis, Eindhoven University of Technology, 2004

[10] STERGIOPULOS, N., SEGERS, P., WESTERHOF, N.: Use of Pulse Pressure Method for Estimating Total Arterial Compliance in Vivo, *Am J Physiol Heart Circ Physiol,* Vol. 276, No. 2, pp 424–428, 1999, ISSN: 0363-6135

[11] JOHN, L. R.: Forward Electrical Transmission Line Model of the Human Arterial System, *Medical & Biological Engineering & Computing,* Vol. 42, pp 312–321, 2004, ISSN: 1741-0444 (Online)

[12] WANG, J. J., PARKER, K. H.: Wave Propagation in Model of the Arterial Circulation, *J. of Biomechanics,* Vol. 37, No. 4, pp. 425–593, 2004, ISSN: 0021-9290.

Marek Hoger – Peter Bracinik – Marek Roch *

SIMULATION OF A POWER SUBSTATION'S CONTROL SYSTEM OPERATION

This paper describes a simulator of power substation automation system developed as part of software suit for complex simulation of power substation operation. This software simulates behavior of a distributed control system built from a group of interconnected and cooperating intelligent electronic devices. The basic structure and communication principles are derived from standard IEC 61850.

1. Introduction

Operation reliability of an electrical transmission or distribution system is markedly affected by the operation reliability of its nodes – power substations.

A power substation is a distributed system built from high number of power and control devices. Its key component is substation control system because it's necessary for proper cooperation of high number of power substation's devices (there can be hundreds of devices in a substation).

Many concepts of substation control system architecture were developed in the past, based on different control techniques (from oldest relay based systems to modern systems based on intelligent equipment and new communication technologies). The evolution of power equipment, protection and control devices, and of course evolution of communication technologies, led to development of new standards in substation automation like UCA2 and IEC 61850. These standards are very flexible. The system can be designed as strongly centralized or highly decentralized, according to local conditions and specific user needs. Improper design can cause markedly decrease of systems performance or unexpected behavior. Therefore, computer simulation can be very useful to simulate and predict the behavior and performance of such a system.

There are some tools for simulation of substation operation, mostly focused on simulation of protective relays and control system. But these tools are proprietary, have (relative) limited functionality and it is difficult (or impossible) to extend the application and add new functions.

Therefore, we decided to develop own substation operation simulation software. The software should be flexible and extensible, usable by solving wide range of problems. The scope of use should be primary the testing of new control and protection functions, developing of algorithms for autonomous substation control and analysis of system behavior in different operation situations (primarily by faults). Another important application of this software is in teaching various subjects related to control of power substations, protection of electrical systems and use of information systems in energetics.

2. The Power Substation Simulator

The power substation simulator consists of three independent cooperating applications – power system simulation (PSS), control system simulation (CSS) and graphical user interface (simple SCADA application). This structure is well corresponding with real operation of a power substation.

The power system simulator performs the calculation of state values (voltages, currents, device state signalization, etc.) and contains models of power equipment (switching devices, power transformers, instrument transformers or sensors). The physical model was created in Matlab/Simulink and uses user defined library of hardware models, based on SimPowerSystems library. The communication with the control system is realized using blocks for TCP communication from Instrument Control Toolbox library. The use of Simulink, as modeling environment, enables to modify the device models easily, so the user can add or remove their functionality according to actual demands.

The control system simulator performs simulation of control and protection devices and their communication. The control system reads the actual state values sent from physical model, process this data and if needed, sends requests for hardware state changes

* **Marek Hoger, Peter Bracinik, Marek Roch**
Department of Power Electrical Systems, Faculty of Electrical Engineering, University of Zilina, Slovakia, E-mail: Marek.Hoger@kves.uniza.sk

(e.g. opening a circuit breaker). It also generates reports for user interface application containing information about important state changes (change of switch position, reactions of protections). Detailed specification of this software is introduced later in this paper.

The user interface application provides user with information about actual system configuration, measured values and important events in graphical form. The application supports control of the power equipment using the hardware manipulation functions of the control system. It also creates an events log to a simple text file and optionally to a SQL database.

The data exchange between these applications is realized over TCP/IP protocol, so each of these applications can run on different computer, which allows effective use of computing capacity of multiple computers.

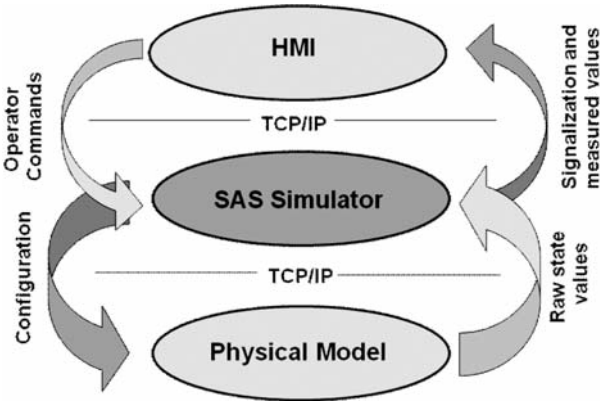

Fig. 1 Structure of power substation simulator

3. The Control System Simulator

The control system simulator is an application simulating the operation of intelligent electronic devices (IEDs), of which modern substation automation systems are built. The application simulates the behavior of each device (protective, control and system functions) and also simulates communication between devices. This application is a key component of the simulation suit of substation operation.

Today, an object oriented approach to modeling of substation automation system is used and this approach is also used in modern standards for communication in power substations (e.g. UCA2 or IEC 61850). Therefore, the application was developed in C# language – an object oriented language based on C language and .NET framework.

A power substation is a very complex system and it's difficult to identify all necessary functions and develop optimal object structure, so the object structure and basic communication principles were adopted from international standard IEC 61850. But, this software is not the implementation of this standard. The full implementation of this standard would be too complicated and in fact useless for the planned scope of use of the application. The object structure, mapping of communication services and configuration language were simplified and modified to meet our needs. The simplified structure of the application in UML notation is in Fig. 1.

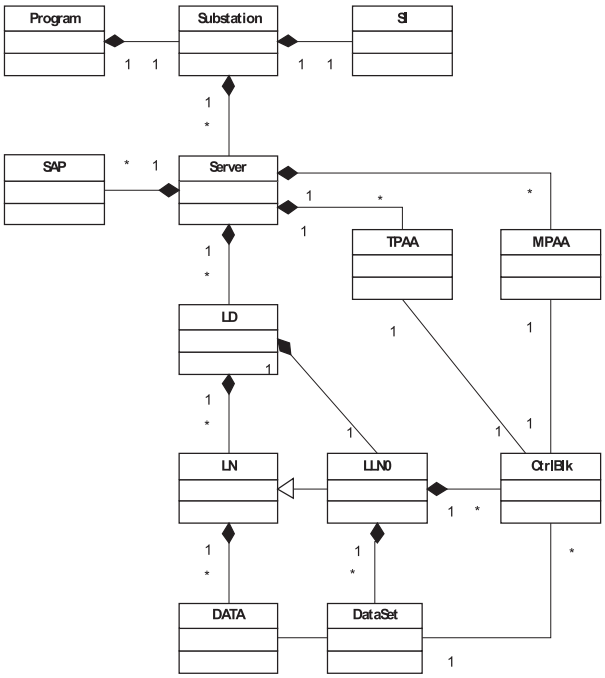

Fig. 2 Simplified structure of control system simulator

On the top of the structure is the *Program* class. It's the root element of the structure. This class loads the configuration on startup and builds the data structure according to configuration specified in a file in XML format. After startup, it provides user interface services and commands interpreting. Program class contains a single instance of *Substation* class.

Substation class acts as a container for *Server* class instances representing IEDs building the automation system. This class itself has no functionality and is used only for better organization of *Server* instances.

Simulation interface (SI) class provides the interconnection to physical model over a TCP/IP connection and controls the execution of functional cores of *Server* class instances. Simulation interface creates a TCP listener and then waits for incoming raw data from physical model. Each data is transmitted with a tag describing the source of the data. SI reads the tag, then searches the signals mapping table for this tag and if an association is found, writes the data to input buffer of associated logical node. If there is no association defined in the signal mapping table, the data is

ignored. Reversely, if a logical node needs to change state of a device in physical model, it writes the command and its own reference to command buffer of the SI, SI searches the signal mapping table and if an association is found, it sends the signal code (and optionally additional parameters) over TCP back to physical model. The last important function of SI is time synchronization. With each raw data message from the physical model the actual simulation time is transmitted to the SI. When a time update signal is detected, SI updates the system clock and runs functional cores of *Server* class instances. The signal mapping table is stored in a file in XML format and can be modified manually in every text editor or using an auxiliary tool (created as part of the software suit) able to automatically detect all available signals and related logical nodes.

Server class instance represents a single IED. It contains services for communication with other *Server* class instances and services for data manipulation on physical device level. Communication services are protocol independent and the final mapping to a real protocol is done using instances of *SAP* class (Service Access Point class used for general purpose communication), *TPAA* class (Two Party Application Association which supports peer to peer connection services) and MPAA class (Multiple Party Application Association class supporting multicast services). *Server* class also contains one or multiple instances of *LD* class. The *SAP* class developed with the simulator provides the mapping of services to TCP/IP and supports the binary serialization of data object instances, so they can be transmitted over TCP. In the future, it's possible to develop a service interface for other network technologies and protocols like SPABUS or MODBUS over a serial line, or map the services to MMS as defined by IEC 61850. For the binary serialization a standard binary formatter provided with .NET framework is used. For proper deserialization of received data in applications created in other programming environments (e.g. LabVIEW) a special data handler must be created in C# (or other .NET language) and imported as .NET component.

LD class acts as a container for logical node instances. Using multiple instances of *LD* class helps keep the data structure more compendious. Typical example of using multiple *LD* instances is using one instance of *LD* for bay control functions and other *LD* instance for protective functions. Each *LD* must contain one instance of *LLN0* (Logical Node Zero).

LN class represents an elementary system function of SAS (e.g. overcurrent protection). These elementary function blocks are called logical nodes. IEC 61850 defines 86 different logical node classes (one for every known elementary system function) divided to 13 basic categories. The requested functionality of an IED is than performed by a collection of cooperating *LN* instances. The LN instance uses *DATA* class instances as an interface for communication with other system blocks. *DATA* is a collection of attributes providing elementary information describing setting of logical node, current state of logical node and additional information, related to the specific function of the LN.

A special kind of logical node is the *LLN0*. This class doesn't perform any system function, but it contains data describing health, mode and vendor of the device and acts as a container for *CtrlBlk* (Control Block) instances and *DataSet* instances.

Control blocs are classes derived from *CtrlBlk* class. These blocks perform messaging and logging functions. Instance of a control block observes a collection of data or data attributes referenced by a *DataSet* instance. Each dataset member ought to have definition of trigger conditions indicating which event should invoke the control block to create and send a message (or write a new log entry). Trigger conditions can be set to data change, quality change or data update. When control block detects an event corresponding to trigger conditions, a report or data message is sent using the appropriate message handling object (e.g. *TPAA* or a *MPAA* instance associated with the control block), or a log entry is added to archive (if the control block is Log Control Block).

Of course, this is only brief description of the structure. The real structure is much more complex, similar to the object structure defined in standard IEC 61850-7.2

The configuration of a substation is described in a collection of configuration files. There are three types of configuration files.

The .sub file describes the structure of a substation and table of all IEDs building the system and device configuration files assigned to these IEDs. It is the main project file and normally each project contains only one file of this type.

The .cid file describes the configuration of a single IED. It contains all information about the internal structure of a *Server* class and setting of all necessary attributes. Format of this file is derived from CID file format defined in IEC 61850-6. There is one .cid file for each server instance.

The .sig file configures the simulation interface. It contains the signal mapping table, describing all transmitted signals, source devices and related logical nodes. If this file is not specified, simulation interface simple ignores all incoming data except the simulation time.

These file types are all in XML format and it is theoretically possible to create and edit these files in any ordinary text editor. But a single .cid file can contain more than two thousand lines of configuration code, so it is practically impossible to create and handle the configuration files without a specialized configuration tool developed as an auxiliary tool for the substation operation simulator. This tool enables to create the whole configuration through a user friendly graphical interface, keeps the consistency of the configuration and contains tools for automatic code generation witch rapidly speeds up the process of creating a new project configuration.

The run of the application is as follows: on startup, application reads configuration files describing the automation system, configuration of each IED and configuration of simulation interface. After the initialization phase, system waits until physical model connects. As mentioned above, interconnection between control

system simulator and physical model realizes an instance of simulation interface class. When the connection is successfully established, simulation interface waits for incoming raw data (state signalization, instantaneous values of voltages and currents, actual simulation time). The simulation interface reads the signal code of each received signal and maps the signal to corresponding instance of logical node. SI also controls the execution of simulation; SI starts functional cores of IEDs each time when a time update signal is received from physical model, so both simulations are synchronized. If the connection to PSS is lost, execution of IED cores is terminated until the PSS reconnects. Sometimes, mostly when debugging new configuration, it's necessary to run the simulation without connection to physical model. Therefore, the SI enables to run the simulation cores using internal timer with user defined step size and delay. This internal timer is controlled using console commands.

The user interface is realized as a simple console with command prompt. Build–in command interpreter supports various commands for data manipulation, browsing the data structure and application control. Command interpreter also supports simple scripting – when frequently performing the same sequence of commands (e.g. initialization of substation to a specific configuration other then default state), the sequence can be stored to a text file and simple reused using the *run* command.

This console interface is primary used for testing and debugging of new configuration. As a standard user interface, SCADA application should be used.

This software suit should be primary used for analysis of control system's behavior. Therefore the simulator is able to store many types of events (value changes, state changes, sending and receiving messages) to SQL database for further analysis. This enables to study behavior of the system in various operation conditions and response of the system to various events.

4. Configuration Utility

The configuration of a single IED can contain thousands of configuration code lines. Even relative small substation contains about 15 IEDs. Because it's difficult to keep the configuration code consistent for a single device, on substation level it is practically impossible, the configuration utility has been developed.

This application has an easy to use graphical user interface. User simply creates the configuration in graphical form by drawing the configuration schema using built-in drawing tools. This process of configuration creation has two phases.

First phase is creating the power equipment structure of the substation. For better orientation in bigger substations, the equipment is concentrated to bays and each bay is related to a voltage level. This hierarchy is used also for addressing of equipment. Each component needs to have a unique system address. This so called object reference is a combination of the related voltage level name, related bay name and the bay component divided by dots (e.g. a circuit breaker QM1 located in bay Q1 related to voltage level E1 has the object reference E1.Q1.QM1). There are often more bays with the same equipment structure in a substation. Therefore a bay cloning function is implemented. It allows the user to use existing bay structures for creating new ones. Afterwards the user is asked to specify the name for a new bay and the program automatically changes the object references according to the new bay name. The user can also define physical connections between power equipment components, but for SAS configuration is the specification of interconnections not necessary (connections are used for proper physical model creation). The whole power system configuration is stored in an .xml file and can be also used in other application (e.g. SCADA application).

When the power system contains at least one bay with an IED, the configuration process can continue to the second phase – IED configuration creation. The user can start building the IED configuration from scratch using the generating tool in Device menu or assign an already existing configuration to the IED instance.

The generating tool creates a new configuration file, associates this file with the IED instance and creates a basic configuration structure with a single LD and all necessary logical nodes according to the structure of power system of the bay containing the IED instance. Then, user can freely add or remove logical devices, logical nodes and other configuration objects according to tasks the IED should perform. After creation of the configuration structure, user has to configure each LN, ControlBlock, DataSet instance (e.g. to define the DATA structure, set triggering conditions, add data references do dataset, etc.). The system automatically checks the consistency of the settings and doesn't allow to create improper data structures (e.g. it doesn't allow to add DATA to a logical node instance, if the specific LN class doesn't support this DATA class or to add a DATA reference to a DataSet, if the referenced DATA doesn't exist). At last, the user must define the relation between blocks. These relations are displayed as wires connecting the blocks.

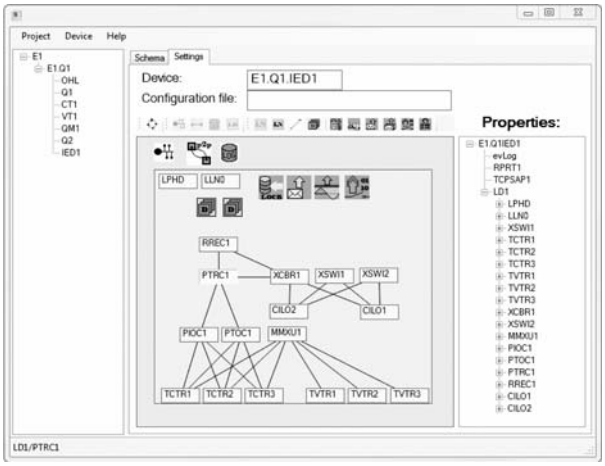

Fig. 3 Example of a simple IED configuration

Assigning an existing configuration is useful when the substation contains bays with the same or very similar configuration. When assigning an existing configuration to an IED, the system checks if the configuration structure is compatible with related power equipment structure. If the configuration is compatible, a copy of the source configuration file is created and all object references are updated automatically.

The configuration of each device is stored in a separate file in XML format, so it's possible to edit the configuration using an ordinary text editor or XML editor, but this is not recommended (because the consistency of so created configuration is not longer guaranteed).

5. Conclusion

The software described in this paper is a key part of an integrated software system for complex simulation of a power substation operation. It provides the simulation of a substation control system operation. The complete suit also contains a power system simulator, SCADA application and some additional tools speeding up the process of configuration of a new substation model (control system configuration tool and physical model configuration tool). In contrast to proprietary software, which is mostly closed and difficult to modify or extend, this system can be modified, extended and upgraded according to our current needs. There are several possible applications of this software.

The first possible application is analysis of data exchange within the substation for purpose of minimization of transferred data volume. The experiences with the real operation of control systems based on IEC 61850 showed that some optimization is often necessary.

The second application is analysis of processes and reactions of the system on faults on distribution lines and acquisition of knowledge usable by fault location on 22 kV distribution lines – the localization of failures in compensated networks with tree structure is a difficult problem. The tree structure of the network causes that many fault location methods can't exactly specify the fault point and are returning more possible fault points. The use of some kind of knowledge processing algorithm could provide additional information about the fault, because the system could specify the probability of correct fault location for each detected potential fault point and so provides additional information for dispatcher saying how trustworthy is the information form fault locator.

Developing and testing of algorithms for autonomous substation operation control is another possible application of this software suit. Such a system could handle most of situations occurring by the operation of a power substation and solve most of problem situations without need of operator's intervention.

Of course this software is well applicable in education process and can help by teaching subjects related to substation automation.

The development of this system has not been finished yet, but the software components are now in final stage of development (testing of stability, bugs fixing, some code cleanup). After finishing this phase, the system will be ready for planned use and start of development of a new generation is planned.

The new generation of the control system simulator shall have more modular structure based on plug–in modules for faster and easier development of new function blocks (or modifying the existing). Also some changes in configuration language are planned, the syntax is still unnecessarily complicated. It is also planned to create new service access point classes implementing real protocols (e.g. SPABUS), so it will be possible to connect the substation model with real devices and create some kind of hybrid model (the system will be built particularly from simulated and particularly from real devices).

Acknowledgement

This work was supported by the Slovak Research and Development Agency under the contract No. APVV-0560-07.

References

[1] HOGER, M.: *Model of Operation for Electrical Station (in Slovak),* Proc. of 10. Int'l conference Electric Power Engineering 2009, Kouty nad Desnou, ISBN: 978-80-248-1947-1

[2] IEC 61850-6: Configuration Description Language for Communication in Electrical Substations Related to IEDs, *IEC*, 2004

[3] IEC 61850-7.2: Basic Communication Structure for Substation and Feeder Equipment –Abstract Communication Service Interface (ACSI), *IEC*, 2004

[4] IEC 61850-7.4: Basic Communication Structure for Substation and Feeder Equipment – Compatible Logical Node Classes and Data Classes, *IEC*, 2004

[5] PENDER, T.: *UML Bible,* Wiley, USA, 2003.

Peter Hurtuk – Martin Priecinsky – Anna Kondelova *

CONVERTER WITH SYNCHRONOUS RECTIFIERS FOR ELECTROPLATING

This paper presents the requirements for resources for electroplating processes, principles of the synchronous rectifier and its control. It describes simulation and experimental verification of the synchronous rectifier, compares the efficiency of switching power supply using a synchronous rectifier and a diode rectifier, where body diode of MOSFET transistor is used for rectification. Finally the paper brings thermal images of synchronous rectifier transistors.

1. Introduction

Switching power supplies for electroplating processes are characterized by low output voltage (tens of volts), which is comparable to the voltage drop of rectifying elements and large current output (thousands of amps). Permissible output current ripple is 2–5% of the average current. Ripple of the output voltage is 1%. Significant losses are caused by current flow through semiconductor structure for required parameters.

The goal of research is minimizing switching power supply losses using synchronous rectifier. It is necessary to use a transistor with low resistance in the conducting state of structure. It is also necessary to select an appropriate topology of the synchronous rectifier circuit with respect to the number of transistors. Very important part of topology is control of MOSFET transistors, which enables the transistor to conduct current from zero voltage UDS. Commutation failure is not acceptable. The article describes the issue of power supplies for electroplating processes, their activities and various topologies; control and principle of synchronous rectifier. It also brings experimental verification of the synchronous rectifier, efficiency comparison of switching power supply using a synchronous rectifier and a diode rectifier, where body diode of MOSFET transistor is used for rectification [1].

2. Requirements for Power Supply

All technological processes take place in an environment of galvanic baths of various sizes and designs. Their activities require (with some exceptions) power supplies of small DC voltage with high output currents. In the aspect of required performance we can divide resources for electrochemical applications to several categories. Power supplies with minimal performance (up to 1 kVA) are less important and used for technological processes as degreasing e.g. Medium performance (up to 40 kVA) is typical for the metallization and small refinery links and big performance supplies (from 100 kVA) are used for large refining links and production of chlorine and aluminum.

Supplies specific characteristics depend on the character of electroplating techniques. It is a particular need for low output voltage, very high currents. The fact that the bath is a source of reverse voltage of variable level is important, too. For some technological processes, it is also necessary to allow change the polarity of the output voltage of power supply. Output current with minimal ripple allows achieve superior surface in most cases, i.e. homogeneous layer of deposited metal. In the case of minimal current ripple of metalized material surface, liquid products are removed worse and we must remove it with additive surface washing. The optimal value of current ripple is topic of debates for years, but acceptable level of current ripple is set to 2–5% of current average value [1].

3. Synchronous Rectifier

In synchronous rectifier, diodes are replaced by MOSFET transistors. Diodes must be engaged with respect to the fact that in presence of driving signal in the gate transistor works in the third quadrant of the static output characteristics (Fig. 1). In the third quadrant, the body diode is conductive, because it is polarized in forward direction. If the supply output voltage is polarized reverse, transistor works in the first quadrant of its static characteristics and transistor is closed. We can also see that the body diode is in the blocking state. MOSFET transistors are able to conduct current at zero voltage U_{DS}. This is not able in the diode due to

* **Peter Hurtuk, Martin Priecinsky, Anna Kondelova**
Department of Mechatronics and Electronics, Faculty of Electrical Engineering, University of Zilina, Slovakia, E-mail: hurtuk@fel.utc.sk

its threshold voltage value. Threshold diode voltage in its conductive state causes loss proportional to the product $U_{TH}.I_{F(AV)}$. In synchronous rectification this part of the losses is eliminated.

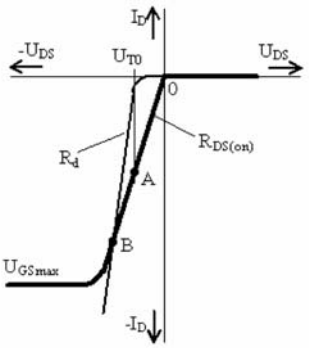

Fig. 1 V-A characteristic of MOSFET transistor and the body diode

If the transistor is open and operates in the third quadrant of its output characteristics, it can conduct current from the zero voltage without applying the threshold voltage of the body diode. Voltage drop on $R_{DS(on)}$ increases with increasing current; in point A this drop reaches the body diode threshold voltage value, the diode opens and starts to conduct current. In this time, both elements are conductive simultaneously as parallel elements and hence the total resistance of MOSFET transistor is formed by parallel connecting $R_{DS(on)}$ and dynamic resistance R_d of body diode (Fig. 2). Increasing voltage on structure (from zero to the threshold voltage of body diode) has characteristic slope of $R_{DS(on)}$. Next increasing of voltage has characteristic slope of parallel connected $R_{DS(on)}$ and R_d. Values of current depend on a value of voltage drop on transistor and body diode. In point B, both currents are equal. In next increasing of voltage higher current is flowing through diode than through the transistor [2] and [3].

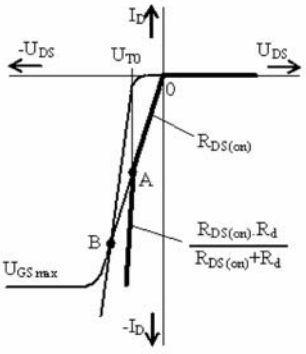

Fig. 2 The resulting output characteristics structure

Power losses of the MOSFET transistor for voltage drops from zero to the value of body diode threshold voltage are expressed in equation 1; losses from A to B are expressed in equation 2. These losses represent a voltage drop of synchronous rectifier:

$$\Delta P_1 = R_{DS(on)} \cdot I_D^2 , \tag{1}$$

$$\Delta P_2 = \frac{R_{DS(on)} \cdot R_d}{R_{DS(on)} + R_d} \cdot I_D^2 . \tag{2}$$

The diode is characterized with permanent voltage drop due to its threshold voltage and the voltage drop due to the dynamic resistance R_d. Power losses of diode are expressed in equation 3:

$$\Delta P_3 = U_{T0} \cdot I_D + R_d \cdot I_D^2 . \tag{3}$$

Fig. 3 shows a comparison of conduction losses for synchronous and diode rectifier.

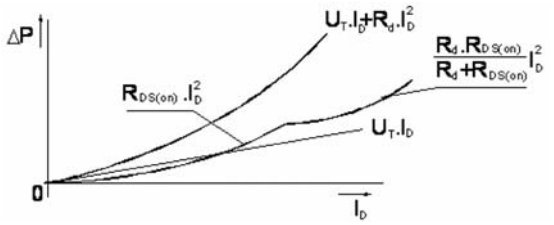

Fig. 3 Comparison of conduction losses

In addition to conduction losses, in semi-conductive structures we can calculate switching losses, control losses and loss in the rectifier commutation. These losses depend on the topology of the rectifier circuit. The energy required for charging and discharging of MOSFET input capacity generates control losses and they are increasing with increasing frequency.

4. Synchronous Rectifier Control

Basic topologies of synchronous rectifiers are derived from conventional ones. There are two types of control, external control and self-control of synchronous rectifier transistors.

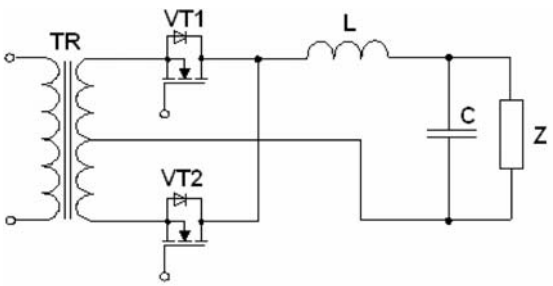

Fig. 4 Control synchronous rectifier

An example of external control is in Fig. 4. Control of synchronous rectifier MOSFET transistor contains control and driver circuit, which generates control signal. We must set precise timing of control signals, which is the most critical point of this work.

Timing of control signals can be obtained by two ways. The first is to obtain control data from the primary site of converter, from control circuit of the converter. Galvanic isolation of control signal in the secondary side of converter from the primary one is needed. Precise timing of control signals to the gates of MOSFET is important.

Additional control losses occur in the external control. The advantage of the external control is non-dependency of control signals due to load variations, simple gate protection and particularly accurate timing of control signals.

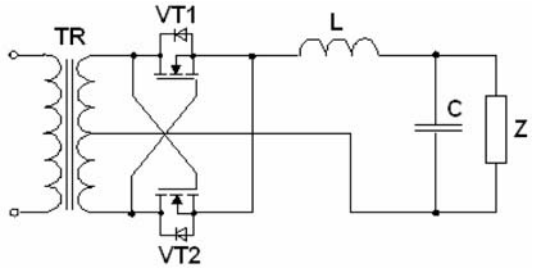

Fig. 5 Self-driven synchronous rectifier

In self-driven synchronous rectifiers voltage from secondary transformer side is directly used for transistor control. The self-driven synchronous rectifier is shown in Fig. 5. With the power supply topology on the primary side of transformer the shape control curves are changing. Certain requirements are placed on the control curve. The voltage levels must be high enough for safe switching of transistors, but not too high because of the security of the gates. Energy for control used to charge the parasitic capacity of MOSFET transistors can be used from the magnetizing or dispersion transformer inductance [4] and [5].

5. Simulation Analysis Switching Power Supply

Simulation analysis is used for verification of the networks operation. With the changing of circuit parameters, the values of its variables (V, I, W) are checked. The most important value is power dissipations on transistor without control signal, where only the inner diode conduct the current, and with control of this transistor. The simulation analysis contains only the power circuits [6].

Scheme of the inverter is shown in Fig. 6. This inverter is powered from the DC voltage $V_1 = 25$ V, where the R5 represents the internal resistance of the input voltage source. To the input side of converter is connected filter capacitance with the parasitic serial resistance. Transistors are controlled by the generator of voltage impulses with desired frequency and shape. Used transistor is IRFI540N. Clamps PIN 1, PIN 2, +V1 are connected to transformer circuit.

Transformer is created by simplified substitution circuit, which is shown in Fig. 7. The network contains the inductors L_2, L_3, L_4, L_5, among which is ideal magnetic coupling. The values of these inductances are specified by the ratio of transformer. Inductances L_6, L_7, L_8, L_9 are representing the dissipation inductances of the transformer and the effective resistances of winding are R_3, R_4 a R_7, R_8. The input pins PIN 1, PIN 2, +V1 are connected to output of inverter and PIN 3, PIN 4 and PIN 5 to the input of synchronous rectifier.

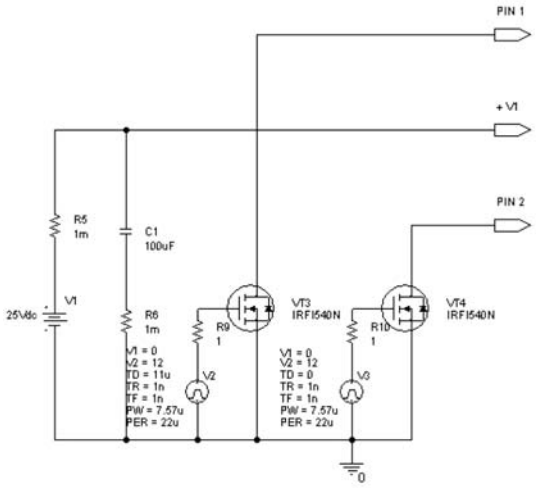

Fig. 6 Scheme of the inverter for simulation analysis

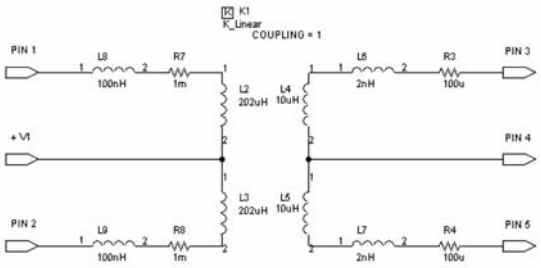

Fig. 7 Scheme of the power transformer used for simulation analysis

Fig. 8 shows the circuit of diode rectifier. Used transistors IRF1310NS are not controlled. With this setting, with zero gate signal, the internal diode of the structure conducts the current. The transistor acts as a diode. The inductor L presents as output filter of the rectifier. Capacitor C_2 is output capacitance with serial parasitic resistance R_1. Resistors R_{11} and R_{12} are used for elimination of the convergence of the computation in simulation. Input clamps PIN 3, PIN 4 and PIN 5 of the rectifier simulation analysis are connected to output pins of the circuit of the transformer.

Circuit of the synchronous rectifier is shown in Fig. 8. The transistors IRF1310NS are also used. The drive voltage supplies are set on 10V. Switching of these transistors is synchronous to the switching of inverter. Input pins PIN 3, PIN 4, PIN 5 are connected to the output of the network of the transformer.

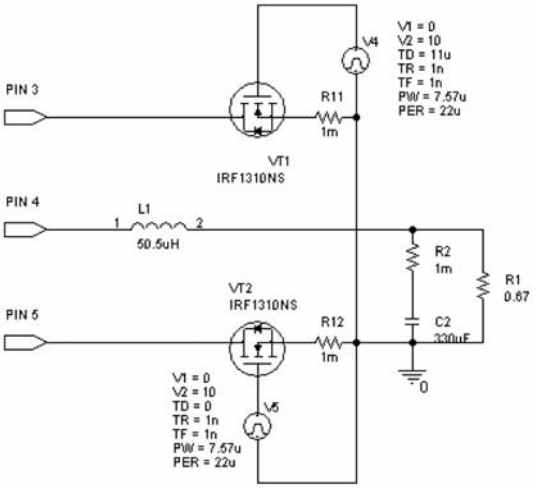

Fig. 8 Scheme of the diode and synchronous rectifier used for simulation analysis

Simulation analysis was done with input voltage of $V_1 = 25$ V. Frequency of the impulse generator of 45kHz. Changing of the current was achieved by changing of the output resistance R_1 and the demanded value of the output voltage of 3.5 V with the right value of duty cycle of the PWM driving signals for inverter and rectifier.

Fig. 9 shows the comparison of the efficiency of the switching converter with diode and synchronous rectifier. It is easy to see that the efficiency of synchronous rectifier is higher. The largest efficiency, 74.613% is with output current 7.44 A. With the nominal output current 18A it is 74.3%. The biggest difference of the efficiency is when the output current is 3.333A.

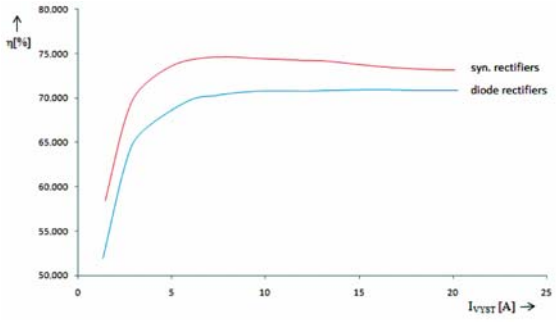

Fig. 9 Efficiency characteristics

In Fig. 10 is shown the comparison of power dissipation on the transistor with and without drive, where it acts as diode. With the increasing output current, the power losses increased too.

In Figs. 11 and 12 are waveforms of the electrical values of the circuit's simulation analysis. It was done with input voltage $V_1 =$ $= 25$ V, input current $I_{IN} = 0.99$ A, output voltage $V_{OUT} = 3.5$ V and output current $I_{OUT} = 5.22$ A.

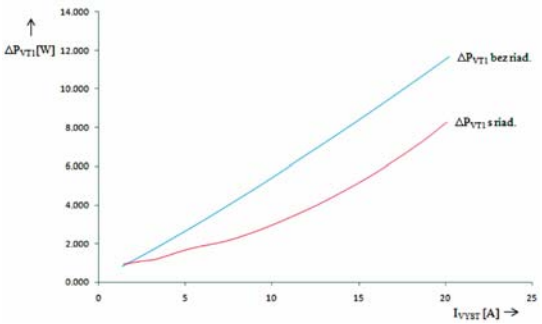

Fig. 10 Comparison of the losses on transistor with and without control

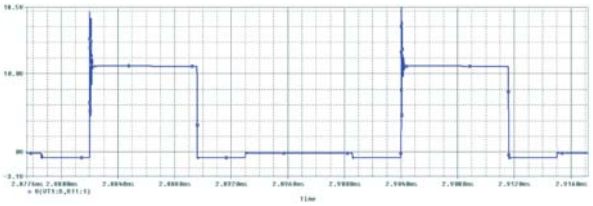

Fig. 11 Waveform of the voltage UDS on the transistor VT1

From the waveforms of the voltage on transistor VT1 it is easy to see that used control of synchronous rectifier is not so efficient, because the transistor was not open at full time until the current dissolves. The inner diode is applied for a long time. With better control, the power losses on the transistor will decrease.

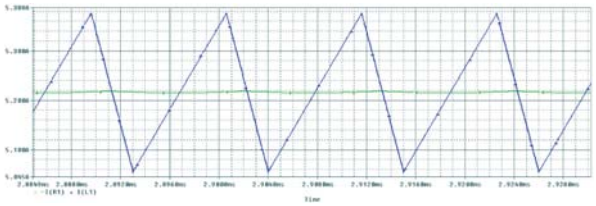

Fig. 12 Waveform of the output current and the current through filter inductor

The ripple of output current is lower than 5% of its average value (Fig. 12). This satisfied the condition for the source used for electroplating.

6. Switching Power Supply Experimental Verification

In experimental verification we used the push-pull inverter connection (Fig. 13), which uses the entire hysteresis core. Converter is able to work with 50% of the pro-open. Control is ensured with

the UCC28083 circuit for both inverter and synchronous rectifier. Parameters for designing switching power supply are as follows:
- input voltage 20–36 VDC
- output voltage 3.5 VDC
- output current 18 A
- switching frequency 45 kHz

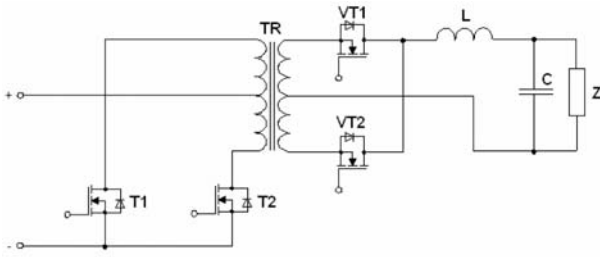

Fig. 13 PUSH-PULL converter with synchronous rectifier

The waveforms are captured for input voltage U_{IN} = 25 V, input current I_{IN} = 0.99 A and output voltage U_{OUT} = 3.5 V, output current I_{OUT} = 5.22 A. The system uses control, which is shown in Fig. 7a. In the waveform of transistor voltage VT1 (Fig. 15) of the synchronous rectifier we can see that the regulation is not fully effective, because the transistor isn't switched throughout the period when current is conducted through a given branch. This fact is caused by the body diode of transistor. Therefore, we used the following synchronous rectifier control circuit, which is in Fig. 14b. The waveform of transistor voltage with this control is shown in Fig. 16.

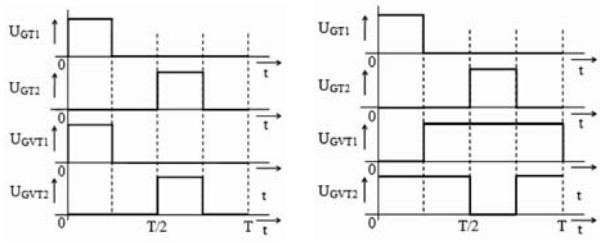

a) Control 1 *b) Control 2*

Fig. 14 Switching diagram of control signals

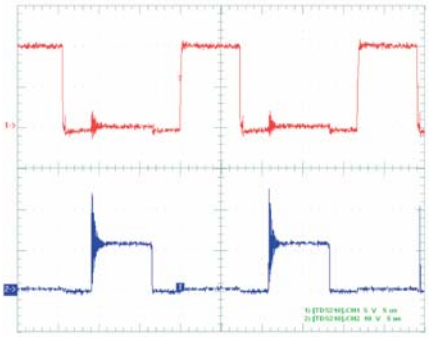

Fig. 15 Waveform of transistor voltage VT1 (1-U_G, 2-U_{DS})

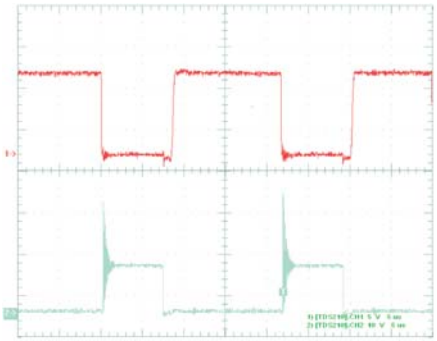

Fig. 16 Waveform of transistor voltage VT1 (1-U_G, 2-U_{DS})

Measurement of efficiency was made at the input voltage U_{IN} = 25V. The efficiency was measured without transistors drivers, when only the body diodes of transistors were applied. To measure the diode rectifier we set the maximum output current on 8A, because the transistor didn't have additional cooling and could be destroyed. Measurement results are in Fig. 17. The transistor efficiency is much better when using drivers. This fact is well visible from characteristics. Efficiency for small output current decreases, which is caused by increasing of mutual ratio between driving the switching losses due to transferred power source. With increasing output current above 8A, efficiency decreases too, because of increasing the conduction losses. In the alternative control, efficiency increased because the body diode wasn't applied.

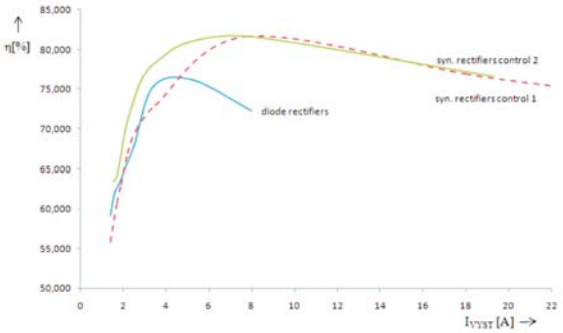

Fig. 17 Efficiency characteristics

In Fig. 18, we can see thermal image of uncontrolled transistors rectifier. Thermal images of the rectifier with the first control are in Fig. 18b and those with the second one in Fig. 18c. Images were made at an output current 5.2 A. In the case of the second control, transistor has the lowest temperature because of there are no losses on the body diode.

6. Conclusion

The main goal of this experiment (simulation analysis) was to increase efficiency of switching power supply using a synchronous

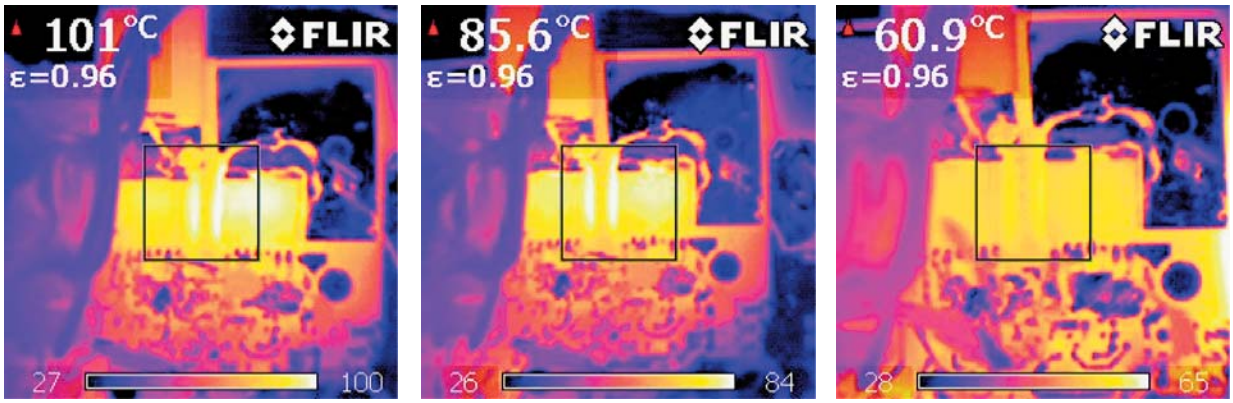

a) Diode rectifier *b) Synchronous rectifier – control 1* *c) Synchronous rectifier – control 2*

Fig. 18 Thermal images of transistors VT1 and VT2

rectifier. The efficiency of switching power supply at output current 18A is 76.9% in the case of "control 1". The maximum efficiency is 81.636% at an output current 7.8 A. In the second type synchronous rectifier control (control 2) the efficiency is 80% (output current is 18A). The maximum efficiency is 81.591% at output current 8.1A. Greater efficiency could be achieved using a suitable transistor synchronous rectifier, where static and dynamic parameters of the transistor and also its body diode are very important: the smallest internal resistance in the conductive state $R_{DS(on)}$, body diode threshold voltage and dynamic resistance R_D. Used topology for this synchronous rectifier is suitable for high currents, because the current always flows through only one transistor to reduce the losses. The results of this experiment will help in the design of the source with output current of thousands of amps for electroplating industry.

Acknowledgement

The authors wish to thank for the financial support of the operational program of R & D Centre of Excellence of power electronic systems and components for material OPVaV-2008/2.1/01-SORO, ITMS 26220120003 funded by the European Regional Development Fund (ERFD) and VMSP-P-0085-09, APVV -0535-07.

References

[1] http://www.odbornecasopisy.cz, 2004
[2] STOIC, G., NGUIEN, C.: MOSFET Synchronous Rectifiers for Isolated, Board-Mounted DC-DC Converters. Proc. of Conference INTELEC'2000 Arizona, USA, 2000
[3] HARGAS, L., HRIANKA, M., LAKATOS, J., KONIAR, D.: Heat Fields Modelling and Verification of Electronic Parts of Mechatronics Systems, *Metalurgija – Metallurgy*, Vol. 49, No. 2, 2010, pp. 268–272
[4] LEE-HUN, KIM, KWANG-SU, CHUN, CHUNG-YUEN, WON, SOO-SEOK, KIM, SE-WAN, CHOI.: An Improved Scheme for High-Efficiency Push-Pull Converter Using Single Winding Self-Driven Synchronous Rectification, *Industrial Electronics Society,* 2004
[5] MOHAN, N., UNDELAND, T.M, ROBBINS, W.P.: Power Electronics: Converters, Applications and Design. *Johny Wiley & Sons*, New York, 1989
[6] OrCAD Pspice A/D: *User's Guide,* Beaverton, 1998.

Ladislav Janousek – Milan Smetana *

UNCERTAINTY IN DEPTH EVALUATION OF PARTIALLY CONDUCTIVE CRACKS FROM EDDY CURRENT TESTING SIGNALS

The paper deals with eddy current non-destructive evaluation of partially conductive cracks. Especially, uncertainty of a depth estimation of such cracks from eddy current testing signals is considered here. A plate specimen having the electromagnetic parameters of a stainless steel SUS316L is inspected in this study by numerical means. A crack with variable depth, width and conductivity is positioned in the middle of the plate. One of the most utilized eddy current probes so called pancake probe is employed for the inspection. Response signals of the crack with different parameters are numerically calculated and further analysed. Presented results clearly demonstrate that the uncertainty of a crack depth estimation considerably increases when conductive cracks are evaluated comparing to non-conductive cracks.

1. Introduction

Many structures require periodical inspection to keep safety, reliability as well as quality of various processes. Recent trends in maintenance are embracing the so-called damage tolerance approach, wherein an element is actively used up to a certain point, beyond which the structural integrity of a structure could be affected. Replacement is thus performed at the end of the service life of the element, which helps in lowering running costs of the whole system. Degradation detection of the construction material must be accompanied by interpretation of the measured data in order to estimate the extent of the degradation and predict future development thereof.

The damage tolerance approach includes four phases – detection, evaluation, analysis and prediction. In case a degradation of construction material is detected, the extent thereof is evaluated along with influence on the behaviour of the whole system and future development. The first two phases are inherently associated with non-destructive evaluation (NDE) of materials.

Different physical principles are utilised for the NDE of materials. Eddy current testing (ECT) is one of the widely utilized electromagnetic methods. It originates from the electromagnetic induction phenomena. The principle of ECT underlies in the interaction of induced eddy currents with structure of an examined body [1].

Commercial ECT systems provide raw data with limited or absent capability of their quantitative interpretation [2]. The progress in powerful computers has allowed developing of automated procedures to estimate dimensions of a detected anomaly; however, they are not commercially available yet. The stochastic or the deterministic methods are employed in the automated procedures for sizing of an indicated crack [3]. Usually, one dimensional signal gained by scanning just above the crack along its length is taken as an input to the evaluation procedure. Mostly three variables of the crack are estimated, i.e. a depth, a length and a position of its centre, while a profile, a width and the electromagnetic properties of the defect have to be adjusted in advance. Satisfactory results are reported by several groups for evaluation of artificial slits [4]. However, evaluation of real cracks, especially stress corrosion cracking (SCC) from ECT response signals remains still very difficult [4]. It has been found out that an SCC is partially conductive [5] while its conductivity is not known in general and can vary from one case to another case.

The paper deals with evaluation of uncertainty in depth estimation of a detected partially conductive crack.

2. Principle of ECT

The principle of the ECT underlies in the interaction of induced eddy currents with a structure of an examined body [1].

An alternating electromagnetic field is generated in the vicinity of a coil driven by a time-varying current. It can be simply considered as a superposition of a primary exciting field and a secondary one generated by eddy currents. The secondary electromagnetic field counterworks to the primary exciting electromagnetic field according to the Lenz's theorem. According to the Ampere's law:

* **Ladislav Janousek, Milan Smetana**
Department of Electromagnetic and Biomedical Engineering, Faculty of Electrical Engineering, University of Zilina, Slovakia,
E-mail: janousek@fel.uniza.sk

$$\nabla \times \mathbf{H}_p = \mathbf{J}_{ex},$$

$$\nabla \times \mathbf{H}_{ed} = \mathbf{J}_{ed},$$

$$\mathbf{H} = \mathbf{H}_p + \mathbf{H}_{ed},$$

where $\mathbf{H}_p$, $\mathbf{H}_{ed}$, $\mathbf{H}$ [A.m^{-1}] denote the magnetic field intensity vector of the primary, secondary and resulting field, respectively, and $\mathbf{J}_{ex}$, $\mathbf{J}_{ed}$ [A.m^{-2}] are the current density vectors of the exciting current and of the eddy currents, respectively. Electromotive force is induced in a conductive object which is in proximity of the coil according to the Faraday's law:

$$\nabla \times \mathbf{E} = -\frac{\partial \mathbf{B}}{\partial t},$$

where $\mathbf{E}$ [V.m^{-1}] is the electromotive force vector and $\mathbf{B}$ [T] is the magnetic flux density vector, while $\mathbf{B} = \mu\mathbf{H}$, and μ [H.m^{-1}] is the magnetic permeability.

Eddy-currents flow in the conductive object according to the Ohm's law:

$$\mathbf{J}_{ed} = \gamma\mathbf{E},$$

where γ [S.m^{-1}] is the electric conductivity. Their vector lines must be closed due to:

$$\nabla \cdot \mathbf{J}_{ed} = 0.$$

The induction coupling therefore exists between the coil and the conductive object. The resulting electromagnetic field of the coil and the conductive object depends on geometrical parameters of the system as well as on the electromagnetic parameters of the conductive object.

The principle of the ECT has been known for several decades. Nowadays, the most wide spread application area of the ECT is the detection and possible evaluation of different discontinuities in conductive materials.

Presence of a defect in a conductive material causes a local change of the material electromagnetic parameters. As the eddy current vector lines must be encircled, the presence of a defect changes the eddy current density distribution and thus influences the resulting electromagnetic field. The perturbation electromagnetic field therefore occurs comparing to the no-crack situation and this perturbation field can be sensed and further evaluated. The ECT is a relative method and the perturbation signal is obtained by subtracting of the crack signal and no-crack signal. The perturbation signal carries quantitative information about an inspected defect.

The ECT posses several benefits:
- high sensitivity for surface breaking defects,
- high inspection speed,
- contact-less inspection,
- versatility,

especially comparing to the ultrasonic testing, one of the most utilized non-destructive techniques. These advantages determine continuously enlarging application area of ECT particularly in nuclear, petrochemical and aviation industries.

On the other hand, also disadvantages of the method should be mentioned. The ECT signals are integral values and they do not carry explicit information about crack dimensions. It means that the inverse problem is ill-posed. Therefore, evaluating the depth of a defect from the ECT signals is quite difficult. In addition, the skin-effect concentrates induced currents on the surface of a tested material. Eddy current density decays almost exponentially into material depth and thus increasing depth of a surface breaking defect causes raising uncertainty of the depth evaluation because of the ECT signal saturation. The situation gets even worse when partially conductive cracks (i.e. SCCs) are expected and need to be detected and evaluated.

3. Numerical Model

A plate specimen having the electromagnetic parameters of a stainless steel SUS316L is inspected in this study. The specimen has a thickness of $t = 10$ mm, a conductivity of $\sigma = 1.4$ MS/m and a relative permeability of $\mu_r = 1$. A surface breaking crack appears in the middle of the plate. It is modelled as the cuboid having different electromagnetic properties from the base material. Configuration of the plate with the crack is shown in Fig. 1. A length of the crack is fixed to $l_c = 10$ mm.

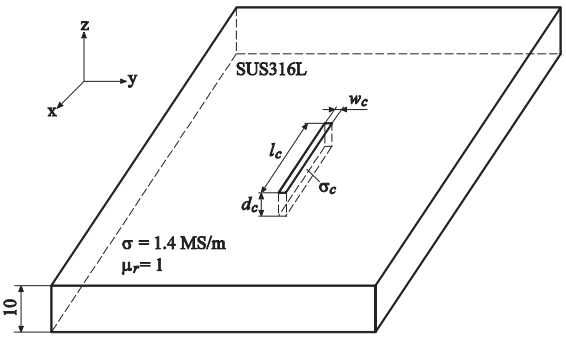

Fig. 1 Layout of specimen

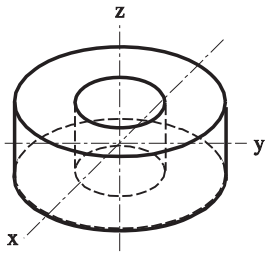

Fig. 2 Configuration of pancake coil probe

A probe shown in Fig. 2 is employed to inspect the crack. This probe is known as the pancake one and it is widely used in practice. The probe is of self-inductance absolute type, i.e. one coil is the exciter and the detector. Outer diameter of the probe has a value of 3.0 mm, its inner diameter is set to 1.0 mm and height of the winding is 1.0 mm in this case. The probe is driven with the harmonic current having a frequency of 10 kHz. The standard depth of penetration equals to $\delta = 4.2$ mm under the given conditions.

Response signals sensed by the probe are calculated by numerical means. One dimensional scanning along the crack length as shown in Fig. 3 is considered here. Such one dimensional signal is usually used by an automated evaluation procedure. Clearance between the plate surface and the probe, so called lift-off is adjusted to 1 mm.

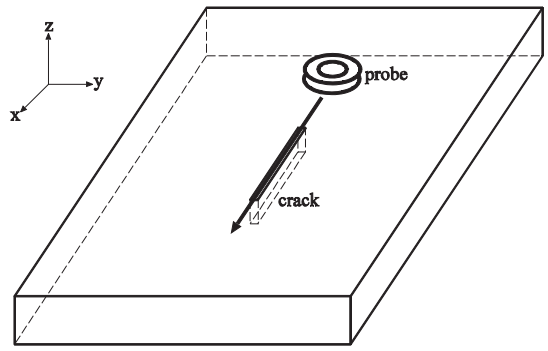

Fig. 3 One dimensional scanning pattern

Three parameters of the crack are varied, i.e. its depth d_c, width w_c and conductivity σ_c to simulate various structures of real conductive cracks. The depth is changed from 10 to 90% of the plate thickness with a step of 10%. The width of crack w_c is adjusted to five values ranging from 0.2 mm until 1.0 mm with a step of 0.2 mm Considered conductivities of the crack are as follows: 0, 1, 2, 5 and 10% of the base material conductivity. Influences of the crack parameters on the sensed ECT response signals are studied. The results are presented and discussed in the next section.

4. Numerical Results and Discussion

Numerical simulations are carried out to evaluate influence of the crack conductivity on uncertainty of the crack's depth estimation. A user developed edge-element code based on the finite element method is used for the calculations. The code calculates the real and the imaginary parts of the complex probe signal under the harmonic excitation according to the symbolic-complex method. The signal is calculated for each probe's position along the scanning line as shown in Fig. 3. The probe moves over the plate surface without crack to get a reference dependence of the signal on the probe position at first. The simulations are then repeated for the cracked scenarios under the same conditions. The dependencies of the crack response signals are calculated for each crack in such a way that the reference dependence is subtracted from the dependence gained under a cracked scenario. Following figures display the dependences of the absolute value of the complex cracks' response signals on the probe position relative to the crack centre as well as they show the complex cracks' response signals in the complex plane.

The response signals of the non-conductive crack with various depths are shown in Fig. 4. It can be seen that the crack signals start to saturate when the crack is deeper than approximately 70% of the plate thickness, i.e. 167% of the standard depth of penetration δ. Similar results are displayed in Fig. 5. However, the crack is partially conductive in this case; the crack conductivity equals to 10% of the base material conductivity. It can be seen that the crack conductivity strongly influences saturation of the crack signals as in this case it is quite difficult to find differences between the signals when the crack is deeper than the standard depth of penetration δ.

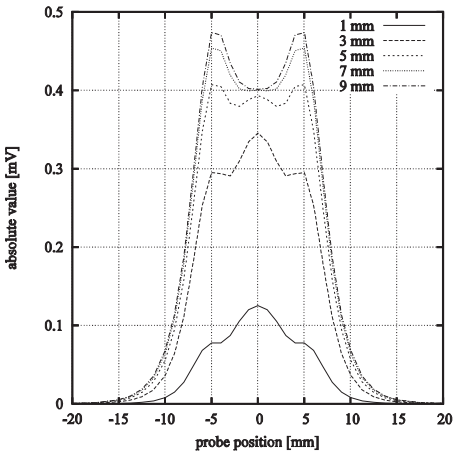

a) dependences of the absolute value on the probe position relative to the crack centre

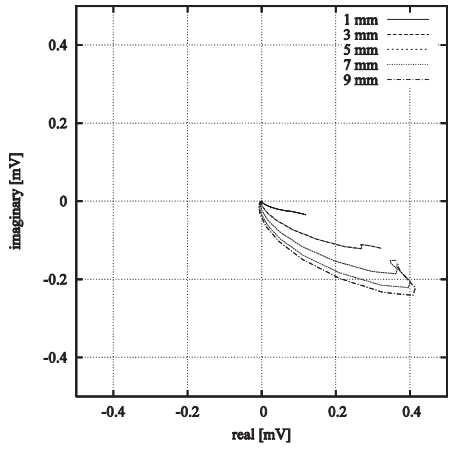

b) dependences of the imaginary part on the real part of the detected signal with respect to the phase of exciting voltage

Fig. 4 Signals of the non-conductive crack with a width of w_c = 0.2 mm and various depths, i.e. d_c = 1, 3, 5, 7 and 9 mm

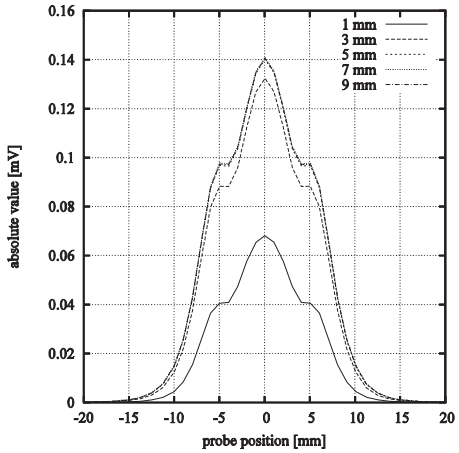

a) dependences of the absolute value on the probe position relative to the crack centre

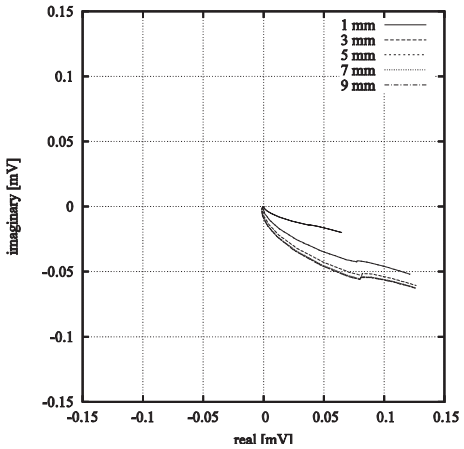

b) dependences of the imaginary part on the real part of the detected signal with respect to the phase of exciting voltage

Fig. 5 Signals of the crack with a width of w_c = 0.2 mm, a partial conductivity of σ_c = 10 % of the base material conductivity and various depths, i.e. d_c = 1, 3, 5, 7 and 9 mm

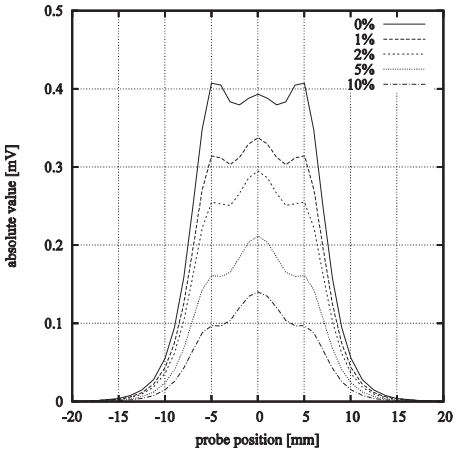

a) dependences of the absolute value on the probe position relative to the crack centre

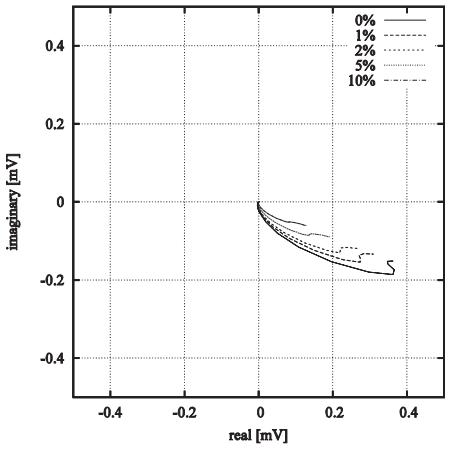

b) dependences of the imaginary part on the real part of the detected signal with respect to the phase of exciting voltage

Fig. 6 Signals of the crack with a depth of d_c = 5 mm, a width of w_c = 0.2 mm and various values of the partial conductivity, i.e. σ_c = 0, 1, 2, 5 and 10 % of the base material conductivity

Influence of the crack conductivity on the crack signals can be observed for the results presented in Fig. 6. The depth of crack is adjusted to 5 mm and its width is set to 0.2 mm in this case while the crack's conductivity is varied. The presented results clearly show that the crack's conductivity strongly influences the response signals, while a crack with higher partial conductivity provides the response signal with lower amplitude.

Several studies [4] have concluded that in case of conductive cracks also a width of the cracking significantly affects the measured responses.

Figs. 7 and 8 show the crack response signals for the crack with variable width, while the crack's depth is adjusted to 5 mm. The crack's partial conductivity is set to 0% for the first case and to 10% of the base material conductivity for the second case. When the crack is non-conductive the response signals only slightly depend on the crack's width; however, when the crack is partially conductive the influence of the crack's width on the response signals is more significant.

Ambiguity of crack's depth estimation due to crack's conductivity is evaluated in a following way. Gained response signals of the crack with variable depth and conductivity are compared in such a way as the deterministic evaluation methods work. A difference between signals of two cracks denoted as *A* and *B* is calculated based on:

$$\varepsilon_{AB} = \frac{\sum_{i=1}^{n} Z_{A,i} - Z_{B,i}^{\ 2}}{\sum_{i=1}^{n} Z_{A,i}^{\ 2}},$$

as proposed in [6]. $Z_{A,i}$ represents the response signal of a crack being considered as an inspected one at the *i*th scanning point.

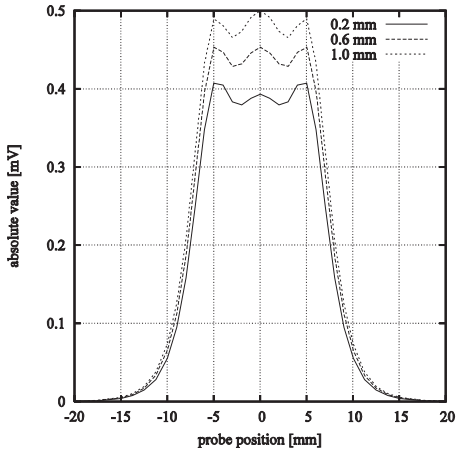

a) dependences of the absolute value on the probe position relative to the crack centre

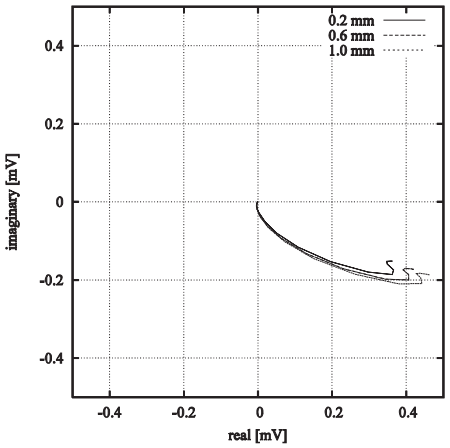

b) dependences of the imaginary part on the real part of the detected signal with respect to the phase of exciting voltage

Fig. 7 Signals of the crack with a depth of d_c = 5 mm, a partial conductivity of σ_c = 0% of the base material conductivity and variable width, i.e. w_c = 0.2, 0.6 and 1.0 mm

Thus a depth of this crack is taken as the true one. $Z_{B,i}$ represents the response signal of a crack being considered as a model of the inspected one at the *i*th scanning point. Its depth is denoted as the estimated one. Total number of scanning points is *n*. Every possible combination of two cracks with different parameters is treated in this manner. If the calculated difference ε_{AB} between the response signals of cracks *A* and *B* is lower or equal to 1%, depth of the crack *A* is estimated to be equal to that one of the crack *B*.

Fig. 9 shows relationship between the true and the estimated depths of the crack A. Only non-conductive cracks with different depths are considered in this case. The full line corresponds to the ideal case when the estimated depth equals to the true one. The relation between the true and the estimated depth according to the above defined criterion is represented by the stars. It can be seen that the uncertainty in the crack depth estimation increases when the crack gets deeper than the standard depth of penetration δ (40% of the plate thickness in this case) due to the signal saturation as mentioned earlier.

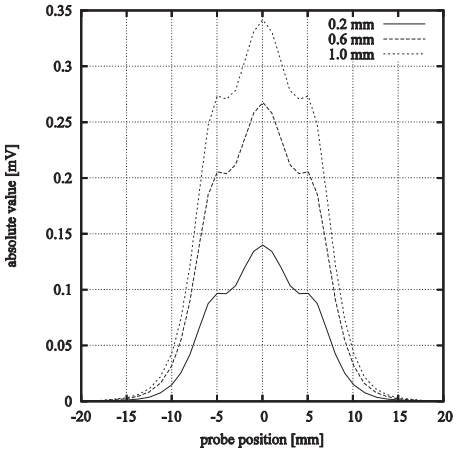

a) dependences of the absolute value on the probe position relative to the crack centre

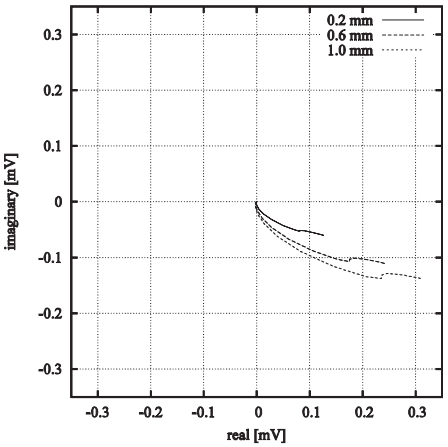

b) dependences of the imaginary part on the real part of the detected signal with respect to the phase of exciting voltage

Fig. 8 Signals of the crack with a depth of d_c = 5 mm, a partial conductivity of σ_c = 10% of the base material conductivity and variable width, i.e. w_c = 0.2, 0.6 and 1.0 mm

It means that the non-conductive crack with a depth of 90% is likely to be underestimated at maximum of approximately 30% of its true depth.

When the crack conductivity is taken into consideration the situation gets considerably worse as shown in Fig. 10. Even depth of shallow cracks can be highly underestimated.

It clearly comes from the presented results that one needs to be very careful when estimating depth of a conductive, i.e. stress corrosion cracks.

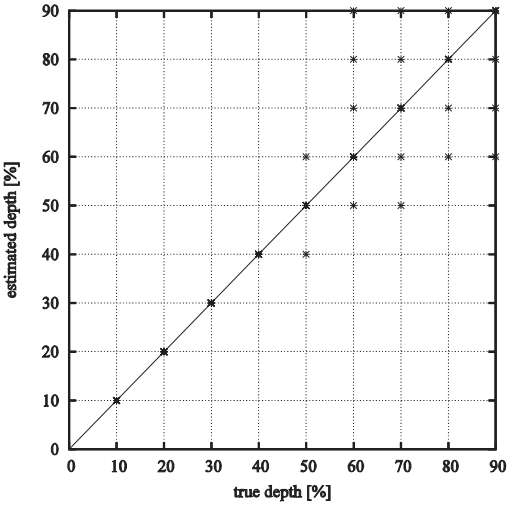

Fig. 9 Relationship between true and estimated depths of a non-conductive crack

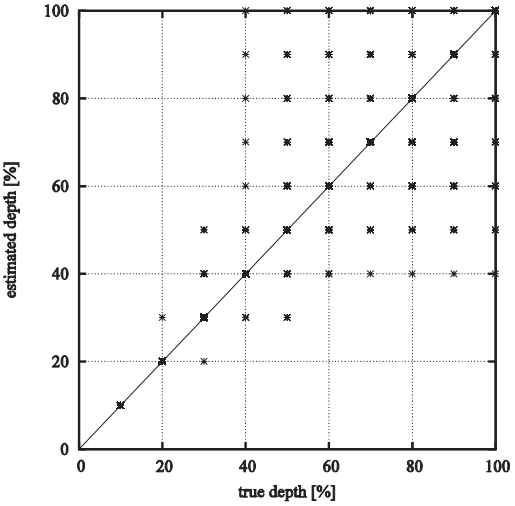

Fig. 10 Relationship between true and estimated depths of a conductive crack

4. Conclusion

The paper focused on depth estimation of partially conductive cracks from eddy current response signals. A plate specimen having electromagnetic characteristics of a stainless steel SUS316L was inspected in this study. Response signals of a crack with rectangular shape were calculated by numerical means for a standard pancake probe. Three parameters of the crack, its depth, width and partial conductivity were varied to simulate heterogeneity of real cracks. It was shown that partial conductivity of a crack strongly influences the response signal's saturation level as well as highlights influence of a crack width on the response signal. Thus the dimension of unknown parameters of a detected crack increases and the inverse problem gets highly ill-posed. The presented results evidently showed that ambiguity of dimensions' evaluation of an indicated crack considerably increases with crack's conductivity. Thus, special attention needs to be devoted to dimensions' evaluation of stress corrosion cracking where not all the ligaments are broken and the crack is partially conductive.

Acknowledgement

This work was supported by the Slovak Research and Development Agency under the contract No. APVV-0194-07. This work was also supported by grant of the Slovak Grant Agency VEGA, project No. 1/0765/11.

The authors wish to thank for the support to the R&D operational program Centre of excellence of power electronics systems and materials for their components, No. OPVaV-2008/2.1/01-SORO, ITMS 26220120003 funded by European Community.

References

[1] JANOUSEK, L., MAREK, T., GOMBARSKA, D.: Eddy Current Non-destructive Evaluation of Conductive Materials, *Communications - Scientific Letters of the University of Zilina,* 1, pp. 29–33, 2006.

[2] RUBINACCI, G., TAMBURINO, A., VENTRE, S.: Fast Numerical Techniques for Electromagnetic Nondestructive Evaluation, *Nondestructive Testing and Evaluation,* 24, pp. 165–194, 2009.

[3] CHEN, Z., YUSA, N., MIYA, K.: Some Advances in Numerical Analysis Techniques for Quantitative Electromagnetic Nondestructive Evaluation, *Nondestructive testing and evaluation,* 24, pp. 69–102, 2009.

[4] YUSA, N.: Development of Computational Inversion Techniques to Size Cracks from Eddy Current Signals, *Nondestructive Testing and Evaluation,* 24, pp. 39–52, 2009.

[5] YUSA, N., MIYA, K.: Discussion on the Equivalent Conductivity and Resistance of Stress Corrosion Cracks in Eddy Current Simulations, *NDT&E International,* 42, pp. 9–15, 2009.

[6] Yusa, N., Huang, H., Miya, K.: Numerical Evaluation of the Ill-posedness of Eddy Current Problems to Size Real Cracks, *NDT&E International,* 40, pp. 185–191, 2007.

Eliska Jurisova – Jarmila Mullerova *

NUMERICAL STUDIES OF OPTICAL BISTABILITY OF ABSORPTIVE TYPE

Theoretical analysis is presented to search for the purely absorptive optical bistability in a Fabry-Perot cavity filled with a saturable absorber. A simple model of singlet absorption is used on numerically solving the relationships between the input and output light fields. The proposed model corresponds well to organic compounds considered as novel optical materials with third-order optical nonlinearities. The effects of saturable absorber parameters on the output light characteristics are studied and purely absorptive optical bistabilities are shown numerically to search for bistable behaviour. The simulated results are indications for promising applications in optical switches for all-optical communication networks.

1. Introduction

Optical bistable devices have a large number of applications in all-optical communication systems. They are building blocks of optical logic, memories, switches, light power limiters etc. that are crucial parts of optical network nodes [1–3]. Optical bistability is a phenomenon in which the bistable device exhibits two stable output states under one input state. The optical bistability arises from the energy exchange between nonlinear optical medium and electromagnetic field. The system is said to be bistable when it can assume two output stable states for the same value of an applied input signal over some range of input signal values, Optical bistability requires a nonlinear medium in presence of feedback. When the nonlinearities are optically-induced, and the feedback is also provided in the optical domain, an all-optical device can be fabricated [4]. The phenomenon of absorptive optical bistability was first theoretically predicted in 1969 by Szoke [5]. Third-order nonlinear materials are mainly metal particles, semiconductors including those of quantum confinement and organics [6–8]. Among organic materials, π-conjugated compounds attract attention due to unique electrical and optical properties including large third-order optical nonlinearities, low-cost manufacturing and flexibility of properties modifications by chemical synthesis as well as deposition techniques. There has been a prolonged research of all-optical switching in organic devices based on optical bistabilities [9]. Parameters of nonlinear medium should be properly chosen to achieve the optical bistability. For the construction of optical bistable devices of absorptive type, saturable absorbers and positive feedback are necessary. A lot of studies report on nonlinear absorption in a great variety of organic compounds [10, 11]. Therefore, the prediction of their bistable behaviour based on theoretical calculations with real experimental data gathered on specific organics is of interest for designing optically bistable devices.

This contribution presents numerical studies of purely absorptive optical bistabilities in saturable absorbers in the Fabry-Perot cavity. Organic dyes with spectral sensitivities such as xanthene, polymethene or coumarin dyes are known for their nonlinear optical properties including saturable absorption. In this paper, we predict and numerically demonstrate the optical bistability in two organic dyes of the xanthenes type dispersed in glass and polymethene dyes dissolved in organic solvents. We simulated their bistable behaviour considering absorption parameters and positive feedback conditions with experimental data from [8, 11].

2. Theory

A simple purely absorptive bistable device can be constructed by placing nonlinearly absorbing medium inside a resonator, e.g. Fabry-Perot cavity (Fig.1).

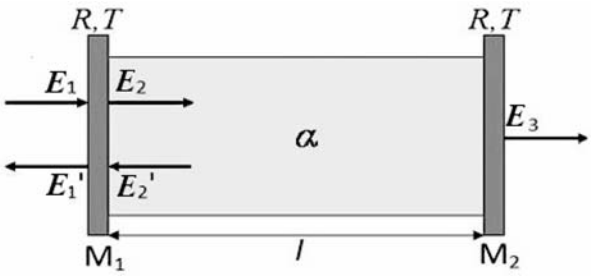

Fig. 1 Fabry-Perot cavity filled with nonlinear absorber of the nonlinear absorption coefficient α and the thickness l. M_1, M_2 are mirrors of reflectance R and transmittance T.
The notifications of electric fields are obvious from the scheme

* **Eliska Jurisova, Jarmila Mullerova**
Department of Engineering Fundamentals, Faculty of Electrical Engineering, University of Zilina, Liptovsky Mikulas, Slovakia,
E-mail: jurisova@lm.uniza.sk

The cavity is formed by two parallel identical flat highly reflective mirrors and demonstrated to provide optical bistability.

The absorption coefficient α is an important wavelength-dependent optical parameter expressing the decrease *dI* of the light intensity *I* in the length *dz* of the absorbing medium

$$dI = -\alpha I dz \tag{1}$$

Eq. (1) is the well-known differential form of the Lambert-Beer law. It is easy to integrate if α is intensity-independent. However, in a nonlinear absorber, α depends on the light intensity. If the intensity of the input radiation is intense enough, the absorption of the medium decreases the consequence of what is the increase of the medium transmittance up to the saturation. If the saturation does not occur and at high intensities decreases again, the so-called reverse saturable absorption occurs. This effect can be used as optical power limiting [12]. According to the absorptive optical bistability model of Szoke [5], the amplitude of electric field entering the Fabry-Perot cavity at normal incidence, electric fields inside the cavity and the output field (Fig.1) obey the following equations

$$E_2 = \tau E_1 + \rho E_2' \tag{2}$$

$$E_1' = \rho E_1 + \tau E_2' \tag{3}$$

$$E_2' = \rho E_2 e^{-2ikl} e^{-\alpha l} \tag{4}$$

$$E_3 = \tau E_2 e^{-2ikl} e^{\frac{-\alpha l}{2}} \tag{5}$$

where *l* is the absorber thickness, *k* is the wavenumber, ρ and τ are Fresnel amplitudes of mirror reflectance and transmittance. If $e^{-2ikl} = 1$ (the Fabry-Perot resonance condition), the relationship between the electric field inside the Fabry-Perot cavity and the input electric field can be expressed as [5, 13]

$$E_2 = \frac{\tau E_1}{1 - \rho^2 e^{-\alpha l}} \tag{6}$$

Then for the light intensities ($I \sim E_2$) the following is valid

$$I_2 = \frac{T I_1}{\left(1 - \mathrm{Re}^{-l}\right)^2} \tag{7}$$

where mirror transmittance $T = \tau^2$, and reflectance $R = \rho^2$ ($R + T = 1$, $R >> T$). Moreover, if $\alpha l << 1$, the equation (7) can be expresses as

$$I_2 = \frac{I_1}{T\left(1 + \frac{\alpha l R}{T}\right)^2} \tag{8}$$

If there is a nonlinear absorber in the Fabry-Perot cavity, $\alpha = \alpha(I_2)$. From Eq. (5) we can see that in case of $\alpha l << 1$ the output electric field $E_3 = \tau E_2$. Then the output intensity is simply $I_3 = T I_2$. Therefore it is sufficient to analyze Eq. (8) to judge if the absorber of the specific absorptive nonlinearity $\alpha = \alpha(I_2)$ will exhibit the bistable output intensity I_3 as a function of I_1.

The simulations of Eq. (8) were performed with real experimental data for nonlinear organic absorbers and the prospects to achieve bistable performance were modelled. The constant spatial profile of the propagating pulses was supposed in our calculations and the optical pulse durations were considered to be larger than the lifetimes of the excited levels. Under this assumption the saturable absorbers act as fast absorbers and the fast relaxation approximation enables to expect their steady state behaviour.

3. Numerical Simulation

We numerically investigated the optical bistability in organic dyes of molecules that contain conjugated bonds with delocalized π – electrons that are responsible for large third-order nonlinear susceptibilities [9]:

- The xanthene dye of fluorescein dispersed in boric acid glass film (BAG) (with 10^{-4} M concentration) of optical parameters as in [11]. Fluorescein is a bright green fluorophore commonly used in fluorescence measurements. The maximum of the absorption spectrum is at ~ 460 nm.
- The xanthene dye of rhodamine 6G dispersed in boric acid glass film (BAG) (with 10^{-4} M concentration) of optical parameters taken from [11]. Rhodamine 6G is chromophore used often as a tracer or a laser dye. The maximum of the absorption spectrum is at ~ 515 nm.
- Polymethine dyes of cationic type dissolved in ethanol or polyurethane. Polymethine dyes are known as organic colorants and media laser technique. The maximum of the absorption spectrum is at ~ 1100 nm. The optical parameters for this study were taken from [8].

All investigated organic dyes dispersed in BAG or dissolved in organic solvents have energy level structure of singlet and triplet states typical for organic media (Fig. 2) with the singlet S_0 as the ground state.

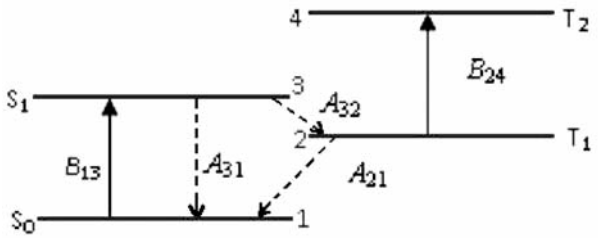

Fig. 2 Energy level model of singlets (S) and triplets (T) typical for organic dyes under study. The model shows optical excitations (upward-pointing arrows) of probabilities given by Einstein's coefficients B_{13}, B_{24}. A_{31}, A_{32}, A_{21} are Einstein's coefficients for the relaxations from excited states (downward-pointing arrows)

After quick excitation to S_1 the molecule may relax to S_0 with the probability $A_{21} = 1/\tau_{21}$ or to T_1 with the probability $A_{32} = 1/\tau_{32}$ (τ_{21}, τ_{32} are the relaxation times). The transition from T_1 to S_1 can be neglected. In liquid state, the dye molecules decay very quickly to from T_1 to S_0. On the contrary, in dye-doped solids,

the $T_1 \rightarrow S_0$ decay is on the millisecond scale. Moreover, by adjusting the excitation wavelength only to the transition $S_0 \rightarrow S_1$, the triplet-triplet absorption $T_1 \rightarrow T_2$ does not occur.

With these assumptions, the absorption coefficient depends on the light intensity I2 in the cavity as follows

$$\alpha(I_2) = \frac{\alpha_0}{1 + \beta I_2} \tag{9}$$

In Eq. (9) α_0 is the absorption coefficient at low intensities of light, β is the so-called parameter of nonlinearity. For the energy level model in Fig. 2 the parameter β is [11]

$$\beta = \frac{\sigma_{13}}{h\nu_{13}} \frac{\tau_{21}\tau_{31}}{\tau_{32} + \tau_{31}} \tag{10}$$

where $\tau_{31} = 1/A_{31}$, σ_{13} is the absorption cross-section for $S_0 \rightarrow S_1$, h is the Planck's constant and ν_{13} is the frequency corresponding to the $S_0 \rightarrow S_1$ excitation. After substituting Eq. (9) into Eq. (8), we have the following transcendental relationship between I_2 and I_1

$$I_2 = \frac{I_1}{T\left(1 + \frac{\alpha_0 l R}{T(1 + \beta I_2)}\right)^2} \tag{11}$$

The product $\alpha_0 l$ of the linear absorption coefficient α_0 and the medium length l is the so-called linear absorbance that is related to the initial linear transmittance T_0 of the sample as $T_0 = \exp(-\alpha_0 l)$.

The values of $\alpha_0 l$ and the parameter of nonlinearity β for ten samples of fluorescein, four samples of rhodamine 6G doped BAG [11] and for three solutions of polymethine dye structures, namely cationic [7] used for the calculations are in Table 1.

In the first course of simulations the absorbers were settled in the Fabry-Perot cavity of the mirror reflectance of $R = 0.9$ and the mirror transmittance $T = 1 - R$.

Table 1: Optical absorption parameters for fluorescein, rhodamin 6G doped BAG films [11] and for solutions of polymethine dye solutions [8]

	BAG doped by Fluorescein		BAG doped by Rhodamine 6G		Solutions of polymethine dyes	
	$\alpha_0 l$	β (cm^2/W)	$\alpha_0 l$	β (cm^2/W)	$\alpha_0 l$	β (cm^2/W)
1	0.247	62.50	0.79	0.463	2.905	$2.50 \cdot 10^{-9}$
2	0.534	18.52	0.95	0.452	2.705	$2.94 \cdot 10^{-7}$
3	0.699	38.46	1.79	0.418	1.520	$2.94 \cdot 10^{-7}$
4	0.814	26.32	3.47	0.420		
5	1.070	55.56				
6	1.390	37.04				
7	1.680	40.00				
8	2.030	52.63				
9	2.310	38.46				
10	2.680	43.48				

4. Results and Discussion

The numerical study of the relationship between I_1 and I_2 according to Eq. (11) was performed under typical input powers from [10]. Results show that the optical bistability depends not only on nonlinear parameter β but also on linear absorbance α0l (Fig. 3). For the values of $\alpha_0 l > 1.39$ for fluorescein the output intensity I_2 is a two-valued function of I_1 and the hysteresis loops increase. The simulation shows that fluorescein under these conditions would exhibit bistable behaviour even with relatively low input intensities of light. From Fig. 3a) for fluorescein dispersed in BAG we also see that onset of the optical bistability for increasing $\alpha_0 l$ requires greater incident light intensities I_1.

The similar results are in Fig. 3b) for rhodamine 6G. The optical bistability could be achieved at input intensities > 20 W/cm^2 at $\alpha_0 l > 1.79$. The input intensities necessary for the optical bistability are higher than those for fluorescein which could be explained by lower values of parameter β representing the nonlinearity of rhodamine 6G in comparison with fluorescein.

The optical bistability is evidenced in solutions of polymethine dyes shown in Fig. 3c) and 3d). However, the input intensities necessary for the bistable performance are much higher in comparison with fluorescein and rhodamine 6G because the nonlinearity represented by the parameter β is very small (Table 1).

In the next course of simulations we investigated the influence of the Fabry-Perot mirror reflectance on the bistable behaviour. Several different values of the mirror reflectance from the range of $0.6 \div 0.98$ were used (Figs. 4 and 5).

From Fig. 4a we can see that fluorescein requires mirrors reflectance at least 0.85 to exhibit slight bistability in the Fabry-Perot cavity. In Fig. 4b the numerical analysis for rhodamine 6G with the same mirror reflectance is shown. We found out that a potential bistable device based on rhodamine 6G of the above $\alpha_0 l$ should be placed in the resonator of the mirror reflectance $R = 0.9$ at least. To improve the data visualisation, the numerical results in 3D are illustrated in Fig. 4 as well. The results proved the important role of the positive feedback in an absorptive bistable device.

The bistable behaviour was numerically investigated in solutions of polymethine dyes (Fig. 5). We see that increasing reflectance R facilitates the optical bistability occurrences, although at very high input light intensities.

The absorption lines of organic dyes are often inhomogeneously broadened inside a host material [6].The inhomogeneous broadening of optical transitions originates from the dye – matrix interaction, especially from different positions of molecules in the matrix. This could occur in case of dye molecules dispersion in glass matrix. On that occasion the intensity-dependent absorption coefficient is given by the following modification of Eq. (9)

$$\alpha(I_2) = \frac{\alpha_0}{\sqrt{1 + \beta I_2}} \tag{12}$$

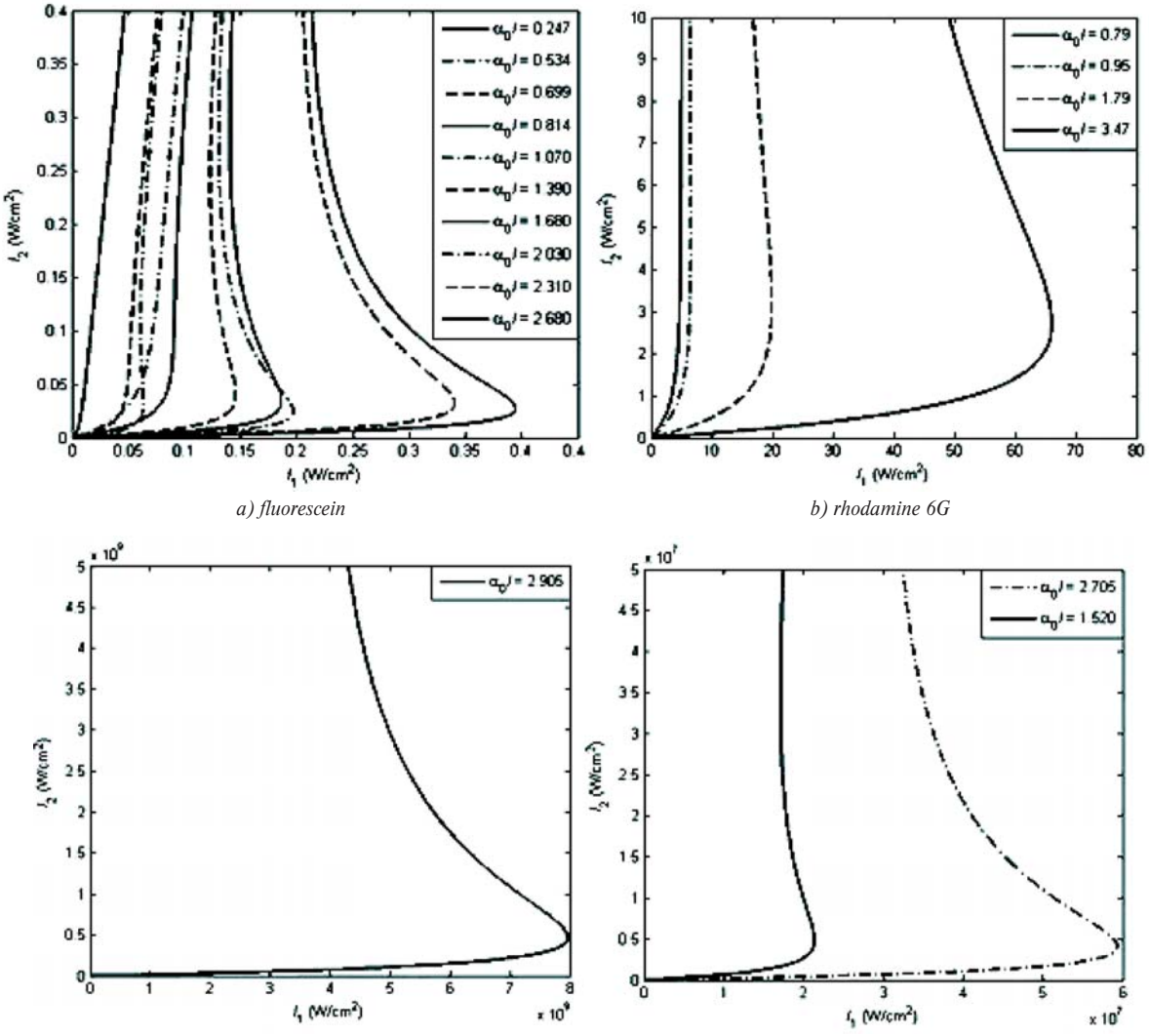

a) fluorescein *b) rhodamine 6G*

c) polymethine dye solution 1 *d) polymethine dye solutions 2 and 3*

Fig. 3 Investigation of the optical bistability in a) fluorescein, b) rhodamine doped BAG and c) polymethine dye solution 1 and d) solutions of polymethine dyes 2 and 3; R = 0.9

Due to inhomogeneous absorption line broadening expressed by Eq. (12) the following relationship between I_2 and I_1 as a result of substituting Eq. (12) into Eq. (8) is valid

$$I_1 = TI_2\left(1 + \frac{\frac{\alpha_0 lR}{T}}{\sqrt{1+\beta I_2}}\right)^2 \qquad (13)$$

The results of numerical studies of the relationships between I_1 and I_2 according to Eq. (13) are in Fig. 6 for BAG doped by fluorescein and for solutions of polymethine dyes. We found out that the inhomogeneous broadening of the optical transitions results in the decay of possible bistable behaviour. Similar results were obtained for rhodamine 6G. Then either the inhomogeneous broadening should remain small or a thorough choice of parameters of the nonlinear medium with inhomogeneous broadening is necessary to achieve the bistable performance. This conclusion is in agreement with the calculations in [15].

4. Conclusion

We numerically analyzed the optical bistable behaviour of organic dyes. It is clearly shown that the bistable behaviour is influenced by the linear absorbance, the parameter of medium nonlinearity and by the Fabry-Perot mirror reflectance as a parameter of positive feedback of a optical bistable device. We numerically established linear absorbance thresholds for the optical bistability in fluorescein and rhodamine 6G doped glass and for polymethine dyes dissolved in organic solvents. At specific values of linear absorbance of all organic dyes, we numerically determined the

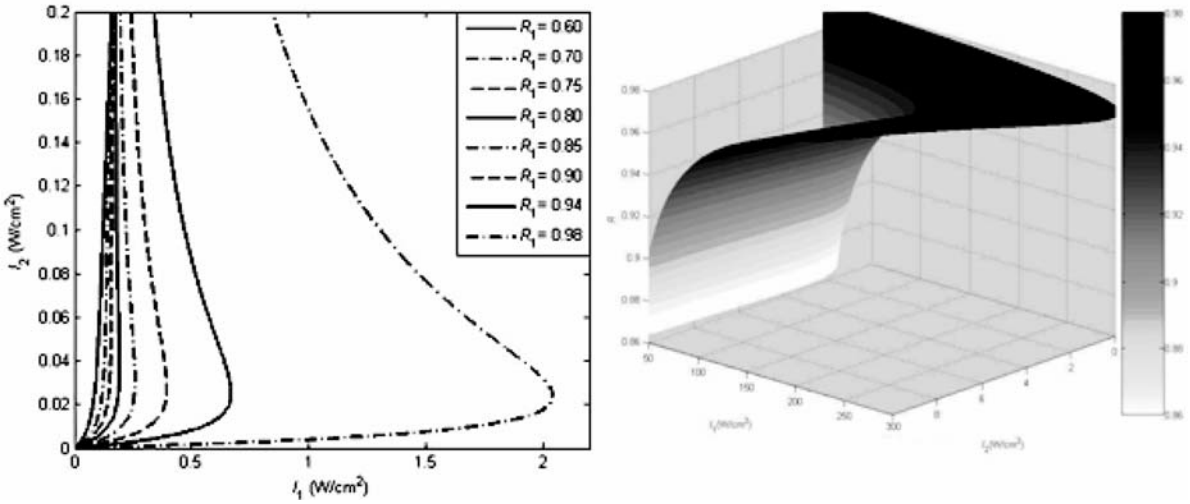

a) fluorescein at $\alpha_0 l$ = 2.68

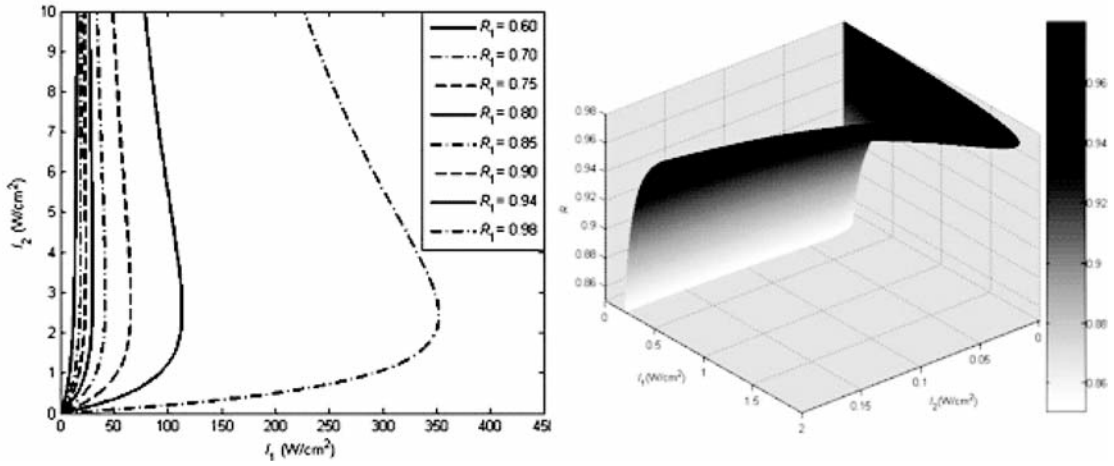

b) rhodamine 6G at $\alpha_0 l$ = 3.47

Fig. 4 Results 2D and 3D simulating optical bistability in BAG doped organic dyes

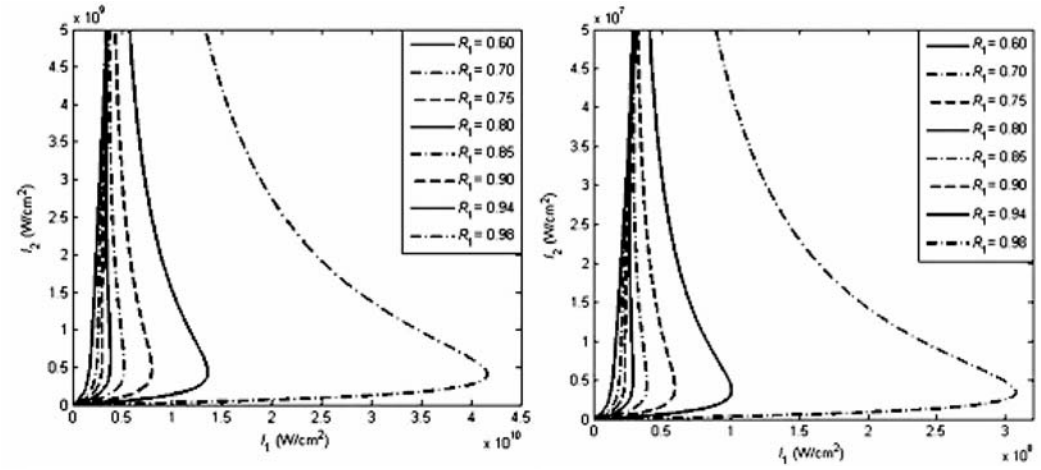

a) polymethine dye 1 at $\alpha 0_1$ = 2.905 *b) polymethine dye 2 at $\alpha_0 l$ = 2.705*

Fig. 5 Results simulating optical bistability in solutions of polymethine dyes

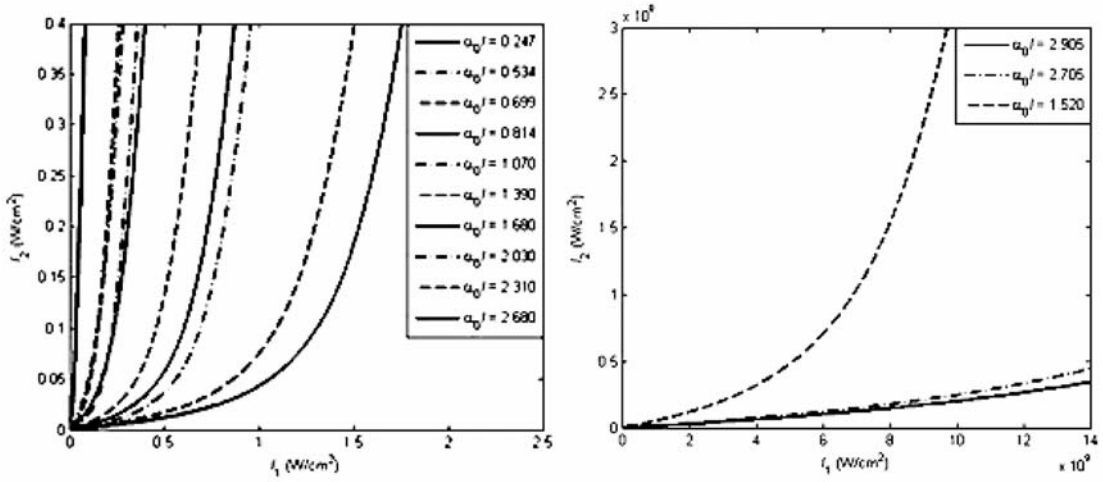

a) fluorescein *b) polymethine dye solutions*

Fig. 6 Investigation of the optical bistability with inhomogeneously broadened spectral lines (varied α0l and β, R = 0.9)

optical bistability threshold of the cavity mirror reflectance. Additionally we found out that in case of inhomogeneous broadening of spectral lines related to the optical excitations and relaxations, the optical bistability is quenched in all investigated organic dyes.

Acknowledgement

This work was partly supported by Slovak Grant Agency under the project No. 1/0411/10.

References

[1] DADO, M., KRAJCI, S., DUBOVAN, J., SABOL, D.: Numerical Investigation of Optical Burst Switching, *Communication - Scientific letters of the University of Zilina,* pp. 20–24, No. 2, 2008.
[2] HENKER, R. et al.: A Review of Slow- and Fast- Light Based on Stimulated Brillouin Scattering in Future Optical Communication Networks. *Communication - Scientific letters of the University of Zilina*, pp. 45–52, No. 4, 2008.
[3] LIU, JIA-MING: *Photonic Devices.* Cambridge University Press, First published 2005.
[4] BHARGAVA, S. et al.: *Optical Bistability in a Nonlinear Resonator With Saturable Losses and Intensity- Dependent Refractive index.* Int'l Conf. on Computers and Devices for Communication, 2009.
[5] SZOKE, I. A., DANEU, V., GOLDHAR, J., KURNIT, N. B.: Bistable Optical Element and its Applications. *Appl. Phys*. Lett. 15, pp. 376–379, 1969.
[6] NIE, WENJIANG: Optical Nonlinearity: Phenomena, Applications, and Materials. *Advanced Materials* 5 (7/8), pp. 520–545, 1993.
[7] MATTU, J., JOHANSSON, T., LEACH, G.W.: Third Order Nonlinear Optical Response from Polythiophene-based thin Films. *J. Phys. Chem.*, 111, pp. 6868–6874, 2007.
[8] GANEEV, R.A. et al.: Characterization of Nonlinear Optical Parameters of Polymethine Dyes. *Appl. Phys.* B 76, pp. 683–686, 2003.
[9] XUE, J., FORREST, S.R.: Organic Optical Bistable Switch. *Appl. Phys.* Lett. 82, pp. 136–138, 2003.
[10] UNNIKRISHNAN, K.P., THOMAS, J., NAMPOORI, V.P.N., VALLABHAN, C.P.G.: Nonlinear Absorption in Certain Metal Phtalocyanines at Resonant and Near Resonant Wavelength. *Optics Communications* 217, pp. 269–274, 2003.
[11] SHARAN, A., SHARMAN, R. C., SANDHYA, S. N., AYYER, A., SHARMA, K. K.: Modeling Absorption in Saturable Absorbers. *Optics Communications* 199, pp. 267–275, 2001.
[12] HU, A.T. et al.: Reverse Saturable Absorption of Copper Phthalocyanines in Toluene and Solgel Tetraethyl Orthosilicate/polyvinyl Butyral Hybrid Film. *Dyes and Pigments* 62 (1), pp. 11–19, 2004.
[13] DJABI, S., DJABI, M.: Study of Optical Bistability in a Laser Containing a Saturable Absorber. *J. of Engineering and Applied Sciences* 2 (9), pp. 1383–1386, 2007.
[14] RENGE I., WILD, U. P.: Inhomogeneous Broadening and Pressure Shifts of the Optical Spectra in Organic Glasses at Low Temperatures. *J. Luminescence* 86 (3-4), pp. 321–247, 2000.
[15] BENIACHE, A., MOUASSA, S., VAN HOANG, D.: Optical Bistability of Fabry-Perot LSA with Inhomogeneous Broadening. *J. Engineering and Appl. Sciences* 2 (1), pp. 66–72, 2007.

Pavol Spanik – Jozef Kandrac – Michal Frivaldsky – Peter Drgona *

VERIFICATION OF OPERATION MODES OF DESIGNED LLC RESONANT CONVERTER

This paper describes the design of the LLC resonant converter, which is done by means of fundamental harmonic approximation (FHA). Output power of proposed converter is 1kW with output voltage 48 V at switching frequency of 500 kHz. Performance of converter at different operational conditions was verified through simulation analysis by utilization of OrCAD PSpice software. The simulation results of multiple parametrical experiments were obtained and consequently evaluated into graphical interpretation of efficiency of proposed converter.

1. Introduction

LLC resonant converter is multi-resonant converter and is characterized by its unique DC – gain characteristic, which has two resonant frequencies (f_0 and f_p). This converter has several advantages compared to standard serial LC resonant topology. One of them is possibility of stable regulation of output voltage in a wide range of input voltages together with the change of output power from 1% to 100%. The next advantage is achievement of ZVS switching mode during various operational modes. LLC resonant converter is composed of three functional parts (Fig. 1). It deals with pulse generator, resonant circuit with high-frequency transformer and rectifier with capacitive filter.

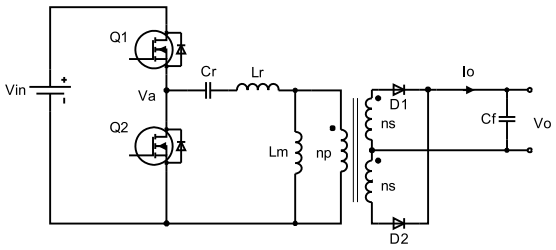

Fig. 1 Principal schematic of LLC converter

From the DC – gain characteristic of LLC converter it could be seen that, when the input voltage is constant and the converter operates at the switching frequency near to resonant frequency f_0, the gain of converter is independent on the variations of load, which results in small regulation range. On the other hand at different operating conditions, the operating point varies between lower and upper resonant frequency in relation to power loading and input voltage. There exist restrictions which are determining boundaries of reliable function and are described more in detail in [1]. Mathematical interpretation of gain characteristic is described by next equation:

$$M = \frac{2nV_0}{V_m} = \left| \frac{\left(\frac{\omega^2}{\omega_0^2}\right) \cdot \sqrt{m \cdot (m-1)}}{\left(\frac{\omega^2}{\omega_p^2} - 1\right) + j \cdot \left(\frac{\omega}{\omega_0}\right) \cdot \left(\frac{\omega^2}{\omega_0^2} - 1\right) \cdot (m-1)Q} \right|$$

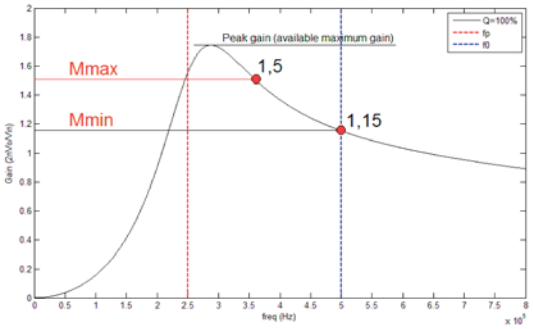

Fig. 2 DC – gain characteristics of proposed LLC resonant converter

2. Operation modes

Operation of LLC converter in different operational modes is described by DC gain characteristic, which should be divided into ZVS and/or ZCS region. ZVS region in dependency on the switching frequency can be further divided into:

- region with switching frequency equal to resonant ($f_s = f_0$)
- region with switching frequency higher than resonant ($f_s > f_0$)
- region with switching frequency lower than resonant ($f_s < f_0$)

* **Pavol Spanik, Jozef Kandrac, Michal Frivaldsky, Peter Drgona**
Department of Mechatronics and Electronics, Faculty of Electrical Engineering, University of Zilina, Slovakia, E–mail: pavol.spanik@fel.uniza.sk

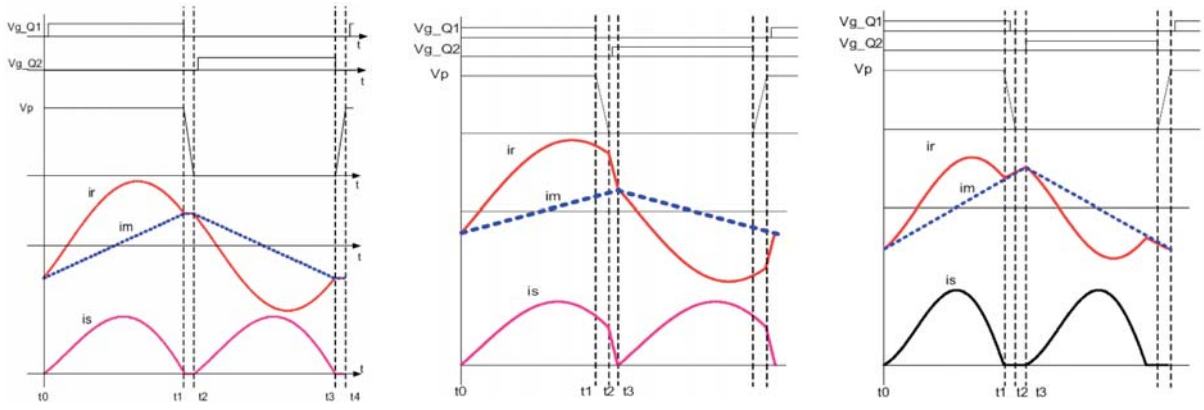

Fig. 3 Waveforms of currents and voltages of LLC converter at different operating conditions a) $f_s = f_0$, b) $f_s > f_0$, c) $f_s < f_0$

According to the operational modes of resonant converters the operation of LLC resonant converter is rather difficult. The principal waveforms of transformer and output diode during each operating mode are shown in Fig. 3.

The impedance of series resonant circuit at the resonant frequency is equal to zero. Therefore the reflected output voltage is equal to the input voltage, which is described by the unity of voltage gain thus the circuit then operates optimally. LLC resonant converter can achieve gain greater, less or equal to 1. If the switching frequency is less than the resonant frequency, magnetization inductance is involved into the resonance of the circuit so the converter can deliver higher gain.

3. Design parameters of the main circuit

Target of the design is to determine the active and passive elements of the proposed converter. Main electrical parameters are:

$f_0 = 500$ kHz, $P_O = 1$ kW, $U_O = 48$ V,
$I_O = 21$ A, efficiency $= 0.96$

A. Estimated efficiency

For the low voltage applications, the efficiency varies from 0.88 to 0.92. For the high voltage applications, the efficiency varies from 0.92 to 0.96. In our case, we expect efficiency with a value of 0.96. Input power is then calculated as:

$$P_{IN} = \frac{P_o}{E_{ff}} = \frac{U_0 I_0}{E_{ff}} = \frac{48.21}{0.96} = \frac{1008}{0.96} = 1050\ W$$

B. Determination of the maximum and minimum input voltage

The advantage of LLC converter is its ability to work in a wide range of input voltages. In our proposal we considered the following values of input voltages:

Minimal input voltage $V_{inmin} = 325$ V
Maximal input voltage $V_{inmax} = 425$ V

Regulation is based on frequency modulation, through which the voltage gain can be changed. The main parameter that determines the value of voltage gain, and thus the range of frequency control, is ratio ("m") of the magnetizing and resonant inductance.

C. Determination of maximum and minimum voltage gains

When converter operates at nominal input voltage $V_{IN} = 425$ V then the switching frequency is determined to be $f_0 = 500$ kHz. Also at the resonant frequency the voltage gain is determined from the value of inductance ratio ($m = L_m/L_r$). During determination, there exist some design tradeoffs. For example, the higher value of m will results in the higher value of conduction losses, the higher regulation range and in the higher volume of the transformer core. On the other hand, the lower value of m deteriorates transformer coupling and reduces efficiency (Figs 4–6).

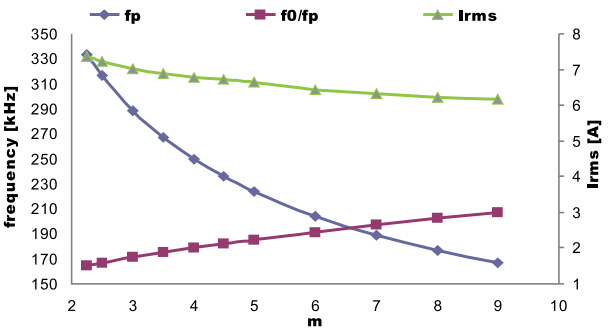

Fig. 4 Dependency of parallel resonant frequency (f_p), ratio of f_0/f_p and I_{RMS} on the value of m

Selection of m value: $m = 4$

$$M_{\min} = \sqrt{\frac{m}{m-1}} = \sqrt{\frac{4}{4-1}} = 1.15$$

$$M_{\max} = \frac{V_{IN\max}}{V_{IN\min}} M_{\min} = \frac{425}{325} 1.15 = 1.5$$

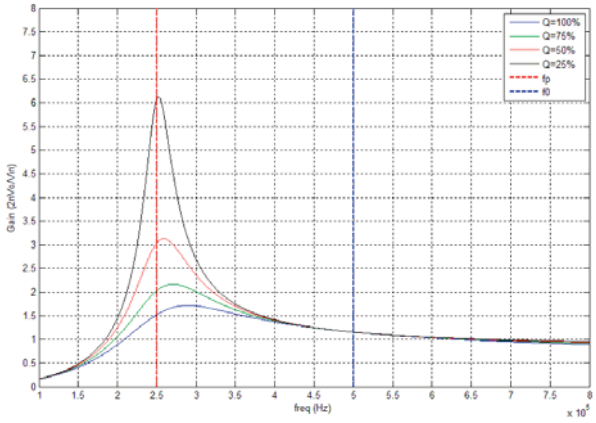

Fig. 5 DC gain characteristic of proposed LLC resonant converter for various values of output power (m = 4)

For selected value of $m = 4$, the regulation range is 250 kHz, whereby the lower resonant frequency f_p is equal to 250 kHz and upper resonant frequency f_0 is equal to 500 kHz.

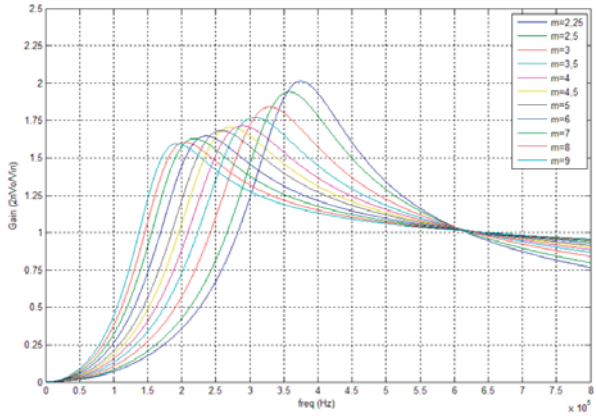

Fig. 6 DC - gain characteristics for different values of m (2.25 to 9) and for 100% of output power

D. Determinations of transformer turns ratio

From the value of minimal gain, we can calculate the ratio of transformer ration using the following formula:

$$n = \frac{N_P}{N_S} = \frac{V_{IN\max}}{2(U_O + U_F)} M_{\min} =$$

$$= \frac{425}{2(48 + 0.96)} 1.15 = 4.99 \cong 5$$

where U_o is output voltage of converter, and U_f is voltage drop of the output diodes.

E. Determination of equivalent load resistance

From the value of transformer ratio we will calculate reflected output load resistance to the primary side:

$$R_{AC} = \frac{8n^2}{\pi^2} \frac{U_o^2}{P_o} = \frac{8.5^2}{\pi^2} \frac{48^2}{1008} = 46.32\ \Omega$$

F. Design of resonant network

To ensure the stable operation of ZVS and sufficient gain it is necessary to determine the correct value of quality factor Q. For this purpose it is necessary to consider margin of voltage gain from 10 ~ 20% of M_{max}. In this design the value of 15% of M_{max} is being considered.

$$M_{PEAK} = 1.15 \cdot M_{MAX} = 1.15 \cdot 1.5 = 1.725$$

For $m = 4$ and $M_{PEAK} = 1.725$ and from Fig. 7 the value of quality factor is $Q = 0.37$.

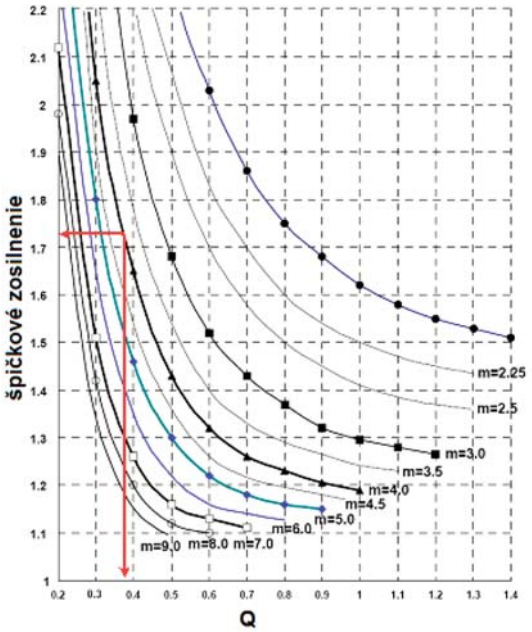

Fig. 7 Peak gain (attainable maximum gain) vs. Q for different m values

After determination of required quantities, we can calculate parameters of a resonant tank using the following formulas:

$$C_r = \frac{1}{2\pi \cdot Q \cdot f_0 \cdot R_{AC}} = \\ = \frac{1}{2\pi \cdot 0.37 \cdot 500 \cdot 10^3 \cdot 46.32} = 18.57\ nF$$

$$L_r = \frac{1}{(2\pi \cdot f_0)^2 \cdot C_r} = \\ = \frac{1}{(2\pi \cdot 500 \cdot 10^3)^2 \cdot 18.57 \cdot 10^{-9}} = 5.45\ \mu H$$

4. Simulation analysis of the operational modes of proposed LLC resonant converter

Operational modes of LLC resonant converter was verified in OrCAD PSpice simulation software. Simulation model of the main circuit of proposed converter is shown in Fig. 8.

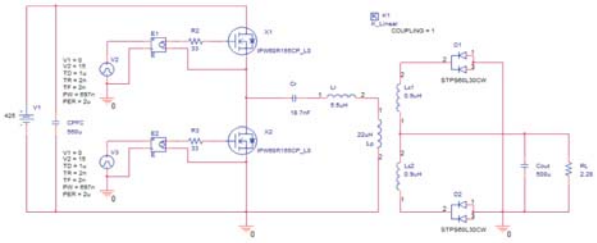

Fig. 8 Simulation model of main circuit of proposed LLC converter

As switching transistors the CoolMOS types from fy Infineon (IPW60R165CP) are being used. Rectifiers are low voltage-drop Schottky rectifier diodes from STMicroelectronics.

Fig. 9 shows the waveforms of voltages and currents on the primary side of transformer, and time waveforms of current of output rectifiers, during simulation experiment, when the switching frequency $f_s = f_0 = 500$ kHz. This is a simulation experiment when the performance of LLC converter is expected to be optimal, since the impedance of a series resonant circuit is zero. Input voltage is clamped on the magnetizing inductance, and the voltage gain at resonant frequency is almost equal to 1.

Fig. 10 shows the time waveforms of voltages and currents of the same elements as in the previous experiment, but the switching frequency $f_s > f_0$ and $f_s = 630$ kHz. Current through resonant circuit is slightly deformed, as well as the current of output rectifier diodes, which is caused due to discharge process of the internal capacitances of switching transistors and its consecutive turn on.

Fig. 11 shows the same situation as in previous cases, but these results were obtained from simulation experiment during which switching frequency $f_s < f_0$ and $f_s = 360$ kHz. Non-sinusoidal shape of the currents is caused due to transfer of stored energy from the magnetizing inductance into the resonant circuit thus converter is then able to increase output gain and, therefore, output voltage. In next simulation analysis, proposed converter was subjected to experiment during which output power was changed. We made 4 different experiments whereby output power was 1 kW and 252 W, at input voltage of 425 V and 325 V.

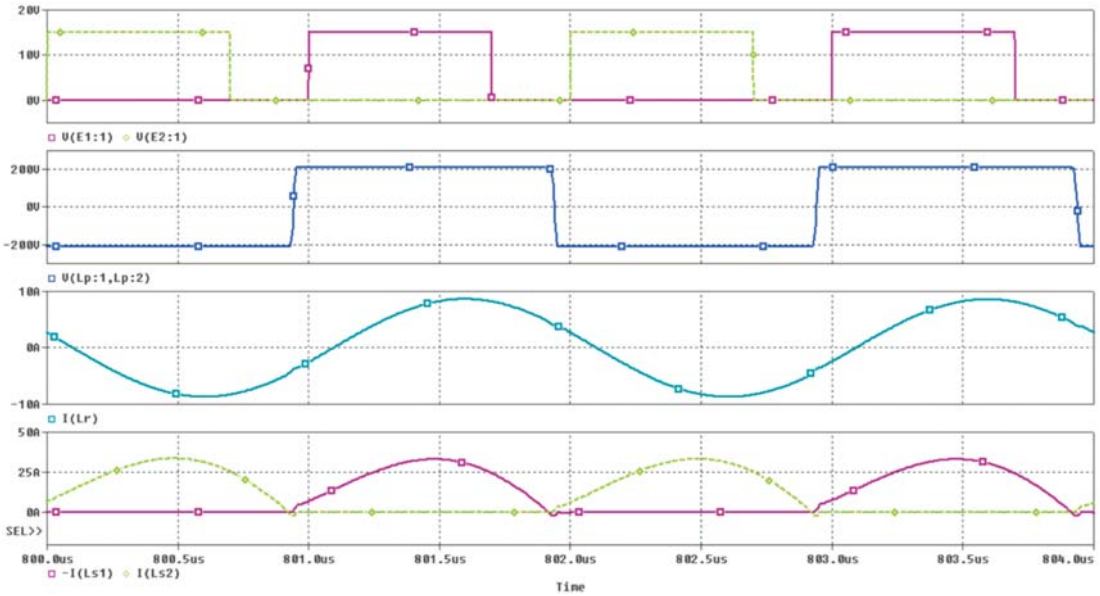

Fig. 9 Time waveforms during the simulation experiment at $f_s = f_0$ (from top - driving signals of transistors X1, X2, voltage on the primary side of transformer, current on the primary side of transformer, currents of the output diodes D1, D2)

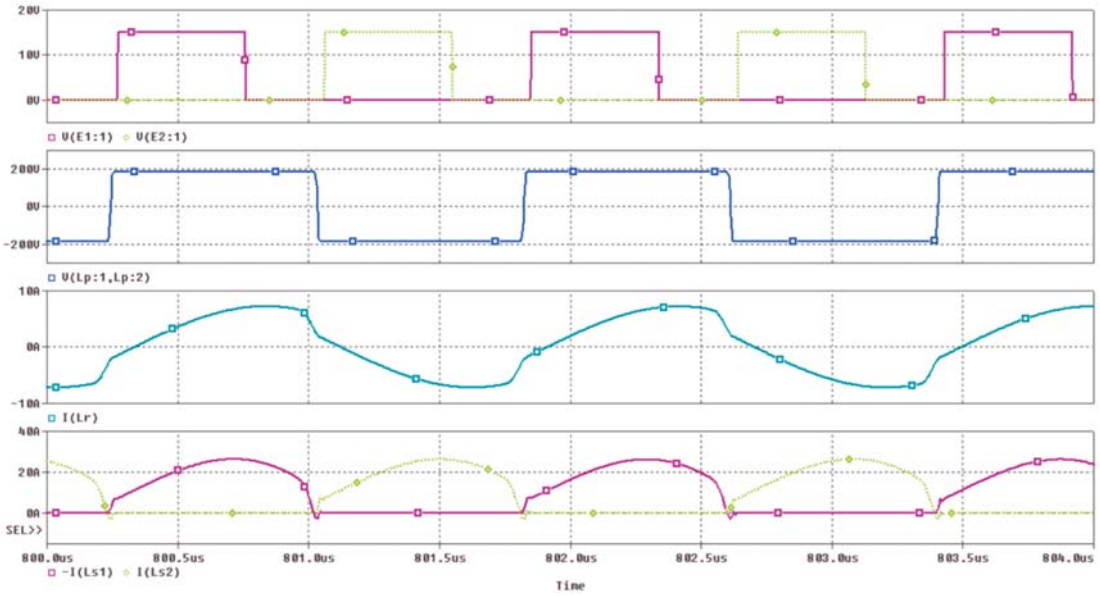

Fig. 10 Time waveforms during the simulation experiment at $f_s > f_0$ (from top - driving signals of transistors X1, X2, voltage on the primary side of transformer, current on the primary side of transformer, currents of the output diodes D1, D2)

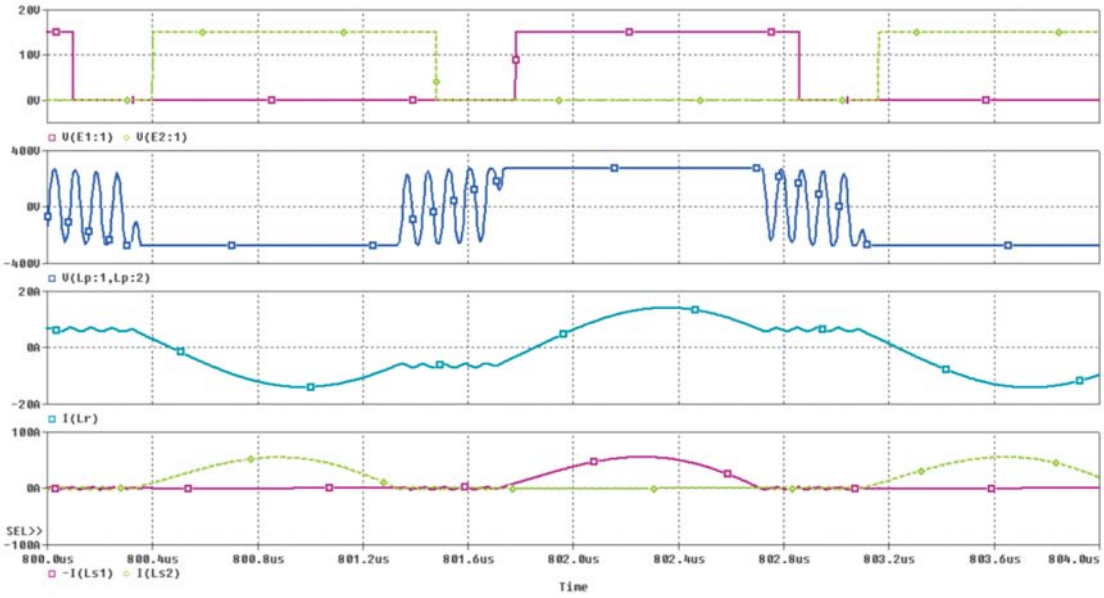

Fig. 11 Time waveforms during the simulation experiment at $f_s < f_0$ (from top - driving signals of transistors X1, X2, voltage on the primary side of transformer, current on the primary side of transformer, currents of the output diodes D1, D2)

Fig. 12 represents results from the simulation experiment, when LLC resonant converter operates at full load (P_{OUT} = 1008 W) when input voltage U_{IN} = 425 V. In this mode, transistors are operating with ZVS conditions and output diodes with character of ZCS switching. The unwanted effect of reverse recovery was eliminated by utilization of Schottky rectifier diodes. Fig. 13 shows the simulation experiment at 25% of load at the input voltage U_{IN} = = 425 V. The picture shows that even at the reduced output power the switching transistors are maintaining excellent operating characteristics of the ZVS mode. In the case of output diodes the ZCS switching character is also still achieved.

Fig. 14 shows the simulation experiment, when LLC resonant converter operates at minimal supply voltage U_{IN} = 325 V and at full load condition. Simulation experiment confirmed proper design of converter. Transistor's current has sinusoidal shape until magnetizing inductance became participating in resonance with other circuit parameters. Output diodes are operating in discontinuous

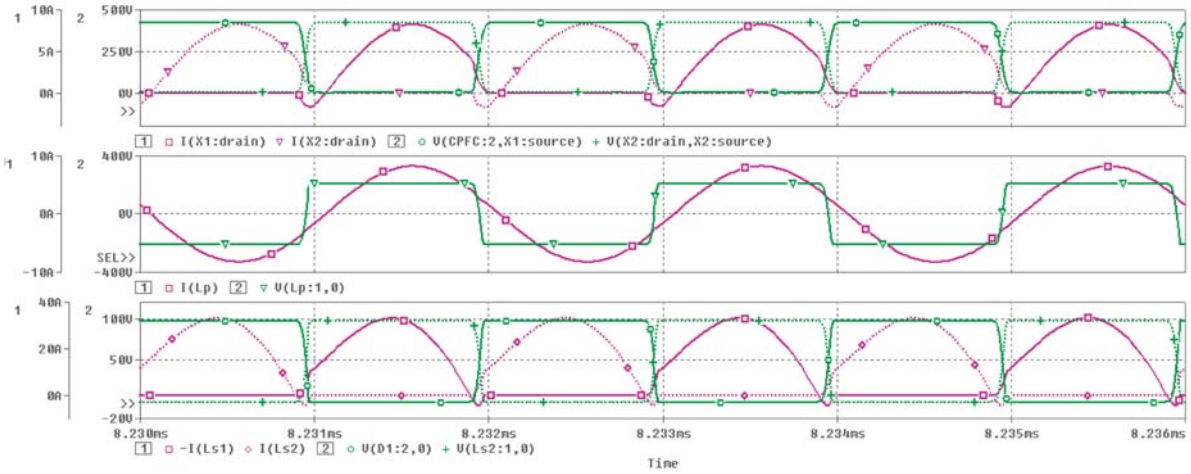

Fig. 12 Time waveforms of voltages and currents during the simulation experiment: U_{IN} = 425V, P_{OUT} = 1008W (from top - transistor X1a X2, transformer primary side, output diode D1 and D2)

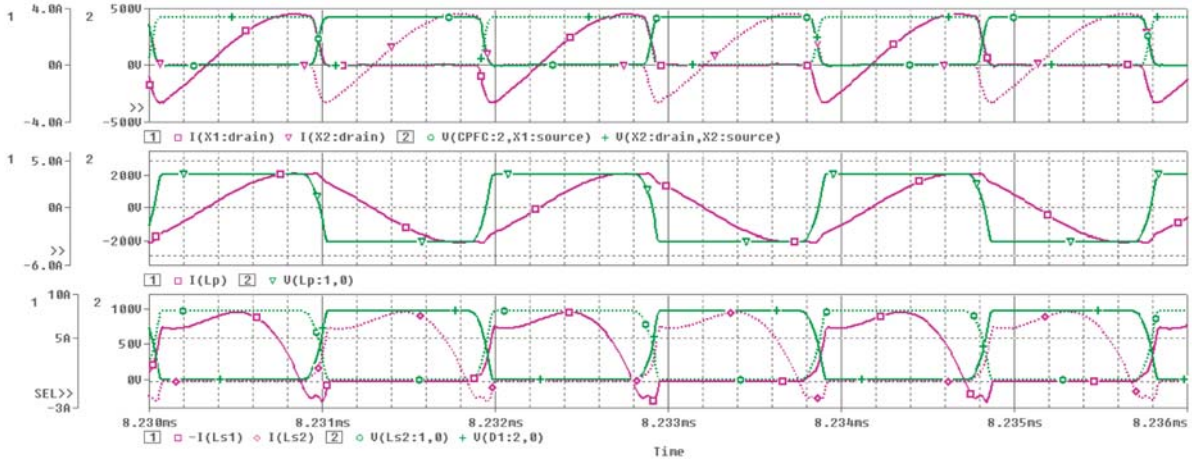

Fig. 13 Time waveforms of voltages and currents during the simulation experiment: U_{IN} = 425V, P_{OUT} = 252W (from top - transistor X1a X2, transformer primary side, output diode D1 and D2)

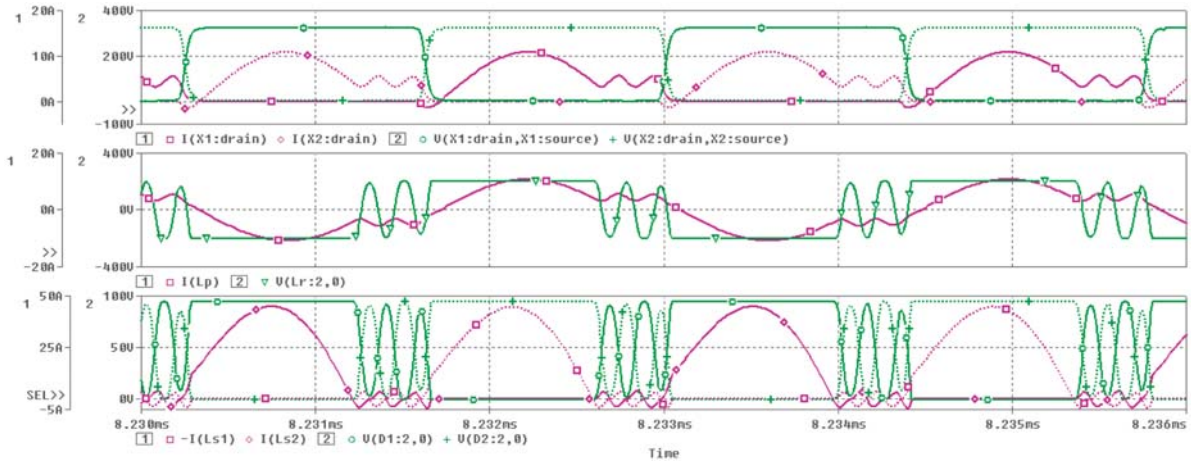

Fig. 14 Time waveforms of voltages and currents during the simulation experiment: U_{IN} = 325V, P_{OUT} = 1008W (from top - transistor X1a X2, transformer primary side, output diode D1 and D2)

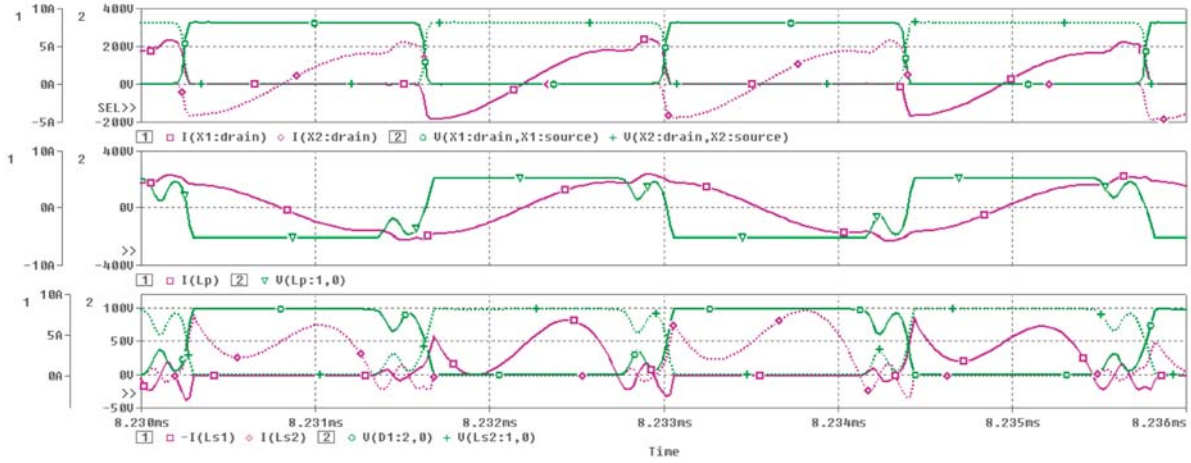

Fig. 15 Time waveforms of voltages and currents during the simulation experiment: U_{IN} = 325V, P_{OUT} = 252W (from top - transistor X1a X2, transformer primary side, output diode D1 and D2)

ZCS mode. The last experiment has been done at the input voltage U_{IN} = 325 V and at output power P_{OUT} = 252 W. As can be seen in this operation mode the inverter is still able to achieve ZVS conditions for the main transistors. Soft commutation with ZCS conditions are also achieved for output rectifier diodes, which are operating in discontinuous mode. After simulation experiments had been made, we made multiple graphic interpretation of converter's efficiency in dependency on converter's output power and input voltage (Fig. 16). These results are good indicators of converter design and are good starting point for experimental verifications.

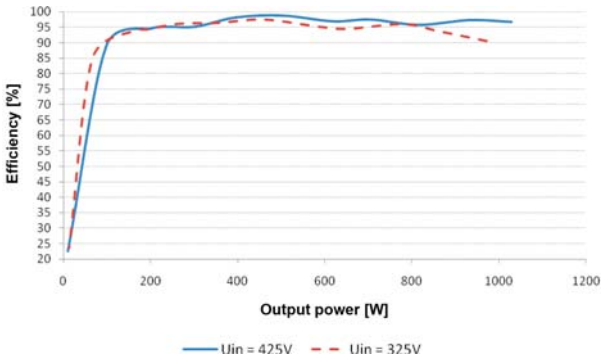

Fig. 16 Efficiency of the proposed converter in dependency on output power and input voltage (U_{IN} = 425 V, U_{IN} = 325V)

5. Conclusion

This paper describes design procedure of the LLC resonant converter. The property of converter is its ability to operate with very high switching frequency. The operation of converter at various operational modes was done through simulation analysis, which confirmed proper design of converter. In terms of design it is important to make the compromise in selection of the inductance ratio *m*. Future work will be focusing on the examination of influence of the parasitic components on the operation of LLC converter.

Acknowledgement

The authors wish to thank for the project VEGA "Research of Topology and Control of Power Electronic Supply System with Single-Phase HF Input and Two-Phase Orthogonal Output for Two-Phase SM/IM Electrical Motors". Next to grant agency APVV for project No. 20-051705 and No. APVV-0535-07. Also we would like to thank for VMSP-P-0085-09 and LPP-0366-09.

References

[1] FAIRCHILD SEMICONDUCTOR CORPORATION.: *Application Note AN4151*, 2007

[2] ELZBIETA SZYCHTA.: *Multiresonant ZVS Switching Converters with Constant Output Voltage, Oficyna Wydawnicza Uniwersytetu Zielonogorskego* 2006, ISBN 83-7481-040-8

[3] BENDA, V.: *Power Semiconductors and Integrated Structures*. CVUT Editor, Prague (CZ), 1994

[4] Liu R., Lee C. Q.: *The LLC-type Series Resonant Converter-variable Switching Frequency Control,* Proc. of the 1999 32nd Midwest Symposium of Circuits and Systems, Vol. 1, pp. 509–512

[5] DUDRIK J., DZURKO P.: *Series-Parallel Resonant DC-to-DC Converter for Arc Welding,* Proc. of the Conference PEMC´98, Prague, September 1998, Vol. 7, pp. 16–20

[6] XIAOGAO XIE, JUNMING ZHANG, CHEN ZHAO, ZHUO ZHAO, ZHAOMING QIAN: *Analysis and Optimization of LLC Resonant Converter with a Novel over-current Protection Circuit,* 0885-8993/07, IEEE.

Juraj Palecek – Martin Vestenicky *

PASSIVE ELECTRONIC COMPONETS PARAMETERS SEARCHING WITH DIFFERENTIAL EVOLUTIONARY ALGORITHM

This paper describes computing of inductor parameters as passive electronic component with algorithm of differential evolution. Computing of parameters is based on substitute model of inductor which is described with three basic parameters such as resistance, inductance and capacitance. Measured frequency response of complex impedance of the real inductor is input parameter to the iterative loop driven by the differential evolution algorithm. There are three output parameters of the algorithm, where resistance value is considered to be a combination of DC coil resistance and skin effect influence, second value describes inductance of a real inductor and third parameter defines interturn parasitic capacitance of a real inductor.

1. Introduction

In the real world one need to find parasitic parameters of real electronic components. This is sometimes a non trivial problem, because of limited measuring equipment capabilities. This paper describes usage of iterative algorithm to compute elements of mathematical model. These components represent parasitic parameters of the real electronic elements. Mentioned iterative algorithm is based on the differential evolution. Mathematical models of basic real electronic components are described in subsequent text.

Equivalent circuit representation of a resistor

Resistor is a most common circuit element in low frequency electronics, whose purpose is simply to produce a voltage drop by converting some of electric energy into heat. In Fig. 1 is displayed equivalent circuit representation of a resistor.

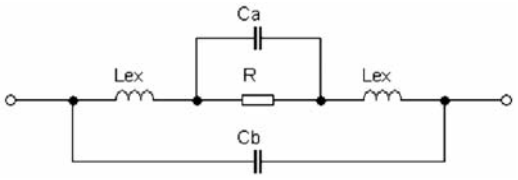

Fig. 1 Electric equivalent circuit representation of a resistor

The interlead capacitance Cb is usually much smaller than the internal or stray capacitance, and in many cases can be safely neglected. For computing the external inductance of the straight wire at high frequencies can be used formula (1), where l=2x (length of single lead) to account for two connections. It should be noted that the preceding formula for the computation of the lead inductance is applicable only for frequencies where the skin depth is smaller than the radius of a wire.

$$L_{ex} = \frac{\mu_0 l}{2\pi}\left[\ln\left(\frac{2l}{a}\right) - 1\right] \tag{1}$$

Knowing the inductance of the leads, the impedance of the entire circuit can be computed.

$$Z = j\omega L_{ex} + \frac{1}{j\omega C_a + \frac{1}{R}} \tag{2}$$

The impedance of resistor at low frequencies is equal to the *R*. With increase of frequency effect of the stray capacitance becomes dominant, which causes the impedance of resistor to decrease. Beyond the resonance the total impedance increases due to the lead inductance. Impedance of resistor may be given by formula (2).

Equivalent circuit representation of a capacitor

Fig. 2 represents equivalent circuit representation of a real capacitor. Impedance of this model of real capacitor is then given by formula (3).

$$Z_c = j\omega L_{ex} + R_s + \frac{R_e}{R_e j\omega C + 1} \tag{3}$$

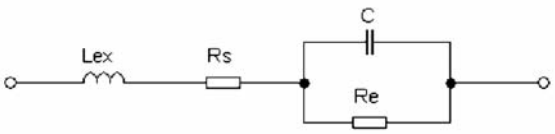

Fig. 2 Electric equivalent circuit representation of a capacitor

* **Juraj Palecek, Martin Vestenicky**
Department of Telecomunications and Multimedia, Faculty of Electrotechnical Engineering, University of Zilina, Slovakia,
E-mail: palecek@fel.uniza.sk

Equivalent circuit representation of an inductor

Although not employed as often as resistors or capacitors, inductors generally are used in transistor biasing networks, for instance as RF chokes (RFCs) to short circuit the device to DC voltage conditions. Since a coil is generally formed by winding a straight wire on a cylindrical former and the windings represent an inductance in addition to the frequency-dependent wire resistance. Moreover, adjacent wires constitute separated moving changes, thus giving rise to a parasitic capacitance effect as shown in Fig. 3.

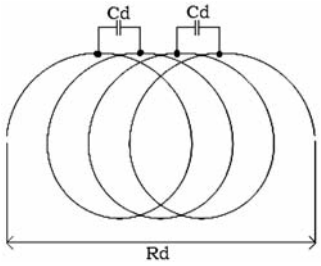

Fig. 3 Distributed capacitance and series resistance in the inductor coil

The equivalent circuit model of the inductor is shown in Fig. 4. The parasitic shunt capacitance Cs and series resistance Rs represents composite effects of capacitance Cd and resistance Rd respectively. Impedance of model of real inductor is then given by formula (4).

$$Z_L = \frac{j\omega L + R_s}{-\omega^2 L C_s + j\omega R_s C_s + 1} \tag{4}$$

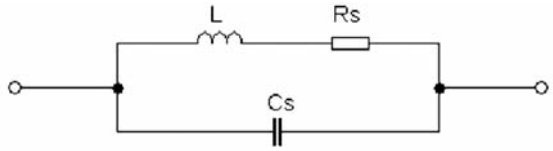

Fig. 4 Electric equivalent circuit representation of an inductor

In the frequency response of the RFC impedance, the impedance increases more rapidly as the frequency approaches resonance. Second, as the frequency continues to increase, the influence of the parasitic capacitance *Cs* becomes dominant and the impedance of the coil decreases. If the RFC has zero series resistance, then the overall impedance behavior at resonance would reach infinity, but due to nonzero contribution of *Rs*, the maximum value is finite. To characterize the effect of the coil resistance, the quality factor *Q* is commonly used. This quality factor characterizes the resistive loss in the passive circuit, and for tuning purposes it is desirable for this factor to be as high as possible. The inductor *Q* generally increases with frequency, levels off, and then drops close to the self-resonance [3].

2. Utilized Algorithm and Cost Function Construction

Differential evolution is a stochastic parallel direct search evolution strategy optimization method that is fairly fast and reasonably robust. Basically, DE adds the weighted difference between two population vectors to a third vector. This way no separate probability distribution has to be used which makes the scheme completely self-organizing [4].

Differential evolution is capable of handling nondifferentiable, nonlinear and multimodal objective functions. It has been used to train neural networks having real and constrained integer weights.

In a population of potential solutions within an n-dimensional search space, a fixed number of vectors are randomly initialized, then evolved over time to explore the search space and to locate the minima of the objective function.

At each iteration called a generation, new vectors are generated by the combination of vectors randomly chosen from the current population (mutation). The outcoming vectors are then mixed with a predetermined target vector. This operation is called recombination and produces the trial vector. Finally, the trial vector is accepted for the next generation if and only if it yields a reduction in the value of the objective function. This last operator is referred to as a selection [5].

The modeling process is based on comparing values of impedance and phase in measured frequencies with values computed with differential evolutionary algorithm. Input parameters of algorithm are values of impedance and angle in measured places of frequency characteristic, and values for algorithm controlling like number of individuals in generation, number of chromosomes of each individual, number of generations, recombination constant and minimum and maximum value chromosome of individual. The output parameter of algorithm is the best individual with the best genes for all of the frequencies in range. That gene is finally used as optimal value for inductor representation.

Each chromosome consists of three genes, where the first gene is used for resistance representation of inductor, second gene describes inductor inductance and third is describing its capacitance.

The genes are represented as decadic numbers. Minimum and maximum values of gene are vectors of least and highest parameters of inductors resistance, inductance and capacity.

Zero generation is generated, where each chromosomes gene is filled with random number from minimum to maximum value of interval at the algorithm start. After that, cost for every chromosome in zero population is computed by "cost" function. Next, the best chromosome with lower cost is considered as "best" chromosome, and its placement is added to new variable. After these steps function of algorithm is stochastic. For defined number of iterations, which is limited by "number of generations" variable, the body of algorithm is processed. There is a randomly generated

number, which is compared with recombination constant, in every iteration. There is generated a new chromosome from the best chromosome from previous iterations with recombination function, if the value of generated number is greater than recombination constant. Otherwise, the next generation chromosome is created by chromosome from previous iteration. After this, the cost of a new chromosome is computed and if this value is lower than the cost of the best previous chromosome, a new chromosome is justified as the best. If this cost value is higher than the cost of previous chromosome, then this cost is written to the vector of the costs.

Cost value is dedicated as difference between measured and computed frequency response of the impedance and frequency response of the phase in eighteen frequency points. Mathematic formulation of cost value is presented in formula (5).

$$cost = \sum_{i=1}^{18}\left(W_1\left|\frac{Z_{computed} - Z_{measured(i)}}{Z_{measured(i)}}\right| + W_2\left|\frac{\varphi_{computed} - \varphi_{measured(i)}}{\varphi_{measured(i)}}\right|\right) \quad (5)$$

Stop condition of algorithm is bordered with a number of generation variable, where the number of iterations is defined as a real number. In the end of algorithm, the frequency response of impedance (Fig. 6) and frequency response of phase (Fig. 7) is displayed, where values of resistance, conductance and capacity are constituted from the genes of the best chromosome with lower cost. The black points in Figs. 6 and 7 are measured values of impedance and phase of a real inductor. A pseudo-code implementation of algorithm is displayed in Fig. 5. Entire algorithm was realized in Matlab computing language.

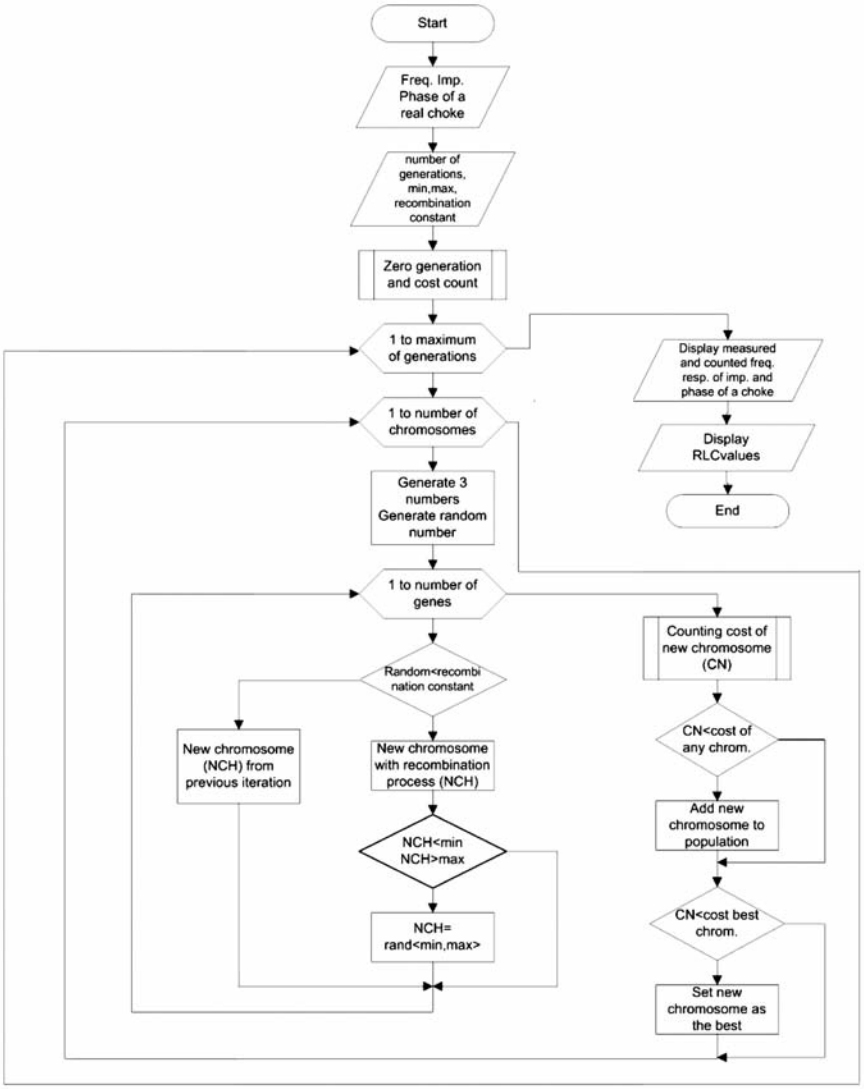

Fig. 5 Pseudo-code implementation of DE algorithm

3. Experimental Part

In this experiment there were computed parameters of a real inductor. This inductor was constructed of 0.5 mm diameter copper wire with air core. Input parameters such a frequency response of impedance and phase was measured by impedance meter TESLA BM 650 in eighteen frequency steps. Measured frequency range was from 0.5 MHz up to 5 MHz. In Table 1 are displayed parameters of differential evolutionary algorithm used in program [1].

Parameters of algorithm Tab.1

Parameter	Value
Chromosome representation	Decadic
Number of unknown coefficients	3
Differential mutation constant 1	0.5
Differential mutation constant 2	0.5
Crossing constant	0.9
Number of chromosomes in generation	600
Number of generations	50
Number of genes of chromosome	3
Calculating time	33 seconds
Calculating time (with skin effect)	72 seconds
W 1	1
W 2	0.25

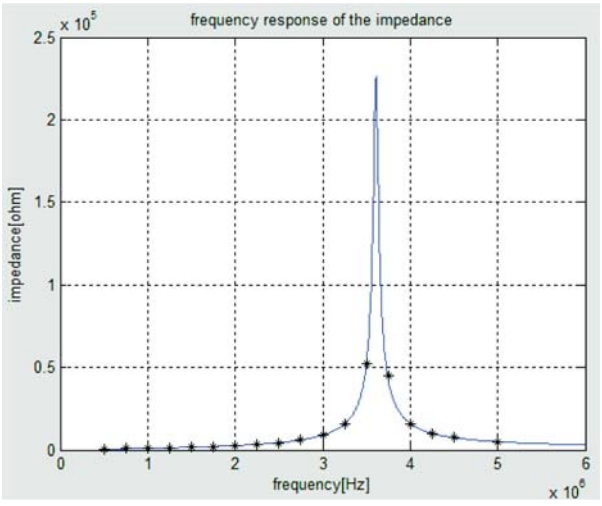

Fig. 6 Frequency response of the impedance of an inductor

Skin effect influence

Skin effect is a tendency for alternating current to flow mostly near the outer surface of a solid electrical conductor, such as metal wire, at high frequencies. The effect becomes more and more apparent as the frequency increases. The main problem with skin effect is that it increases the effective resistance of a wire for AC at moderate to high frequencies, compared with the resistance of the same wire at direct current and low AC frequencies (Fig. 8). The effect is most pronounced in radio-frequency systems [6].

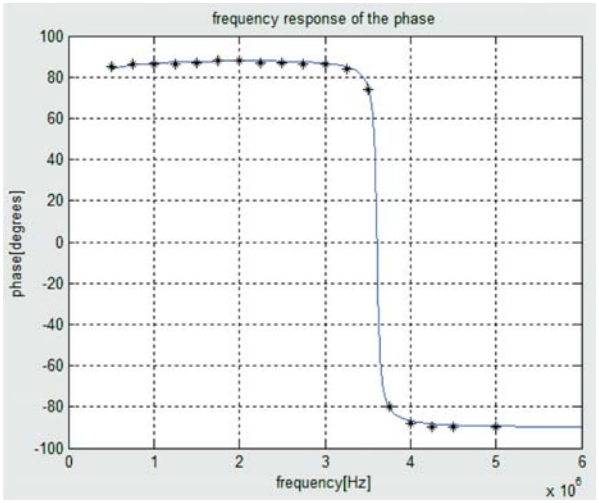

Fig. 7 Frequency response of the phase of an inductor

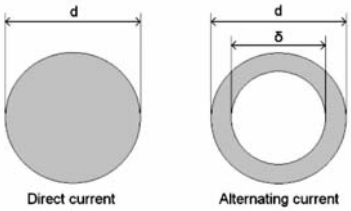

Fig. 8 Skin effect influence

For calculation of skin effect influence formula (6) may be used where $R\sim$ is resistance of inductor with applying skin effect, R is resistance of a wire, d is diameter and δ is skin depth (7).

$$R_{\sim} = R\frac{d}{4\delta} \tag{6}$$

The skin depth is defined by formula (7) where material parameters of a wire such specific resistance and permeability of copper are used [4].

$$\delta = \sqrt{\frac{\rho}{\pi.\mu.f}} \tag{7}$$

Total resistance of inductor is defined as addition of wire resistance R_{dc} and skin effect resistance $R\sim$.

Frequency response of the impedance and frequency response of the phase with applying skin effect influence are displayed in Figs. 9 and 10. The black points in these figures are measured values of impedance and phase of a real inductor. In Table 2 are displayed results of algorithm like resistance, capacity and inductance without and with applying skin effect influence.

Results Tab. 2

Skin effect influence/component value	Without skin effect	With skin effect
Resistance [Ω]	48.496	49,804
Inductance [mH]	14.61	14.61
Capacity [nF]	133.15	133.15

4. Conclusion

The model of inductor with algorithm of differential evolution based on measured values of impedance and phase of frequency characteristic was created in this experiment. The resistance found by DE algorithm was comparable with the resistance of real inductor with applying skin effect influence to the model of this inductor. By the similar advancement equivalent capacitor parameters can be found.

Acknowledgement

This project was supported by the Vega grant No. 1/0375/08 of Ministry of Education of the Slovak Republic, EU.

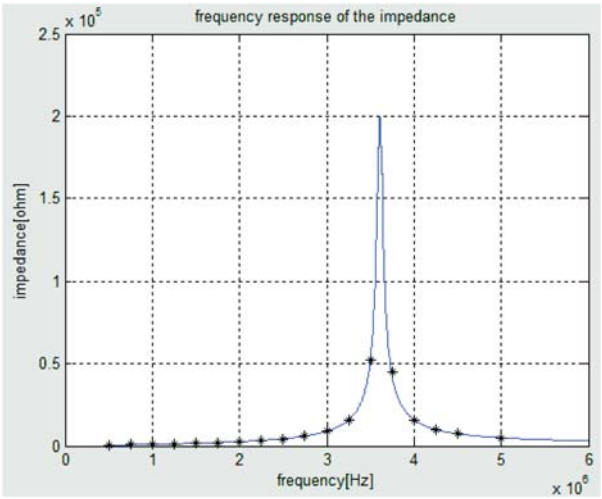

Fig. 9 Frequency response of the impedance of an inductor

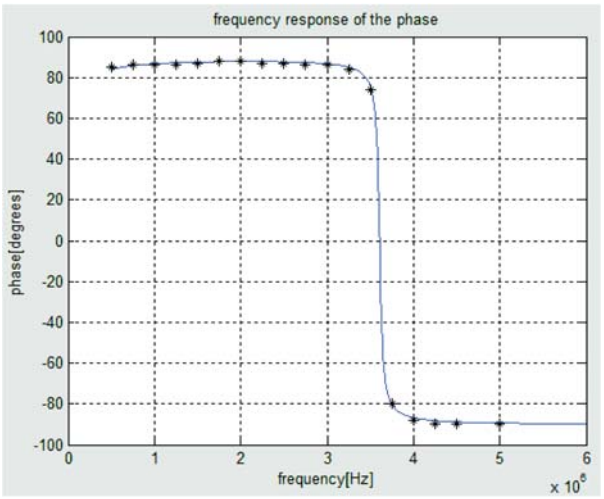

Fig.10 Frequency response of the phase of an inductor with skin effect influence

References

[1] PALECEK, J., VESTENICKY, M.: *Real Passive Components Parameters Finding With Genetic Algorithm,* Proc. of the 8th Int'l Conference ELEKTRO 2010, Zilina, Slovakia, 2010, ISBN 978-80-554-0196-6.

[2] LUCKA, M., PIECKA, S.: Multi-threaded ant Colony Optimization with Asynchronous Communications for the Vehicle Routing Problem, *Communications - Scientific Letters of University of Zilina,* Vol. 4, 2010, ISSN 1335-4205.

[3] LUDWIG, R., BOGDANOV G.: *RF Circuit Design: Theory and Applications,* New Jersey, USA, 2009, ISBN 978-0-13-147137-5.

[3] TICHA, D., MARTINEK, P.: *OTA-C Lowpass Design Using Evolutionary Algorithms,* Proc. of the 2005 European Conference on Circuit Theory and Design. Cork, University College Cork, 2005, Vol. 2, p. 197–200.

[4] STORN, R.; PRICE, K.: Differential Evolution - a Simple and Efficient Heuristic for Global Optimization over Continuous Spaces, *J. of Global Optimization 11*, pp. 341–359, 1997.

[5] PRICE, K., STORN, R. M., LAMPINEN, J.A.: *Differential Evolution: A Practical Approach to Global Optimization* Springer, ISBN 978-3-540-20950-8, 2005.

[6] KUNDERT, K.: Modeling Skin Effect in Inductors, *The Designer's Guide*, 2006.

Jan Slezak – Juraj Spalek *

INCREASE SAFETY OF TRAFFIC CONTROL ON THE MINOR RAILWAY-TRACKS

The paper aims at detecting the existing safety risks on the minor railway-tracks being operated in accordance with the provision CD-D3 of the Czech Railways, and at providing the solutions and technologies suitable for the mentioned minor railway-tracks. These tracks are currently equipped with out of date safety related systems monitoring the railway, whose operation depends purely on human factor. The latest railway accidents were reported just on these low traffic frequency tracks.

1 Introduction

This study aims at providing the solutions and technologies for the minor railway-tracks currently operated according to the provision CD–D3 of the Czech Railways. The above mentioned tracks are characterized by a minimum number of safety related devices - as for the infrastructure, by the track offices not operated by the railway personnel and by the absence of the communication lines in the form of the track combined cables along the whole length of the railway track.

2 Current State of Traffic Control on the Minor Railway-Tracks

The current trend in the field of the safety related technologies is aimed at their development and the subsequent introduction in association with the main railway-tracks with the sufficient intensity of the railway traffic frequency. As for the economic aspect, the usage of these technologies on the low traffic frequency railway tracks is too expensive and non–profitable. As a result, these tracks are currently equipped with out of date safety related systems monitoring the railway, whose operation depends purely on human factor. The latest railway accidents were reported just on these low traffic frequency tracks.

Centralized controlling of the railway traffic on the integrated sequences or areas of minor tracks is not possible due to the currently used safety related systems. In order to be operated, this type of safety systems needs a high number of railway employees whose working capacity is not fully applied. Meanwhile, the maintenance of the outdated safety systems is time consuming and economically ineffective. Consequently, there comes the necessity of the low frequency railway track safety system innovation. With particular respect to the facts mentioned above, the philosophy and structure of the low frequency tracks safety system must be different from the system solutions used on the corridor tracks. The safety system solutions on such tracks can be basically approached in two different concepts.

- The first concept consists in building simple safety systems based on the principle of track permissions among the particular track offices, since frontal collisions of trains usually imply tragic consequences. To apply this concept, it is essential to provide and maintain the necessary infrastructure corresponding to the minor railway tracks i.e. laying cables (or using the cables already laid), and at least the minimal outside safety system (departure signal devices, axle counters etc.). With reference to the fact that the tracks, operated in accordance with the provision CD–D3 of the Czech Railways, rank among those whose future is disputable (i.e. the tracks are being closed, their owners are being changed due to the assignments to private subjects, municipalities etc.), the present owner is not definitely guaranteed the infrastructure investment return. Since the afore-mentioned reasons and the analysis of the issue are not considered to be the subject matter of this study, they shall not be dealt with in the ongoing chapters.
- The second concept consists in transferring the safety system management from the infrastructure section to the vehicle section. Due to the considerable technical advance in the fields of telecommunications and new technologies based on satellite navigation, such concepts are prospective. The principle of these concepts is based on the fact that the directives and track permissions from the system operator are transmitted via available data networks directly to the vehicle in the front of the train, not to the safety devices of the track infrastructure. The currently used safety systems placed in the track offices are either operated or can even be removed. The solution proposed obviously provides the possibility of transferability to another track, in case the current track is temporarily closed. The aspects of such approach are dealt with in this study.

* **Jan Slezak[1], Juraj Spalek[2]**
[1] Railway Research Institute, j.s.c., Czech Republic, E- mail: slezakj@cdvuz.cz
[2] Department of Control and Information Systems, University of Zilina, Slovakia

The study is based on the basic distinction of the two terms "safety improvement" and "consequence elimination", which is a prerequisite of this study. While the notion of safety improvement assumes that the device itself eliminates the risk of danger leading to an accident, the notion of consequence elimination assumes that the consequences of the risk accrued are relieved by means of technologies i.e. stopping the vehicle, or more vehicles (trains) if any of the moving vehicles is involved in the accident with the track of another vehicle. In terms of safety, the study does not deal with the aspects eliminating the possible consequences, but it deals with the technologies enabling a real safety improvement. However, the usage of factors leading to the consequence elimination is considered within the safety improving devices.

3 Radio Block Descriptions

Radio block is a technical device enabling controlling and monitoring of the railway traffic within the defined area in the form of authentic transport permissions reported to the leading railway vehicle (VDV), i.e. the driving and pilot vehicles by means of movable wireless network transferring data information and monitoring the railway vehicles track according to the permissions issued.

Radio block consists of the following subsystems:
RBC – radio block central
RBV – vehicle part of the radio block
Wireless transmission network

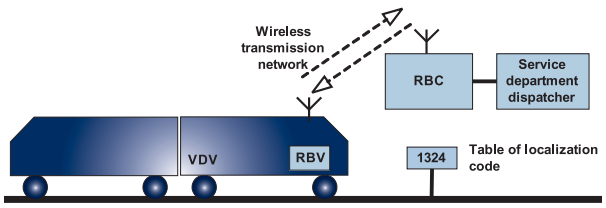

Fig. 1 Principle of the radio block system

According to the level of ability to monitor the vehicle movement by means of radio block, the radio-block devices can be categorized to several levels, while the lowest RB 0 provides the minimal functions as stated in the chapter 4.

RB 0+ level provides the functions equal to those of RB0. The only difference detected consists in the fact that some of the safety critical functions (answer-back signal, vehicle answering and its movement in the area in compliance with the corresponding permission) performed by only human operation on the RB0 level, shall be completed by the functional check via the satellite navigation (SN) on the 0+ level.

4 Basic Functions of the Basic Parts of the Radio Block

4.1 Radio Block Central

- RBC acquires information on the state of the single elements and systems of the safety devices, it processes the information to the form applicable in the process of checking and controlling the travel of the vehicle, it secures the data authenticity conditions and their communication with the vehicle on the radio block via wireless network. The information on the state of the particular elements is provided by the safety system (YXL- station interlocking system, LX- level crossing).
- RBC performs the information authenticity check (in compliance with the EN 50 159-2) received from RBV via wireless transfer system, the information acquired is further evaluated and used in the process of controlling and securing the traffic.
- Displays the information acquired from RBV, YXL, LX, units on the operator's control board and enables to control the entire process of traffic.

4.2 Vehicle Part of the Radio Block

- RBV performs the authenticity control of the information received from the RBC via the specialized module
- RBV evaluates the information received from the RBC, safely displays its importance to the engine-driver and sufficiently ensures the vehicle travel monitoring with respect to the information received, all of the aforementioned is provided in the form of commands addressed to the vehicle control system.
- Receives the information on the vehicle position entered by the engine-driver via driver machine interface (DMI) within the vehicle localisation and transmits the information via the wireless data network to RBC.
- In the form of answer-back signals, the RBC provides the information necessary for cancelling the planned drives and for checking the availability of the particular track sections.
- RBC takes over the information on the movement (or waiting) of the vehicle acquired from the vehicle system.
- In the defined modes of the VDV, the RBC checks the availability of the key in the radio-block locks.

4.3 Wireless Transmission Network

- The network mediates the data communication between the RBC and RBV.
- It can as well provide voice connection between the operation point and the other mobile receivers, or among the mobile receivers themselves.

Note: In order to achieve voice connection, different wireless transmission networks can be used. If constructed, the communication connection on the unswitched network is used in case of wireless transmission network failure

A coherent coverage by the wireless transmission network along the track in its whole length is not required by radio block. Data communication is required in track offices. The availability of the voice communication on the entire track as well, is not a condition of the traffic on the track. The date authenticity in compliance with the EN 50 159-2 shall not be ensured by the transmission network, but by the safety communication modules of the final receivers' devices.

5 Possiblities of Radio Block Use

The radio-block device of the RB 0+ level is intended to use on the minor tracks characterized in the chapter 6, it enables:

- Traffic safety improvement on the tracks equipped with the movement permission for VDV monitor – in the form of the vehicle movement permission delivery. The permissions are issued in RBC on the ground of the information provided by the safety devices (YXL, LX), the information from the driven vehicles and the commands given by the dispatcher on the utility point. In case of the track offices not equipped with signalling devices, the permissions displayed to the engine driver on the DMI VDV replace the signals of the system signalling devices. If the system signalling devices are present on the track (signalling lights, flashing lights of the cross switches...) they are considered as effective.
- Displaying the reception and the range of the corresponding permission (to drive or to shift) in the form of a text message, and being confirmed by the engine driver, it enables the transition of the VDV to the appropriate mode of the vehicle movement.
- Completing the displayed permission by text messages on the restraints possibly occurring on the track the permission was issued for. The danger of neglecting the handover of the command is thus eliminated (as the information so far transmitted to the engine driver in written via RB 0 is transmitted in this way), and the RB qualities are considerably improved.
- Implementing at least a marginal test of the vehicle inquiring the vehicle conduct in accordance with the given commands. The vehicle command check consists in the following: VDV with an active RBV is allowed to move only upon an authorization of RBC, i.e. after receiving and accepting the corresponding command on the vehicle. If there appeared a vehicle movement in the absence of such authorisation, the RBV issues the command stopping the vehicle. RBV does not check if the real vehicle speed corresponds to the actual speed limit, the speed limit in the particular track sequences permitted by the command is even not displayed to the engine-driver. The engine-driver follows the traffic signals or the track signalling devices, if present. In some case, when the different speed according to the track needs to be distinguished, the defined speed is transferred to the vehicle by means of restraints together with the permissions.
- The RB 0 level does not permit the check of the aim defined by the permission issued. Whereas, such a check is permitted by the RB0+ level within the extent as follows. In the SR (mod Staff Responsible) and IS (mod Isolation) module, and in case of vehicles without RBS, the currently transmitted data permission from RBC is commonly replaced by the dispatcher's voice permission – pursuant to the information on the VDV vehicles provided to RBC by the dispatcher.
- In respect of the RB0+, the SN monitors if the vehicle with an issued permission is moving in the area covered by the permission (MA-movement authority, SH–shunting, JOV– ride of the service rail-switch), and if the data on the vehicle position entered by the engine driver (answer-back signal) comply with the vehicle's position ensured by the SN devices. In case of any discrepancy, the engine driver is given a warning by an acoustic or optic signal.
- By means of the RBC point the vehicle movement is monitored via the vehicle localisation referred by the engine driver entering the numerical code of the position (number of the localisation section). With respect to the answer back signals, the automatic cancel of the given drives on the RBC.
- Issuing an emergency command to stop the VDV by the RBC, this serves as a prompt solution of stopping the vehicle in case of an impending danger.
- Minimizing the needs of the safety system infrastructure parts by means of providing the technical check of the lockable cross-switches key in the particular track offices in the RBC via the lock on the VDV checked in the RBV.

6 Characteristics of the Tracks Suitable for the Radio Block Usage

The radio-block technical devices must be selected in the way enabling the radio-block application on the tracks conforming to the characteristics as follows:

- Single track line in an arbitrary traction.
  Recommendation: The drive in the controlled sequence is enabled mainly by the VDV equipped with RBV. The vehicles not equipped with the RBV system are allowed only exceptionally.
- The traffic before the RB implementation is simple, defined by minimal over-taking, the shifts being secured by the train crew.
- The maximum number of the track offices in the area controlled by one RBC unit is 35, whereas there is a possibility of integrating up to 35 offices from four different tracks, however there shall be the safe traffic organisation among the given track within one RBC unit secured.
- Track speed: RB0 – max. 60 km/h, RB0+ – max. 90 km/h. The given speed limit may be restricted due to the construction and the cross-switches criteria and safety parameters.
- The number of VDV signed up in the system (within one RBC unit) is max. 16.
- The monitored area (sequences between the stations, station gridiron and the track point disposal's tracks) does not imply the necessity of being equipped with the signalling devices. In case any of these track sequences are equipped with the signalling devices, these can be integrated in the RBC functions.
- The trains shall not necessarily be equipped with the devices securing the vehicle integrity, however such devices are recommended.

- In case the train involves more driving engines, or one or more control engines, only one of the driving engines shall be considered VDV and therefore it shall be controlled by the RBC.
- VDV unit shall be equipped with the KBS (vigilance of driver) device providing the edge to the electromagnetic valve of the service brake.

Note: RB 0 ad RB0+ is therefore intended for the tracks used with respect to the provision CD – D3, while the usage of RB0+ is recommended.

7 Radio Block Principles

The voice communication between the engine driver and the operating dispatcher is replaced by the secured wireless data communication of the terminal points – RBC and RBV, which brings the elimination of errors in the process of the data transmission and reception.

The RBC monitors the dispatcher's activity and disables the usage of conflicting driving tracks. GDV modifications, delays, changes in the train crossings do not have any impact on safety, while the RBC can command and check the external interlocking systems factors.

RBV further monitors the engine driver's activity and disables the drive (shift) of the VDV without RBC permission. It provides a continuous display of the permission including the LX restraints in the field of vision. RBV addresses warnings to the engine driver in case the engine leaves the authorised section defined in the given permission (the train is stopped) and finally the RBV checks the state of the cross-switch keys.

Principle of assignment movement authority and conferment of an answer – back signal from train is illustrated on the figure number 2. Chronology of award procedures is obvious from the numbers in the picture.

8 Conclusion

The newly proposed RB system complying with the provision CD–D3 of the Czech Railways represents a higher level of traffic safety standards. The RBC and RBV devices are examples of safe traffic. The dispatcher's activity is continuously monitored by the system (in the course of the data entering, through driving the engine, shifting...). The communication between the dispatcher and the engine driver as provided by the RB system shall be realised mainly as data communication (the main technical medium of the traffic safety systems as defined by the provision CD–D3 consists in voice communication between the dispatcher and the engine driver by means of wireless network directly from the engine cabin, or on the line from the track office). The proposed RB system, as well as communication in the system, considerably contributes to the general traffic safety improvement.

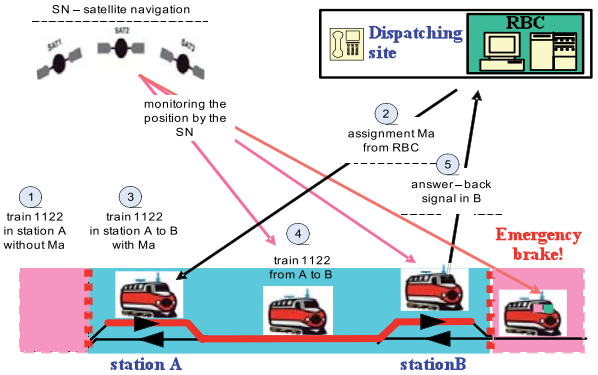

Fig. 2 Principle of assignment movement authority and conferment of an answer – back signal from train

List of Abbreviations Used in This Publication

CD-D3	provision of the Czech Railways
DMI	driver machine interface
IS	mod of system radio block – Isolation
JOV	mod of system radio block – ride of the service rail-switch
KBS	vigilance of driver
LX	level crossing
MA	movement authority
RB	system radio block
RBC	radio block central
RBV	vehicle part of the radio block
SH	mod of system radio block –shunting
SN	satellite navigation
SR	mod of system radio block – Staff Responsible
VDV	leading railway vehicle
YXL	station interlocking system

References

[1] Czech Railways: Provision of Simplified Control of the Railway Traffic, CD-D3, Official edition, Olomouc: JERID, 1997.
[2] FRYBORT, Fr.: Definition of System and Conditions of Use RB 0+, version 1.05, AZD Prague, 2007.
[3] SLEZAK, J.: Safety Conception of RB-net, version 1.13, VUZ Prague, 2009.
[4] ROFAR, J., FRANEKOVA, M., HOLECKO, P.: Modelling of Safety Characteristics of Redundant Safety-Related Transmission System via Markov's Analysis, *Communications - Scientific Letters of the University of Zilina,* Vol. 12, No. 3a, pp. 93–96, ISSN 1335-4205.
[5] RASTOCNY, K., FRANEKOVA, M.: Modelling in Development of Safety-related Communication Systems, *Communications - Scientific Letters of the University of Zilina,* No. 1, 2008, pp. 24–30, ISSN 1335-4205.

Tatiana Strapacova – Klara Capova – Ladislav Janousek *

ARTIFICIAL HEART VALVE INSPECTION USING EDDY CURRENT TECHNIQUES

This paper discusses about minimally invasive techniques to detect the single leg fracture in special type of artificial heart valve called Bjork Shiley Convexo - Concave (BSCC). The fracture affects the outlet strut of these artificial heart valve and it is needed to detect it. For this purpose the electromagnetic methods based on eddy current testing were used. The coils are excited in the selected range of the frequencies for identification of the fractures in the outlet strut. The fractures occurring in BSCC heart valve and their numerical simulations are described. The results obtained with a prototype setup are presented and they demonstrate the usefulness of described techniques for detection of the outlet strut fractures in BSCC artificial heart valve.

1. Introduction

Dysfunction of the heart valves is a common complication after heart valve diseases. When the symptoms become intolerable for a normal lifestyle, the normal course of action is to replace the damaged valve with an artificial one. These prosthetic valves are usually made from metal and are called – mechanical ones or they are made from biological tissue. The special type of mechanical heart valve prostheses is a Bjork-Shiley Convexo Concave (BSCC) heart valve which was introduced in 1979. BSCC heart valve has been used to replace the aortic or mitral valves and the design was developed in order to improve the hemodynamic and to reduce the risk of thromboembolism. This model of the heart valve became the subject of a lawsuit because it was shown to malfunction, usually fatally, in a number of cases. During the eight years that the valve was on the market, approximately 86000 valves were implanted in to patients. Six hundred and fifty valves experienced outlet strut fractures. As a result, the opportunity to evaluate the state of the BSCC heart valve, a non-destructive test of each individual valve may help to detect the fractures presented in outlet strut and so precede the damage of the valve.

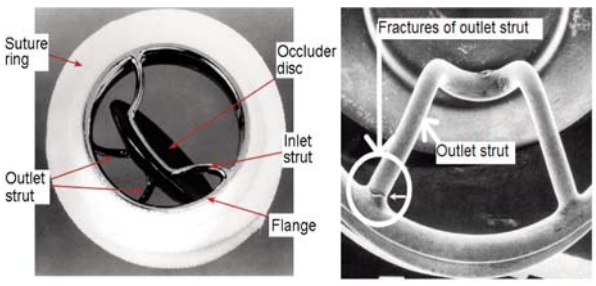

Fig.1 Typical design of the BSCC heart valve with fracture at the outlet strut [1]

The BSCC valves have a carbon occluder disc held in place by two metallic struts. Of the two struts, the inlet strut is integral to the valve suture ring, while the other strut called the outlet strut is welded to the suture ring, Fig. 1 [3]. Artificial heart valves are engineered devices which must be designed to survive more than 40 years of operation. Furthermore, the process of cyclic slamming open and shut of the occluder disc during heart function subjects the valve to percussive impact stress, which can cause fatigue failure. These failures have been observed at the outlet strut flange junction near or at the weld. The failure of both struts allows for dislodgement of the occluder disc and embolization of the disc. A dual strut failure results in abrupt onset of dyspnea, loss of consciousness, or cardiovascular collapse due to embolization of the disc and acute severe valvular regurgitation. Patient with strut fracture of aortic prosthesis dies in minutes, but those with strut fracture of mitral prosthesis may survive long enough to undergo valve replacement. Several types of mechanical BSCC heart valve failure have been reported in literature

1. An outlet strut fracture (OSF), fracture of both legs of the outlet strut, the strut is completely separated from the flange
2. A single leg fracture (SLF), fracture of the one leg of the outlet strut, both ends grate against each other
3. A single leg separation (SLS), fracture of the one leg of the outlet strut, both ends of the fractured strut are separated, Fig. 1.

Although the function of the valve can continue under these conditions in points 2, 3, it increases the stress concentration on the intact end of the welded strut and it is not clear how long the other end of the strut can remain intact [1]. The period of the

* **Tatiana Strapacova, Klara Capova, Ladislav Janousek**
Department of Electromagnetic and Biomedical Engineering, Faculty of Electrical Engineering, University of Zilina, Slovakia,
E- mail: strapacova@fel.uniza.sk

time between the first and the second fractures is highly variable. Due to this fact there is a considerable interest, therefore, in development of methods for assessing the state of the valve in general condition of the outlet strut weld. In the present paper we propose electromagnetic techniques – eddy current testing (ECT) for non-destructive examination of the outlet strut of BSCC heart valve. To investigate the given problem, it is convenient to realize it with the aid of numerical simulation techniques.

2. Eddy Current Testing – ECT

Non-destructive testing (NDT) of conductive materials requires high reliability to detect cracks and defects in advance. ECT is one of the non-destructive techniques often used to detect them. In EC testing, the probe coil excited with alternating current is placed on an electrically conductive material (metallic biomaterial), eddy current are induced in the material. Presents of inhomogeneities, defect, variations in electrical conductivity, magnetic permeability, and geometry of the material, and lift- off, etc. disturb the eddy current flow and in turn, alter the impedance of the pick up coil. The change in impedance is usually measured and correlated with defect dimension or the causes producing it. In order to detect the defects sensitively, high frequency exciting currents or appropriate lift-off have to be applied. This method is applicable for surface or subsurface flaw detection because of significant decrease in magnetic flux and eddy current density with depth. The depth of penetration of eddy current is limited by skin-effect, which depends on operating frequency, material conductivity, and permeability [2]. The theoretical background of the ECT was given e.g. in [3] and [4].

3. Numerical Evaluation Using ECT – Model Configuration

Possibilities of the eddy current inspection of BSCC are investigated in the paper using numerical means. The commercially available software OPERA-3D based on finite element method is utilized for the purpose.

The problem deals with absolute coil type, placed above an outlet strut of BSCC heart valve replacement. The probe coil with dimensions, Fig. 2a, has axis-symmetric shape and has 10 turns. It is supplied with current density $J = 1$ A/mm^2. Simulations were performed with various settings of lift-off $s_1 = 1$ mm, $s_2 = 2$ mm, $s_3 = 3$ mm, $s_4 = 5$ mm (analogy to real motion of outlet strut in the real human body). Frequency of the driving harmonic coil signal was also changed from 10 kHz up to 500 kHz.

Properties of the investigated material, dimensions and electromagnetic parameters of the heart valve replacement were set according to the real dimensions and electromagnetic parameters of the heart valve replacements. The materials commonly used for the conductive heart valves replacement are Stainless steel 316L, CoCr -F 75, F 90 alloys and Titanium alloy -Ti-6Al-4V. For our simulation the BSCC heart valve was made from titanium alloy Ti-6Al-4V thus the conductivity was $\sigma = 1.4.10^6$ [S/m] and relative permeability $\mu_r = 1$.

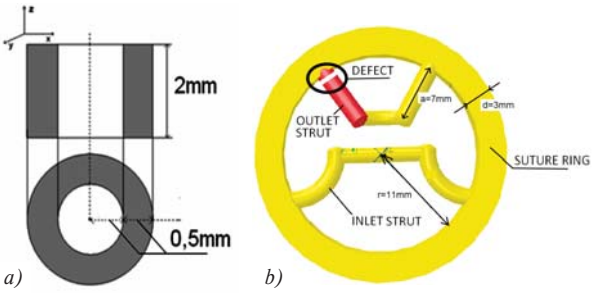

Fig. 2 a) Dimension of the coil, b) Dimension of the BSCC heart valve

The defect was localized on the one end of the outlet strut, Fig. 2b. The defect width was $w = 0.1$ mm, the defect depths were changed during inspection. The depths of defect were following $r_1 = 0.1$ mm, $r_2 = 0.3$ mm, $r_3 = 0.5$ mm, $r_4 = 0.7$ mm, $r_5 = 0.9$ mm. The defects occurs in direction of the outlet strut diameter. The diameter of the outlet strut was set $d = 2$mm. Material defect has zero conductivity $\sigma = 0$ [S/m]. The dimensions, orientation and depth of the defect were set up according to the real dimensions and depth of defect that affects outlet strut of BSCC heart valve. Such types of the defect can be presented as fatigue cracks.

Numerical simulations of the developed model are carried out to calculate the probe response signal. The finite element mesh of the simulated problem has approximately 3 million elements of two types, linear and quadratic ones. The following sections present the results.

4. Numerical Evaluation Using ECT with Helmholtz Coils – Model Configuration

The ECT with Helmholtz coils based approach was considered. The problem deal with Helmholtz coils placed on each side of the heart valve. These coils are configured to ensure the uniformity of the generated magnetic field. The excitation coils with dimensions, Fig. 3, are supplied with current density $J = 1$ A/mm^2. Frequency of the driving harmonic coils signal was changed from 10kHz up to 500kHz. The EM field excited by Helmholtz coils was oriented in parallel direction to the suture ring. The detection coil was positioned in distance lift-off = 1 mm above the outlet strut where the crack arises. The coil detect the perturbation of the generated field due to defect. The voltage induced in the detection coil was evaluated and the results are displayed on the Fig. 7.

5. Numerical Simulation Results the ECT Results

The material object (BSCC heart valve) and the coil with given dimensions were used for numerical simulation of eddy current evaluation. The depth of defect, lift-off and the frequency of the

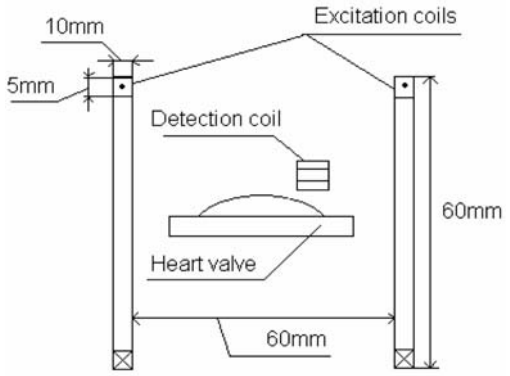

Fig. 3 Geometry of the electromagnetic system

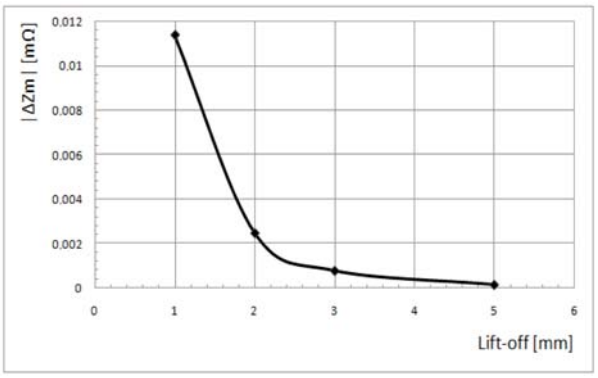

Fig. 5 Dependence of maximum impedance module on lift-off

driving signal were changed during the simulations. It represents 124 simulations realized. The $|\Delta Z_m|$ represents the difference amplitude impedance signal Zm from material with defect and without defect. The graphs, Fig. 4, were made with lift-off $s_1 = 1$ mm and $f_4 = 50$ kHz and the depths of defect were changed r_1, r_2, r_3, r_4, r_5 (as was mentioned in the previous chapter).

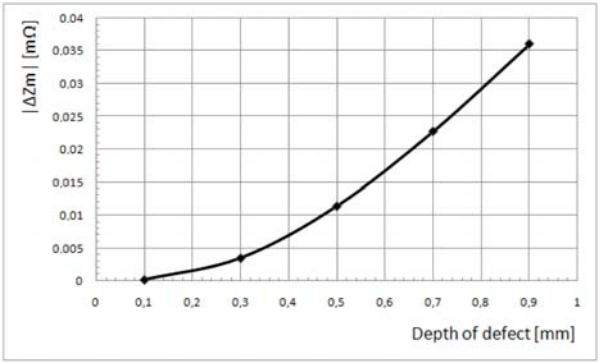

Fig. 4 Dependence of maximum impedance module on defect depth

From the obtained results in graphic form, Fig. 4, showing dependence of maximum impedance module $|\Delta Z_m|$ on the defect depth we can see that with increasing depth of defect also the maximum of impedance module is rising. From the different values of the $|\Delta Z_m|$ it is possible to determine the depth of defect. The points on the waveform for individual depths of defects are well-separated.

The following obtained results, Fig. 5 were calculated with depth of defect $r_3 = 0.5$ mm, exciting frequency $f_4 = 50$kHz and the lift-off was changed $s_1 = 1$ mm, $s_2 = 2$ mm, $s_3 = 3$ mm and $s_4 = 5$mm.

As can be seen from the Fig. 5, with increasing lift-off the $|\Delta Z_m|$ is decreasing. From the waveform, it is evident that the $|\Delta Z_m|$ fall to zero-value. From these results it is possible to determine the lift-off value which is necessary for the sufficient information value of the detected signal. The inductive component is dominant in the probe response signal and thus the dependence of the impedance phase does not show almost any differences for both results graph.

Regarding to these results and to the design of the valve the simulation of the heart valve evaluation for detection of SLF of outlet strut was performed. Because of the complicated design of the valve which does not enable to make a scan of the outlet strut the sweep frequency technique was chosen. According to Fig. 4, the simulations for different values of depth of defect were realized. The choice of the defect depth $r_5 = 0.9$ mm was given by largest difference between gained response signals. Results presented in Fig. 6 were performed for depth of defect $r_5 = 0.9$ mm (it represents SLF) and for lift-off $s_1 = 1$ mm. During the simulation the exciting frequency was changed from $f = 10$ kHz to $f = 500$ kHz (it represents the frequency sweep with discrete value of frequency). Fig. 6 shows the results of the simulation where the signal from SLF and IOS (intact outlet strut) represents two different waveforms.

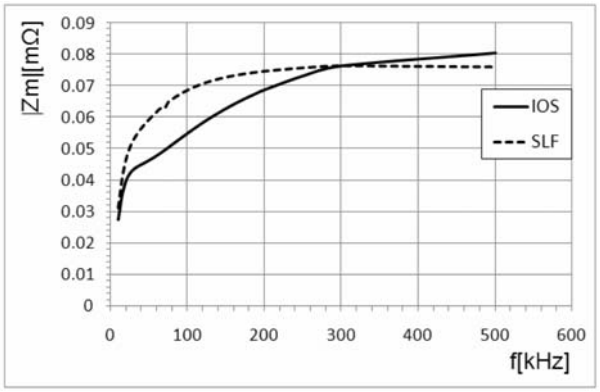

Fig. 6 Dependence of maximum impedance amplitude on frequency

The results show that the detected signal is different for the IOS and SLF valve because of different eddy current flow. This demonstrates that a SLF can be detected by the measuring of the detected signal variation in dependence on frequency. As can be

seen from Fig. 6, the difference in the dependences between the IOS response signal and the SLF response signal is largest in a frequency range from 70 kHz up to 150 kHz.

6. The ECT with Helmoltz Coils Results

Fig. 3 shows the simulation results of the electromagnetic system with connected the ECT method with Helmholtz coils shows. The obtained results, Fig. 7, were performed for lift-off $s_1 = 1$ mm and the excitation frequency of the Helmholtz coils was changed from 10 kHz to 500 kHz.

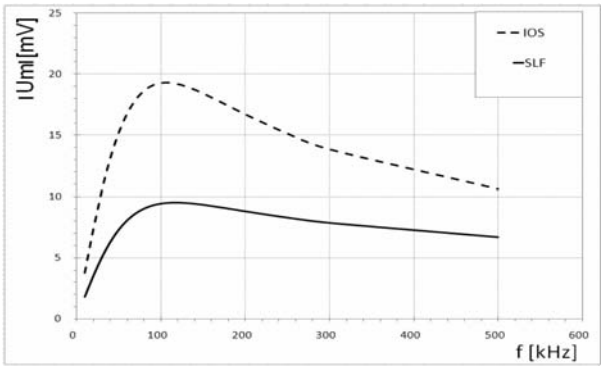

Fig.7 Dependence of the induced voltage amplitude on frequency

The results, Fig. 7, show that in the vicinity of the outlet strut, the magnetic field perturbations are different for the SLF and IOS heart valve. As can be seen, the magnetic field generated by Helmholtz coils and also the U_m response signal which was detected by detection coil are of a higher intensity. These results demonstrate that a SLF can be detected by measuring of the magnetic field changes.

7. Conclusion

This paper deals with two electro- magnetic techniques for detection of the SLF in BSCC heart valve. The numerical simulations results confirm that these methods are useful for this purpose. Both methods were presented for both surface and sub-surface cracks detection in conductive materials of the outlet strut. Material defects that can be present in BSCC prosthetic replacement were simulated and the obtained results were discussed. The main inspection parameters such as lift-off, depth of the defect and frequency of the driving coil signal were inspected and analyzed regarding to the coil impedance changes.

Acknowledgement

This work was supported by the Slovak Research and Development Agency under the contract No. APVV-0194-07. This work was supported by grant of the Slovak Grant Agency VEGA, project No. 1/0308/08.

References

[1] VAN NEER, P.: The Bjork-Shiley valve: *Detecting Broken Struts Using Standards Diagnostic Ultrasound Instruments,* MSc Thesis, 2005

[2] BRAUER, H., ZIOLKOWSKI, M.: Eddy Current Testing of Metallic Sheet with Defects Using Force Measurements, *Serbian J. of Electrical Eng.*, Vol.5, No.1, May, pp. 11–20

[3] CHAN SHIU C., YUE LI, UDPA LALITA, UDPA SATISH S.: Electromagnetic Techniques for Detecting Strut Failures in Artificial Heart Valve, *Electromagnetic Nondestructive Evaluation,* Vol. 26, Studies in Applied Electromagnetics and Mechanics, G. Dobmann, ISBN 1- 58603-594-0

[4] STRAPACOVA, T., CAPOVA, K.: *Influence of Selected Parameters on Detection of Heart Valves Outlet Strut Fractures Using ECT Method,* Int'l Conference AMTEE 2009, Cheb, ISBN 978-80-7043-821-3.

[5] JANOUSEK, L., MAREK, T., GOMBARSKA, D.: Eddy Current Non-destructive Testing of Conductive Materials, *Communications - Scientific Letters of the University of Zilina,* No. 8, 2006, pp. 29–33, ISSN 1335-4205.

Jiri Svarny *

THE MEASURING SYSTEM FOR EVALUATION OF PARAMETERS OF INTEGRATED MACH-ZEHNDER MODULATOR

The paper deals with some issues linked to practical application of the analog intensity electro-optic modulator of Mach-Zehnder type. An accurate adjustment and long-term stabilization of optimal operating point of the modulator belongs to the most severe problems linked to implementation of the appliance like this. The paper describes functionality of Mach-Zehnder modulator, highlights some of the problems the designer is faced to and presents the methodology that has been used to measure parameters of the modulator that are not specified in the manufacturer data-sheet and might be helpful to solve the problem.

1. Introduction

A specialized electro-optic remote-antenna system is under development at our department. The system should be able to transmit very weak and broadband analog signals via optical fibre. In terms of the most critical parameters there is a necessity: a) to cover the frequency range from virtual DC up to 2.5 GHz at least, b) to ensure 50 Ω matched input and output, c) to ensure high level of galvanic insulation between input and output, d) to achieve positive gain of the system and e) to maintain a high fidelity of transmitted signal. Probably the only way to achieve the features mentioned above simultaneously is to implement the system by using an external modulation technique. A simplified structure of the proposed system can be seen in Fig. 1. The broadband external modulating unit (Intensity modulator) forms its core and vital part. The modulating unit shall be based on the analog intensity electro-optic modulator of Mach-Zehnder type (MZM).

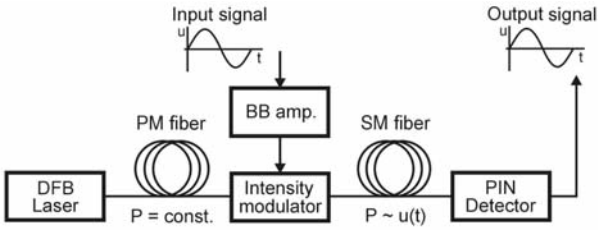

Fig. 1 Electro-optic remote antenna system

During the last few decades a lot of external electro-optic modulators have been developed and upgraded. Nowadays, some of them are even commercially available in integrated form. A modulator of Mach-Zehnder type belongs to the most mature ones. Basically, it can be described as two-arm interferometer integrated in convenient material. A $LiNbO_3$ substance seems to be the most widespread substrate in use, due to its good electro-optic features. The waveguide arms are made of indiffused titanium for example. Both the arms are connected by means of two Y-junctions, see Fig. 2. The junction Y1 is the input one and ensures balanced split of incoming light into the arms. The junction Y2 is the output one and thus recombines the outgoing light-waves.

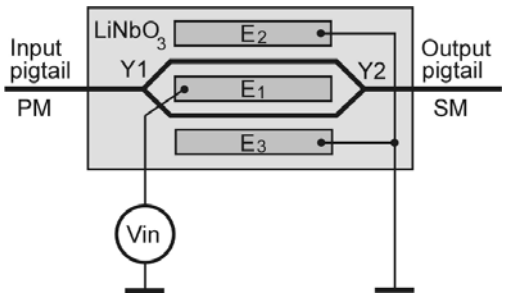

Fig. 2 Basic configuration of MZM

The integrated structure is equipped with system of electrodes (E_1, E_2, E_3) appropriately positioned above the waveguides. A voltage V_{in} applied across the electrodes induces electrical field around them and thus in the electro-optic material too. The field changes refractive index of the active material. The phenomenon produces the phase shift of the light waves travelling through the particular arms. Due to the recombination of the light-waves in the Y_2 junction, the interference of the light arises. If the phase difference between the waves is zero, the recombination is constructive and maximum amount of the light is leaving the output pigtail. If the phase shift difference is exactly 180°, the recombination is destruc-

* **Jiri Svarny**
Department of Technologies and Measurements, Faculty of Electrical Engineering, University of West Bohemia, Univerzitni 8, Plzen, Czech Republic, E-mail: svarny@ket.zcu.cz

tive and thus the outgoing light is attenuated maximally. By means of gradual transition between these two extremes, the smooth change of light intensity can be achieved. That is the way, how to modulate intensity of optical power by means of applied voltage.

2. Theoretical Background

Unfortunately, the MZM transfer function describing dependency of outgoing optical power P_o on driving voltage V_{in} is not linear.

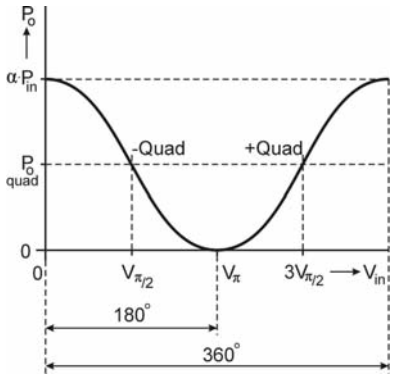

Fig. 3 Typical transfer function of an ideal MZM

In accordance with Fig. 3, the transfer function of the MZM can be described by means of cosine. The function (1) is periodical and the basic pattern (Fig. 3) repeats as the voltage V_{in} grows up,

$$P_o = \frac{P_{in}\alpha}{2}\left[1 + \cos\left(\frac{\pi V_{in}}{V_\pi}\right)\right] \tag{1}$$

where P_o and P_{in} are output and input optical power respectively, V_{in} is input voltage and V_π is so called half-wave voltage representing a value of V_{in} needed to change output power of MZM from one extreme to opposite one. The α-coefficient represents insertion loss of the modulator.

To operate the MZM properly, it is necessary to set-up the operating point by appropriate value of DC component of V_{in} (bias voltage V_{bias}). In case of analog optical link the desired value corresponds to the point, where the electro-optic gain is ultimate. The value of desired bias voltage can be found by substituting V_{bias} for V_{in} in (1), solving the second derivative of the function and putting it equal zero (2).

$$\frac{d^2P_o}{dV_{bias}^2} = -\frac{P_{in}\alpha\pi^2}{2V_\pi^2}\cos\left(\frac{\pi V_{bias}}{V_\pi}\right) = 0 \tag{2}$$

From the equation (2) a condition (3) can be derived, provided k is an integer.

$$V_{bias} = \frac{V_\pi}{2}(2k+1) \tag{3}$$

As far as the input voltage V_{in} is obtained as a superposition of DC bias voltage V_{bias} and modulating AC voltage V_{mod} (4) the function (1) can be decomposed to formula (5) [1].

$$V_{in} = V_{bias} + V_{mod} \tag{4}$$

$$P_o = \frac{P_{in}\alpha}{2}\left[1 + \cos\left(\frac{\pi V_{bias}}{V_\pi}\right)\cos\left(\frac{\pi V_{mod}}{V_\pi}\right)\right] - \\ - \frac{P_{in}\alpha}{2}\left[\sin\left(\frac{\pi V_{bias}}{V_\pi}\right)\sin\left(\frac{\pi V_{mod}}{V_\pi}\right)\right] \tag{5}$$

Provided the DC bias voltage V_{bias} is kept at optimal value (3), the formula (5) can be simplified to the form (6). The particular, desired operating point is called the quadrature point of the modulator.

$$P_o = \frac{P_{in}\alpha}{2}\left[1 - \sin\left(\frac{\pi V_{mod}}{V_\pi}\right)\right] \tag{6}$$

A setting of the operating point to the quadrature one brings next important benefit. Under the condition a supreme linearity of transfer function is achieved. If the modulating voltage is a low amplitude signal ($V_{mod} << V_\pi$), the function (6) can be rewritten in the linearized form (7).

$$P_o \cong \frac{P_{in}\alpha}{2}\left(1 - \frac{\pi V_{mod}}{V_\pi}\right) \tag{7}$$

In fact, there are some important differences between a simplified modulator depicted in Fig. 2 and a real, commercially available, integrated intensity MZM. The driving electrodes are usually separated into two systems in order to facilitate the implementation of the MZM. Typically one system serves as a DC bias port to adjust the operating point. The second system is connected to RF input and it is adapted to process AC high frequency signals up to several GHz or even tens of GHz (depending on particular model).

3. Problem Definition

In real situation the chart depicted in idealized figure Fig. 3 is shifted to the left or right alongside the V_{in} axes. The disproportion originates in difference between lengths of the waveguide arms and is caused by technological limits. In real application it is necessary to compensate the intrinsic offset V_{off} by additional adjustment of DC bias voltage. The value of particular offset is not specified in MZM data-sheet and has to be found by measurements.

Furthermore, even more severe problem originates in the fact that biased operating point of MZM suffers from infinite time-drift. The reasons for this behaviour are inherent in complex combination of pyroelectric, photorefractive and photoconductive phenomenon taking action in electro-optic materials of MZM devices [2].

Despite of rapid progress in development of MZMs, the impact of the phenomenon mentioned above has not been resolved in a satisfactory manner yet. That is why, the operating point has to

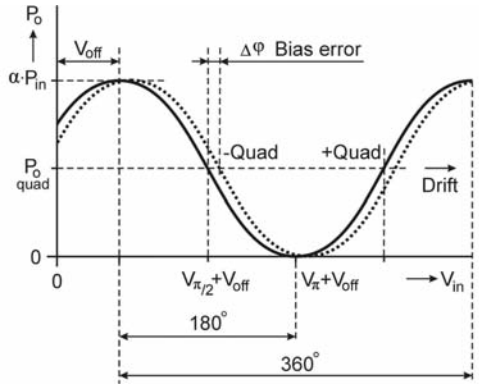

Fig. 4 The MZM transfer chart affected by intrinsic offset and time-drift

be monitored and adjusted from time to time. In case of long-term operating MZMs it is felicitous to implement some automatic feedback to adjust the operating point continuously. There have been developed various methods to keep the operating point at desired position. One of them is depicted in Fig. 5. The method works on principle of automatic adjustment of DC bias voltage in order to keep the value of average output optical power at constant level. For this purpose the optical power exiting the modulator must be monitored. Traditionally an optical tap coupler with external photodiode (PD) is used to sample small percentage of output optical power. Thanks to the linearity of the monitor PD transfer characteristic the current generated by the PD is proportional to the output power. The current is used as an input signal for the bias controller (Feedback circuit). The bias controller works as an efficient integrator. The integrated value of the monitor PD signal is compared to the desired predefined value and difference is used to adjust the bias voltage in proper manner.

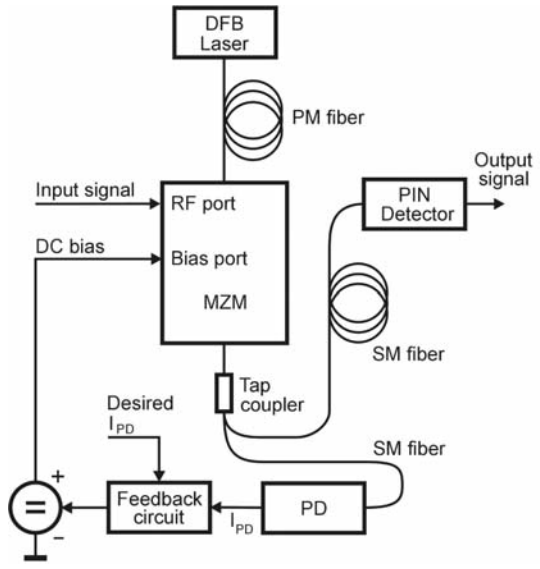

Fig. 5 Constant output power stabilizing method implementation [3]

Nowadays, some of the manufacturers provide modulators with integrated photodiode. The inner PD enables to monitor output optical power and the external tap coupler is no longer needed then. In that case the transfer chart of the inner PD as well as the PD responsivity represents very valuable information for development of prospective feedback system.

4. Experimental Part

The integrated intensity MZM, FA20 type [4] was chosen here as a key component of the system. It is a typical $LiNbO_3$ interferometric modulator with titanium indiffused waveguides. The device is tailored to work in infrared range from 1525 up to 1615 nm. The modulator is remarkable thanks to its low V_π voltage, low insertion loss and wide bandwidth (S_{21} 13 GHz for −3 dB drop). The model uses separated RF and DC bias ports and it is equipped with monitor photodiode integrated in radiating mode. That means the photodiode current decreases as the output optical power increases. The input pigtail is single mode, polarization maintenance (SM/PM) Panda fiber ended with standard, polished connector (SC/PC). The output pigtail is single mode (SM) fiber ended with SC/PC connector too.

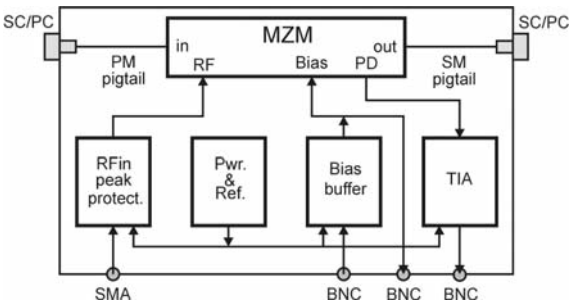

Fig. 6 The block diagram of the base-board of the MZM

There has been designed and developed testing base-board for the external MZM. The block diagram of the device can be seen in Fig. 6 and its final implementation is in Fig. 11. Its primary purpose was to provide safe measurements of parameters of the particular modulator because some of the parameters are not included in the data-sheet. Simultaneously, the board was designed in such a way it could be easily expanded in the future. It is expected that there will be necessity to equip the base-board with additional circuitry (broadband preamplifier of RF port, circuit for stabilization of operating point, etc.).

The base-board includes linear voltage regulator, reference voltage source, DC bias input buffer, the monitor photodiode transimpedance amplifier (TIA) with adjustable gain, protective circuits for RF port and GPO to SMA connector adaptor. By means of the appliance the value of responsivity of monitor photodiode, transfer characteristic of the modulator, $P_o = f(V_{bias})$ and monitor photodiode characteristic, $I_{pd} = f(P_o)$ were measured.

All of the measured charts and parameters were obtained using optical source that is expected to be an integral part of the future electro-optic remote antenna system. The optical source is thermally stabilized DFB laser that was designed and manufactured during the previous stage of the project. It generates output optical power of 21.68 mW with long-term (3 hour) stability better than ±0.009 dB [5].

While measuring the characteristics the voltage V_{in} applied to the DC bias input was considered to be the only independent variable. In order to ensure mutual correlation among measured charts it was necessary to measure all the parameters with sufficient velocity (rejection of the bias drift influence). The ideal method is to measure all the charts in one go.

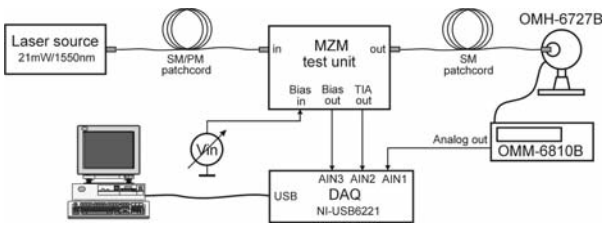

Fig. 7 The measuring system designed for evaluation of parameters of the MZM

That is why the measurements were done by means of system depicted in Fig. 7. The output optical power was measured by means of optical multimeter OMM-6810B equipped with OMH-6727B sensing head [6]. The multimeter disposes with analog output generating voltage that is proportional to the value of measured optical power. The output voltage was recorded by means of DAQ system NI-USB-6221 and PC working under LabVIEW application. Simultaneously, a signal from trans-impedance amplifier and DC bias voltage were recorded too. The RF input of MZM was unplugged. The measurements were done at the room temperature of 23 ±1 °C.

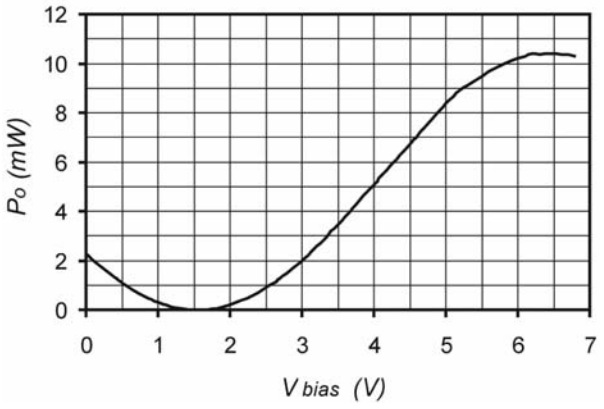

Fig. 8 The MZM transfer characteristic, $P_o = f(V_{bias})$, provided P_{in} = 21.68 mW

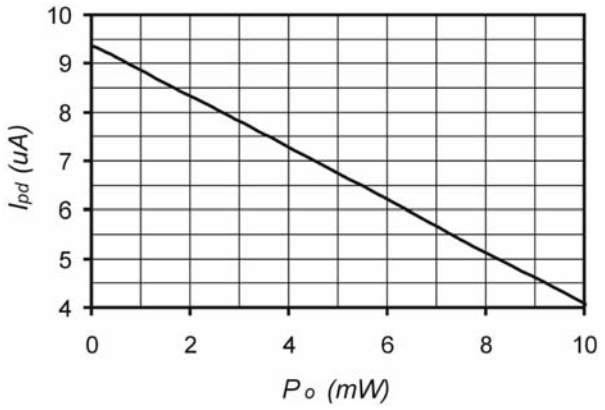

Fig. 9 Dependency of inner PD current on output power, $I_{pd} = f(P_o)$, provided P_{in} = 21.68 mW

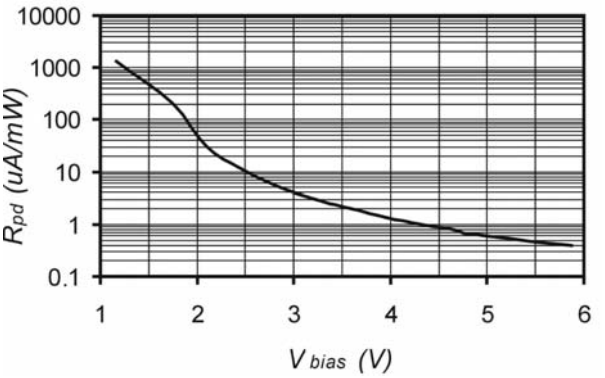

Fig. 10 Dependency of inner photodiode responsivity on set-up operating point, $R_{pd} = f(V_{bias})$

Consequently, charts depicted in Figs. 8, 9 and 10 were plotted using recalculated and measured voltages. The transfer chart view revealed that DC intrinsic offset is 1.55 V and output power related

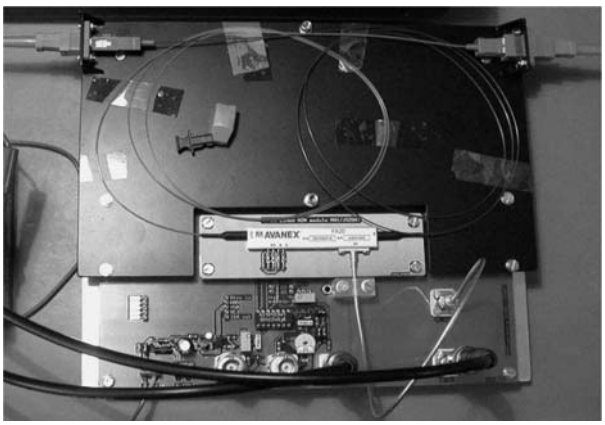

Fig. 11 The base-board with the MZM and auxiliary circuitry

to the quadrature point adjustment is around 5.2 mW. The dependency in Fig. 9 can be easily described by linear regression (8),

$$I_{pd} = \eta P_o + \delta\,, \tag{8}$$

where $\eta = -0.53$ μA/mW represents monitor photodiode relative gain and $\delta = 9.39$ μA is photodiode current in case of fully destructive recombination, provided $P_{in} = 21.68$ mW. Using data from Figs. 8 and 9, the chart describing dependency of absolute photodiode responsivity on position of operating point (represented by V_{bias} value) was obtained (see Fig. 10). The chart proves the correctness of measurements. Regard to the data-sheet values there is responsivity $R_{pd} = 1.3$ μA/mW at quadrature point. This value is in accordance with value found in Fig. 10.

5. Conclusion

Important parameters and information necessary to carry-on design of electro-optic remote-antenna system were acquired and verified. There was found the value of intrinsic offset of transfer characteristic. Furthermore, there was found average value of output optical power for quadrature point set-up. Insertion loss value ($\alpha = 0.5$) was verified too.

The measured transfer characteristic, $P_o = f(V_{bias})$, helped to specify demands on receiver of the electro-optic system. It is supposed that receiver should be designed as a passive one i.e. without any post-amplification. This precaution should help to improve both the flatness of the frequency response and the noise figure of receiving unit as well. That is why the receiver PIN diode should have capability to handle relatively high input optical power (up to 10 mW) and simultaneously be able to cover the desired frequency range up to 2.5 GHz. This strict requirement is driven by the effort to take a full advantage of high optical gain obtained by MZM unit.

Thanks to linear regression (8) the value of relative sensitivity of inner photodiode to changes of output optical power is well known now. This parameter is very important for design of prospective DC bias feedback loop. Consequently, final result can be declared: If the DC bias feedback system has to be able to keep operating point of the MZM with acceptable error, to say less than ±1°, it translates to necessity to maintain the photodiode current at value of 6.67 μA with fluctuations less than ±48 nA.

Acknowledgement

This work was financially supported by Research project MSM 4977751310 of Ministry of Education of the Czech Republic: "Diagnostics of Interactive Processes in Electrical Engineering".

References

[1] COX, C. H.: *Analog Optical Links-Theory and Practice,* Cambridge University Press, 2004.
[2] ACKERMAN, E., ROUSSELL, H., COX, C. H.: Bias Controllers for External Modulators in Fiber-Optic Systems, *Photonic Systems,* Inc. 2001. http://www.photonicsinc.com
[3] Photonic Systems, Inc.: *Modulator Bias Controllers Appl. Note,* http://www.photonicsinc.com
[4] Avanex, Inc.: *PowerLog™ FA-20, 20 GHz Analog Intensity Modulator with Small Form Factor,* Data-Sheet. http://www.avanex.com
[5] SVARNY, J.: *Highly Stable 20 mW Infrared Laser Source.* In Proc. Int'l Conf. Applied Electronics 2009, ISBN 978-80-7043-781-0, Plzen, pp 249–252.
[6] ILX Lightwave, Inc.: *Optical Multimeter OMM-6810B User's Guide, InGaAs Power/Wavehead OMH-6727B User's Guide.* http://www.ilxlightwave.com.

Martin Vestenický – Peter Vestenický *

LPG CONCENTRATION MEASUREMENT IN VEHICLES TRANSPORTING DANGEROUS GOODS

This paper describes the design of intelligent sensor unit for LPG (Liquefied Petroleum Gas) concentration measurement in the air. The sensor unit is a part of sensor network which has been designed for vehicles transporting dangerous goods. The described sensor unit uses sensor element based on SnO_2 structure which is vapoured on the aluminum substrate. Main part of the paper is focused on hardware solution of the sensor unit, signal processing applied on signal from its sensor element, compensation of air temperature and relative humidity influence on the sensor resistance and description of its application layer communication protocol.

1. Basic Conception of Inteligent Sensor Unit

The presented sensor unit is designed as an autonomous subsystem which is able to inform the onboard unit (OBU) – about concentration of LPG in ambient air. The sensor unit consists of analog sensor elements whose output signals are processed by microcomputer in real time (Fig. 1). The result values are transferred into master unit by using of CAN bus [1] and proprietary communication protocol on the application layer.

For LPG concentration measurement the sensor Figaro TGS 813 [6] based on the SnO_2 structure vapoured on aluminum substrate was selected. The LPG influences the resistance of sensor. This influence can be modeled by formula (1), where A, α are constants for given type of LPG sensor, C is LPG concentration (in ppm) and R_{S20} is sensor resistance at temperature 20 °C and relative humidity 65 %. Moreover, the value of sensor resistance depends on air temperature and relative humidity. For compensation of their influences the sensor unit is equipped with temperature sensor and relative humidity sensor. The compensation of LPG concentration is being performed in real time by microcomputer software which uses mathematical apparatus described in next text.

$$R_{S20} = A \cdot C^{-\alpha} \tag{1}$$

2. Measurement of LPG Concetration

The LPG sensor element is connected into the microcomputer in accordance with schematics in Fig. 2. The LPG in ambient air influences its resistance so that measurement of LPG concentration is changed to measurement of sensor resistance. Therefore the sensor element is connected as a part of voltage divider with variable ratio of division together with resistor R_M. Input of the divider is connected to the supply voltage U_{CC}. The voltage U_{RM} from resistor R_M is connected to the input of A/D converter whose reference voltage is connected to U_{CC}, too. Therefore the resistance of sensor element can be calculated from formula (2). Voltage U_{RM} is measured by the A/D converter with resolution *rb* according to formula (3) where RES_{AD0} is the result of A/D conversion. Combining the formulae (2) and (3) the sensor resistance R_S can be calculated from formula (4). Note that the formula (4) is independent on supply voltage U_{CC}. This fact has positive influence on precision of measurement.

$$R_S = R_M \cdot \frac{U_{CC} - U_{RM}}{U_{RM}} \tag{2}$$

$$U_{RM} = RES_{AD0} \cdot \frac{U_{CC}}{2^{rb} - 1} \tag{3}$$

$$R_S = R_M \cdot \frac{(2^{rb} - 1) - RES_{AD0}}{RES_{AD0}} \tag{4}$$

The value of LPG concentration (in ppm) can be calculated according to formula (5) which comes out from (1). In the formula (5) the R_{S20} is resistance of sensor element after compensation of temperature and relative humidity influence. This compensation is given by formula (14). The constant R_0 is resistance of sensor element at $C = 1800$ ppm, $T_{MEAS} = 20$ °C and $RH = 65$ %. K and α are specific constants for the given type of sensor.

$$C = 10^{\frac{\log\left(\frac{R_{S20}}{R_e \cdot K}\right)}{\alpha}} \tag{5}$$

* **Martin Vestenický[1], Peter Vestenický[2]**
[1] Department of Telecommunications and Multimedia, Faculty of Electrical Engineering, University of Zilina, Slovakia,
E-mail: martin.vestenicky@fel.uniza.sk
[2] Department of Control and Information Systems, Faculty of Electrical Engineering, University of Zilina, Slovakia,

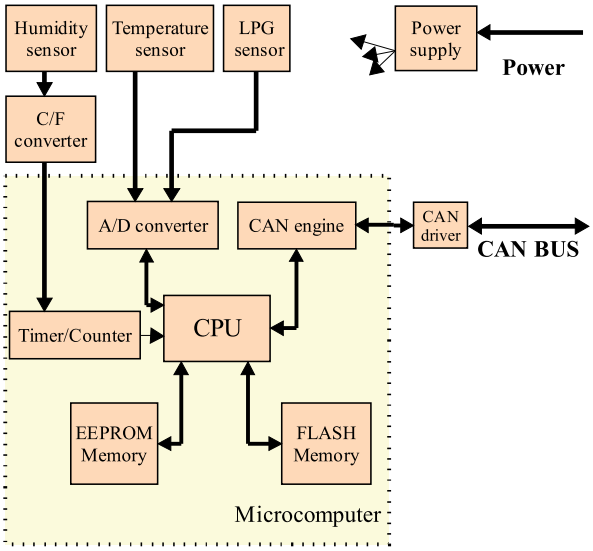

Fig. 1 Block diagram of LPG sensor unit

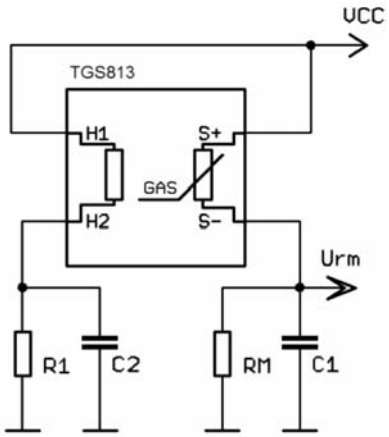

Fig. 2 Schematic diagram of the LPG sensor

3. Measurement of Relative Humidity

For measurement of relative humidity a capacitive sensor element Philips 2322 691 90001 was selected. Capacity C_S of this sensor depends on the relative humidity. Inverse function of this dependence is shown in Fig. 3 (points). This dependence can be approximated by polynomial function of the second order which is given by formula (6) – curve in Fig. 3.

Measurement of the relative humidity is converted to the measurement of capacity. One of the simplest but sufficiently accurate methods of capacity measurement is utilization of measured capacity as element which determines the frequency of oscillator. In the described sensor unit the oscillator with well known CMOS timer 555 was used. The signal of astable flip – flop circuit configured according to Fig. 4 has duty cycle 1:1 and frequency is given by formula (7) where $a_F = 1.4$ is constant and R_t is timing resistance (Fig. 4). The frequency of oscillator is measured by two timers / counters which are built into used microcomputer. The first timer/counter works as counter and the second one works as time base generator. Resultant formula (8) which goes out from (6) and (7) determines the relative humidity. Values of constants for the described sensor unit are summarized in Table 1.

$$RH = a_{C_2} \cdot C_S^2 + a_{C_1} \cdot C_S + a_{C_0} \tag{6}$$

$$f = \frac{1}{a_F \cdot R_t \cdot C_S} \tag{7}$$

$$RH = a_{C_2} \cdot \left(\frac{1}{a_F \cdot R_t \cdot f}\right)^2 + a_{C_1} \cdot \left(\frac{1}{a_F \cdot R_t \cdot f}\right) + a_{C_0} \tag{8}$$

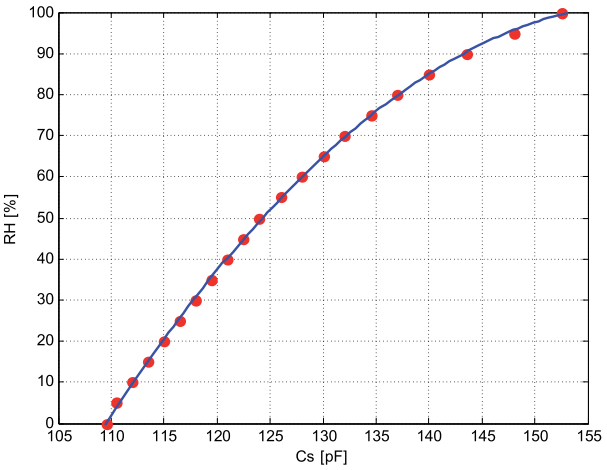

Fig. 3 Dependence of relative humidity on the sensor capacity and its approximation

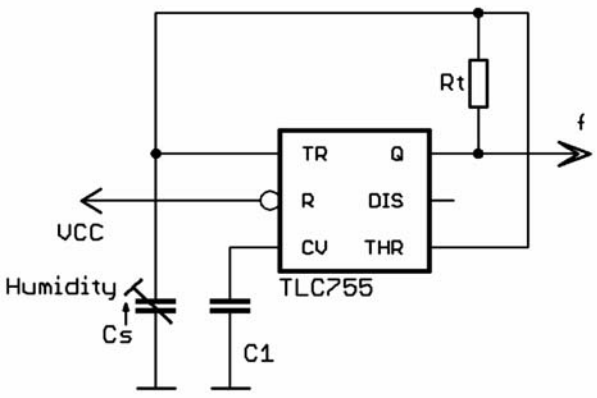

Fig. 4 Convertor of capacity to frequency

4. Measurement of Temperature

The temperature is being measured by linear temperature sensor LM335 (product of National Semiconductor Corp.) whose output voltage depends on absolute temperature linearly. This dependence is described by formula (9) where a_{TS1} and a_{TS0} are constants for the given type of sensor. The temperature sensor can be calibrated by proper selection of these constants [5]. Measured temperature can be calculated from formula (10). Taking A/D process into account (11) the resultant formula for temperature calculation is (12).

$$U_{TS} = a_{TS1} \cdot T_{MEAS} + a_{TS0} \tag{9}$$

$$T_{MEAS} = \frac{U_{TS} - a_{TS0}}{a_{TS1}} \tag{10}$$

$$U_{TS} = RES_{AD1} \cdot \frac{U_{CC}}{2^{rb} - 1} \tag{11}$$

$$T_{MEAS} = \frac{RES_{AD1} \cdot U_{CC} - (2^{rb} - 1) \cdot a_{TS0}}{(2^{rb} - 1) \cdot a_{TS1}} \tag{12}$$

5. Compensation of Temperature and Humidity Influence on the LPG Sensor

Since the temperature and relative humidity influence the LPG sensor resistance it must be compensated. The real temperature dependency of relative resistance (R_S/R_{S20}) of the LPG sensor with relative humidity as parameter is shown in Fig. 5 as points which are taken from [6]. This dependency is approximated by function of two variables R_H and T_{MEAS} according to formula (13) whereby constants for given sensor unit a_2, a_1, a_0, c_2, c_1 and c_0 are listed in Table 1. The result of approximation is depicted as curves in Fig. 5. The compensation function (14) is derived from the formula (13). Then the compensated value R_{S20} from (14) enables to calculate the LPG concentration from formula (5) if the temperature of air T_{MEAS} and the relative humidity R_H are known.

$$\frac{R_S}{R_{S20}} = (a_2 \cdot \ln(RH + 1) + c_2) \cdot T_{MEAS}^2 + (a_1 \cdot \ln(RH + 1) + c_1) \cdot T_{MEAS} + a_0 \cdot \ln(RH + 1) + c_0 \tag{13}$$

Values of constants for LPG sensor unit — Tab. 1.

α [-]	K [-]	a_{TS1} [V°C^{-1}]	a_{TS0} [V]
0.5413	57.82	0.01	2.73
a_F [-]	rb [-]	a_{C2} [F^{-2}]	a_{C1} [F^{-1}]
1.4	10	$-3.77 \cdot 10^{22}$	$1.21908 \cdot 10^{13}$
a_{C0} [-]	a_2 [°C^{-2}]	c_2 [°C^{-2}]	a_1 [°C^{-1}]
−882.9328	4.382·10-5	5.359·10-5	−0.003517
c_1 [°C^{-1}]	a_0 [-]	c_0 [-]	R_0 [Ω]
−0.007298	−0.1052	1.7970	1149
R_M [Ω]	R_t [Ω]	U_{CC} [V]	
4700	8200	5	

$$R_{S20} = \frac{R_S}{(a_2 \cdot \ln(RH + 1) + c_2) \cdot T_{MEAS}^2 + (a_1 \cdot \ln(RH + 1) + c_1) \cdot T_{MEAS} + a_0 \cdot \ln(RH + 1) + c_0} \tag{14}$$

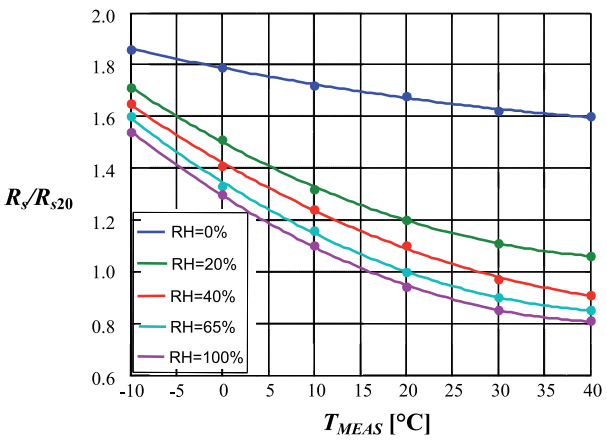

Fig. 5 Dependency of LPG sensor relative resistance on temperature and relative humidity

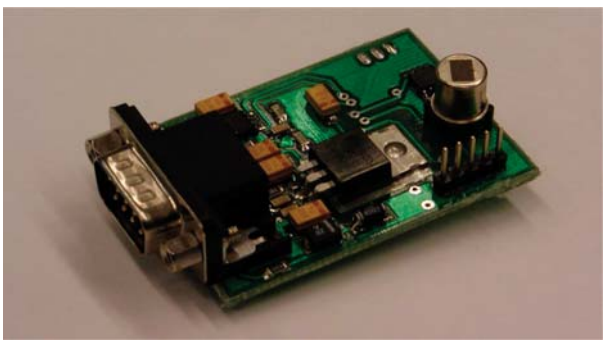

Fig. 6 Manufactured LPG sensor unit

6. Communication Protocol on the Application Layer

A simple communication protocol was designed for communication between sensor unit and the OBU. Standardized application protocols working on the CAN bus (CANOpen, DeviceNet) were not used for their complexity. The protocol is based on command

Structure of the PDU Tab. 2.

ID	D0	D1	D2	D3	D4	D5	D6	D7
SENS_ID	CMD_ID/ ANS_ID	MES_NBR	SENS_NBR_L	SENS_NBR_H	VAL_1_L	VAL_1_H	VAL_0_L	VAL_0_H

– answer principle. Protocol data units are transferred by using standard data frames with 8 octet data field in accordance to CAN 2.0A specification [4]. The PDU structure is given in Tab. 2. The CAN message identifier (11 bits) is used to address group of sensor units which measure the same quantity (000H – OBU, 010H – inclination sensors, 020H – pressure sensors, 030H – gas sensors, 040H – temperature sensors). The sensor unit uses CAN filter to select only the messages relevant for its group. The whole sensor network is addressed by message with identifier 000H. Individual sensors can be addressed on the application layer by the 16 bits sensor unit number SENS_NBR.

The command, answer or alarm is identified by the CMD_ID/ ANS_ID field (Table 3). Command parameters or measured values are transferred in the fields VAL1_L – VAL0_H. If longer message must be fragmented the field MES_NBR gives number of fragments (4 bits) and fragment order (4 bits). Fig. 7 shows an example of communication.

7. Conclusion

The described intelligent sensor unit (Fig. 6) was manufactured as a part of system for monitoring dangerous load transport [1, 2] which was solved within the international project Connect, subdomain 4.9 “Dangerous goods monitoring and information system” [3]. The method of LPG concentration measurement including compensation of temperature and relative humidity influences was implemented into firmware of the sensor unit.

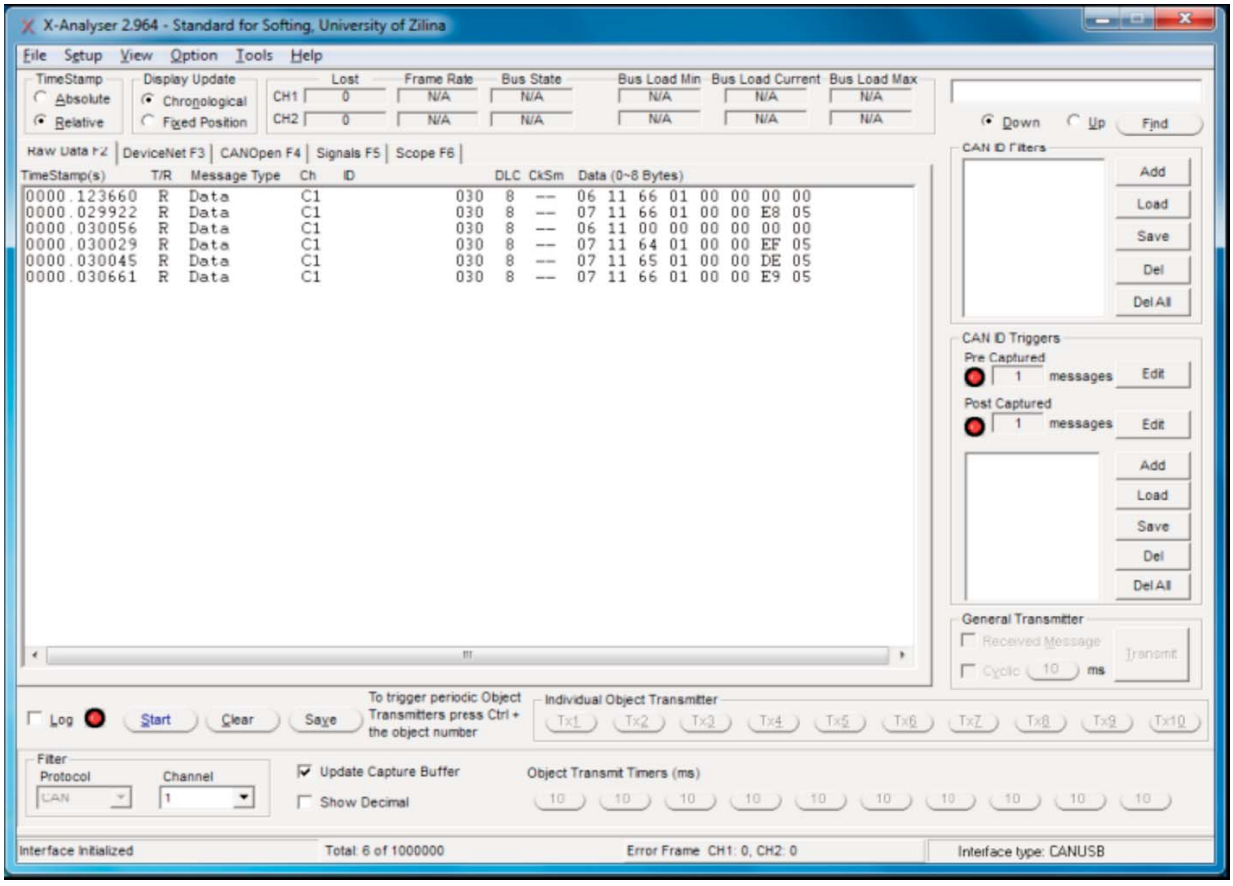

Fig. 7 Snapshot of CAN protocol analyzer

Definition of commands, answers and alarms Tab. 3.

CMD_ID/ ANS_ID	TYPE	Description
00H	CMD	Get sensor unique identifier
01H	ANS	Number of sensor unit
02H	CMD	Set number of sensor unit
04H	CMD	Get sensor unit status
05H	ANS	Sensor unit status
06H	CMD	Get actual sensor data
07H	ANS	Actual sensor data
08H	CMD	Set sensor limit value
0AH	CMD	Get sensor limit value
0BH	ANS	Sensor limit value
0DH	ALM	Upper limit exceeded
0FH	ALM	Lower limit exceeded
11H	ALM	Sensor error
12H	CMD	Sensor reset
13H	ANS	OK
15H	ANS	Error

For the test purposes three sets of master units and sensor networks (including sensor units for measurement of pressure, inclination, and temperature) were manufactured. The tests were performed on the territory of north Slovakia by staff of Transport Research Institute, Inc. and University of Zilina. Results of the tests prove full functionality of manufactured sensor unit prototypes. Next development will be focused on design of new sensor units, for example "black box" for road traffic accident analysis.

Acknowledgment

This work was created as a part of solution of international project "Coordination and Stimulation of Innovative ITS Activities in Central and Eastern European Countries – CONNECT", TEN-T Programme EC. Project number: Addition no. 3 to Contract no. 472/ VÚD 2002.

This work has been supported by the Grant Agency VEGA of the Slovak Republic, grant No. 1/0023/08 "Theoretical Apparatus for Risk Analysis and Risk Evaluation of Transport Telematic Systems."

References

[1] VACULIK, M., FRANEKOVA, M., VESTENICKY, P., VESTENICKY, M.: On-Board Unit and its Possibilities of Communications on Safety and Security Principles. *AEEE 7*, 2008, No. 1-2, pp. 235–238. ISSN 1336 – 1376

[2] VACULIK, M., VESTENICKY, P., VESTENICKY, M.: *Vehicle On-board Unit (in Slovak).* Proc. of Int'l conference ITS, Bratislava, 2007, ISBN 978-80-254-0207-8

[3] CONNECT, *Co-ordination and Stimulation of Innovative ITS Activities in Central and Eastern European Countries.* [online]. URL <http://www.connect-project.org/>

[4] CAN specification, Version 2.0. Robert Bosch Gmbh. 1991. [online] URL <http://www.semiconductors.bosch.de/pdf/can2spec.pdf>

[5] BLAGOJEVIC, M., PETKOVIC, D.: A New Approach to the Interpretation of Signals from Temperature Sensors. *Communications - Scientific Letters of University of Zilina,* Vol. 8, Nr. 4, 2006, pp. 57–60. ISSN 1335-4205.

[6] Figaro product information: *TGS 813 - for the detection of Combustible Gases,* rev. 9/02. [online] URL http://www.figarosensor.com/products/813pdf.pdf.

Jakub Vonkomer – Milan Zalman *

MRAS BASED SENSORLESS AND SENSOR VECTOR CONTROL AND SMOOTH TRANSIENT BETWEEN THEM

Dynamic control, like vector control is an essential feature of every modern AC drive. In some cases it might be very important to provide continuous operation in case of encoder failure. It further means that the transient between sensor vector control and sensorless vector control has to be smooth. To obtain that a modified vector and sensorless vector control algorithms were designed. To allow smooth transitions, both sensor and sensorless control share common flux model. In this paper a novel robust MRAS-based speed estimator based on error between current estimators output and measured current and modifications of direct sensor vector control are presented. Theoretical analysis of estimators and design of adaptation loop is described. Finally, simulation and experimental results are shown.

1. Introduction

As known, induction motors are still the most commonly used motors in the industry, thanks to their good performance and low cost.

Kinds of dynamic control of Induction machines, like Vector Control (Field Oriented Control) or Direct Torque Control have become standard feature of industrial AC drives years ago. Original structures require the using of mechanical speed sensors, but even at that time, the need for mechanical speed sensor elimination was important. During the last two decades many and many different methods and algorithms of speed estimation for vector control have been published; both for induction and synchronous machines [5]. But for high-performance control for speed or position systems still rely on mechanical sensor – quadrature encoder, selsyn, etc. And often it might be important to provide operation even in case of mechanical sensor failure.

In this paper we will focus on direct vector control with sensor feedback and adaptive structures of sensorless vector control – Model Reference Adaptive Structure (MRAS). Both of these structures share common flux model for providing continues, smooth transient between sensorless and sensor vector control.

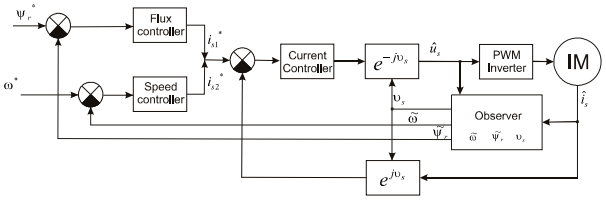

Fig. 1 Basic schema of proposed vector control structure

2. Sensor vector control

Proposed sensor vector control is a light modification of "classical" indirect vector control oriented on rotor magnetic flux reference frame to direct vector control. Basic component of proposed control structure is the current model for rotor flux estimation. This model is based on equation originally formulated by Blaschke (often known as Blaschke equation)[1]. This model is mostly used in closed-loop systems where rotor speed is known or at speed close to zero thanks to its reliability. Its main advantage comparing to voltage model of rotor flux is absence of pure integrators.

Current model for flux estimation in stator reference frame (α, β):

$$s\hat{\psi}_r = -\frac{1}{T_r}\hat{\psi}_r + j\omega\hat{\psi}_r + \frac{L_m}{T_r}\hat{i}_s \tag{1}$$

Current model for flux estimation in reference frame oriented to rotor position (*d*, *q*):

$$\hat{\psi}_r = \frac{L_m}{T_r s + 1}\hat{i}_s,\ T_r = \frac{L_r}{R_r} \tag{2}$$

Model for current estimation in stator reference frame (α, β):

$$\hat{i}_s = \frac{1}{R_1(T_1 s + 1)}\left(\hat{u}_s + \frac{k_r}{T_r}\hat{\psi}_r - j\omega k_r\hat{\psi}_r\right) \tag{3}$$

where:

$$R_1 = R_s + R_r k_r^2,\ k_r = \frac{L_m}{L_r},\ L_{s1} = \sigma L_s,\ T_1 = \frac{L_{s1}}{R_1}$$

Using estimator oriented to rotor position gains several advantages over estimator in stator reference frame. Main advantage is the decoupling of both (α, β) components and processing of signals

* **Jakub Vonkomer, Milan Zalman**
Institute of Control and Industrial Informatics, Faculty of Electrical Engineering and Information Technology, Slovak University of Technology in Bratislava, E-mail: jvonkomer@ieee.org

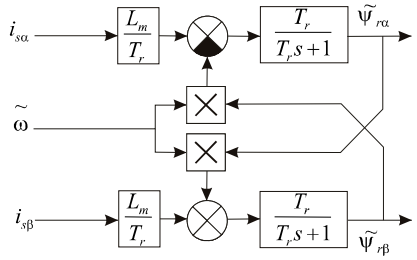

Fig. 2 Flux estimator in stator reference frame (a, β)

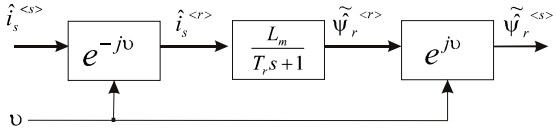

Fig. 3 Flux estimator in reference frame oriented to rotor position (d, q)

rotating at the slip frequency only, which is usually not more than a few of Hz. Furthermore park transform is non-dynamical transform.

3. MRAS Systems

MRAS (Model Reference Adaptive System) estimators are usually observing mechanical speed by using two different estimators or observers, one of which is speed dependent. Basic schema of MRAS model is shown in Fig. 4.

The difference between estimator outputs is used for speed error reduction, commonly by PID controller, but recently many papers describing adaptation by Fuzzy Logic / Artificial neural networks have been published.

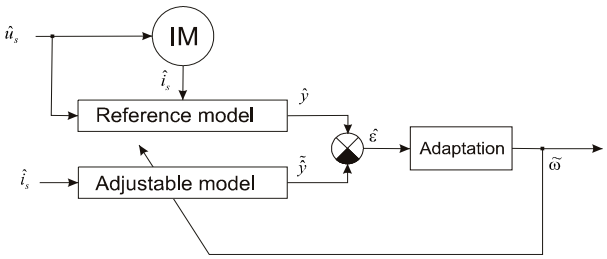

Fig. 4 General schema of MRAS system

There are several groups of MRAS speed estimators. We will focus on the least known structure – structure based on the error of stator current. This estimator was first described by Kowalska [4]. Stator current vector is observed by stator current observers and then compared to measured values. In MRAS terminology, real motor is reference model. As mentioned above, main advantage of this structure is absence of voltage flux model which is unreliable and, therefore unusable at speed close or equal to zero.

Proposed stator current error based MRAS will be later marked as MRASC in this paper.

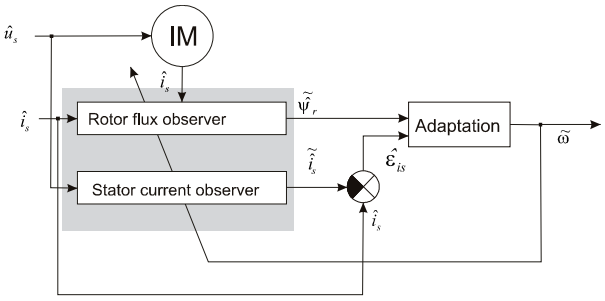

Fig. 5 Simplified schema of proposed MRASC system

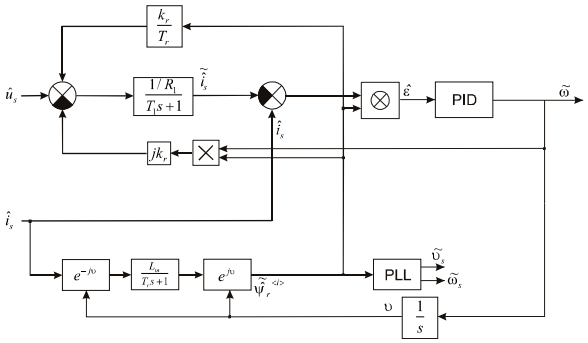

Fig. 6 Detailed schema of proposed MRASC system

Error signal is defined as:

$$\varepsilon = \Im\left(\tilde{\hat{\psi}}_r^{*} \cdot \hat{e}_{is}\right) = \left(i_{s\alpha} - \tilde{i}_{s\alpha}\right)\tilde{\psi}_{r\beta} - \left(i_{s\beta} - \tilde{i}_{s\beta}\right)\tilde{\psi}_{r\alpha} \tag{4}$$

$$\hat{e}_{is} = \hat{i}_s - \tilde{\hat{i}}_s \tag{5}$$

Design of the adaptation loop

Adaptation loop was designed from the linearized mathematical model.

Under assumption that flux (1) is function of change of speed only (6), flux model equation results to (7).

$$\tilde{\hat{\psi}}_r = f\left(\tilde{\hat{i}}_s, \tilde{\omega}\right) \rightarrow \Delta\tilde{\hat{\psi}}_r = f_1\left(\Delta\tilde{\omega}\right) \tag{6}$$

$$\Delta\tilde{\hat{\psi}}_r = \frac{jT_r\hat{\psi}_{ro}}{\left(T_r s + 1\right)}\Delta\tilde{\omega} \tag{7}$$

Model of stator current [2]:

$$\tilde{\hat{i}}_s = \frac{1}{R_1\left(T_1 s + 1\right)}\left(\hat{u}_s + \frac{k_r}{T_r}\tilde{\hat{\psi}}_r - j\hat{\omega}k_r\tilde{\hat{\psi}}_r\right) \tag{8}$$

Now the effect of voltage change is neglected, only flux and speed changes are important:

$$\tilde{\hat{i}}_s = f\left(\hat{u}_s, \tilde{\hat{\psi}}_r, \tilde{\omega}\right) \rightarrow \Delta\tilde{\hat{i}}_s = f_2\left(\Delta\tilde{\hat{\psi}}_r, \Delta\tilde{\omega}\right) \tag{9}$$

$$\Delta\tilde{\hat{i}}_s = \frac{\frac{k_r}{T_r}\Delta\tilde{\hat{\psi}}_r - jk_r\Delta\tilde{\omega}\hat{\psi}_{ro}}{R_1\left(1 + T_1 s\right)} \tag{10}$$

By combining together equations (7) and (10), following results are obtained:

$$\Delta\tilde{\hat{i}}_s = -\frac{T_r s}{R_1\left(1 + T_1 s\right)\left(T_r s + 1\right)} jk_r\hat{\psi}_{ro}\Delta\tilde{\omega} \tag{11}$$

$$\Delta\varepsilon = \Im\left(\tilde{\hat{\psi}}^*_{ro} \cdot \Delta\hat{\tilde{e}}_{is} + \Delta\tilde{\hat{\psi}}^*_r \cdot \hat{\tilde{e}}_{is}\right) \tag{12}$$

$$\begin{aligned} \Delta\hat{e}_{is} &= \Delta\hat{i}_s - \Delta\tilde{\hat{i}}_s \\ \Delta\varepsilon &= -\hat{\psi}^*_{ro} \cdot \Im\left(\Delta\hat{e}_{is}\right) = -\Im\left(\Delta\hat{i}_s - \Delta\tilde{\hat{i}}_s\right)\hat{\psi}^*_{ro} \end{aligned} \tag{13}$$

$$\Delta\varepsilon = \left[\Delta\omega - \Delta\tilde{\omega}\right]\frac{T_r s}{\left(1 - T_1 s\right)\left(T_r s + 1\right)}\frac{k_r\hat{\psi}^*_{ro}}{R_1} \tag{14}$$

Adaptation loop controller

PID controller was chosen as the most appropriate controller structure. Parameters were designed using pole-placement method. By implementing an integrator into controller structure, simple second order transfer function was obtained.

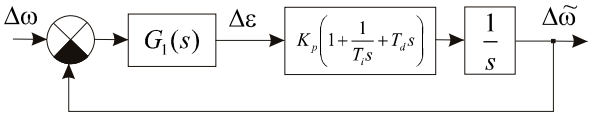

Fig. 7 Control loop for controller design

$$G_1(s) = \frac{\Delta\varepsilon}{\Delta\omega - \Delta\tilde{\omega}} \tag{15}$$

Final transfer function for calculating the controller parameters:

$$G_1(s) = \frac{K_0}{\left(1 + T_1 s\right)\left(T_r s + 1\right)},$$

where

$$K_0 = \frac{k_r\psi_{ro}^2 T_r}{R_1} \tag{16}$$

Closed loop transfer function then results to:

$$\frac{\Delta\tilde{\omega}}{\Delta\omega} = \frac{\frac{K_p K_0\left(T_1 s + 1 + T_d T_1 s^2\right)}{T_i T_1 T_r}}{s^3 + \frac{\left(\left(T_1 + T_r\right) + K_p K_0 T_d\right)}{T_1 T_r}s^2 + \frac{\left(1 + K_p K_0\right)}{T_1 T_r}s + \frac{K_p K_0}{T_i T_1 T_r}} \tag{17}$$

Reference (characteristic) polynomial:

$$P_{ref} = s^3 + \omega_0\left(2\zeta + k\right)s^2 + \omega_0^2\left(2\zeta k + 1\right)s + k\omega_0^3 \tag{18}$$

ω_0 – system's natural frequency
ζ – system damping ratio
k – shift pole index

By comparing closed loop denominator polynomial to reference polynomial, parameters for PID were gained.

Transient between sensor and sensorless

Failure of the encoder can be detected in several ways. The most simple and used in industrial applications is violation of the conditions of complementary signals: $A \neq \bar{A}$, $B \neq \bar{B}$ etc...

For ensuring the drive operation to continue, the transient to sensorless control must be as smooth as possible. To achieve this when switching from sensor to sensorless control, proper initial values of sensorless control must be set. In our models we assume that the sensorless estimators are in separate block and they are not executed during the sensor control operation. Estimators are executed during the sensorless operation only. In the model of stator current, the discrete filters initial outputs have to be set to actual values of $i_{s\alpha}$, $i_{s\beta}$ respectively. Otherwise initial value of error signal is unpredictable, thus a strong torque jerk or instability may be caused, especially in high speed region.

The same has to be done in the adaptation PID controller – initial output of last integrator has to be set for last known value of electric angular speed from the encoder.

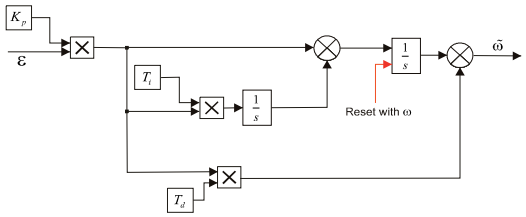

Fig. 8 Structure of MRASC adaptation controller, including RESET signal to achieve smooth transient between sensor and sensorless control

Moreover, it is worth to mention another issue. Usually the knowledge of motor electric parameters for sensor vector control does not need to be as exact as for sensorless vector control. As a result, the transition to sensorless vector control could be unstable.

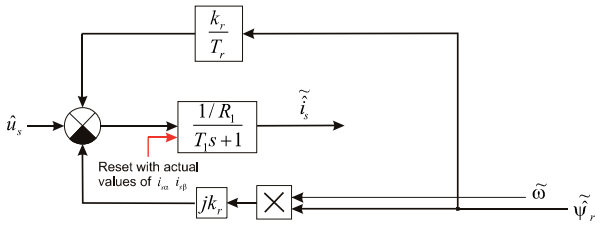

Fig. 9 Schema of model of stator current, including RESET signal to achieve smooth transient between sensor and sensorless control

Therefore, proposed sensorless vector control should be stable and immune against minor parameters variation. To acquire information about this immunity, several experiments have been done in Simulink. By building a close-to-reality simulation model in Simulink with intensive using of SimPowerSystems toolbox blocks, experimental test to parameter variation was done. This test is a complex test of behaviour, it does not only include stability analysis of the adaptation control loop, because the parameter variation affects the other loops, including current and flux controllers as well.

Following tables demonstrate the overall performance and stability of entire systems due to variation of electrical parameters of the motor. These tables differ in dynamics of speed controller (f0SC) and MRAS adaptation controller (f0MRAS).

Regarding the 4th parameter in the table:

$$L_r = L_{r\sigma} + L_m$$
$$L_s = L_r \tag{19}$$

As might be seen in the previous tables, proposed MRASC does not suffer much from loss of stability or worsen performance caused by small parameter change. Furthermore, this sensitivity is strongly dependent on the dynamics of MRAS adaptation loop, speed controller, sample time / PWM frequency, current loop, flux loop and others, so it is hard to present any universally acceptable results. Nevertheless, after implementing simple online estimation algorithms the entire drive performance in the whole speed range could be improved.

4. Results

To present excellent behavior of proposed sensor, sensorless control and on-the-run transients between these control methods, both simulation and experimental results are shown below.

Sensorless benchmark test

Test consists of a simple speed reference signal containing several steps to explore the dynamic properties of sensorless control at various speeds. First is step to 50 Hz, then reverse to −50 Hz followed by steps to lower frequencies down to zero.

Experimental analysis of motor's electric parameters variation Tab.1

Current-based MRAS, Tsam = 0.2ms, f0MRAS = 40Hz,f0SC=4Hz												
		Parameter variation										
Par.	Speed	-50%	-40%	-30%	-20%	-10%	0%	10%	20%	30%	40%	50%
Rs	< 100%											
	< 50 %									X	X	X
	< 5%	X	X	X					X	X	X	X
Rr	< 100%											
	< 50 %											
	< 5%		X									
Lm	< 100%											
	< 50 %				X	X						
	< 5%				X	X						
Lrσ	< 100%											
	< 50 %	R	R									
	< 5%											

Current-based MRAS, Tsam = 0.2ms, f0MRAS = 70Hz,f0SC=5.6Hz												
		Parameter variation										
Par.	Speed	-50%	-40%	-30%	-20%	-10%	0%	10%	20%	30%	40%	50%
Rs	< 100%									X	X	X
	< 50 %								X	X	X	X
	< 5%	X	X						X	X	X	X
Rr	< 100%											
	< 50 %											
	< 5%											
Lm	< 100%											X
	< 50 %				X	X						
	< 5%				X	X			X	X		
Lrσ	< 100%	X										X
	< 50 %	X										X
	< 5%											

Legend
- No significant change
- speed error less than 5%
- X: speed error less than 5%, torque ripples
- R: minimal speed error, not able to fast speed reversation
- speed error higher than 5%
- X: speed error higher than 5%, defluxing or orientation loss
- edge of stability, significant speed error
- unstability
- unspecified - causes errors, reaches limits at start

This test shows overall performance of proposed method, including speed reverse possibilities and operation in the low speed region at the end.

Transient from sensor to sensorless control, ramp-up.

This test verifies the quality of transient during the ramp-up. No steady-state for speed reference. Time of transient, $t = 0.6$ s.

This test also proved very good response, although the dynamics of adaptation is visible on the error between estimated and measured speed. However, the real speed continues smoothly.

Transient from sensor to sensorless control – high speed region

This test had to verify the behaviour of transient from sensor to sensorless control in high speed region under load. This transient is done in $t = 2.2$ s.

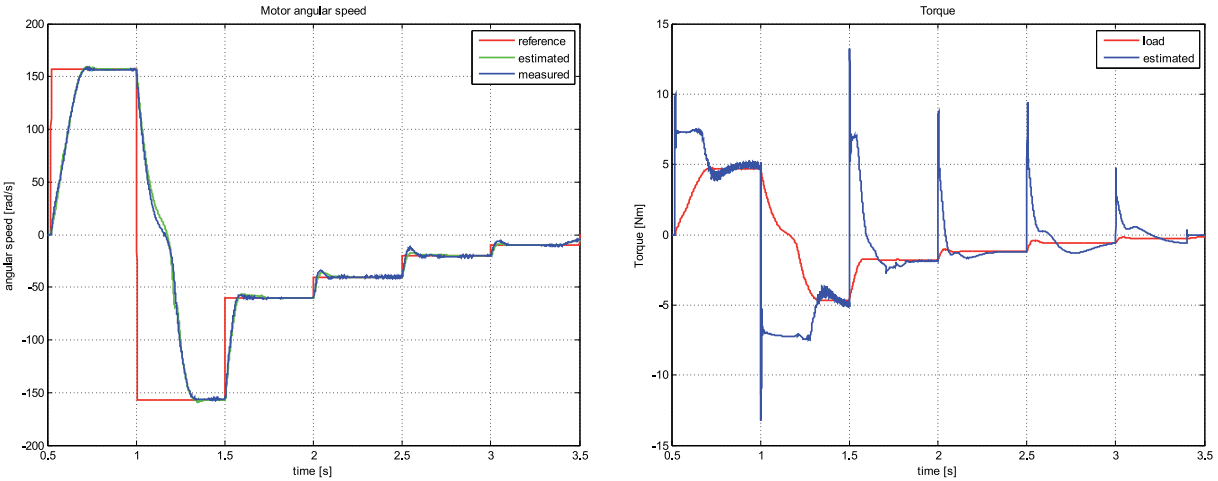

Fig. 10 Sensorless benchmark test: speed and torque

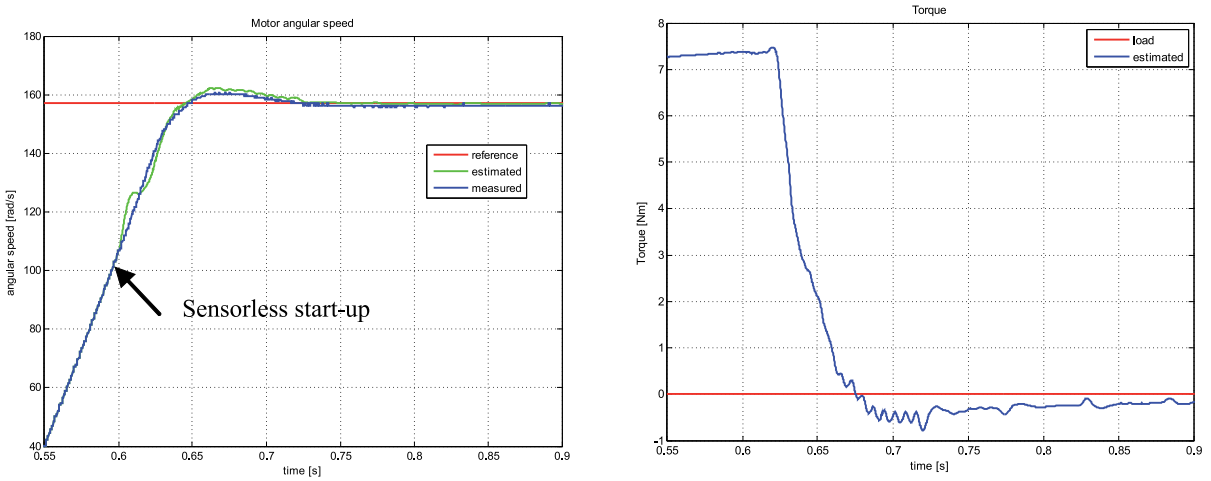

Fig. 11 Ramp-up transient test

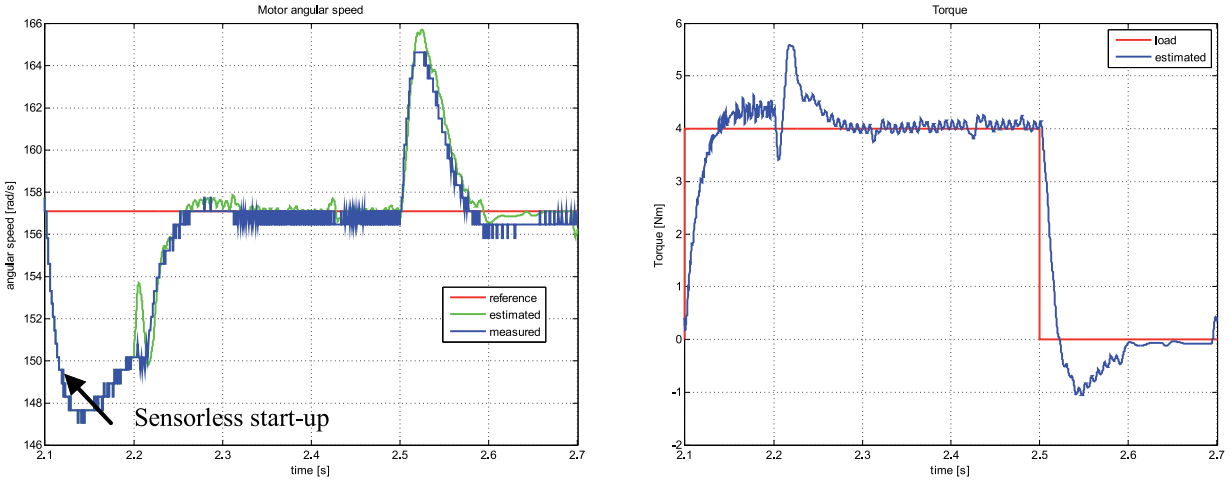

Fig. 12 High speed region transient from sensor to sensorless control, t = 2.2 s

Test also showed excellent dynamics and smoothness of the transient between sensor and sensorless control.

Experimental tests:

Experimental verification was performed in a laboratory setup with PC equipped with dSpace 1104 controller board which controls frequency converter feeding the 1.1 kW induction machine.

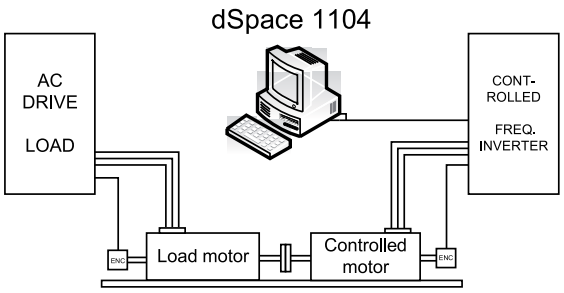

Fig. 13 Diagram of the laboratory test bench

Transient from sensor to sensorless control, low speed region

This test had to verify the behaviour of transient from sensor to sensorless control in low speed region.

Previous test shows non-problematic transient from sensor to sensorless direct vector control.

Transient from sensor to sensorless control, medium speed region

Following test shows the dynamics of a transient in medium speed region. It can be seen that although sensorless control introduces some ripple, the transition itself is smooth.

5. Conclusion

The primary objective of our project was to achieve continuous operation of vector control of the drive even in case of encoder's failure. Transient between sensor and sensorless control must be smooth without any significant torque or speed jerk. Moreover, the modified indirect vector control method was described to allow

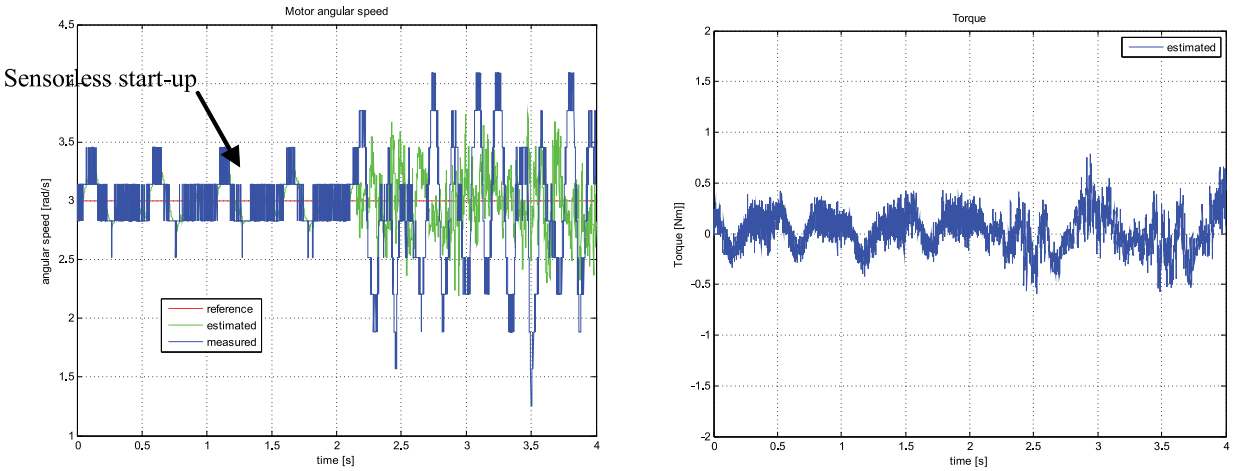

Fig. 14 Low speed experimental results

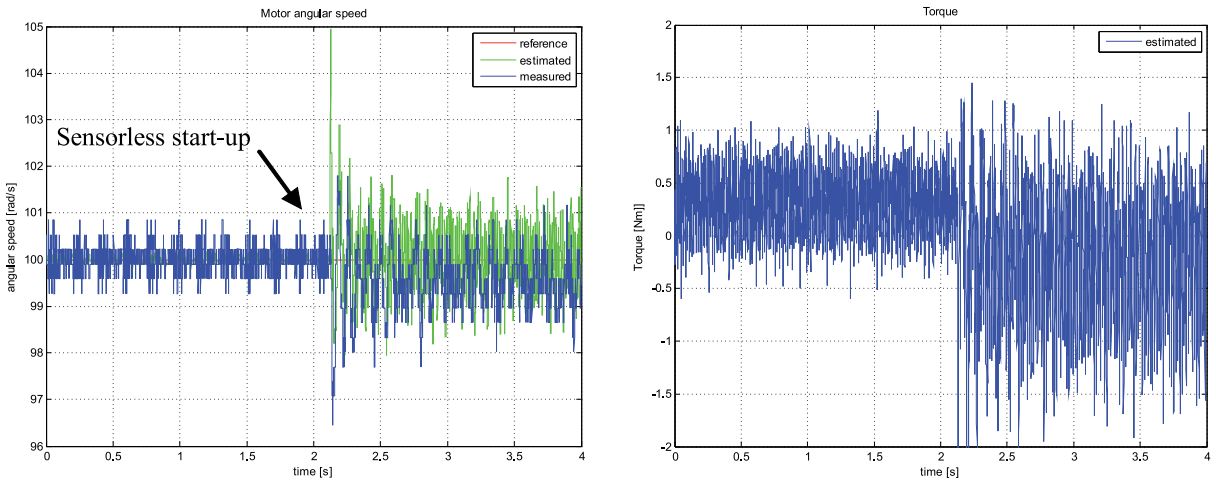

Fig. 15 Medium speed experimental results

using same flux model with sensorless control. Not very well known approach of MRAS-based sensorless speed control method was demonstrated. Proposed MRASC shows very good dynamic response and appears to be very immune against parameters variation, which is necessary in the industry, where stability and robustness against disturbances is essential. The mathematical model of the estimator including the design of adaptation loop controller was described. Finally, the very good performance of sensorless vector control and the transient between sensor and sensorless vector control were proven by figures.

Acknowledgement

This work has received support from the Ministry of education, science, research and sport of the Slovak Republic. Project reference number is VEGA 1/0690/09.

Appendix

Motor data (rated values) - wye connection used:

$P_n = 1.1$ kW

$U_n = 230/400$ V (delta, wye)

$I_n = 5 / 2.9$ A

$N_n = 1380\ \text{min}^{-1}$

Pole pairs = 2

Electric parameters:

$R_s = 7.66\ \Omega$ – stator resistance

$R_r = 5.12\ \Omega$ – rotor resistance

$L_m = 0.386$ H – mutual inductance

$L_r = 0.421$H – rotor inductance

$L_s = 0.421$ H – stator inductance

$J = 0.005\ \text{kg.m}^2$ – moment of inertia

Nomenclature

$\hat{x}$ – vectors

$\tilde{x}$ – estimated quantities

References

[1] BOSE, B. K.; *Modern Power Electronics and AC Drives,* Prentice Hall, 2002

[2] ZALMAN, M.: *The Actuators (in Slovak),* STU Bratislava 2003.

[3] ZALMAN, M.: Lectures for Intelligent Servosystems, 2007/2008.

[4] http://servo.urpi.fei.stuba.sk/index.php?option=com_content&task=view&id=15&Itemid=26

[5] DYBKOWSKI, M., ORLOWSKA-KOWALSKA, T.: *Application of the Stator Current-based MRAS Speed Estimator in the Sensorless Induction Motor Drive,* Power Electronics and Motion Control Conference, 2008. EPE-PEMC 2008. 13th , Vol., No., pp. 2306–2311, 2008, URL: http://ieeexplore.ieee.org/stamp/stamp.jsp?arnumber= 4635607& isnumber=4635237

[6] FILKA, R., BALAZOVIC, P., DOBRUCKY, B.: A Sensorless PM Synchronous Drive for Electric Washers, *Communications - Scientific Letters of University of Zilina,* No 1., 2007, pp.24-32 URL:http://www.uniza.sk/komunikacie/menu/komunik.asp?id=4&rok= 2007&cislo= 1&p=o.

Milan Slivka *

SAFETY OF RAILWAY SYSTEMS AND FORMAL/SEMIFORMAL METHODS

The contribution deals with computer based railway safety systems. It shortly concerns problems associated with using computer systems in comparison with traditional safety systems. The attention is paid to formal and semiformal methods in development and approval of railways systems, seen in the context of standardization and legislation framework. The author summarizes current state of using formal and semiformal methods from whole life cycle point of view of railway safety system in the area of Slovak and Czech railways and possible reasons for their rare use.

1. Introduction

The system with safety responsibility is a system whose incorrect function (failure) may have very serious consequences such as loss of human life, severe injuries, large-scale environmental damage, or considerable economic penalties [10]. Many safety-critical systems are typically fail-safe systems, i.e. once a fault has occurred the system must remain in the previous state (provided that this state does not represent a hazard to the controlled system) or must enter a pre-defined safe state.

Safety is then the freedom from unacceptable risk of physical injury or of damage to the health of the people, either directly or indirectly as a result of damage to property or to the environment. Functional safety is a part of the overall safety that depends on a system or equipment operating correctly in response to its inputs.

Systems with safety responsibility are applied in almost all fields of modern technology today: nuclear power plant control, medicine, space programs and transport, including interlocking systems for control and command of train movements. In the next part we will be interested only in the systems mentioned as last.

The control tasks become more complex in railway and metropolitan transport systems and their realization is hardly possible without computer systems. Nowadays the computer controlled systems with safety responsibility are applied in almost all the fields of modern technology as well as in traffic (e.g. in signaling and train control systems on the railway).

2. Background

The railway area has established a very strong safety culture during its hundred years' operation. Safety in electromechanical railway signaling was based on simple fail-safe principles that rely on impermeability of the mass and gravity attraction. By the construction of this system it was ensured that any occurrence of a critical event brought a system to the fail-safe state (e.g. all signals to stop). For example, the relay type N (safety relay) is constructed in such a way that the force of gravity itself causes the relay armature to drop off if the relay is not powered, and also the contacts are made of non-weldable materials.

These properties are taken into account by a relay system design in such a way that a controlled circuit is in error case always off (except for the unlikely case the attraction force does not work).

Computer and SW based system required an adaptation of safety approaches in order to use innovative technical systems on a high safety level. The reason is that there are some problems associated with using computers to control safety-critical systems. It is generally much more difficult to demonstrate that a computer program operates correctly than to demonstrate correct operation of traditional engineering devices. For traditional engineering hardware it is possible to use continuous analysis and rely on interpolation of test results. For example, for modeling, analyzing and predicting the track circuit properties it is possible to use mathematics based on partial differential equations (which have been studied for many years and there is a firm theoretical basis). But for computer systems the discrete nature means that traditional testing methods cannot be used: the smallest change in system state (one bit) may have enormous consequences. One of the reasons is the discrete nature of computer systems [10].

All software failures, however, are systematic. Software does not wear out or break. Most software failures are the result of errors in the software which themselves result from failures in the development process, such as incorrect specification (for instance spe-

* **Milan Slivka**
Railway Research Institute, j.s.c (VUZ), Prague, Czech Republic, E-mail: slivkam@cdvuz.cz

cifying the wrong behavior in the event of an error), or a mistake when implementing this specification.Confidence in software in safety-critical systems has to be built on the confidence in the software engineering methods used, confidence in the personnel, confidence in the management, and assurance through formal methods as well as testing. These techniques which, when used effectively, are considered to provide an appropriate level of confidence in the realization of a system to a stated integrity level.

3. Formal and Semiformal Methods in Safety Standards

Existing software engineering techniques provide structured methodologies for design, implementation, testing, verification and validation of software. These methodologies were standardized. The overriding world standard is IEC61508 – Functional safety of Electrical / Electronic / Programmable Electronic safety-related Systems. However, railway industry currently relies on the group of CENELEC sector specific related standards. These standards describe processes to be followed in order to be able to assure the safety of a railway application in all life cycle phases:

- EN 50126 Railway applications – The specification and demonstration of Reliability, Availability, Maintainability and Safety (RAMS)
- EN 50128 Railway applications – Communications, signalling and processing systems – Software for railway control and protection systems
- EN 50129 Railway applications – Safety related electronic systems for signalling.

EN 50126 addresses system issues on the widest scale, while EN 50129 addresses the approval process for individual systems which may exist within the overall railway control and protection system. This standard concentrates on the methods which need to be used in order to provide system which meets the demands for safety integrity which are placed upon it by these wider considerations.

This standard recommends the use of semiformal and formal methods, graphical description, structured specification, hierarchical separation using formalized methods, automatic consistency checks, and refinement down to functional level and model oriented procedures with hierarchical subdivision, description of all objects and their relationship in system requirements specification phase.

EN50128 identifies requirements, life cycle issues and documentation. It gives detailed descriptions of objectives, input documents, output documents and software requirements specification, as well as architecture, design and implementation, verification and testing. It covers software/hardware integration, software validation, quality assurance and maintenance. In Annex A, which is normative, it provides criteria for the selection of techniques and measures, depending on the safety integrity level. In Annex B, which is informative, it gives descriptions of the techniques identified in Annex A.

Also in this standard it is recommended to use semiformal and formal techniques in the software requirements specification. There is demand for a description of the problem in natural language and any necessary mathematical notation that reflects the application. Technique of formal proof is highly recommended in the verification and testing phase of software. Semiformal and formal methods are generally recognized as a fault avoidance technique that can increase dependability by removing errors during the specification of the requirements and design stages of development.

4. Semiformal and Formal Methods Generaly

Next, we will try to sketch what semiformal and formal methods are.

Semiformal methods are considered to be the methods that for identification and domain problem analysis use phraseology with precise defined structure and rules (syntax). They may include many CASE methodologies, diagrammatic techniques, graphical languages, pseudocode, and other systematic ways for describing the requirements, specification, or operation of computer systems. These methods eliminate disadvantages (ambiguity and imprecision) of natural language when used for technical descriptions.

The topic of formal methods covers the development and application of mathematically-based approaches in computing. Techniques founded on formal methods can offer a rigorous and an effective way for specification, modeling, designing and analyzing of computer systems and software. The idea of this approach is in description properties and behavior we are concerned with, in the terms of concepts from discrete mathematics sets, graphs, partial orders finite state machines and so on. This kind of notation is identified as a formal language. Specification in the formal language is very precise, with well defined syntax and semantic and can be mathematically manipulated. Calculation in these domains is based on the methods of formal (or mathematical) logic. Using laws of mathematical logic, it is possible to make (calculate) proofs of theorems and refutation checks, whether certain requirements are satisfied by a given specification [12]. The advantage is, that the correctness check can be performed automatically by machine and avoid reliance on human intuition.

5. Practical Use

Formal methods have been a topic of research for many years and during this research a lot of case studies of formal methods application were made. However, they are rarely used in commercial contexts, especially in area Slovak and Czech railways and development companies. Admittedly there are some examples of real use in the signaling industry, but not from whole lifecycle point of view. In these examples, they are normally used only to a limited extent (for example writing functional specification) and usually taking prototyped, non standardized tools and notations (company design language).

Incorporation of the formal methods in development process from the whole lifecycle point of view is not an easy task to do and some difficulties have to be overcome.

At first, people in railway signaling area are very conservative. Rather than adopting new technologies, they use traditional, trusted methods in development process. Each new technology is a priory considered untrustworthy. Moreover, development and approval of railway signaling systems without these methods are also possible, or, in accordance with safety standards.

Adaptation of formal methods assumes some level of education in formal logic. As it was mentioned, these methods are based on mathematics, more exactly, on mathematical logic. Formal approach requires dealing with formal logic semantics independently, although in a restricted form. People in railway practice are not usually experts in this domain. Formal science training is the way how to understand the fundamentals of these techniques. The understanding plays a crucial role especially for assessors and the supervising authority, because only then they can accept and trust in the used techniques.

A necessary issue that has to be solved by introducing formal methods into practice is to choose a kind of a method and a (formal) language that should be used for solving the tasks. This choice is not easy. Nowadays, plenty of individual notations, methods and tools exist. Following an online internet resource [7] the count is over one hundred. Probably, the real number can be higher. Formal methods may be classified according to different criteria: according to whether their primary purpose is descriptive or analytic (descriptive and analytic methods), according to the level of formality (with low, medium and high level of formality) and/or according to the type of the used specification language (algebraic and model-oriented) [11]. We have to take in consideration that it is obviously suitable to use different approach or language for different purpose. Probably, the annotation suitable for the system engineer describing an early lifecycle stage of the system might be less suitable for a programmer describing data structures and program control.

Another obstacle is that not only one side is involved in the development of railway signaling system. At the beginning of a railway application development, system requirements specifications had to be prepared. According to the standards, this is a duty of the railway operating authority (usually railway company, in the Czech Republic it is SZDC – Sprava zeleznicni dopravni cesty). The operating authority is the first side. The second side involved in the development process is represented by developers (manufacturers, suppliers). Their role is to develop the system on the basis of the system requirements specification. The third side is formed by the supervising authority (safety assessor, in the Czech Republic it is for example VUZ – Vyzkumny ustav zeleznicni), who have to inspect if the system was developed satisfying the safety standards and if the system achieves a desired safety level. A selected formal method has to be compatible with all the mentioned practitioners. Only then, the model made for specification can be reused for development and approval process and takes the advantage of the used method.

Another issue is that an appropriate computer tool suitable for industrial usage has to be available for the chosen formalism. The quality of the tool, as a software product, has to provide some level of engineering, good documentation, user's interface, the support and customer specific consultancy by the supplier.

Last but not least question is the cost of the new technology. Industrial companies have established their own development processes and introduction of a new technology within the development process takes some effort. For example, the shape of a development process using formal methods is rather different: a lot of the effort is concentrated on specification and verification, while rather less is devoted to coding and testing. The uptake of formal methods into the traditional industrial development process is also limited by cost/benefits ratio.

6. Possible Way to Introduce

Problems with introducing formal methods into practice are considerable, but not insolvable. All in all "formal" development process has to begin with formalizing system requirement specification. This is what can be characterized as the basic level of formal methods use. The development process itself may be non-formal, but benefits are still gained since many bugs can be removed by formalizing and discussing the system at an early stage. Translation of needs and requirements into specifications is one of the most delicate steps – if errors made during specification phases remain undetected, they become potential sources of systematic faults during the system operation. This is confirmed by a study performed by the HSE (Health & Safety Executive, of United Kingdom) concerning the primary causes of failures, based on 34 catastrophic incidents, which shows the primordial proportion (44.1%) caused by poor specifications [6].

Taking advice from the project aiming integration of techniques used by railway-engineers with formal techniques from the software-engineering area, it seems to be a good way to begin the formalization process with formalization of functional specifications using semi-formal notation or methods. The semiformal model allows the team developing the model to eliminate possible ambiguities of the non-formal descriptions and works as a bridge between the non-formal descriptions and the formal ones. One of the semiformal languages successfully applicable and suitable for making functional specifications of railways systems is UML (Unified Modeling Language). The UML is one of the most widespread and often used modeling standards, based on the object-oriented paradigm, which does justice to engineers. The standard UML 2.0 offers various modeling and visualization elements to capture and model functional requirements. Its means of description are based on graphics and are easy to understand. The UML is implemented and supported by many SW-tools that make it possible to generate the source code directly from the diagrams. Next advantage of the UML is the animation capability of the model. Animation allows verification of the functional correctness before producing a real system.

From practical point of view, the character of the railway system as such is that it is composed from smaller components with very similar behavior. For example, a station interlocking system is

composed of signals, track sections, switch points, etc. In practice, in the railway domain, the system requirements specification usually contains definition of the behavior of subsystems, the system structure and description of operational scenarios [1].

Subsystems and their parts can be regarded as objects. The whole system is then defined as a set of interacting objects or classes of the model. The relationships between these objects then describe the relationships between the system components. In this form, the static structure of a system can be grasped.

The dynamic system behavior is described by the local behavior of single objects and by interactions between the objects. This description defines the behavior of objects, including the various states that an object can enter into over its lifetime and the messages or events that cause it to transit from one state to another.

The operation scenarios can be modeled in form of interactions between the system components.

The way of UML application reflecting different aspects system definition mentioned above is demonstrated in figures included. It shows fragments (due to the limited size of the paper) of most often used diagram types. The application domain is a part of the station interlocking, in this case the control of a switch point. In Fig. 1 there is a Class Model Diagram, describing static structure of a station interlocking system. Included are only parts related to the switch point, i.e. parts (class) which can, for example, ask for changing point position etc.

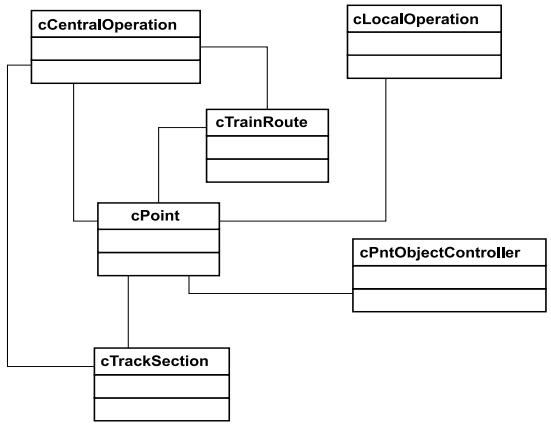

Fig. 1 Class Diagram

Operational scenarios in this example are modeled by means of the Use Case diagram Fig. 2. This kind of diagram shows typical interactions between the system under design and external objects that may want to interact with it. Dynamic system behavior is described by the state diagram in Fig. 3. This diagram is presenting realization of one of the use cases – individual control. In this diagram we can recognize the condition which has to be fulfilled to change the point position (in form of guards of transitions between states).

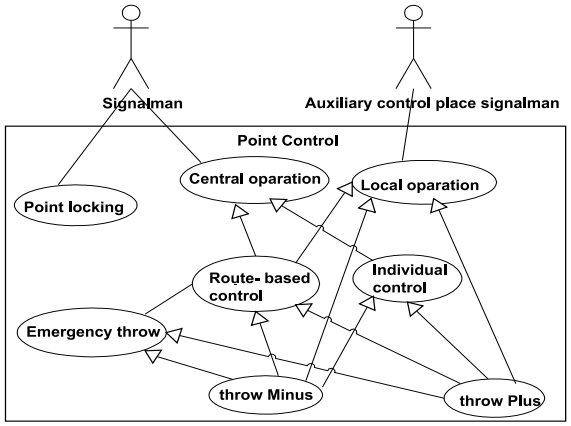

Fig. 2 Use Case Diagram

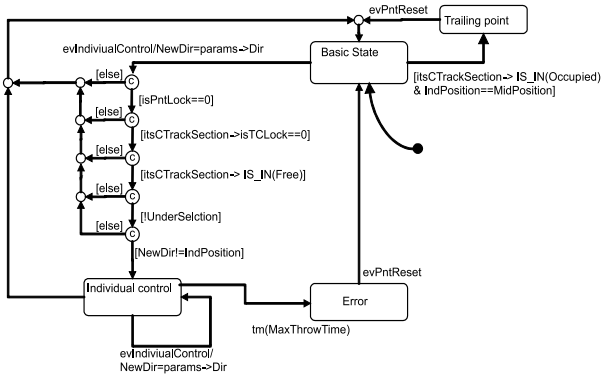

Fig. 3 Statechart Diagram

7. Functional Safety and Technical Safety

The given examples show that semiformal methods are good tools for describing or modeling functional requirements of the railway interlocking system. But, there are some additional factors. Railway interlocking is a safety system and requirements of such a system are considered in two parts: Safety functional requirements (functional safety) and Safety integrity requirements (technical safety).

Safety functional requirements are the current safety-related functions which the system, sub-system or equipment is required to carry out. These requirements concern correct operation of the system/sub-system/equipment under fault-free conditions (that is, with no faults in existence), in accordance with the specified operational and safety requirements.

Safety integrity requirements define the level of safety integrity required for each safety-related function. The term integrity refers generally to the probability of a system, or a piece of equipment, satisfactorily performing the required safety functions. Fulfillment

of safety integrity requirements ensures that in the case of faults occurrence in the system itself, the safety of the controlled process is still not endangered. If we assume only one independent error/failure can arise in a given instant, the technical safety requirements can be briefly recapitulated as follows:

- No failure must jeopardize the train movement safety.
- Any failure must be conveniently and promptly, considering failure frequency, detected so that it is possible to eliminate any further failure that may arise and jeopardize safety in conjunction with the previous one.
- If a failure goes undetected, the possible emergence of other failures is to be assumed.
- If a failure could possibly result in other subsequent failures, all combinations of these must be taken into account.
- After a failure detection, the faulty equipment or part should be shut down automatically without delay. At any rate, the output of the equipment or the part must remain in, or immediately change to, a state not jeopardizing operational safety.
- Equipment that was shut down because of a failure must not be reactivated by another failure occurrence [9].

The use of semiformal or formal techniques for describing technical safety requirements or checking their fulfillment (in case of formal methods) for concrete system is hardly possible and question is, if ever possible. Fulfillment of technical safety requirements is very important part of the development process and plays important role by the assigning of certain safety integrity level.

8. Conclusion

The computer and SW based system required an adaptation of safety approaches in order to use computer systems in railway interlocking on a high safety level. Formal methods are one of the ways of increasing confidence in computer systems in this area. The design and verification of systems based on formal or semi-formal methods give a chance to check functional correctness just before creating the system itself (in term of functional safety). This approach to a system design is in accordance with requirements of the European standards. But, some difficulties have to be overcome to introduce these methods in the development process and take advantages from their use. One of the possible ways to begin the formalization process is using semi-formal methods for the system specifications. It produces an environment suitable for communication not only between development teams, but also towards other subjects involved in the process of the system verification and approval. But, we have to keep in mind that the safety systems have to be considered also from the technical safety point of view. Semiformal and formal methods in this field are very hardly applicable, if applicable at all.

References

[1] BITSCH, F.: *Process Model for the Development of System Requirements Specifications for Railway Systems.* Internnatonal Workshop on Software Specification of Safety Relevant Transportation Control Tasks, Fortschritt-Berichte VDI, Reihe 12, Verkehrstechnik/Fahrzeugtechnik, Nr. 535, 2002.

[2] CENELEC EN 50126: *Railway applications: The Specification and Demonstration of Dependability - Reliability, Availability, Maintainability and Safety (RAMS),* 1999.

[3] CENELEC EN 50128: *Railway applications: Software for Railway Control and Protection Systems, 2001.*

[4] CENELEC EN 50129 *Railway Applications - Communications, Signalling and Processing Systems - Safety Related Electronic Systems for Signalling, 2003.*

[5] CIMATTI, A., GIUNCHIGLIA, F., MONGARDI, G., PIETRA, B., ROMANO, D., TORIELLI, F., TRAVERSO, P.: *Formal Validation & Verification of Software for Railway Control and Protection Systems: Experimental Applications in ANSALDO,* Proc. of World Congress on Railway Research (WCRR'97), 1997. Vol. C, p. 467–473.

[6] *Final Report. Safety-Related Complex Electronic Systems.* Contract SMT 4CT97-2191, Project "Standards for Safety Related Complex Electronic Systems (STSARCES)", 2000. p. 137.

[7] *Formal methods, Individual notations, methods and tools.* [Online]. http://formalmethods.wikia.com/wiki/Formal_methods.

[8] FRANEKOVA, M., RASTOCNY, K: Modelling in Development of Safety-related Communication Systems, *Communications - Scientific Letters of the University of Zilina,* 2008. Vol 10, Nr.1, p 24–30. ISSN 1335-4205.

[9] CHUDACEK, V., LOCHMAN, L., STOLIN, M.: Navigation Satellite Systems in Railway Signalling? *Signal+draht International* 2002, No.5, p. 44–47. ISSN 0037-4997.

[10] ISAKSEN, U., BOWEN, J. P., NISSANKE, N.: *System and Software Safety in Critical Systems.* The University of Reading, Department of Computer Science, 1996.

[11] JANOTA, A.: Using Z Specification for Railway Interlocking Safety. *Periodica Polytechnica, Ser. Transport Engineering,* Hungary, 2000. Vol. 28, No. 1-2, p. 39–53. ISSN 0303-7800.

[12] RUSHBY, J.: Formal Methods and their Role in the Certification of Critical Systems *Computer Science Laboratory,* SRI International, Menlo Park, 1993.

Jan Turcek – Matej Hrasko – Juraj Altus *

PHOTOVOLTAICS IN PRESENT DAYS AND THEIR COEXISTENCE WITH POWER SYSTEM

The article deals with the issue of presentation of photovoltaic power and photovoltaic power plants, describes their main features, their advantages and disadvantages, and also deals with the possible massive deployment of these power sources to the power system and their impacts on power system operation.

1. Introduction

Photovoltaic power plants (PV) have become nowadays a major phenomenon. Progress in science, especially in semiconductor technologies, enabled the development of various types of photovoltaic applications. In 70's of the 20th century during the oil crisis large number of photovoltaic power plants was built especially in Western Europe and in the USA, of which many are still operating successfully. Advancements in this area quietened after decay of crisis.

Today, however, the situation is set that makes renewable sources very attractive. Increase in the consumption of all non-renewable sources results in the raising pressure on the stocks of these commodities. For example if we compare years 1999 and 2009 we can see that the consumptions of fuels like oil, gas and coal increased over 23%. When comparing years 1989 and 2009 we get 40% difference. Looking at the stocks of primary energy sources we get next image. According to [4] the reserves of oil are in proportion to today's consumption available for 46 years, reserves of natural gas are available for 63 years and reserves of coal are predicted for 119 years. These numbers are obviously predicted only for constant consumption. But the rapid development of economies such as China and India means that the reserves will decrease from year to year. Not even reserves of uranium ore don't look very optimistically. These are predicted for 85 years [5].

Now we can return back to the photovoltaic energy. In the past, a factor that limited development in this area was high cost of acquisition of photovoltaic technology. An effort to relieve the dependence on imported energy resources has led the governments to adapt the legislation to increase the interest on technology of photovoltaic power plants of potential investors. High values are motivating and are increasingly evocating creation of projects to use the energy almost unused till today. However, photovoltaic brings with it many issues which have to be solved most effectively.

2. Sun Energy in Slovakia

The sun is for the Earth unimaginable and for mankind endless source of energy. The amount of solar radiation reaching the earth is not changing and is approximately 118 000 TW, which is several thousand times more than the current requirements for energy consumption [6]. Distribution of solar energy is homogeneous, not as is the case with fossil fuels, but energy density is hundredfold lower in the comparison to conventional thermal or nuclear sources. The impact energy on Earth's atmosphere upper edge is at any time around 1367.13 W on $1m^2$. This is so-called solar constant. It must be said, however, that not all the energy that hits the surface of the Earth's atmosphere also hits the Earth's crust. Approximately 30% of energy is immediately reflected from the atmosphere and goes back into space. The rest of it warms up the oceans, makes the wind blowing or is diffused in atmosphere. So Earth's surface is directly hit only with a portion of incident solar radiation. Radiation which is diffused in atmosphere due to molecules and suspensoids and radiation that is reflected from the Earth's crust and goes back to space or is re-diffused in atmosphere is called diffuse sky radiation. Summary of direct and diffuse sky radiation is the global radiation [7].

The big difference in amounts of hitting solar radiation is also created due to different latitudes. In Europe, we are going to compare two counterparts. Amount of solar radiation perpendicularly incident in northern Sweden and Russia is reaching 400–600 kWh/m^2 per year but in the Mediterranean region it is approximately 2000 kWh/m^2 per year. In Slovakia, the value of the intensity of solar radiation varies between 1000–1205 kWh/m^2 per year [6]. After some calculations we can determine that it is several times more energy than we are nowadays able to consume.

Solar power represents the largest potential source of renewable energy in Slovakia. Technically exploitable potential for elec-

* **Jan Turcek, Matej Hrasko, Juraj Altus**
Department of Power Electrical Systems, Faculty of Electrical Engineering, University of Zilina, Slovakia, Email: Jan.Turcek@fel.uniza.sk

tricity production from photovoltaic power plants was for the Slovak Republic established as 1540 GWh per year [8].

3. Exploitation of Sun Energy for Electricity Production

There are several ways of production of the electricity from sunlight. We can distinguish between indirect conversion of sunlight into electrical energy and direct conversion. For example the indirect conversion includes concentrated solar power plants. These are a tower-type plants or plants using trough mirrors. These plants operate on the principle of mirror, which is turning against the sun to warm up working medium, which flows through pipes that are located in the focus of the mirror. This heated fluid drives the turbine to produce electricity. Another way may be a solar power plant that uses the stack effect. Sufficiently high tower – the chimney is surrounded by a system of pipelines placed on the surface through which the air flows. Air in the pipelines is thanks to the sun's rays heated and then due to stack effect rising through chimney upwards. Wind turbine that is located in the chimney is spinning because of upward wind blowing and produces electricity.

All of these mentioned methods are very difficult to be realized in Slovakia and can be placed for instance in desert areas with high solar radiation intensity and low pressure for land occupation.

Direct conversion means that the energy of sunlight is converted by semiconductor materials into electricity. As it is direct method, photovoltaic power plant is not a burden for environment, it emits no gases and the only drawback is the production of photovoltaic technology.

We can nowadays distinguish several types of photovoltaic cells. First types are cells made from crystalline silicon. These are cells made from monocrystalline silicon referred as Mono c-Si, whose efficiency varies from 12% to 19 %, polycrystalline or multicrystalline silicon (multi c-Si) whose efficiency varies from 11% to 15 % and ribbon sheets (ribbon-sheet c-Si). These cells are most prevalent, and their share is about 90% of the total quantity of modules.

Moreover there are other materials in today's market. For example amorphous silicon, cadmium telluride (CdTe), copper indium (di)selenide (CIS) or copper indium gallium (di)selenide (CIGS) which is based on material CuInSe2 that absorbs 99 % of light in its first micron. Another type of modules is based on multi junction cells (a-Si/m-Si).

Maximum efficiency is achieved in concentrator solar cells. These are using optical concentrators for example Fresnel lens. Their disadvantage is that they can not use diffuse sky radiation and must be constantly turned against the sun. Such systems, however, reach up to 31% efficiency [6][9].

The essence of electricity production through semiconductor solar cell is the fact that the impact of sunlight on the PN transition results in the emergence of direct electrical current between P and N layers of semiconductor. Direct current can be consequently changed by converter, strictly speaking inverter, to commonly used AC supply voltage 230 V, 50 Hz. Thus equipped photovoltaic power cell can be connected into the mains.

The amount of electricity E (kWh) produced by photovoltaic system with a nominal power P_k (Wp / 1 000 Wm^{-2}) and the total efficiency r_p, which is the ratio between real and nominal power, can be derived from global solar radiation G (kWh/hm^{-2}).

$$E(t) = P_k r_p G \quad [\text{kWh}] \tag{1}$$

Real power is influenced by the size of the external temperature, solar radiation variability, cloudiness, which has a significant impact and because of its local character is almost unpredictable, by the cabling, by the voltage converters, etc. [6]

Increase of installed capacity can be shown on following numbers. At the end of the year 2009 installed capacity of photovoltaic power plants was 22928.9 MWp worldwide and in Europe it was 16065.8 MWp. In 2008 worldwide installed capacity was 15599.1 MWp and in Europe 10428.7 MWp. Regarding the installed capacity in 2009 it means increase over 47% worldwide and over 54% in the Europe. Even more interesting numbers are obtained in comparison with the year 1999. Worldwide installed capacity was 1013.6 MWp and 143.4 MWp from that volume was in Europe. So in comparison with installed capacity at the end of year 2009 it is worldwide increase over 2000% and in the Europe the increase is over enormous 11000% [4]. The results are illustratively shown in the Fig. 1 and Fig. 2.

Further increase of the installed capacity of photovoltaic power plants is expected in the next years. Currently the biggest photovoltaic power plant is the Finsterwalde Solar Park with installed capacity 80.7 MW_p [10]. However gigantic power plant is in preparation in China. It is going to be built in the Ordos region near border with Mongolia and its installed capacity should be 2 GWp. Its completion is planned in 2019 [11].

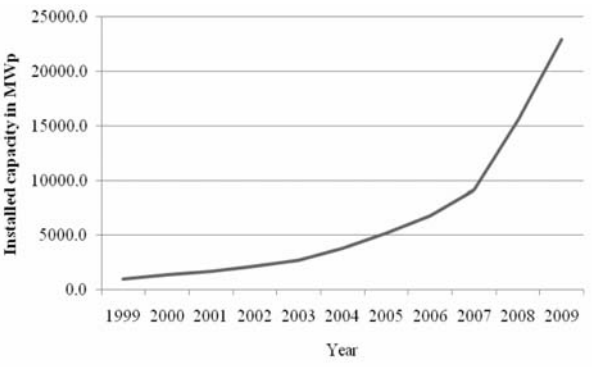

Fig. 1 Development of installed capacity of PVs in the World

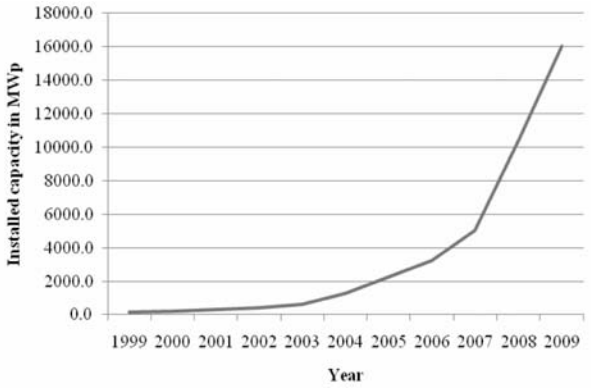

Fig. 2 Development of installed capacity of PVs in Europe

4. Photovoltaics in Slovakia

Photovoltaic power plants are dependent on the sunlight and its intensity. This, however, varies considerably during the day.

In Fig. 3, we can see the daily load curve of Slovakian power system. As it can be seen the maximum load occurs from 19 to 20 o'clock. On the other hand the smallest load occurs at night around 4 o'clock in the morning. At six to seven o'clock a morning peak occurs due to initiation of industrial plants operations and at lunch hour the energy consumption decreases.

Another important fact is also a great difference between the system load in summer and winter months. Annual minimum of consumption occurs in July, but increasing amounts of air conditioning units are likely to increase energy demand in summer months. On the contrary maximal energy demands are in winter months. From the long-term observations it's documented that the maximum load of the system occurs in the January. As a result of global warming winters are milder, but still there may be situations when the arrival of severe frosts results in significant energy consumption increase.

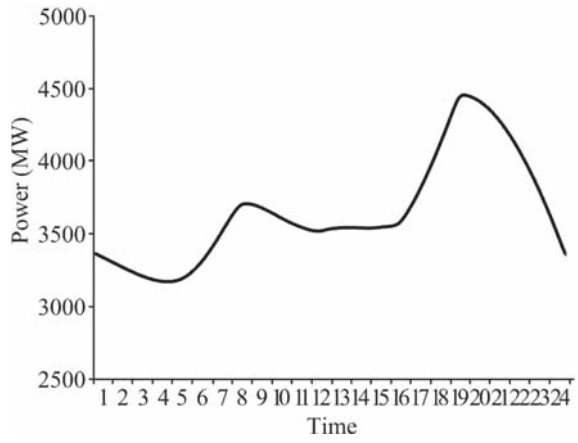

Fig. 3 Daily load curve

When talking about behaviour of the photovoltaics, it is precisely the opposite. In the summer, the influence of stronger intensity of solar radiation and the influence of longer day duration causes the fact that the electricity production reaches its maximum. In winter, resulting from shorter day duration and dominant diffuse sky radiation, amount of electric energy produced by photovoltaic power plants reaches minimum. As seen in Fig. 4 photovoltaic power output varies greatly during twenty-four hours. At the dawn it begins to raise from zero, at noon the sunlight intensity reaches maximum values, which results in maximal electricity production, and when the evening comes it starts to fall back till zero is achieved.

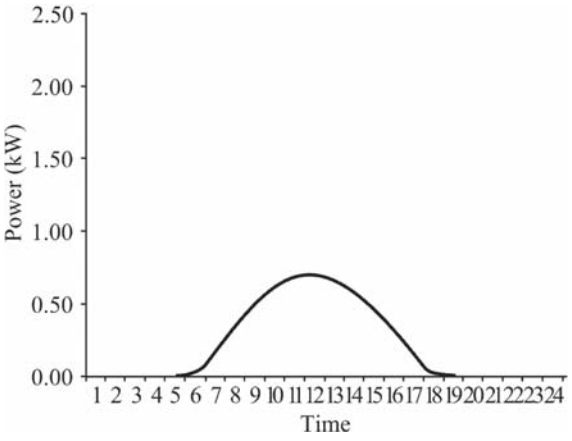

Fig. 4 Map line of photovoltaic electricity production during the day

By comparing these two curves, we find out that these waveforms are not similar at all. Although a photovoltaic power plant is working during the daylight, its power performance during the morning peak reaches the minimum values. In winter, the starting point of photovoltaic power curve shifts to 8 o'clock and ending point is moving already to 16 o'clock. As mentioned photovoltaic maximum output power is achieved in the summer, but this does not correspond with the system load which is lowest in summer. Another important part of the daily load curve is the evening peak, which cannot be covered from photovoltaic power plants. These facts will create serious problems for operation of power system if there is a massive deployment of photovoltaic power plants.

Nowadays there is only small installed capacity of photovoltaic power plants in Slovakia in comparison with neighbouring countries. In 2006 there were installed according to [12] 64 kWp. By the end of 2011 installed capacity of 120 MW is assumed. List of 36 power plants with allotted certificates was published already in December 2009. Sum of their power performance is previously mentioned 120 MW [13].

Most resources connected to the electricity system will have installed power from 1 MW to 4 MW. Others are smaller sources or sources operated in standalone mode, i.e. not connected to the electricity system. These are autonomous resources in inaccessible locations or telephones.

Photovoltaic power plant in Cerenany is one example of photovoltaic power plants connected to the network with output of 500 kWp which was completed in May 2010. Another example is photovoltaic power plant in the eastern Slovakia in the village of Mala Domasa with the performance of 735 kWp. It is quite interesting because 3000 panels are located here and are placed on trackers which are tracking the movement of Sun and are moving panels always perpendicular to the sun beams. Moreover it is the largest photovoltaic power plant in eastern Slovakia.

In close connection with photovoltaic power plants there are wind power plants. As photovoltaics, these are also sources, that are helping to decentralize production of electricity, but with their major properties, they are considerably influencing electrical power system. Installed capacity of wind power in Slovakia is currently 3 MW.

Photovoltaic and wind power sources are hardly predictable and therefore are referred as unpredictable renewable energy sources. While the first are dependent on the intensity of solar radiation, exterior temperature and also the cloudiness, the second depend mainly on the speed of airflow, but the final production characteristics are also affected by many other factors. Most of these factors are very difficult to predict. Therefore the operation of these power plants causes bigger pressure on the operation of power system.

Until now there has not been installed any larger unpredictable renewable energy source in Slovakia and this implies in lack of experience with their operation. But from current experiences we know what consequences may have the massive deployment of wind power plants into electrical power system.

In Germany, at the end of the year 2009, there was installed 25813 MW in wind power plants. Germany also holds the world's primacy in installed capacity of photovoltaic power plants. Situation in Europe in the amount of installed capacity is as following. Installed capacity of photovoltaic power plants was in the Czech Republic at the end of 2009 411 MWp [14], in Italy at the end of 2009 1181 MWp [15] and at the end of 2008 Spain had got 3354 MWp [16]. To compare, the sum of off grid installed and grid connected applications in Germany was 9845 MWp at the end of 2009 [17].

Nowadays we are experiencing the impacts of this massive installation. Germany is surrounded mostly by countries whose energy balance is settled, in addition to the two adjacent exporters France and the Czech Republic, and one smaller exporter Poland. So the question raises what to do with the electric energy, when there is a massive production from wind power and solar energy. Forasmuch as in the south Europe there are mostly countries whose energy balance is strongly deficit, there are efforts to send the generated energy to them. Of course this is happening through power grid. This may cause serious problems, because the requirements on the power lines such as these can eventuate in lowering reliability. As a result of an accumulation of adverse factors there can be disintegration into island operations and in the worst case so called blackout.

The most serious problem is to adjust the production curves of these resources to the needs of the power system. As the sources are mainly small scaled, decentralized, it is very difficult to find a suitable way to control their performance. In the case of photovoltaic power they are typically sources with installed capacity around kW. It may seem that this is a small number, but due to the massive deployment, and so the resulting numbers, the sum of their installed capacity may be very large.

The big problem is that power performance is very variable due to time. If we neglect other factors and we would count only with the sun's movement their power performance would have been easy to foreseen with a relatively high value of certainty. Thus the Pvs can be used most efficiently. But the reality is different and operating performance and the quantity of produced power are under big influence of other factors such as temperature, and especially cloudiness. This means greater demands on the transmission system operator and distribution system operators.

Another thing is daily power performance of photovoltaic power plants. From that it is obvious that it would be necessary to store the energy at the time of their maximal production. In the present day the most effective way is to consume this energy by pumping and so to store it in tanks of pumped storage plants, that would commercialize it again in the morning and evening, especially when there is in shortage.

Here come the issues of effective utilization of pumped storage power plants. In Slovakia there are 4 pumped storage power plants. One is connected to the 400 kV level and three to the 110 kV level. Most photovoltaic power plants will be connected to a 22 kV level. Pumped storage power plants have the nature of centralized sources and photovoltaic power stations are decentralized resources. But this is not only about pumped storage power plants. The system functions thanks to numerous regulators that will have to eventually regulate the power fluctuations caused by photovoltaic power plants. These are issues of primary and secondary frequency regulation.

One possibility of best usage of solar energy is the establishment of virtual power plant. It would involve the combination of a number of energy sources into a single unit that would offer certain guaranteed parameters equal to required production diagrams.

Other fact is that in the winter, photovoltaic power plants achieve low production levels and consumption is higher than in summer. So the sources which can replace these power outages are needed.

Another thing is that the production of photovoltaic power plants depends not only on the season, but also on the ambient temperature and mostly on cloudiness. Predictability of cloudiness is very difficult, since its local character, and that's why the consequent prediction of electric energy production is not exact. This again causes pressure on network operators.

Given the rapid changes in power performance is necessary to establish sufficient reserves of production capacities, especially

in quickly starting sources, such as pumped storage power plants, water power plants with peak-load operation and combined cycles.

As mentioned above, only small number of unpredictable renewable energy sources was installed in Slovakia. The power system was designed to operate with conventional thermal, nuclear and hydroelectric power plants. All these are resources whose production is easily predictable. Naturally the producer does not determine the amount of generated energy but the consumer does. Therefore, Slovakia has installed capacities that can meet these consumer demands.

With the arrival of photovoltaic power plants, however, new problem rises. Requirements for the support services that can ensure stability of power system operation will grow. These demands will increase not only because of requirements on the consumption side but also on the production side. All these changes will obviously result in increased operating costs and maybe even in construction of new production units.

4. Conclusion

Installation of photovoltaic power plants signifies for Slovakia, a country which imports about 90 percent of all energy sources, a great potential. It is the way to relieve dependence on the energy sources from other countries. Photovoltaic is also the cleanest way how to get the electric energy. But its operation causes considerable problems for the transmission power system operators and operators of distribution systems. Possible way to compensate these impacts is to buy the high price regulatory electric energy from other countries. Another possibility is to build new blocks of power plants that will replace production of photovoltaic power plants during their inactivity or on the other hand to use generated electric energy in time of its maximal production. Building of such sources may however take several years.

References

[1] RYBAR, P., RYBAR, R., TAUS, P.: *Alternative Energy Sources – Part 1 (in Slovak)*, TU FBERG, Kosice, 2001, p.121
[2] JANICEK, F. et al.: *Renewable Energy Sources - Part 1 (in Slovak)*, FEI STU, Bratislava 2007
[3] MULLEROVA, J., SUTTA, P., JURECKA, S.: Thin Film Silicon in Photovoltaics: The Role of Structure and Microstructure, *Communications – Scientific Letters of the University of Zilina,* No. 1, 2006, pp. 5–9
[4] http://www.bp.com/productlanding.do?categoryId=6929&contentId=7044622, (accessed 10/10)
[5] *Uranium 2005 – Resources, Production and Demand,* ISBN 92-64-024263, http://www.nea.fr/ndd/reports/2006/uranium2005-english.pdf, (accessed 08/10)
[6] http://www.solarenergia.sk/slnecna-energia/, (accessed 03/10)
[7] http://www.seps.sk/zp/fond/2002/slnko/slnko.html, (accessed 03/10)
[8] HUDCOVSKY, S.: *Renewable Energy Sources and their Application in Power System (in Slovak),* Coneco-Racioenergia 2009 Bratislava, www.tzs.sk/upload/TZSprezentacie/ Hudcovsky-EGU.ppt, (accessed 03/10)
[9] http://www.epia.org/solar-pv/pv-technologies-cells-and-modules.html, (accessed 11/10)
[10] http://www.pv-tech.org/news/_a/good_energies_nibc_infrastructure_partners_acquire_finsterwalde_ii_and_fins/, (accessed 11/10)
[11] http://news.cnet.com/8301-11128_3-10347438-54.html, (accessed 10/10)
[12] http://www.energies-renouvelables.org/observ-er/stat_baro/observ/baro178.pdf, (accessed 11/10)
[13] http://www.sepsas.sk/seps/informacia2009_12_11.asp?Kod=25&Nadrad=423, (accessed 09/10)
[14] http://www.czrea.org/cs/druhy-oze/fotovoltaika/inst-vykon2009-eru, (accessed 11/10)
[15] http://www.iea-pvps.org/countries/download/nsr09/NSR%%20202009%%2020Italy.pdf, (accessed 10/10)
[16] http://www.iea-pvps.org/countries/download/nsr08/NSR%% 20Spain 202008_v2.pdf, (accessed 10/10)
[17] http://www.iea-pvps.org/countries/download/nsr09/Country% 20Report% 202009.pdf 20Germany%, (accessed 10/10).

Jerzy Mikulski – Jakub Mlynczak *

THE FIRST APPLICATION OF THE ELECTRODYNAMIC WAGON RETARDER IN POLAND

The article discusses design and installation method of the EDG Electrodynamic Wagon Retarder at the railway siding of the Power Plant Rybnik. It is the first structure of its kind in Poland. Up to now mostly hydraulic brakes have been used in Poland. They were difficult to operate and hardly environmentally friendly due to contamination and noise. Electrodynamic wagon retarders are free from such defects. The issue of introducing new railroad brake construction in Poland is very important because the Polish Railway Lines (PLK) are confronted with the need of devices modernization on a humps. The German railways' experience confirms the effectiveness of this type of brake. Especially the field tests in Germany and Poland show that the electrodynamic retarders do not have a negative impact on the occupancy control system.

1. Introduction

At present, mostly hydraulic brakes are used in marshalling of wagons. They are generally in the form of platforms, sometimes poppet brakes. Maintenance of the hydraulic brakes is difficult due to their outdated design. They also constitute a threat to the environment. The threat consists in brakes utilising oil, which leaks out to the environment, and both oil-feeding system and retarder shoes generate noise, which is a nuisance to people living nearby. To eliminate the said disadvantages, the Power Plant Rybnik has erected a test installation of the electrodynamic wagon retarder system type EDG. It is the first structure of its kind in Poland.

The article discusses applications and test results of electromagnetic radiation generated by the retarder, with emphasis on the requirements regarding the protection of persons working near the retarder.

2. Characteristic of EDG Retarder

The purpose of the electrodynamic wagon retarder (EDG) (Fig. 1), considering the safety requirements and quality of marshalling, is to reduce the speed of individual wagons and groups of wagons in gravitational marshalling system. The system is already proven, and it does not require frequent repairs and maintenance. The major advantages of electrodynamic wagon retarders are low-noise missions during operation, both during tests of retarding jaws and during actual retarding of wagons. The symmetrical braking force of the jaws (two-sided retarders) continuously affects wagon wheels, eliminating the effect of wheel-set lifting while braking. The smoothly applied braking force and additional magnetic effect on the wagon wheel prevent the transfer of forces from a rolling wagon onto the retarder and its foundation in pulses.

Basic features of the Electrodynamic Retarder EDG – 93 are summarized below:
- It can be used as a service, group or an additional brake;
- It can be operated as a destination and distance brake;
- It enables manual, semi-automatic, or fully automatic control;
- Its installation length is of 5 m to 20 m (by 2.5 m);
- The maximum height of the situate retarder beams to the lateral side of a railway wagon wheel ring is equal to 63 mm;
- It can function as a retarder when installed on both rails. Braking forces are generated by 3 simultaneous factors: friction between the wheels and the retarder beams, friction between the retarder beams and the retarder body, caused by the cutting of the wheel through braking beams and the eddy current;
- It is fitted with electric actuators of braking beams;
- It is fitted with electronic retarder control, including the Profibus connection system;
- It is fitted with electronic controls.

The main elements of the construction (Fig. 2):
- Retarder (consists of a body of the retarder, the bearing beams of retarder and excitation winding) (1);
- Container with the control devices and power (rectifier) (2);
- Operation place with a control panel (touch screen) (3).

Operating position:
- Locomotive passage position – in that position, braking beams move freely in the bodies, and the retarder can be driven through with no resistance whatsoever;

* **Jerzy Mikulski, Jakub Mlynczak**
Faculty of Transport, Silesian University of Technology, Katowice, Poland, Email: jerzy.mikulski@polsl.pl

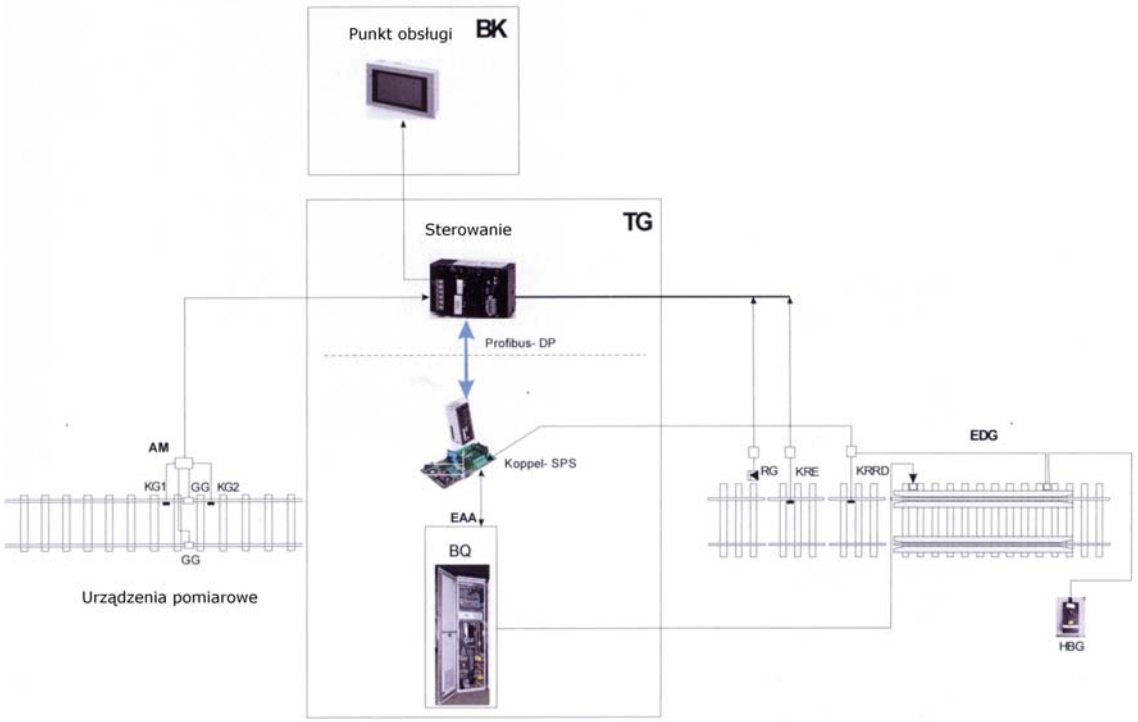

Fig. 1 Diagram of electrodynamic retarder installation at the Power Plant Rybnik; EDG – Electrodynamic Wagon Retarder, AM – system providing detection of wheel load, KG1 – wheel detection sensor (on-switch), KG2 –wheel detection sensor (off-switch), GG – weight sensor, RG - radar, KRE – wheel detection sensor (entrance), KRRD – wheel detection sensor (entrance, reserve), TG – technical building, BQ – rectifier.

Fig. 2 Electrodynamic Wagon Retarder system at the railway siding of the Power Plant Rybnik.

– Braking position - DC voltage is supplied to the retarder, braking beams are moved to the braking position.

Controls:
– Commands are sent from the control panel and via respective controls;
– There is manual enforcement of indicated or calculated optimum (target) speed of leaving the retarder;
– The required braking force is reached by the electromagnetic force field.

Brief characteristics of the installation

The purpose of the EDG retarder (Fig.3) at the railway siding of the Power Plant Rybnik is to brake the wagons going down the cradle of tippler 3 to one of the destination tracks. Tracks of the remaining tipplers are fitted with ETH retarders.

The EDG retarder is erected on the track. Between the retarder and switch, there is a manual brake skids launcher acting as the braking component in the event of EDG retarder failure.

The track where the EDG retarder is erected is an access track to destination tracks for empty wagons. Leaving the tippler (Fig.3 b, 4a), empty wagons pass through the cradle (Fig. 4b), where the direction of wagon movement is changed. Wagons moving from the cradle to the destination tracks (Fig. 5) need to have the speed suitable for the active length of tracks, i.e. for wagons that are supposed to park at the end of the destination track, such speed is to be high enough to allow the wagon to travel the required distance; in the event when the track is already full, such speeds can be lower. Until now, the brake skids launcher was used for that purpose. The said solution features low accuracy in the selection

Fig. 3 a) EDG retarder, b) Tippler

Fig. 4 a) Wagon on tippler, b) Cradle

of speed of marshalled wagons, resulting in the need to push the wagons further (in case of insufficient speed), or in wagons hitting the buffers with excessive force, resulting in excessive buffer wear and noise.

Fig. 5 Unloading rail tracks

3. Assessment of Parameters of the Electrodynamic Retarder EDG

The retarder manufacturer has a package of documents evidencing that the EDG retarder meets the parameters referring to electromagnetic compatibility, the requirements regarding electronic traffic control systems, software for traffic control systems, as well as safety and reliability.

Electromagnetic Compatibility

Pursuant to those documents, the EDG Wagon Retarder, including the accessories, meets the requirements regarding electromagnetic compatibility as per the scope of standards [4].

Software and hardware

The EDG Wagon Retarder meets the requirements of railway standards [5], [6] and [7] with regard to reliability, availability, maintenance susceptibility and safety, and the software for railway traffic control systems, including electronic traffic control systems.

Permanent way and structure clearance

It is to be noted that the EDG Wagon Retarder was fitted with a diagnostic system of permanent way diagnostic system notifying

the operator on inter alia defective track sub-base, or material differences in the condition of rail courses of both retarder rails. In addition, the manufacturer is executing the retarder in all kinds of rails, depending on local conditions, in order to avoid implementation of the intermediate rail.

A radar is used in the EDG Wagon Retarder to measure the speed of marshalled wagons. The radar is erected so as to ensure the keeping of structure clearance.

It is to be stated that the device meets the requirements of Polish regulations regarding the permanent way and clearance as per the scope of assessed requirements.

4. Measurements of the Electromagnetic Field Intensity at the Retarder and Supply Point

Measurements of the electromagnetic field were carried out to the requirements of standards [9] and [10]. The measurements were carried out for the wagon retarder and the adjacent area, as well as for the control room and control point. The layout of measuring points at the retarder is shown in Fig. 6. The measurement of the static magnetic field is shown in Fig. 7a and the rotating magnetic field in Fig. 7b. Results of measurements for the wagon retarder are shown in Table 1. During the measurements in the control room and at the control point, no magnetic field exceeding the background value was observed.

Measuring points 1 to 6 are located, respectively, 0.1, 0.3, 0.5, 1, 2, 3 m from the rail, at the height of 0.3 m.

No variable electromagnetic radiation exceeding the background level was observed at the retarder.

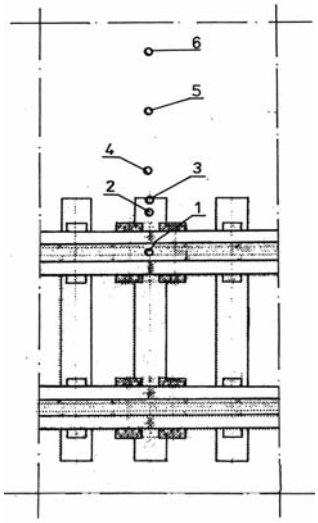

Fig. 6 Measurement zones

The zone limits for the work stations are:
- The limit between the safe zone and intermediate zone is 3.3 mT;
- The limit between the intermediate zone and the risk zone is 10 mT;
- The limit between the risk zone and the hazard zone is 100 mT.

In the safe zone, workers can stay without any restrictions. In the intermediate zone, workers can stay for 8 hours during work shift. Measurements suggest that the range of the intermediate zone is up to 1 m from the retarder, which means that during the occurrence of the magnetic field (passage of wagon), workers cannot

Fig. 7 Measurement of the a) static magnetic field b) rotating magnetic field

stay in this zone. Regarding other measuring points, the respective zones are considered safe.

Table 1

Results of measurements of magnetic fields around the wagon retarder		
Item	Maximum intensity	Characteristics of the location of measuring stack
	[mT]	
1	4.1	Idle run
	200	Simulation of max. load
2	0.57	Idle run
	11.2	Braking of wagon
	12.1	Simulation of max. load
3	0.29	Idle run
	2.8	Braking of wagon
	3.3	Simulation of max. load
4	0.28	Idle run
	2.2	Braking of wagon
	3.2	Simulation of max. load
5	0.23	Idle run
	1.2	Braking of wagon
	1.4	Simulation of max. load
6	0.12	3 m from the rail (idle run)
	0.21	3 m from the rail (braking of wagon)
	0.4	3 m from the rail (simulation of maximum load)

5. Conclusion

The first wagon retarder installation in Poland was executed at the railway siding of the Power Plant Rybnik. The retarder is used to reduce the speed of empty wagons leaving the tippler cradle. Such a location of the test field enables testing of the solution in Polish conditions.

In case of this application, the risk connected with possible brake failure is minimised since only empty coal wagons, the speed and weight of which are low, are being retarded. As the investor is aware of the fact that such a solution is new in Poland, the brake skids launcher installation is maintained to increase the reliability of operation. That shall increase the safety of the railway siding at the Power Plant Rybnik.

The dimensions of the retarder (including weight) and requirements regarding supply parameters render the laboratory tests of the device impossible. It was only the erection of the test installation at the facility that enabled the performance of the functional tests of the device.

The test installation enabled also the measurements of the intensity of the magnetic field around the EDG wagon retarder and in the control room. The said measurements carried out according to relevant standards enabled to ensure that the solution examined is safe to the operating personnel. In the control room and at the control point, no electromagnetic radiation exceeding the background was observed, too.

References

[1] Regulation by Minister of Infrastructure on the scope of examinations required to obtain Commissioning Certificates of types of buildings and facilities designated for management of railway traffic and types of railway vehicles, dated 12 October 2005 (JoL No. 212, item 1772, dated 12/10/2005)

[2] Regulation by Minister of Infrastructure on general engineering conditions for operation of rolling stock, dated 12 October 2005 (JoL No. 212, item 1771, dated 12/10/2005).

[3] Rail Transport Act dated 28 March 2003.

[4] EN 50121 – Railway Applications – Electromagnetic Compatibility

[5] EN 50126 – Railway Applications – Specification of reliability, availability, maintenance susceptibility and safety

[6] EN 50128 – Railway Applications. Communications, signalisation and control systems - Programmes for railway control and protection systems.

[7] EN 50129 – Railway Applications – Communication, data processing and traffic control systems. Safety-related electronic traffic control systems.

[8] PN-T-06580-1:2002 – Protection of work in fields and electromagnetic radiation with frequency 0 Hz to 300 GHz. Part 1: Terminology

[9] PN-T-06580-3:2002 – Protection of work in fields and electromagnetic radiation with frequency 0 Hz to 300 GHz. Part 3: Terminology

[10] OPERATIONAL AND ENGINEERING DOCUMENTATION Electrodynamic Wagon Retarder EDG – 93 by FEW for application in humps, Rev. 01/2008, Wichary Technologies. Siemianowice, 2008.

[11] Engineering Conditions for Execution and Acceptance of Electrodynamic Wagon Retarder Type EDG – 93, Rev. 01/2008, Wichary Technologies. Siemianowice, 2008.

COMMUNICATIONS – Scientific Letters of the University of Zilina
Writer's Guidelines

1. Submissions for publication must be unpublished and not be a multiple submission.
2. Manuscripts written **in English language** must include **abstract** also written in English. The submission should not exceed **10 pages** with figures and tables (format A4, Times Roman size 12). The **abstract** should not exceed 10 lines.
3. Submissions should be sent: **by e-mail** (as attachment in application MS WORD) to one of the following addresses: *komunikacie@uniza.sk* or *holesa@uniza.sk* or *vrablova@uniza.sk* or *polednak@fsi.uniza.sk* **with a hard copy** (to be assessed by the editorial board) **or on a CD** with a hard copy to the following address: Zilinska univerzita, OVaV, Univerzitná 1, SK-010 26 Zilina, Slovakia.
4. Abbreviations, which are not common, must be used in full when mentioned for the first time.
5. Figures, graphs and diagrams, if not processed by Microsoft WORD, must be sent in electronic form (as GIF, JPG, TIFF, BMP files) or drawn in contrast on white paper, one copy enclosed. Photographs for publication must be either contrastive or on a slide.
6. References are to be marked either in the text or as footnotes numbered respectively. Numbers must be in square brackets. The list of references should follow the paper (according to **ISO 690**).
7. The author's exact **mailing address of the organisation where the author works, full names, e-mail address or fax or telephone number,** must be enclosed.
8. The editorial board will assess the submission in its following session. In the case that the article is accepted for future volumes, the board submits the manuscript to the editors for review and language correction. After reviewing and incorporating the editor's remarks, the final draft (before printing) will be sent to authors for final review and adjustment.
9. The deadlines for submissions are as follows: September 30, December 31, March 31 and June 30.

COMMUNICATIONS

SCIENTIFIC LETTERS OF THE UNIVERSITY OF ZILINA
VOLUME 13

Address of the editorial office:
Zilinská univerzita
Office for Science and Research
(OVaV)
Univerzitna 1
SK 010 26 Zilina
Slovakia
E-mail: komunikacie@nic.uniza.sk,
pavel.polednak@fsi.uniza.sk

Each paper was reviewed by two reviewers.

Journal is excerpted in Compendex and Scopus

It is published by the University of Zilina in
EDIS – Publishing Institution of Zilina University
Registered No: EV 3672/09
ISSN 1335-4205

Published quarterly

Single issues of the journal can be found on:
http://www.uniza.sk/komunikacie